# Combustion Synthesis of Nanomaterials Using Various Flame Configurations

Dissertation by

**MOHAMED ANWAR ISMAIL**

In Partial Fulfillment of the Requirements

For the Degree of

Doctor of Philosophy

In Mechanical Engineering

Supervisor

**Prof. SUK HO CHUNG**

King Abdullah University of Science and Technology (KAUST)

Thuwal, Kingdom of Saudi Arabia

## EXAMINATION COMMITTEE APPROVALS FORM

The dissertation of **Mohamed Anwar Ismail** is approved by the examination committee.

Committee Chairperson : William L. Roberts

Committee Member : Suk Ho Chung (Supervisor)

Committee Member : Mani Sarathy

Committee Member : Mansoo Choi

Committee Member : Nasir Memon

# ABSTRACT

Combustion Synthesis of Nanomaterials Using Various Flame Configurations

Mohamed Anwar Ismail

Titanium dioxide ($TiO_2$) is an important semiconducting metal oxide and is expected to play an important role in future applications related to photonic crystals, energy storage, and photocatalysis. Two aspects regarding the combustion synthesis have been investigated; scale-up in laboratory synthesis and advanced nanoparticle synthesis.

Concerning the scale-up issue, a novel curved wall-jet (CWJ) burner was designed for flame synthesis. This was achieved by injecting precursors of $TiO_2$ through a central port into different flames zones that were stabilized by supplying fuel/air mixtures as an annular-inward jet over the curved wall. This provides a rapid mixing of precursors in the reaction zone with hot products. In order to increase the contact surface between the precursor and reactants as well as its residence time within the hot products, we proposed two different modifications. The CWJ burner was modified by adding a poppet valve on top of the central port to deliver the precursor tangentially into the recirculating flow upstream within the recirculation zone. Another modification was made by adopting double-slit curved wall-jet (DS-CWJ) configuration, one for the reacting mixture and the other for the precursor instead of the central port. Particle growth of titanium dioxide ($TiO_2$) nanoparticles and their phases were investigated. Ethylene ($C_2H_4$), propane ($C_3H_8$), and methane ($CH_4$) were used with varying equivalence ratio and Reynolds number and titanium tetraisopropoxide (TTIP) was the precursor. Flow field and flame structure were quantified using particle image velocimetry (PIV) and OH planar laser-induced fluorescence (PLIF) techniques, respectively. $TiO_2$ nanoparticles were characterized using high-resolution transmission electron microscopy

(HRTEM), X-ray diffraction (XRD), Raman Spectroscopy, and BET nitrogen adsorption for surface area analysis.

The flow field quantified by PIV consisted of a wall-jet region leading to a recirculation zone, an interaction jet region, followed by a merged-jet region. The modified CWJ burner revealed appreciable mixing characteristics between the precursor and combustion gases within these regions, with a slight increase in the axial velocity due to the precursor injection. This led to more uniformity in particle size distribution of the synthesized nanoparticles with the poppet valve (first modification). The double-slit modification improved the uniformity of generated nanoparticles at a very wide range of stable experimental conditions. Images of OH fluorescence showed that flames are tightly attached to the burner tip and TTIP has no influence on these flames structures. The particle size was slightly affected by the operating conditions. The phase of $TiO_2$ nanoparticles was mainly dependent on the equivalence ratio and fuel type, which impact flame height, heat release rate and high temperature residence time of the precursor vapor. For ethylene and methane flames, the anatase content is proportional to the equivalence ratio, whereas it is inversely proportional in the case of propane flames. The anatase content reduced by 8% as we changed Re between 8,000 and 19,000, implying that the Re has a slight effect on the anatase content. The synthesized $TiO_2$ nanoparticles exhibited high crystallinity and the anatase phase was dominant at high equivalence ratios ($\phi$ >1.6) for $C_2H_4$, and at low equivalence ratios ($\phi$ <1.3) for the $C_3H_8$ flame.

Concerning advanced nanoparticle synthesis, a multiple diffusion burner and flame spray pyrolysis (FSP) were adopted in this study to investigate the effect of doping/coating on $TiO_2$ nanoparticles. The nanoparticles were characterized by the previously mentioned techniques in addition to thermogravimetric analysis (TGA) for carbon content, X-ray photoelectron spectroscopy (XPS) for surface chemistry, ultraviolet-visible spectroscopy (UV-vis) for light absorbance, inductively coupled plasma (ICP) for metal traces, and superconducting quantum

interference device (SQUID) for magnetic properties. Results from multi diffusion burner show that doping $TiO_2$ with vanadium changes the phase from anatase to rutile while doping and coating with carbon or $SiO_2$ does not affect the phase. Doping with iron reduces the band gab of $TiO_2$ particles by reducing the conduction band. FSP results show that iron doping changes the valance band of the nanoparticles and enhances their paramagnetic behavior as well as better light absorption than pure titania, which make these particles good candidates for photocatalytic applications.

# ACKNOWLEDGMENT

First of all, all praise be to ALLAH for helping and supporting me in everything.

I would like to express my profound sense of gratitude & appreciation to my Supervisor Prof. Suk Ho Chung who guided and supported me in every possible way with his experience, motivation, and the positive attitude. Also I am very grateful to my committee members Prof. William Roberts, Prof. Mansoo Choi, and Prof. Mani Sarathy.

I feel responsible to express my thanks and gratitude to Dr. Nasir Memon and Dr. Morkous Mansour for their support, helpful comments and assistance. Also I am very thankful to all people who are working in the Clean Combustion Research Center at KAUST. I would like to express my heart-full thanks to my friends at CCRC, Saeed Al-Noman, Ossama Mannaa, Dr. Ahmed El-Wardani, and Issam Al-Khesho, who made my life at KAUST very pleasant.

I am very grateful to staff of XRD, BET, TEM, and XPS labs at KAUST for their help in offering the proper training and help during the experiments.

I can't forget to thank my parents who supported me with their kind, patience and encouragement. Finally, I would like to express my deep gratitude, thanks, and love to my wife, who gave me the motivation and support to finish this work.

*Allah bless you all*

*Mohamed Anwar Ismail*

# Table of Contents

# List of Tables

# List of Figures

# Chapter 1

# Introduction

## 1.1 Overview

Nanomaterials and nanotechnology are an important research topic since their applications cover many areas of daily life. Nanomaterials are used for home applications such as pigments, paint, tooth paste, and food additives, and for various industrial and transportation applications (e.g., airplanes and aerospace industries). Recently, their very advanced applications for energy issues such as photocatalysis and water splitting for hydrogen generation have drawn attentions.

Nanomaterials have different physical and chemical properties other than their corresponding bulk materials. They can be classified to 0-D, 1-D, 2-D, and 3-D nanomaterials [1]. The 0-D nanomaterials are mainly nanoparticles that have an average diameter ranging from 1-100 nm. The 1-D nanomaterials are those materials which have one of their dimensions in the nano scale whereas the other dimension can be in micro scale, such as nanowires and nanoneedles. The 2-D and 3-D nanomaterials are those materials which have at least one or more of their dimensions in the nano scale, such as nanoflakes and nanoflowers.

Titanium dioxide ($TiO_2$) is the second nanomaterial after carbon black based on the rate of production and its value point of view. It is produced in the range of mega tons per year and has versatile range of applications due to its natural abundance, low production cost, and non-toxicity. Different materials can be added to $TiO_2$ as dopants, coating, or mixed oxides to change its properties, such as band gab, optical properties, and magnetic properties. Flame synthesis is one of the most important methods used for the production of nanomaterials and it

has been widely used in industry for large scale production. Many types of burners have been used in flame synthesis in laboratory scale research starting from flat flames and simple diffusion flames to turbulent and spray flames.

Advanced $TiO_2$-based nanoparticles are interesting because of their possible applications in photocatalytic splitting of water [2], dye-sensitized solar cells [3], air/water purification [4], and catalyzing many chemical reactions [5]. The commonly observed phases of $TiO_2$ include the anatase and rutile phases. Rutile $TiO_2$ is widely produced in industry for pigment applications, while anatase $TiO_2$ is more photocatalytic.

In this study, we will mainly focus on the combustion synthesis of $TiO_2$ nanoparticles. We will start with laminar multi-diffusion burner to prepare $TiO_2$ nanoparticles doped/coated with different materials, such as carbon, silicon, vanadium, and iron. Next, a turbulent flame spray pyrolysis technique will be used to study the effect of various dopant materials on $TiO_2$ nanoparticles and other materials such as bismuth and cerium.

Apart from these two burner configurations (based on diffusion flames), we will study a new burner named as a curved wall-jet burner (CWJ) [6, 7]. A premixed mode of CWJ burner is used for $TiO_2$ and $SiO_2$ productions. The burner is designed for rapid mixing between flame gases and nanomaterial precursor, which exists in a high temperature and rich oxygen region, leading to high production rate of pure and well-crystallined nanoparticles.

We have tested three modified CWJ burner configurations starting with a simple central tube for precursor delivery, a poppet valve type installation at the exit of the central tube, and a double-slit CWJ configuration. In all of the CWJ burner configurations, the effect of equivalence ratio, Reynolds number, fuel, and precursor loading rate are studied.

## 1.2 History of Nanomaterials

The Romans used smoke particles from flames in preserving food and Chinese collected these smoke particles and made the high quality black ink. Nanoparticles were first used by the Chinese in making inorganic dye for their colorful paintings more than a thousand of years ago. Pharos and Romans used these nanoparticles for paint and decoration of their temples [8]. Colloidal gold (Faraday 1857) still used in medical applications (Arthritis) and from that time, nanomaterials spread over many fields of applications.

Over the past decades, numerous techniques have been developed for the production of metal-oxide nanoparticles, including laser ablation, microwave plasma synthesis, precipitation from solution, plasma arc synthesis, hydrodynamic cavitation, spray pyrolysis, and flame synthesis. When utilizing flames, energy is generated from chemical reactions which result in particle formation. In essence, flames provide both high temperature and chemical species necessary for particle growth. The released energy is removed rapidly by radiation and convection which is essential for synthesis of nanostructured particles [9]. The size of primary particles ranges from a few to several hundred nanometers in diameter, depending on material and process conditions. More recently, premixed and diffusion flames were used for generating carbonaceous materials like fullerene, carbon nanotubes, and graphene films [10, 11].

## 1.3 Titanium Dioxide Nanoparticles

$TiO_2$ has been manufactured on a very large scale, more than 5 million metric tons per year, and increasing with about 15% every year. $TiO_2$ is abundant and non-toxic material with many fascinating properties such as high photostability, strong UV light filtering which makes it a very good candidate for the applications of paint additives, sunscreen, and pigments to name a few uses. During the last two decades, $TiO_2$ has been extensively investigated especially for environmental and energy applications [12]. Fujishima and Honda [13] in 1972 published the

first work on photocatalytic splitting of water on a $TiO_2$ electrode under ultraviolet (UV) light. This discovery was the spark for a tremendous amount of research related to photocatalytic applications of $TiO_2$ including water and air purification. In the same year, Tributsch [14] introduced the idea of a dye-sensitized solar cell, using zinc oxide (ZnO) electrode to collect most of the visible light radiation and produce an electric current by charge injection from the excited dye molecules into the wide band gap metal oxide. Although ZnO was reported in the first dye-sensitized solar cell, $TiO_2$ soon became the most popular semiconductor material for later dye-sensitized solar cells, mainly due to its better photostability and its band gab. These two reports in 1972 can be considered as the milestone research reports for $TiO_2$ and they were the momentum of other $TiO_2$ research and development.

$TiO_2$ nanostructure has attracted significant attention in the last two decades due to its interesting electrical [15] optical [16] and magnetic properties. Because of these properties, $TiO_2$ is used in a number of advanced applications starting from biomedical applications [19], functionalized hybrid materials [20], catalysis [17], energy conversion [18], and nanocomposites [21]. Because of its semiconductivity, photoelectrical and photochemical activity under UV light, $TiO_2$ nanostructures can be used as dye-sensitized solar cells [22] and photoelectrochemical cells (PEC) [23], photocatalysis, chemical sensors [24], self-cleaning coating [25], and $TiO_2$/polymer nanocomposites [26].

$TiO_2$ nanoparticles has mainly three crystal structures; anatase, rutile, and brookite phases as shown in Fig. 1.1. The phase identifies the way titanium and oxygen atoms are arranged in the crystal which has three dimensions a, b, and c in each of the Cartesian coordinates. Anatase (ditetragonal dipyramidal structure, a =b= 3.785 Å, c = 9.513 Å), rutile (tetragonal structure, a =b= 4.593 Å, c = 2.959 Å), and brookite (orthorhombic structure, a = 9.181 Å, b = 5.455 Å, c = 5.142 Å) [15]. The rutile phase is the most stable phase and has 3.06 eV band gab energy, whereas anatase and brookite are less stable than rutile and have band gab energies of

3.3 eV and 3.5 eV, respectively. The unit cell volume of anatase contains four $TiO_2$ groups, whereas it contains two and eight $TiO_2$ groups for the rutile and brookite, respectively. The brookite phase is very rare in the nature as it transforms very quickly to one of the other two phases (anatase or rutile). Rutile has a very white color, so it can mainly be used for paints and advanced pigments. The anatase and brookite are mainly used in sensors, dye-sensitized solar cells, and photocatalysis due to their high surface area and large porous aggregates [16].

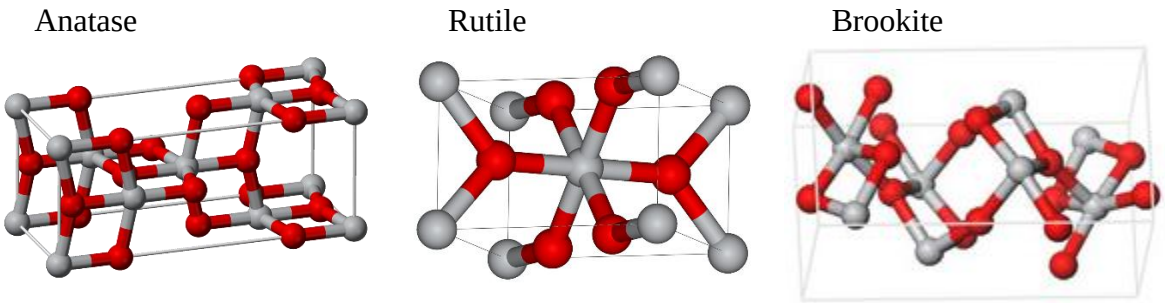


**Figure 1.1:** Representations of $TiO_2$ anatase, rutile, and brookite forms [15].

## 1.4 Gas Phase Synthesis Methods

Nanomaterials are synthesized mainly using two approaches; up-bottom and bottom-up approaches [17]. In the up-bottom approach, the bulk material is grinded until reaching the nanoscale size. But it is very hard to control the size of the resulted nanomaterials and contains a wide range of size distribution. While the bottom-up approach uses a precursor for a material and with chemical reaction, aerosol formed first, then coalescence, collision, and sintering occur until having primary particles which grow with time leading to aggregates and agglomerates of the nanomaterial. In this approach, most of the parameters (particle size, morphology, phase, and composition) can be controlled.

Many wet chemistry methods have been used for nanomaterials production. They are precise in controlling most of the parameters but they possess a lot of disadvantages as; solid-liquid separation, washing, drying, and calcination which take long time to produce small quantity of required nanomaterial. Gas-phase processes (combustion synthesis) are considered as one of

the effective ways for nanoparticle production. They are single-step process and do not involve all the extensive steps related to wet-chemistry methods. Moreover, the nanoparticles produced through this route are very pure with high yield and continuous production.

To prepare nanoparticles, one should create high nucleation density by inducing a very high degree of supersaturation and then quench the system immediately. The system quenching is required to prepare small nanoparticles and can be performed by slowing the kinetics or removing the source of supersaturation. Once a precursor is exposed to high flame temperatures, it rapidly evaporates and pyrolyzes into radicals that then react to form intermediate and product molecules and clusters that quickly grow to nanosize particles by coagulation, coalescence, and/or surface reactions. As the aerosol stream leaves the high temperature zone, and travels toward a cooled collection plate or a filter, particle growth continues mostly by coagulation (coalescence is suppressed due to decreased temperature), resulting in aggregates of primary particles agglomerates (soft agglomerates) and aggregates (hard agglomerates) [18]. This whole process happens very rapidly (in the order of milliseconds or at maximum in seconds). In the coming sections, we will focus on the gas-phase methods for synthesizing nanoparticles. It is better to classify them based on the precursor phase and the energy source used to achieve a supersaturation state.

In general, to achieve supersaturation that is necessary for homogeneous nucleation and consequently for primary particle formation, a precursor should be vaporized into a background gas. Then this gas has to be cooled to condensate the nanomaterial. Methods using solid precursors in wet chemistry processes include inert gas condensation [19-24], pulsed laser ablation [25-29], spark discharge generation [30, 31], and ion sputtering [32]. Methods using liquid or vapor precursors include chemical vapor deposition [33-39], laser pyrolysis [40-42], thermal plasma synthesis [43], spray pyrolysis [44, 45], and low-temperature reactive synthesis [46].

## 1.5 Flame Synthesis

Flame synthesis can readily offers high temperature and oxidizing environment necessary for the growth of nanoparticles (NPs). In the previously mentioned wet chemistry methods, energy is supplied externally to induce reaction and particle nucleation. . In a flame, particle synthesis can be carried out within a flame since combustion reactions provide the process with the heat needed to form particles. Flame synthesis produces millions of metric tons per year of carbon black, $TiO_2$, and other metal oxides and considered as the most commercially successful method for nanoparticle production [47]. Flame synthesis is a large scale production, one-step and continuous process which provides very high temperature gradient at high temperatures and very short residence times [48]. In this introduction, the experimental research on flame synthesis of metal oxides is highlighted.

Ulrich and co-workers [18, 49] took the initiative steps into the investigations of flame synthesis of ceramic powders by studying synthesis of $SiO_2$ by $SiCl_4$ oxidation in laminar premixed and turbulent jet flames. For the first time, coagulation rather than nucleation was recognized as the dominant particle formation mechanism. Additionally, self-preserving size distributions among the synthesized particles were predicted, which were also observed in the experiments by Vemury and Pratsinis [50]. However, different particle size distributions have occurred due to the contributions of different particle formation mechanisms.

Wooldridge [51] summarized the fundamental processes governing gas-phase combustion synthesis of NPs; production of non-oxide, single-oxide, and mixed-oxide powders; parameters influencing particle morphology and composition, nucleation and growth models of NPs. The processes of nucleation, deposition, coalescence and agglomeration were found to be strong functions of the system conditions (temperature, pressure, burner configuration, reactant concentrations, etc.).

Most of the lab-scale experiments for flame synthesis are based on laminar flames including premixed [52] and diffusion flames [53]. Detailed reviews of various burner geometries used for $TiO_2$ synthesis have been reported previously [54-56]. Turbulent flames are used in real large-scale production of nanomaterials but they suffer from the complexity of physical processes involved in flame stabilization and nanomaterial growth [48] and basic studies using lab-scale turbulent flames are very limited.

Girshick and Chiu [57] studied particle formation in turbulent flames within a plasma reactors. At the reactor entrance, chemical reaction occurs at high temperatures and particle coalescence is faster than collision which results in spherical particles. Downstream, particles grow further and particle coalescence becomes slower than collision due to lower temperatures. Far downstream, due to low temperatures, collision dominates which results in irregular particles that are hard or soft agglomerates of smaller spherical unitary particles. A premixed, turbulent oxygen-acetylene flame, using a commercial brazing torch was used to synthesize high quality polycrystalline diamond films on molybdenum substrates [58, 59].

Xiong and Pratsinis [60] developed a theoretical study to analyze the interaction between chemical reaction, Brownian and shear-induced coagulation in highly non-isobaric, non-isothermal, turbulent flows, during gas phase production of silica. It was found that initially, particle growth is controlled by chemical reaction and Brownian coagulation while later shear-induced coagulation becomes predominant. They deduced that particle size increases with increasing pressure while it decreases with increasing temperature, initial mole fraction of the reactants, and turbulence intensity. Away from the burner tip, cooling has a major effect on particle coalescence rate which causes the formation of non-spherical agglomerates.

Due to their unique advantages, flame aerosol reactors can be considered as one of the most important ways to generate nanoparticles. These advantages include; producing a wide range

of oxide nanomaterials, self-purifying process, high temperature with high temperature gradient, good control of the nanomaterial properties, and very fast process [61]. In the process of flame spray pyrolysis (FSP), liquid precursor can directly be sprayed into the flame without any need of additional heating to get supersaturated vapor. This method allows the use of viscous precursors that do not have sufficiently high vapor pressure to be delivered as a vapor. The injected precursor enters the flame region as very fine droplets, which later on start to vaporize and react to form the nanomaterial.

Pratsinis [55] reviewed the history of flame aerosol synthesis of ceramic powders (commodities) such as pigmentary titania, fumed silica, and alumina. He summarized the dynamics of spherical particles and advances in theory of aggregate particle dynamics encountered in flame synthesis of powders. Mädler et al. [62] presented a very detailed, systematic investigation and description of FSP method, as applied to the synthesis of $SiO_2$ nanoparticles using hexamethyldisiloxane (HMDSO) as a precursor. They made a good combination of experimental and modeling work which showed that oxidant flow rate and precursor/fuel composition can control the primary particle size and consequently the surface area of the produced silica particles. Teoh et al. [47], discussed the evolution of aerosol reactors (including FSP) during the last century and the first decade in 21$^{st}$ century. They also studied the different formation mechanisms of nanoparticle evolution. FSP has been used to prepare nanomaterials with controlled properties [63] under controlled atmosphere. Iskandar [64] reviewed the use of spray methods to prepare nanoparticles for optical applications. Flame spray pyrolysis technique has been used to prepare different nanomaterials [5, 63, 65-70]. Strobel et.al., [71] provided a review of flame-made catalysts (photocatalysts, vanadia-based catalysts, $TiO_2/SiO_2$ epoxidation catalysts, ceria-based catalysts, perovskites, $NO_x$ storage reduction catalysts, and supported metal catalysts). They also discussed the particle formation processes occurring during different flame configurations. They stated the two basic particle

formation processes that can be observed; particle formation in a droplet leading to large or hollow particles (spray pyrolysis and partly in FSP) and particle formation from the gas phase resulting in small nano-sized particles (VAFS, FSP and partly spray pyrolysis). These two routes (gas-to-particle and droplet-to-particle routes) for nanoparticles synthesized using flame technology were studied experimentally and numerically [55, 64, 72-75].

## 1.6 Introduction to Curved wall-Jet Burner

Turbulence is a major parameter and has been involved in most of combustion processes. Turbulent flames have many features, outstanding one of them is the high rates of transfer and mixing. These rates are more than one order of magnitude higher than in laminar flames. The main reason of these higher rates is the presence of eddies, which have higher effective diffusion coefficient than molecular diffusion coefficient. According to Reynolds number, the effective diffusion coefficient can be as higher as two order of magnitudes more than the molecular diffusion coefficient [58]. Consequently, the transport of momentum, heat, species, and particles are greatly enhanced when moving from laminar flow towards turbulent flow.

Turbulent premixed flames have been widely used in several important applications. The major one is the (homogeneously charged) spark-ignition engine. Other examples are industrial tunnel burners, gaseous explosions in a turbulent atmosphere, and reheat systems in jet engines [76]. Simple jet flames suffer from stabilization problems especially at high turbulent intensities [77, 78]. Many studies have been conducted to enhance the stabilization characteristics of the turbulent premixed flames using weak swirl [79], Pulsed plasma [80], bluff-body [81], and by changing the burner geometry [82].

Many parameters are controlling the growth of nanoparticles such as burner geometry, fuel/oxidizer flow rates, precursor loading rate, residence time, and fuel type [54]. Common fuels investigated include carbon monoxide [83], hydrogen [84], methane [3], propane [85] and

ethylene [86]. Of particular interest is the use of propane, as it can further reduce the cost of flame synthesized nanoparticles. Moreover, nanoparticles produced using a propane/air mixture resulted in nanoparticles with properties comparable to commercially made Degusa P25 $TiO_2$ [87]. For the continued advancement of flame synthesis technologies, it is important to develop novel reactors and to extend our understanding of growth processes.

The curved wall-jet (CWJ) burner was first proposed by Gil et al. [6] and tested for premixed turbulent flames. This burner was designed based on the principle of the Coanda effect discovered by the Romanian inventor Henri Marie Coanda (1886- 1972) [88]. The Coanda effect is based on the phenomenon of attachment of a jet flow to a nearby surface and to remain attached even when the surface bends away from the initial jet direction [89]. The CWJ burner [6] showed good flame stabilization characteristics and short flame length. Later on, Kim et al. [7] modified the burner tip by introducing a concave cavity, which further improved flame stabilization. Recently, Mansour and Chung [90] proposed a new configuration of the CWJ burner by having double-slit, one for the air flow and the other for the fuel flow. They studied the flame stabilization characteristics and structure of propane/air flames under non-premixed and turbulent conditions.

A modified curved wall-jet (CWJ) burner (Chapter 5) is designed for flame synthesis, by injecting precursors through a center tube and by supplying fuel/air premixtures as an annular-inward jet for rapid mixing of the precursors in the reaction zone. A modification of the premixed CWJ burner (Chapter 6) has been done by using a poppet valve type precursor flow guide on the top of the central tube to enhance mixing and particle size distribution. A further modification for the CWJ burner (Chapter 7) is made by using a double-slit configuration instead of the previous premixed CWJ burner with single slit and central tube. This double-slit curved wall-jet (DS-CWJ) burner is designed to supply precursors and fuel/air premixtures in

parallel and having overlapping recirculation zones for better mixing between the precursor and combustion gases.

## 1.7 Motivation and Research Objectives

Although many techniques have been utilized for the preparation of nanomaterials, flame processes are by far the most popular ones for the commercial production of various nanoparticles [51]. However, problems of scaling-up of laboratory burner configurations remains a limiting factor. Most of studies conducted in laboratories used laminar flames with limited contributions from turbulent ones.

Laminar burners have long residence time, so that the particles start to agglomerate/aggregate and particle size become larger. Non-agglomerated nanoparticles are preferred as the starting material for various applications due to the difficulties facing the start with aggregated nanoparticles. Some of these difficulties are; forming coatings, maintaining nanoscale quantum properties, sintering to full density, dispersing in a liquid medium, and mixing homogeneously. Also, the difficulty for the aggregated nanoparticles to cleave into their individual primary particles. Thus, despite having small primary nanoparticles, the evolution of large aggregates due to particle coalescence (>100nm) deteriorates the purpose of producing a high surface area powder. To solve the aggregation problems, turbulent flames with shorter flame length and residence time should be used.

Diffusion burners do not make use of all entering heat content (from fuel and/or precursor) whereas premixed flames solved this problem by having higher combustion efficiency due to good mixing. CWJ burner has short flame length and small residence time as well as high heat content, large temperature gradient, and stable operation, which nominate it to be used for efficient generation of small nanoparticles for large scale of production.

The use of carbon-coating provides an advantageous tool for process control and has not been extensively explored [54]. In turbulent flames, any carbon (from fuel and/or precursor) enters flame region burns very quickly and no available time for coating. Hence, multiple diffusion burner (laminar flame) will be used for coated nanoparticles. In this burner we might get bigger particles but there is enough time for the coating material to sinter and melt on the host particles forming a homogeneous coating layer.

The major objectives of this thesis work are to:

1. Study the effect of metal oxides-coating/doping on the nanoparticles' structure and their catalytic effect using a multi-jet diffusion flame burner.
2. Utilize the curved-wall jet burner (CWJ) and its modifications to examine the effect of different parameters in turbulent premixed flame on the synthesis of ceramic nanoparticles, such as $TiO_2$ and $SiO_2$.
3. Use PIV to study the residence time of the nanoparticles in the flame, and use OH-PLIF to study the effect of precursor on flame characteristics.
4. Synthesize multi-component ceramics using the flame spray pyrolysis. Iron-doped titania nanoparticles are chosen for the study because of the important industrial applications and also to study their catalytic effect on diesel soot oxidation. The effects of various flame parameters on the microstructure of the nanomaterials will be explored.

## 1.8 Dissertation Outline

This study is aimed at describing the synthesis and applications of $TiO_2$ nanoparticles with/without other dopant or coating materials. The dissertation has been divided into several chapters. Next chapter briefly introduces the experimental setups and the characterization techniques used in this thesis. Subsequent chapters cover studies which demonstrate the

successful usage of different flame configurations to synthesis advanced nanomaterials and suggest the future work which can be undertaken to expand the current work.

Chapter 2 provides a brief description of experimental setups for different burners, flame characterization techniques, and material characterization techniques used in this study.

Chapter 3 discusses the use of multi-diffusion burner in generating doped and coated $TiO_2$ nanoparticles and their catalytic applications.

Chapter 4 demonstrates the flame spray pyrolysis method for preparing various nanomaterials and the photocatalytic application of the iron-doped titania nanoparticles.

Chapter 5 describes the use of curved wall-jet (CWJ) burner in synthesizing $TiO_2$ and $SiO_2$ nanoparticles.

Chapter 6 presents the study a modification of the CWJ burner using a poppet valve-type flow guide at the exit of the central port.

Chapter 7 discusses a modification of the CWJ burner using double-slit openings for flame mixtures and precursors.

Chapter 8 summarizes the work presented in the thesis. Continuation of this work for future project has been discussed. Furthermore, new studies have also been proposed which can be carried out with combustion synthesis of nanomaterials.

# Chapter 2

# Experiment and Characterization Techniques

This chapter briefly describes the setups for various flame configurations used in this study along with flame characterization and material characterization techniques.

## 2.1 Flame Configurations

We will be using various flame configurations in this report for the synthesis of nanoparticles. A schematic diagram containing all used burners is shown in Fig. 2.1. The first burner is the multiple diffusion flames burner introduced first by University of Michigan and a detailed description will be provided in Chapter 3. Secondly, we will discuss the flame spray pyrolysis (FSP) method for the production of iron-doped $TiO_2$ nanoparticles. A detailed description for this burner will be discussed in Chapter 4. Third, the curved wall-jet burner (CWJ) will be used for $TiO_2$ and $SiO_2$ nanoparticles. The burner principle is based on the Coanda effect in which annular-inward premixed jet (fuel/ air mixture) is issued over a hemi-spherical surface of the burner center body and a central tube is used for the precursor delivery. A detailed description of this burner will be discussed in Chapter 5. Fourth, a poppet valve type is added to the central tube of the CWJ burner and this modification will be discussed in Chapter 6. Finally, a double-slit CWJ burner is studied for a better precursor/combustion gases mixing (Chapter 7).

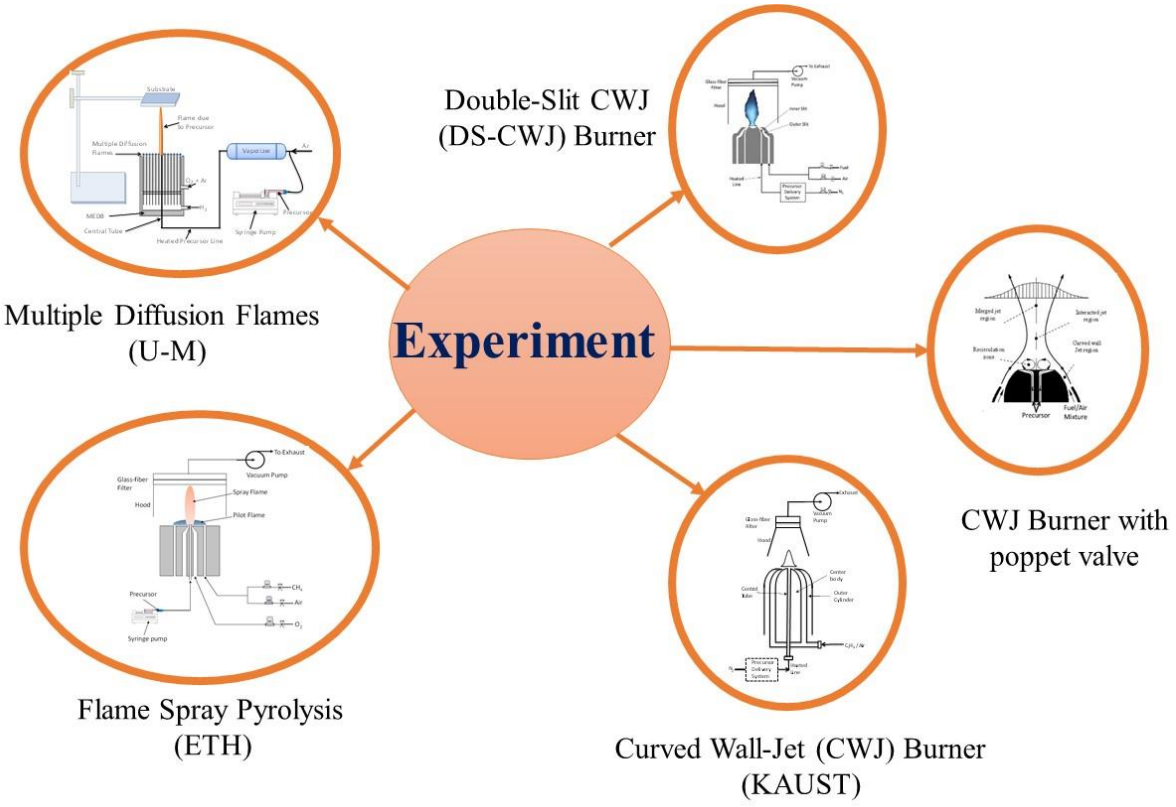


**Figure 2.1:** A schematic diagram showing various burner types used in this study.

Figure 2.2 shows various precursors used for the preparation of nanoparticles. For our main nanoparticles ($TiO_2$), titanium isopropoxide (TTIP) is used as a precursor. For the doping material of our prepared nanoparticles vanadium (V) oxytriisopropoxide (VTIP) is used as a precursor for vanadium doping and ferrocene is used for iron-doping. Hexamethyldisiloxane (HMDSO) is used as a precursor for $SiO_2$ or silica-coated nanoparticles whereas ethylene fuel is used as a precursor for the carbon in carbon-coated nanoparticles.

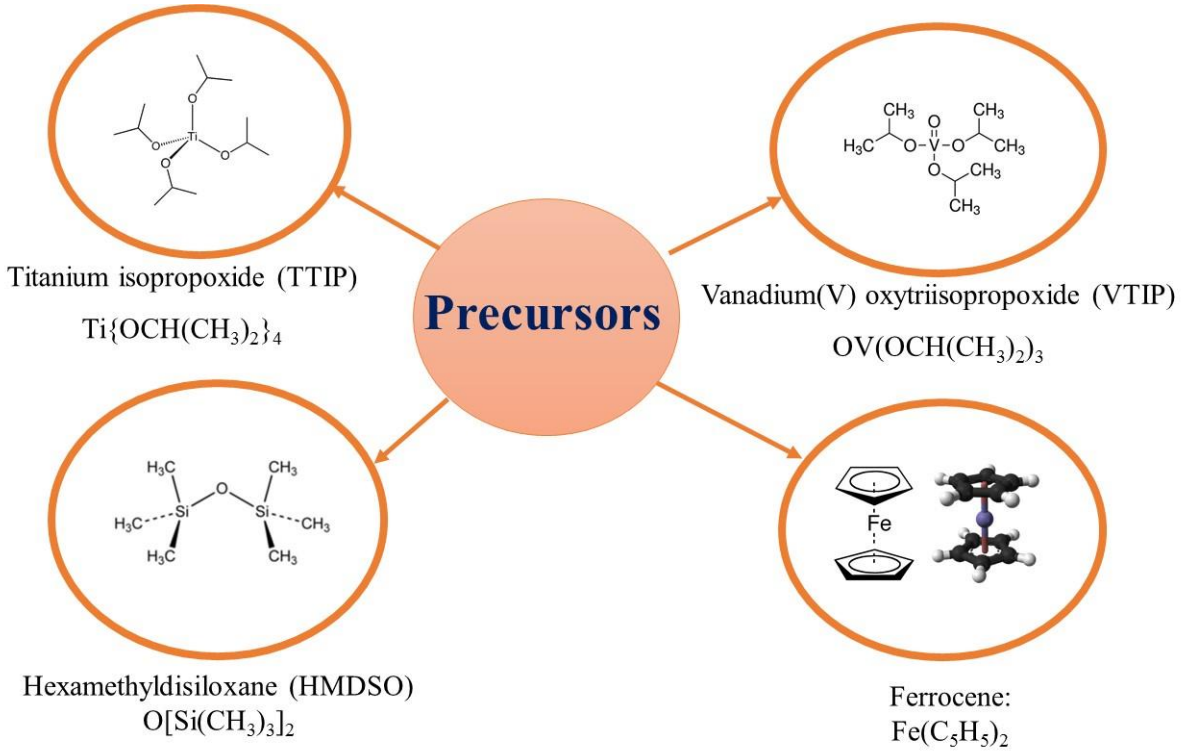


**Figure 2.2:** A schematic diagram showing various precursors used in this study.

## 2.2 Flame Characterization Techniques

Flame characteristics are studied using various complementary experimental techniques ranging from direct imaging to laser diagnostic techniques. Visible flame height is measured using a cathetometer and the results are compared with the average values obtained from photographs. The temperatures are monitored for the cases without supplying precursor using S-type thermocouples. In the following subsections, we will discuss techniques for flow field and flame characterizations using particle image velocimetry (PIV) and planar laser-induced fluorescence of OH radicals (OH-PLIF) in reaction zones.

### 2.2.1 Particle image velocimetry (PIV)

The flow field can be identified using a PIV technique which becomes common and reliable in measuring velocities on a plane [91]. To perform PIV measurements, the flow has to be seeded with particles so that sufficient scattering is generated. There are many types of particles used (i.e., $TiO_2$ and $Al_2O_3$) with nominal diameters in the micrometer range. The seeding particles

(following fluid motion) are exposed to two laser pulses whose timing is precisely synchronized and the scattered signals are recorded using a CCD camera. Velocities are determined from a cross-correlation PIV method [92]. Lagrangian displacements of particles in a small interrogation region are determined from the two-dimensional cross-correlation of the interrogation region from corresponding two images. The velocity of fluid is obtained assuming the flow velocity the same as the particle velocity. Detailes of the used PIV system (schematic in Fig. 2.3) will be discussed in Chapters 5-7.

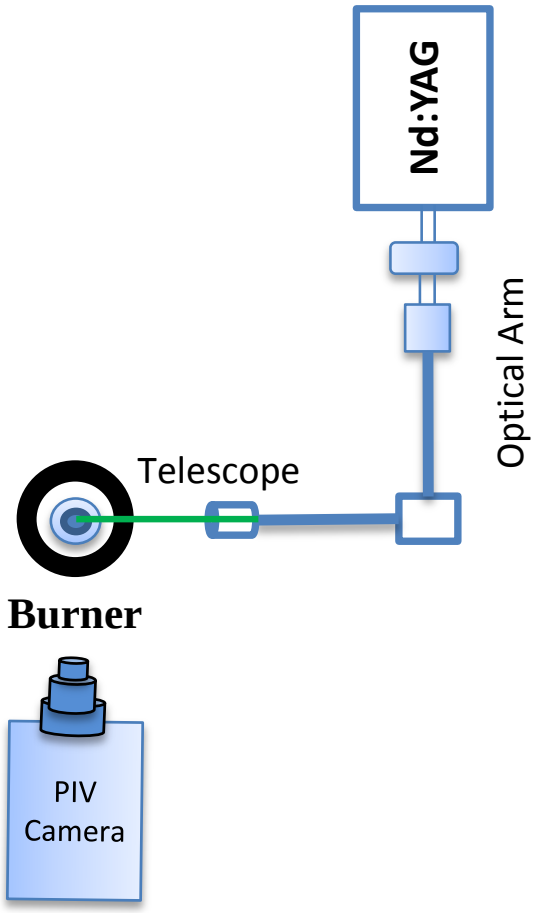


**Figure 2.3:** Schematic of 10 KHz double pulsed PIV laser system.

### 2.2.2 Plannar laser-induced fluorescence (PLIF)

Laser-induced fluorescence (LIF) is a common spectroscopic (non-intrusive) technique, which is widely applied in combustion diagnostics to measure the distribution of specific species in a

flame [93]. Using a continuous or pulsed laser, LIF can be achieved by exciting a specific electronic transition and observing the fluorescence at a normal direction with respect to the incident laser. A planar laser-induced fluorescence (PLIF) technique captures two-dimensional distribution of specific species by using a sheet beam laser and 2-D imaging system. In this study, the PLIF technique is mainly used to determine the distribution of OH radicals which give a good indicator for reaction zones. More details can be found in [94, 95]. The high-speed PLIF system (Fig. 2.4) used in this study will be described in detail in Chapters 6 and 7.

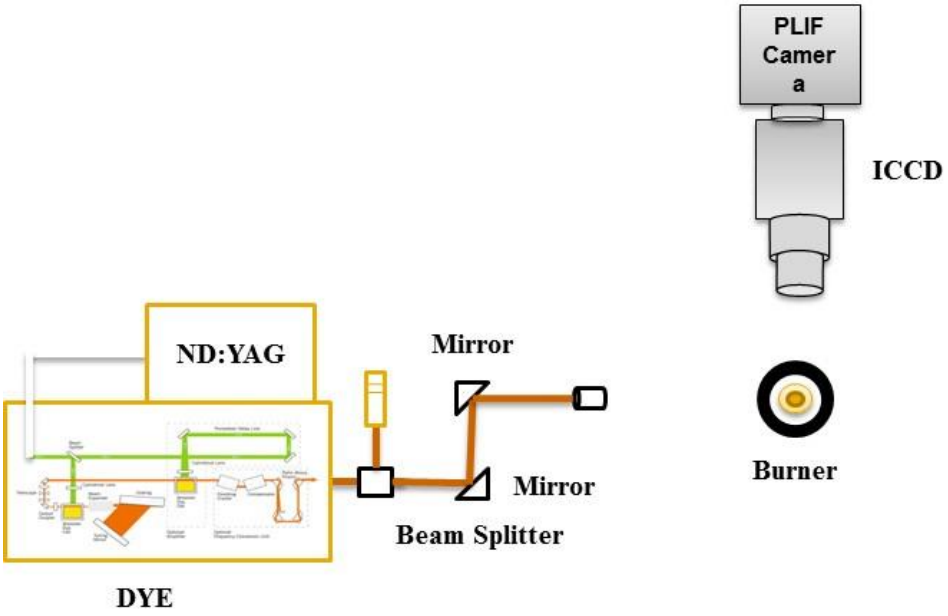


**Figure 2.4:** Schematic of high-speed OH-PLIF system.

## 2.3 Material Characterization Techniques

There are numerous characterization techniques used in material science to determine various material properties. Some of these techniques (Fig 2.5) will be discussed to identify the crystallinity and morphology of material in addition to other physical and chemical properties.

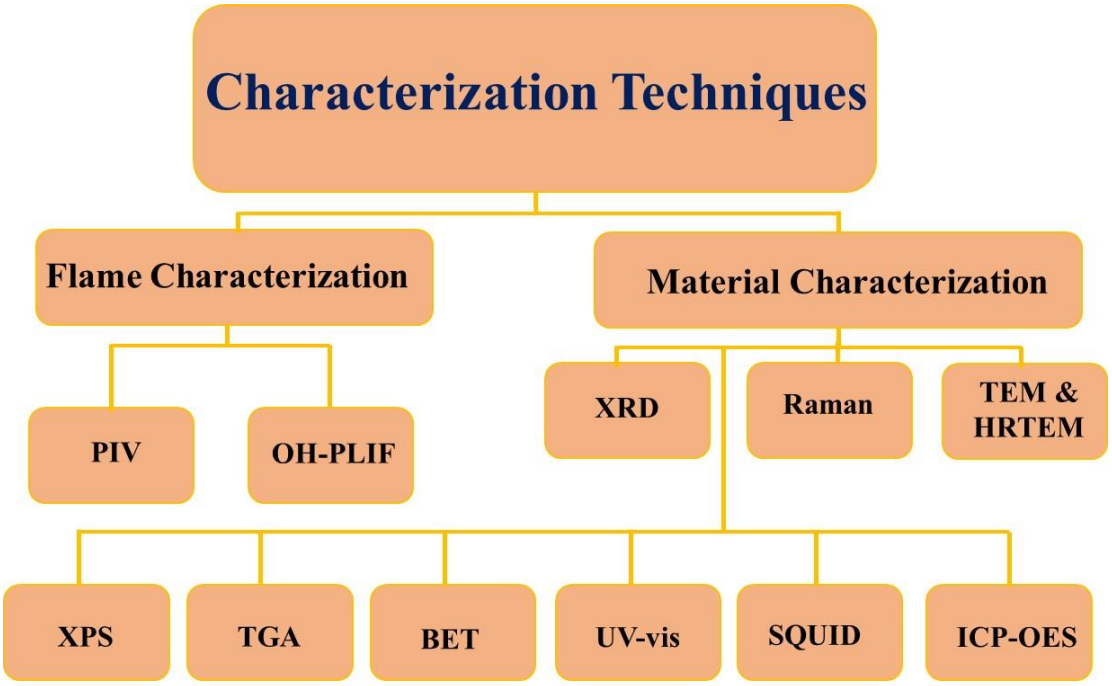


**Figure 2.5:** Various flame and material characterization techniques used in the current study.

### 2.3.1 X-ray diffraction (XRD)

X-ray can interact with matter in different ways, one of them is diffraction which considered as coherent scattering of X-ray by crystalline substance. X-ray diffraction (XRD) is mainly used to determine the crystal structure of material (crystalline vs amorphous). Crystalline substances have ordered arrangement of atoms. The positions of atoms are regularly repeated in space led by a pattern defined by crystal lattice. The atoms are separated by different axis length (*a*, *b*, and *c*) and angles (α, β, and γ) in each crystal system (Fig. 2.6). The axis length and angles determine the crystal system (e.g., for tetragonal crystal: $a = b \neq c$ and $\alpha = \beta = \gamma = 90^{o}$). A particular plane of the atom can be defined using Miller index [96]. The spacing of atoms in crystal lattices is of the same order as the wavelength of X-radiation (0.1 to 100 Å) such that this crystal could be used as a diffraction grating of the X-rays [97]. Bragg discovered (1913) law relating the spacing between atoms in a crystal to the angle at which X-rays are scattered when they strike the crystal [98]. More details about XRD and different crystal structures can be found in [99].

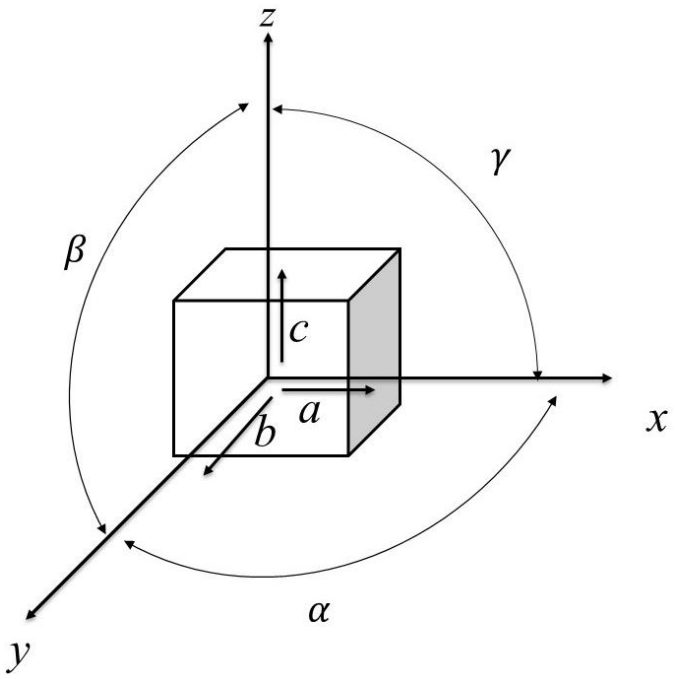


**Figure 2.6:** Crystal system of a crystalline material.

The collected nanoparticles are characterized using X-ray diffraction (XRD) by an X-ray powder diffractometer (Bruker, D8 Advance) with Cu Kα (λ=1.5406 Å) radiation.

### 2.3.2 Raman spectroscopy

Laser beam interacts with phonons in a solid material inducing a polarization of dipoles excited in a solid. As polarizability changes for different kinds of bonds, Raman spectroscopy can be utilized to determine the amount of different phases in the material and is a complementary technique to XRD to identify the crystallinity of tested material. Principle of Raman spectrometer is shown in Fig. 2.7. The laser source is often built-in with a beam section of ~1 $mm^2$ and the laser spot can be reduced to ~1 μm diameter by using high-magnification microscope objectives which mostly used with commercial Raman spectrometers [100]. The main additional options are motorized stages for XYZ mappings and optical fiber plugs for connection to remote optical heads equipped with microscope objectives [101]. Spectra recorded at discrete points of a sample can generate Raman maps as images. They show the variation of any fitted parameter (i.e. intensity, width or position of one band) as a function of

the point of analysis. The peaks generated during Raman spectroscopy are proportional to active optical modes of the material and considered as fingerprint for those phases.

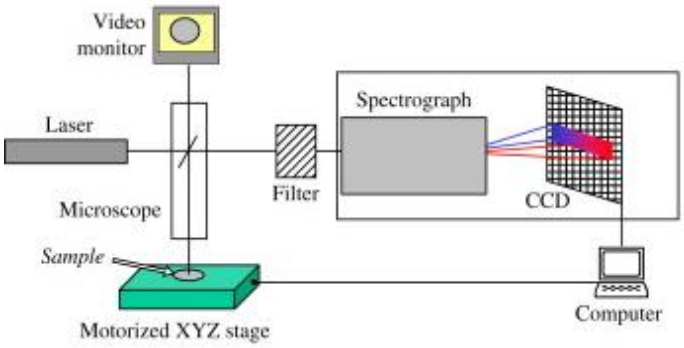


**Figure 2.7:** Principle of a conventional micro-Raman spectrometer [101].

Raman spectroscopy measurements are performed on a Raman spectrometer (Aramis, LabRAM HR Visible) using 473 nm excitation from a diode-pumped solid-state (DPSS) laser (7 mW with a 1.1 $cm^{-1}$ spectral resolution).

### 2.3.3 Thermogravimetric analysis (TGA)

Thermogravimetric analyzer measures the amount and rate of change in the mass of any material as a function of time or temperature in a controlled environment. This technique can characterize materials that exhibit weight change because of oxidation, dehydration, or decomposition. It is mainly used to predict the thermal stability of materials at temperatures up to 1000 $^{o}$C and to determine the composition of these materials as well as their decomposition kinetics. The analysis can be done using constant heating rate or isothermal treatment of the sample using inert gas or air/oxygen.

Non-isothermal thermogravimetric analysis (TGA; TA Instruments, Q5000) is performed to determine the percentage of carbon and its activation energy for the carbon-coated samples. About 7.0 mg of $TiO_2$ is loaded in an alumina crucible and heated in ultra-high purity air (flow rate of 100 ml/min) from 25 to 800$^{o}$C at different heating rates of 2, 4, 6 and 8 $^{o}$C/min.

### 2.3.4 Transmission electron microscopy (TEM)

Light microscopes are limited by physics of light (use visible light). To achieve 10,000x plus magnification and 10 nm resolution, electron microscope was first practically used in 1938 [102]. Unlike light microscopes, electron microscopes operate in high vacuum using magnetic lens and have large depth of field, higher magnification and better resolution. Electron microscopes use a beam of highly energetic electrons to examine objects on a very fine scale to get information about their topography, morphology, chemical identity, and crystallographic information. Electrons, as one type of ionizing radiation, can produce a wide range of secondary signals from a sample and some of these are shown in Fig 2.8. Most of these signals can be detected in various types of TEM.

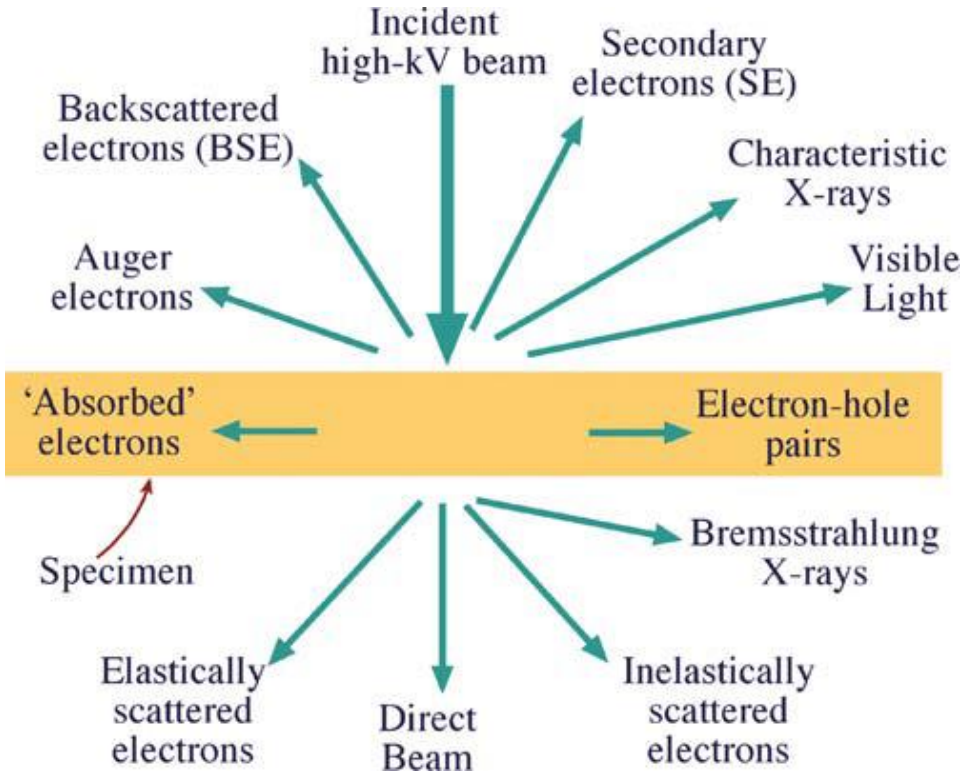


**Figure 2.8:** Signals generated when a high energy beam of electrons interacts with a thin specimen [102].

Transmission electron microscopy (TEM) is a microscopy technique in which a beam of electrons is transmitted through an ultra-thin specimen. The electron beam interacts with the

specimen as it passes through it and an image is formed from the interaction of these transmitted electrons through the specimen. The formed image is focused and magnified onto an imaging device (screen) or to be detected by a sensor such as a CCD camera (Fig. 2.9) [103].

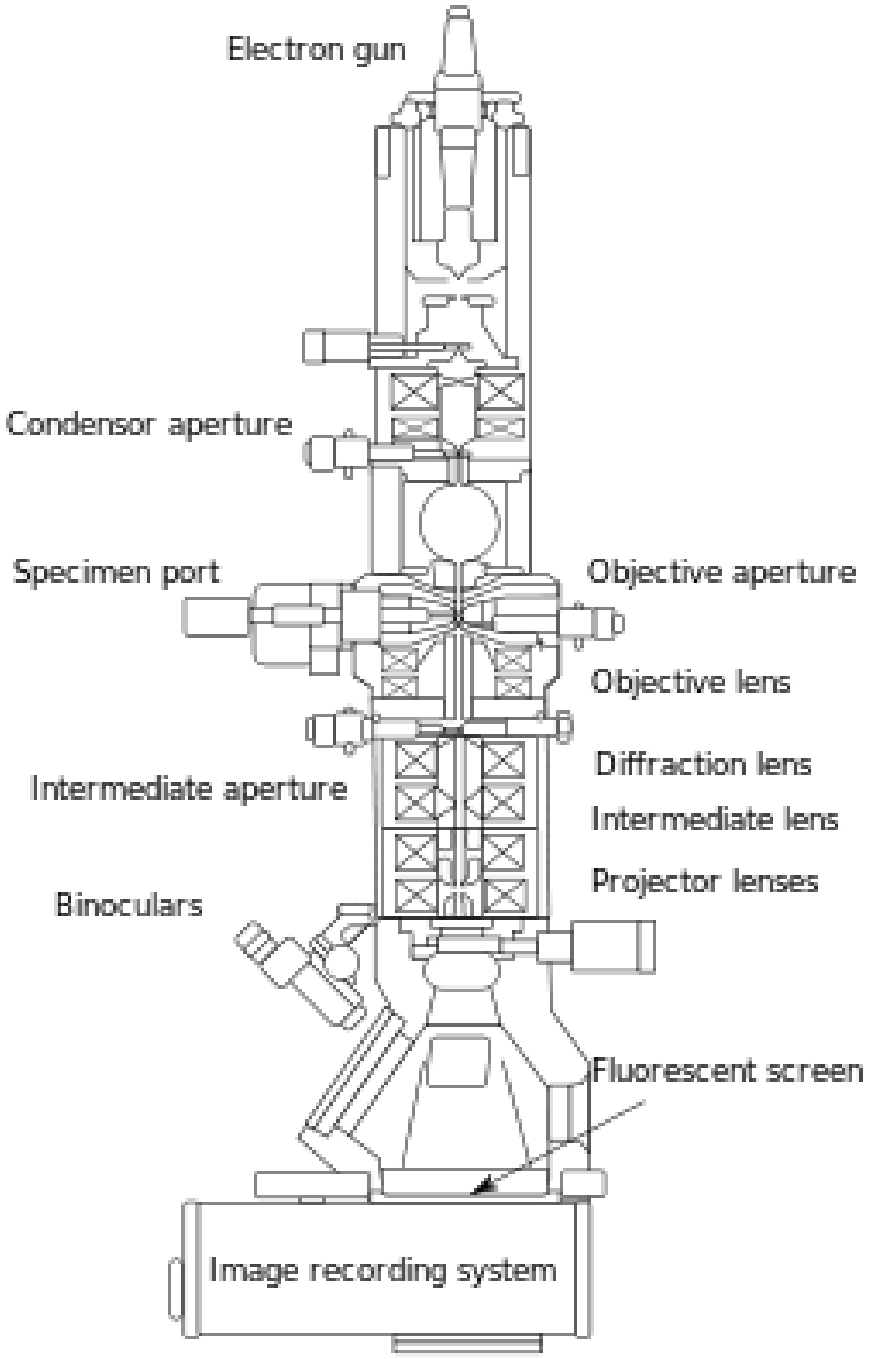


**Figure 2.9:** Layout of optical components in a basic TEM [103].

Particle crystallinity and morphology are examined by a transmission electron microscope (TEM) (FEI, Titan $G^2$ 80-300 CT). The TEM is operated at electron beam energy of 300 keV.

Bright-field TEM (BFTEM) micrographs provide a magnification of 30-80 kX for particle size distribution analysis. Similarly, high-resolution TEM (HRTEM) micrographs are acquired by setting the magnification in the range of 250-400 kX to investigate the crystal structure of $TiO_2$ particles. Electron micrographs are recorded on a 4k × 4k pixel charged couple devices (CCD) camera (Gatan, Inc., US4000). Energy-filtered TEM (EFTEM) analysis is carried out in this microscope by using a post-column energy filter (Gatan, Inc., GIF Tridiem). The so called 3-window method is adopted [104] in generating an elemental mapping of titanium, oxygen, iron, carbon, and silicon elements during the EFTEM analysis of the samples.

### 2.3.5 X-ray photoelectron spectroscopy (XPS)

XPS is a spectroscopy technique which provides information about elemental composition and oxidation state at the surface (up to 10 nm deep in the sample) of any material. A monochromatic X-ray beam of known energy displaces an electron from a K-shell orbital. The kinetic energy of the emitted electron ($E_k$) is measured in an electron spectrometer. The binding energy ($E_b$) can be calculated using the equation $E_b = h\nu - E_k$ where $h\nu$ is the photon energy. This binding energy is characteristic of the atom and orbital from which the electron is emitted. Fig. 2.10 shows a sample result from XPS experiment for the C 1s peak of diesel soot sample and its convolutions which indicate different carbon bonds existing in this sample.

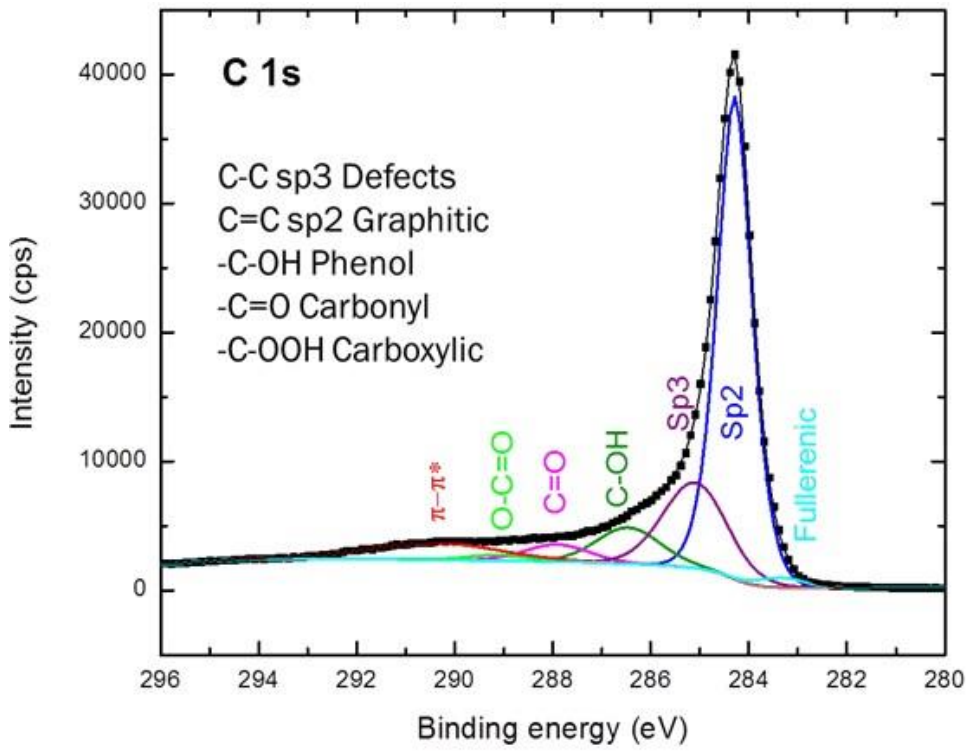


**Figure 2.10:** High resolution C 1s peak for diesel soot sample.

Chemical composition at the surface of powdered samples is analyzed using a high resolution X-ray photoelectron spectroscopy (XPS). XPS studies are carried out in a Kratos Axis Ultra DLD spectrometer equipped with a monochromatic Al Kα x-ray source ($h\nu$=1486.6 eV) operating at 150 W, which also has a multichannel plate and delay line detector under a vacuum of $1{\sim}10^{-9}$ mbar. The data is analyzed with commercially available software program CASAXPS.

### 2.3.6 BET surface area analysis

BET named after Brunauer, Emmet and Teller first developed in 1983 [105]. They developed a basic analysis to measure specific surface area using the theory of physical adsorption of gas molecules on a solid surface. The BET theory used multi-layer adsorption of non-corrosive gases (as nitrogen) as adsorbate to measure the surface area (Fig 2.11). Adsorption and desorption isotherms are obtained at liquid nitrogen temperature, then the surface area can be

calculated from these isotherms. This technique has been widely used in catalytic, soot oxidation, cements and pharmaceutical applications.

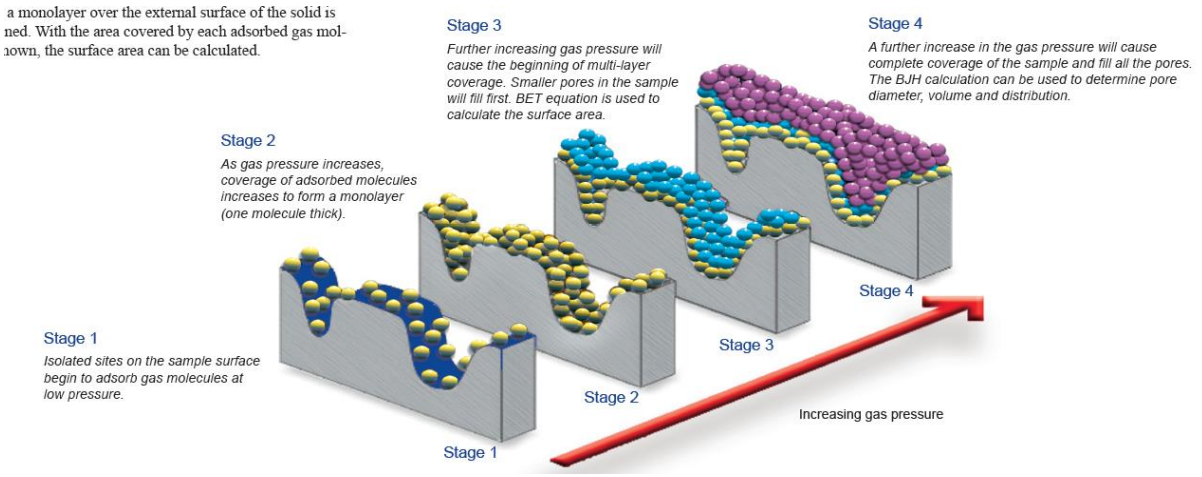


**Figure 2.11:** Schematic of Multi-layer adsorption [106].

A specific surface area (SSA) is calculated based on multi-point Brunauer–Emmett–Teller (BET) nitrogen adsorption (Micromeritics, ASAP 2420). Samples are degassed for 16 h at 150 $^{o}$C and the standard BET isotherms, based on 46 points, are used to calculate SSA. Pore size distribution is modeled using the Barrett-Johner-Halenda (BJH) method on the desorption data obtained from the ASAP 2420.

### 2.3.7 Ultraviolet-visible (UV-vis) spectroscopy

Absorption spectroscopy is an analytical technique which concerns with the measurement of absorption of electromagnetic radiation. The UV radiation region extends from 10 nm to 400 nm and the visible radiation region extends from 400 nm to 800 nm. Electromagnetic radiations interact with a matter inducing changes in its electronic energy levels. The change in energy levels is proportional to the wavelength absorbed. If the electrons are easily excited, the material can absorb longer wavelength of light due to its lower energy gap [107].

UV–vis diffuse reflectance spectra (DRS) are obtained for the dry-powder samples using a scan UV–vis-NIR spectrophotometer (Varian Cary 500) equipped with an integrating sphere assembly, using $BaSO_4$ as reflectance sample.

### 2.3.8 Superconducting quantum interference device (SQUID)

Magnetism and science are coeternal. It started with the discovery of magnets and their ability to attract ferrous objects acting at a distance [108]. According to magnetic properties, materials can be classified as; paramagnetic, ferromagnetic, antiferromagnetic, and ferrimagnetic. The type of each material can be extracted from its coerresponding hysteresis loop (Fig. 2.12). A paramagnetic material, which has the lowest field strength of the above materials can be transformed to a strong magnet at very low temperatures. $TiO_2$ is not a magnetic material but when doped with some ferromagnetic materials with very small percentages start to obtain some magnetic properties and can be used in spintronic applications [109, 110].

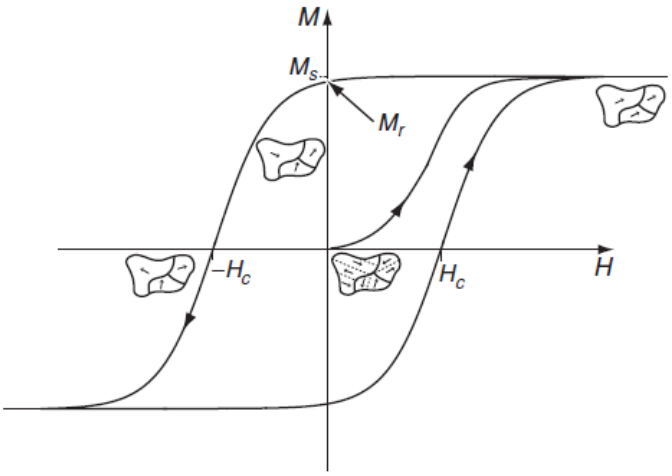


**Figure 2.12:** The hysteresis loop of a ferromagnet. Initially in an unmagnetized, virgin state. Magnetization appears as an imposed magnetic field *H*, modifies and eventually eliminates the microstructure of ferromagnetic domains magnetized in different directions, to reveal the spontaneous magnetization $M_s$. The remanence $M_r$ which remains when the applied field is restored to zero, and the coercivity $H_c$, which is the reverse field needed to reduce the magnetization to zero, are marked on the loop [108].

Magnetic properties of Fe doped $TiO_2$ nanoparticles are studied in a superconducting quantum interference device-vibrating sample magnetometer (SQUID-VSM Quantum design, USA) in the temperature (T) range of 5 K – 300 K and field (H) ranging from +/-3 Tesla. In order to obtain the intrinsic magnetic properties of samples, the temperature variation of magnetization measurements (M vs. T) are carried out initially by cooling the sample to 5 K under nominal zero field, then applied a field of H = 1000 Oe. The M (T) data are recorded while warming the sample from 5-300 K.

### 2.3.9 Inductively coupled plasma optical emission spectrometry (ICP-OES)

ICP-OES is an analytical technique used for the detection of trace metals with very small concentrations. Inductively-coupled plasma is used in this emission spectroscopy technique to produce excited atoms and ions which in their turn, emit electromagnetic radiation at wavelengths characteristic of a particular element. ICP is a flame technique but possessing a very high flame temperature ranging from 6,000 to 10,000 K. It is also a solution technique and standard silicate dissolution methods are employed [111, 112]. The intensity of this emission is indicative of the concentration of an element within a sample.

Trace metals in the synthesized samples are examined using inductively-coupled plasma optical emission spectrometry (Varian ICP-OES 720 ES). The spectrometer is equipped with a CCD detector with image mapping (I-MAP™) technology, providing complete wavelength coverage in the range of 167-785 nm.

# Chapter 3

# Synthesis of Doped/Coated $TiO_2$ Nanoparticles Using Multiple Diffusion Flames

Titanium dioxide ($TiO_2$) nanoparticles containing iron, silicon, and vanadium are synthesized using multiple diffusion flames. The growth of carbon-coated (C-$TiO_2$), carbon-coated with iron oxide (Fe/C-$TiO_2$), silica-coated (Si-$TiO_2$) and vanadium-doped (V-$TiO_2$) $TiO_2$ nanoparticles are demonstrated using a single-step process. Hydrogen, oxygen, and argon are utilized to establish the flames, with titanium tetraisopropoxide (TTIP) as the precursor for $TiO_2$. For the growth of Fe/C-$TiO_2$ nanoparticles, TTIP is mixed with xylene and ferrocene. While for the growth of Si-$TiO_2$ and V-$TiO_2$, TTIP is mixed with hexamethyldisiloxane (HMDSO) and vanadium (V) oxytriisopropoxide, respectively. The synthesized nanoparticles are characterized using high-resolution transmission electron microscopy (HRTEM) with energy filtered TEM for elemental mapping (of Si, C, O, and Ti), x-ray diffraction (XRD), Raman spectroscopy, x-ray photoelectron spectroscopy (XPS), nitrogen adsorption BET surface area analysis, and thermogravimetric analysis.

## 3.1 Introduction

Titanium dioxide ($TiO_2$) is an important nanoparticle as it is used in a number of advanced applications, especially in relation to energy and water [113, 114]. Such applications of $TiO_2$ based nanoparticles (NPs) include next-generation of perovskite solar cells [115], photocatalytic water splitting [116, 117], and waste-water treatment [118]. Flame synthesis is currently the dominant method for mass production of $TiO_2$ nanoparticles in industrial

processes [47]. Thus, it is important to investigate the production of advanced $TiO_2$ nanoparticles using flames, as it can be readily applicable for commercial applications.

Iron based nanoparticles are a promising material for catalytic oxidation of carbon, as they can be used for reducing of diesel engine exhaust and regeneration in diesel particulate filters [119]. Additionally, iron oxide has been used for soot oxidation [120] and Fe-based perovskite-type oxides can be used for the simultaneous elimination of soot and $NO_x$, from the exhaust of diesel engines [121, 122]. Fe-doped $TiO_2$ is of significant interest in magnetism [123]. The presence of magnetic ions in non-magnetic matrices has a great potential in spintronic applications and magneto-optic devices [124]. Doped anatase $TiO_2$ has also been widely studied as a photocatalyst [125, 126]. Tryba et al. [127] investigated the photocatalytic effect of doping $TiO_2$ with iron on phenol decomposition under UV irradiation. A higher formation of $OH^*$ radicals on the Fe-$TiO_2$ surface was observed under UV irradiation in comparison with $TiO_2$. The increase in $OH^*$ radical formation was probably due to the reduction of $Fe^{3+}$ to $Fe^{2+}$ under UV irradiation. Deng et al. [128] synthesized Fe-doped $TiO_2$ nanotubes using a sol-gel process. The photocatalytic activity of Fe/$TiO_2$ NTs was evaluated through photodegradation of aqueous methyl orange. Doping $TiO_2$ with iron (III) was demonstrated to enhance its photocatalytic efficiency [128].

$TiO_2$ and $SiO_2$ based composites have been used for a number of applications such as gas sensors [129], catalysts and photocatalysts [130-132]. Yoshida and Prasad [133] prepared $SiO_2$-$TiO_2$ nanoparticles using sol-gel method as a composite materials for optical waveguides. $TiO_2$ can also be used in a number of applications related to coatings, UV filters, and lenses, where the photocatalytic effects of $TiO_2$ are harmful [134]. To overcome this challenge, $TiO_2$ can be coated with $SiO_2$ to limit the photocatalytic activity of the nanoparticles [135]. Teleki et al., [136] synthesized silica-titania composites. They studied the evolution of composite particle morphology from ramified agglomerates to spot- or fully coated particles. They could have

silica coating layer on the surface of titania particles for lower ratio of silica in the mixture (< 20%). If silica ratio increases above the 20%, a segregated regions of silica and titania were found. V-doped $TiO_2$ has proven to be an effective photocatalyst [137]. Vanadia-titania prepared by flame spray pyrolysis [138] has been used for selective catalytic reduction of NO by $NH_3$. Ren et al. [139] studied the mechanism of vanadia/titania doping by in situ diagnostic of phase selective laser-induced break-down spectroscopy (LIBS). They proposed that the doping of V significantly reduced the band gap of $TiO_2$, while Ti doping did not affect the band gab of $V_2O_5$. Finally, Strobel et al. [71] prepared a detailed review on flame-made catalysts involving $TiO_2/SiO_2$ and $TiO_2$/vanadia.

Diffusion flame aerosol reactor has been used to prepare carbon-coated titania using TTIP and acetylene as precursors [140]. Recently, Memon et al. [54], synthesized carbon-coated $TiO_2$ using multiple diffusion flames. It was found that coating $TiO_2$ with carbon maintains the anatase phase and enhances its optical properties [141]. The present chapter focuses on the production of $TiO_2$ nanoparticles containing C, Fe, Si, and V, considering the potential application of such nanoparticles as explained. Multiple diffusion flames were utilized under atmospheric pressure condition. The setup offers a high degree of flexibility in controlling precursor delivery when compared with premixed flames. For carbon-coated samples, the oxidation characteristics of carbon were also investigated.

## 3.2 Experiment

Multiple diffusion flames are used to synthesize titanium dioxide $TiO_2$ nanoparticles doped and coated with different elements. The burner, as schematically shown in Fig. 3.1a, was composed of a square array of small tubes, a honeycomb, and a center tube. Detailed dimensional information can be found in our previous paper [54]. Hydrogen ($H_2$; purity 99.9999%) is used as the fuel (0.77 SLPM) and 2.63 SLPM of oxygen ($O_2$; purity 99.9995%)

mixed with 7.5 SLPM of Argon (Ar; purity 99.9999) was used as the oxidizer for the multiple diffusion flames. The global equivalence ratio was maintained at 0.5 (without the precursor), thus providing a highly oxygen-rich environment. Figure 3.1b shows an image of the multiple diffusion flames that provide a homogeneous gas-phase temperature of ~600 $^{o}$C, at 3.5 cm above the burner [54].

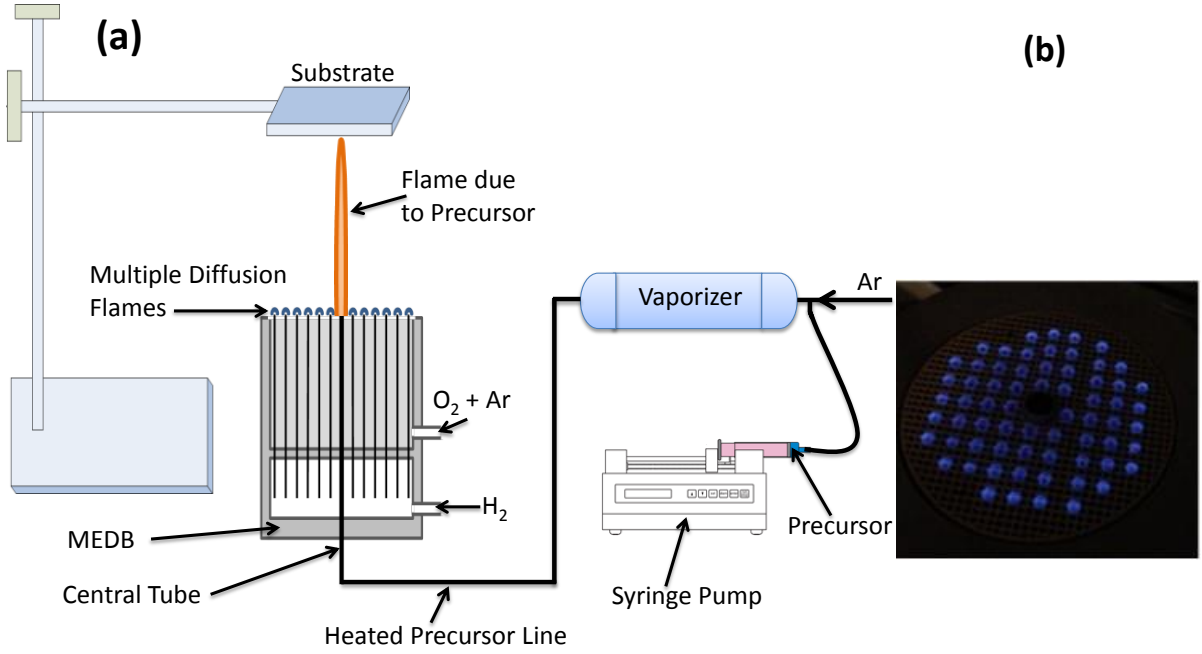


**Figure 3.1:** (a) Schematic diagram for the multi-element diffusion flame burner (MEDB), and (b) image of actual multiple diffusion flames without precursor loading.

Titanium tetraisopropoxide (TTIP; Sigma-Aldrich, 97% purity) was used as the main precursor for $TiO_2$ NPs. Hexamethyldisiloxane (HMDSO; Sigma-Aldrich, ≥98% purity) was mixed with TTIP for the silica-coated titania (Si-$TiO_2$) and vanadium (v) oxytriisopropoxide (Sigma-Aldrich) was used for vanadium-doped titania NPs (V-$TiO_2$). To synthesize carbon-coated titania (C-$TiO_2$), 0.234 SLPM of ethylene (99.95% purity) was used as the carrier gas, while ferrocene dissolved in xylene (Sigma-Aldrich) was mixed with TTIP to synthesize carbon-coated iron-doped titania (Fe/C-$TiO_2$). Elemental ratio of Si/Ti, V/Ti, and Fe/Ti was kept constant at 5% and the appropriate amounts of precursors were calculated according to this ratio. All precursors were injected using a syringe pump into a vaporizer with a flowrate of 20

ml/hr (Fig. 3.1a). Argon (Ar) with a flowrate of 0.22 SLPM was used as the carrier gas for silica and vanadia-doped samples. The carrier gas was supplied through the center tube at a flow rate of 0.4 SLPM (Fig. 3.1). The vaporizer and precursor lines were heated to 180 $^{o}$C to prevent any precursor condensation. The synthesized nanoparticles were collected on an aluminum plate downstream from the burner for only 30 s to prevent any sintering on the substrate. We have collected about 60-80 mg for the silica and vanadia-doped cases and this amount increased to ~120 mg for the carbon containing samples. All experiments were conducted at atmospheric pressure.

The collected nanoparticles were characterized using X-ray diffraction (XRD) by an X-ray powder diffractometer (Bruker, D8 Advance) with Cu K$\alpha$ ($\lambda$=1.5406 Å) radiation. Raman spectroscopy measurements were performed on a Raman spectrometer (Aramis, LabRAM HR Visible) using 473 nm excitation from a diode-pumped solid-state (DPSS) laser (7 mW with a 1.1 $cm^{-1}$ spectral resolution). Particle crystallinity and morphology were examined by transmission electron microscope (TEM) (FEI, Titan $G^2$ 80-300 CT). The TEM was operated at electron beam energy of 300 keV. The bright-field TEM (BFTEM) micrographs were acquired at a magnification of 30-80 kX for particle size distribution analysis. Similarly, high-resolution TEM (HRTEM) micrographs were acquired by setting the magnification in the range of 250-400 kX to investigate the crystal structure of the $TiO_2$ particles. Electron micrographs were recorded on a 4k × 4k pixel charged couple devices (CCD) camera (Gatan, Inc., US4000). Energy-filtered TEM (EFTEM) analysis was carried out in this microscope by using a post-column energy filter (Gatan, Inc., GIF Tridiem). The so called 3-window method was adopted [104] in generating an elemental mapping of titanium, oxygen, and silicon elements during the EFTEM analysis of the samples. It should be noted that the ionization edges of Ti-$L_{23}$ (455 eV), O-K (532 eV), and Si-$L_{23}$ (99 eV) were selected for generating the Ti, O, and Si elemental maps, respectively. A specific surface area (SSA) was calculated based on multi-point

Brunauer–Emmett–Teller (BET) nitrogen adsorption (Micromeritics, ASAP 2420). Samples were degassed for 16 h at 150 $^{o}$C and the standard BET isotherms, based on 46 points, were used to calculate SSA. Pore size distribution was modeled using the Barrett-Johner-Halenda (BJH) method on the desorption data obtained from the ASAP 2420.

Chemical composition at the surface of powdered samples was analyzed using high resolution X-ray photoelectron spectroscopy (XPS). XPS studies were carried out in a Kratos Axis Ultra DLD spectrometer equipped with a monochromatic Al Kα x-ray source (hv=1486.6 eV) operating at 150 W, which also has a multichannel plate and delay line detector under a vacuum of 1~$10^{-9}$ mbar. Measurements were performed in hybrid mode using electrostatic and magnetic lenses, and the take-off angle (angle between the sample surface normal and the electron optical axis of the spectrometer) was 0°. All spectra were recorded using an aperture slot of 300 μm×700 μm. The survey and high-resolution spectra were collected at fixed analyzer pass energies of 160 eV and 20 eV, respectively. Samples were mounted in a floating mode in order to avoid differential charging. The data was analyzed with commercially available software program CASAXPS.

Non-isothermal thermogravimetric analysis (TGA; TA Instruments, Q5000) was performed to determine the percentage of carbon and its activation energy for the carbon-coated samples. About 7.0 mg of $TiO_2$ was loaded in an alumina crucible and heated in ultra-high purity air (flow rate of 100 ml/min) from 25 to 800$^{o}$C at different heating rates of 2, 4, 6 and 8 $^{o}$C/min.

## 3.3 Characterization of $TiO_2$ Nanoparticles

Various $TiO_2$ nanoparticles were investigated with the addition of precursors containing iron, silicon, and vanadium, as summarized in Table 3.1. $TiO_2$ nanoparticles were coated with carbon using a one-step process (C-$TiO_2$). The nanoparticles were prepared without having any metal precursor, ethylene ($C_2H_4$) was used as the precursor carrier gas for carbon-coating. In the case

of iron, the $TiO_2$ samples were coated with carbon, Fe/C-$TiO_2$, and doped with iron. While for Si-$TiO_2$, the samples were coated with silica and finally for V-$TiO_2$ the samples were doped with vanadium.

XRD is commonly used to identify the crystalline structure of $TiO_2$ nanoparticles. Figure 3.2 shows the XRD patterns of the various synthesized materials. For the case of C-$TiO_2$, Fe/C-$TiO_2$, and Si-$TiO_2$, the dominant phase is anatase, while for V-$TiO_2$ it is rutile. The anatase to rutile ratio in the samples was calculated by integrating the respective XRD peak intensities (anatase (101) peak at $2\theta = 25.4^o$ and rutile (110) peak at $2\theta = 27.5^o$) using the following equation [142]

$$W_R = \frac{A_R}{0.884A_A + A_R} \qquad (3.1)$$

where $W_R$ is the weight fraction of rutile in the $TiO_2$ sample and $A_A$ and $A_R$ are the integrated areas under the anatase and rutile peaks, respectively. The values of anatase percentage ($1-W_R$) in the mixtures are listed in Table 3.1.

**Table 3.1:** Summary results for the generated nanoparticles.

| Particles | Precursor | Anatase % | $d_{XRD}$ [nm] | BET [$m^2/g$] | $d_{BET}$ [nm] | Degree of aggregation |
|---|---|---|---|---|---|---|
| C-$TiO_2$ | TTIP + $C_2H_4$ | 90.8 | 33.6 | 27.6 | 54.1 | 4.18 |
| Fe/C-$TiO_2$ | TTIP + Ferrocene/Xylene | 90.4 | 36.2 | 55.3 | 27.0 | 0.42 |
| Si-$TiO_2$ | TTIP + HMDSO | 80.0 | 42.8 | 23.14 | 64.1 | 3.36 |
| V-$TiO_2$ | TTIP + V-oxytriisopropoxide | 28.9 | 30.7 | 22.1 | 64.9 | 9.44 |

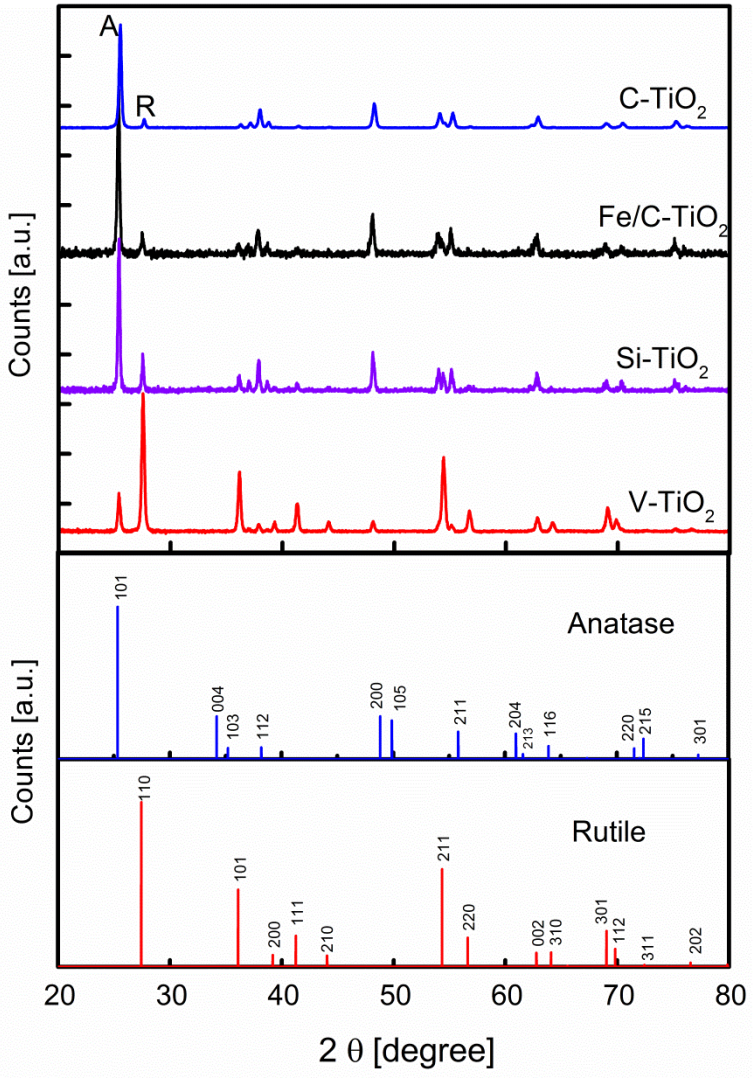


**Figure 3.2:** XRD patterns for $TiO_2$ nanoparticles with the lower part indicating XRD-database for anatase and rutile phases.

The crystallite size $d_{XRD}$ of $TiO_2$ NPs can be obtained from the position of the (101) and (110) peaks using the Scherrer formula [143]

$$L = \frac{K.\lambda}{\beta.\cos\theta} = d_{XRD} \qquad (3.2)$$

where $L$ is the crystallite size, $K$ is 0.89, $\theta$ is the Bragg's angle, $\beta$ is the full width at half-maximum of the corresponding peaks, and $\lambda$ is the wavelength of X-ray radiation (Cu Kα 1.5418 Å). The crystallite size calculated from XRD experiments ranges from 30- 43 nm and is summarized in Table 3.1.

Raman spectroscopy was performed to further characterize the $TiO_2$ nanoparticles. It is known [144] that anatase $TiO_2$ has 15 optical modes and 6 of these are Raman active (irreducible representation of $A_{1g}$(515 $cm^{-1}$), $2B_{1g}$(399 and 519 $cm^{-1}$), and $3E_g$(144, 197 and 639 $cm^{-1}$)), whereas rutile $TiO_2$ has 11 optical modes, among which 4 are Raman active (irreducible representation of $A_{1g}$(612 $cm^{-1}$), $B_{1g}$(143 $cm^{-1}$), $B_{2g}$(826 $cm^{-1}$), and $E_g$(447 $cm^{-1}$)). The Raman spectra in the visible region (Fig. 3.3) also show that the anatase phase is dominant for the C-, Fe/C- and Si-$TiO_2$ samples, while the rutile phase is dominant for the V-$TiO_2$ sample, which are consistent with previous XRD data. Raman spectroscopy is a unique method in characterizing the order-disorder effect in carbonaceous materials, which typically have two major bands [145, 146], with the graphitic G-band around 1580 $cm^{-1}$ and the disordered or amorphous D-band around 1340 $cm^{-1}$. These two carbonaceous bands appear in the carbon-coated samples, which indicate the existence of both crystalline and amorphous carbon in these two samples. Fe/C-$TiO_2$ sample shows higher intensity of D- and G-bands than C-$TiO_2$ sample, which is an indication for a higher carbon content (shown below in TGA analysis).

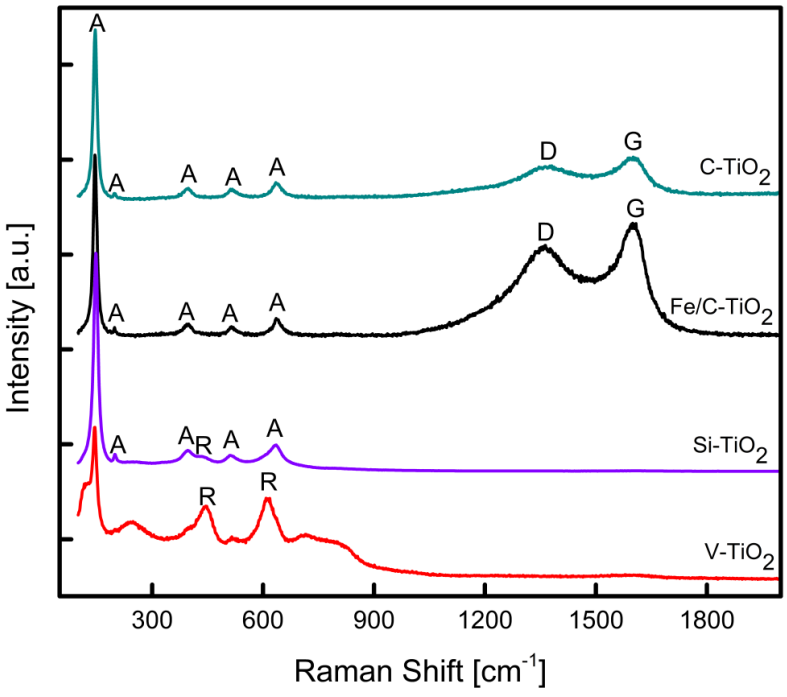


**Figure 3.3:** Raman spectra for $TiO_2$ nanoparticles; A(anatase), R(rutile), D(amorphous) and G(graphitic)

The specific surface area (SSA) of the nanoparticles is measured using BET nitrogen adsorption technique and the results are shown in Table 3.1. The SSAs for the titania NPs were in the range of 22.1-27.6 $m^2/g$ when doping with vanadium, silicon or carbon. This SSA was almost doubled (55.3 $m^2/g$) when the NPs are doped with iron and coated with carbon (Fe/C-$TiO_2$). Based on the surface area obtained from BET analysis and assuming spherical particles, the average primary particle size $d_{BET}$ is calculated by

$$d_{BET} = \frac{6}{[V_A.\rho_A + V_R.\rho_R] \times SSA} \tag{3.3}$$

where $V_A$ and $V_R$ are the volume fractions of anatase and rutile phase, respectively, $\rho_A$ is the density of anatase (3.99 $g/cm^3$) and $\rho_R$ is the density of rutile (4.26 $g/cm^3$) [147]. For Si-, V-, and C-coated/doped $TiO_2$ NPs, the average particle sizes, $d_{BET}$, are larger than the average primary particle diameter calculated from XRD analysis (Table 3.1), which can be attributed to particle aggregation [148]. In the case of Fe/C-$TiO_2$, the degree of aggregation is very low as compared with other samples, as $d_{BET}$ is smaller than $d_{XRD}$. The pore size of the $TiO_2$ samples determined from the BJH method is in the range of 6- 22 nm depending on the dopant material and is comparable with the reported pore size distribution of heat treated or coated $TiO_2$ with different materials [149, 150].

## 3.4 Carbon-Coated $TiO_2$ Nanoparticles with Iron-Oxide

TEM and HRTEM images of the carbon-coated $TiO_2$ nanoparticles are shown in Fig. 3.4. A coating thickness of 5 nm can be seen around the nanoparticles. The growth of carbon on $TiO_2$ has been investigated previously [141] and this has been attributed to a potential diffusion process, where carbon initially enters the $TiO_2$ structure and then upon saturation, carbon precipitates onto the surface.

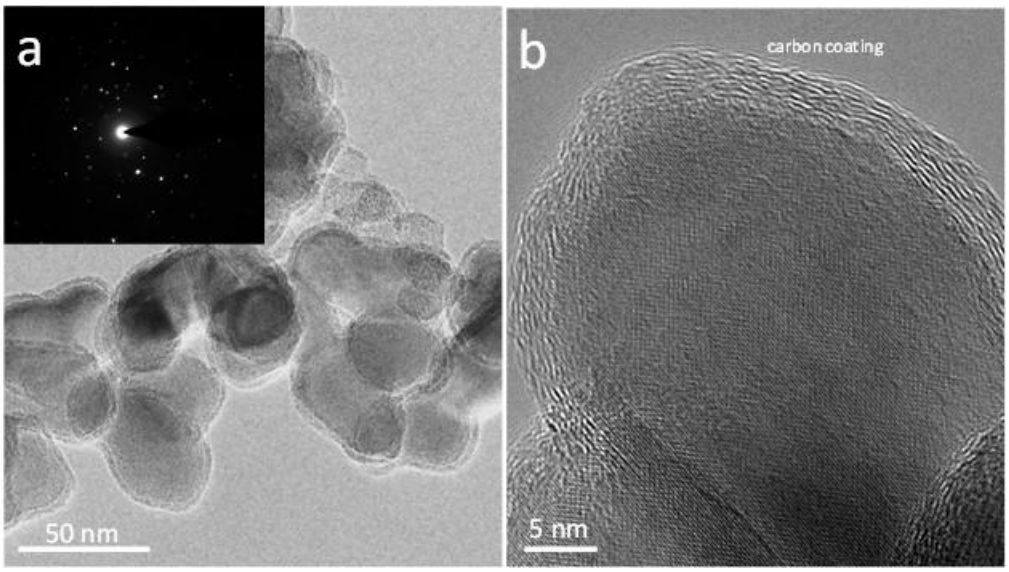


**Figure 3.4:** TEM (a) and HRTEM (b) images of C-$TiO_2$ nanoparticles (inset with electron diffraction pattern).

Chemical composition of the samples was analyzed using the high resolution XPS. High resolution XPS spectra of C 1s and Ti 2p core levels are obtained as shown in Fig. 3.5. The Ti $2p_{3/2}$ core level is fitted using two components. The dominant peak centered at 458.6 eV is associated to Ti ions with a formal valence 4+ ($Ti^{4+}$), while the peak at the lower binding energy ~ 456.6 eV is associated to Ti ions with a reduced charge state ($Ti^{3+}$) [151]. $Ti^{3+}$ species represent 2% of the total Ti ions present on the surface of the C-$TiO_2$ powder and is typical of commercially available $TiO_2$ samples [152]. The O 1s core level is centered at 529.8 eV, which corresponds to the metal oxide ($TiO_2$) [151] and the C 1s core level is centered at 284.4 eV. These C 1s, Ti 2p, O 1s peaks are also observed for all the $TiO_2$ samples (C-$TiO_2$, Fe/C-$TiO_2$, Si-$TiO_2$, and V-$TiO_2$).

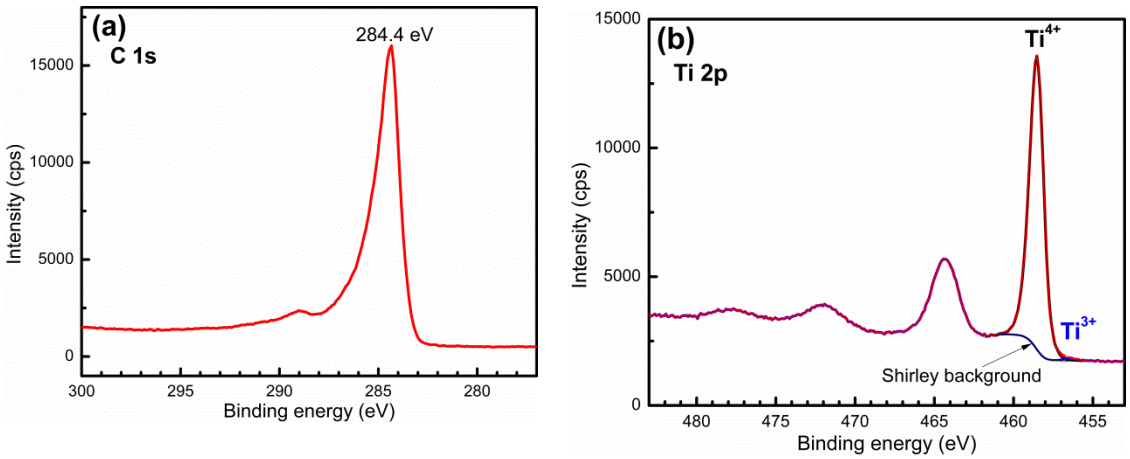


**Figure 3.5:** High resolution XPS spectra of C 1s peak (a) and Ti 2p core level (b) for C-$TiO_2$ samples.

For the growth of carbon-coated $TiO_2$ nanoparticles containing iron (Fe/C-$TiO_2$), TTIP was mixed with ferrocene (dissolved in xylene) and $H_2$ was used as the precursor carrier gas. Thus, the source of carbon is the precursor liquid. Note that the pyrolysis of ferrocene has been used in a number of experiments for the synthesis of iron-oxide [153, 154] and carbon-nanotubes [155, 156]. XRD and Raman spectroscopy (Figs. 3.2 and 3.3) confirm that the Fe/C-$TiO_2$ nanoparticles are predominately in the anatase phase. The TEM image shown in Fig. 3.6a shows the formation of isolated iron-oxide nanoparticles together with $TiO_2$ particles. Additionally, HRTEM image confirms the coating of the $TiO_2$ nanoparticles with carbon (Fig. 3.6b).

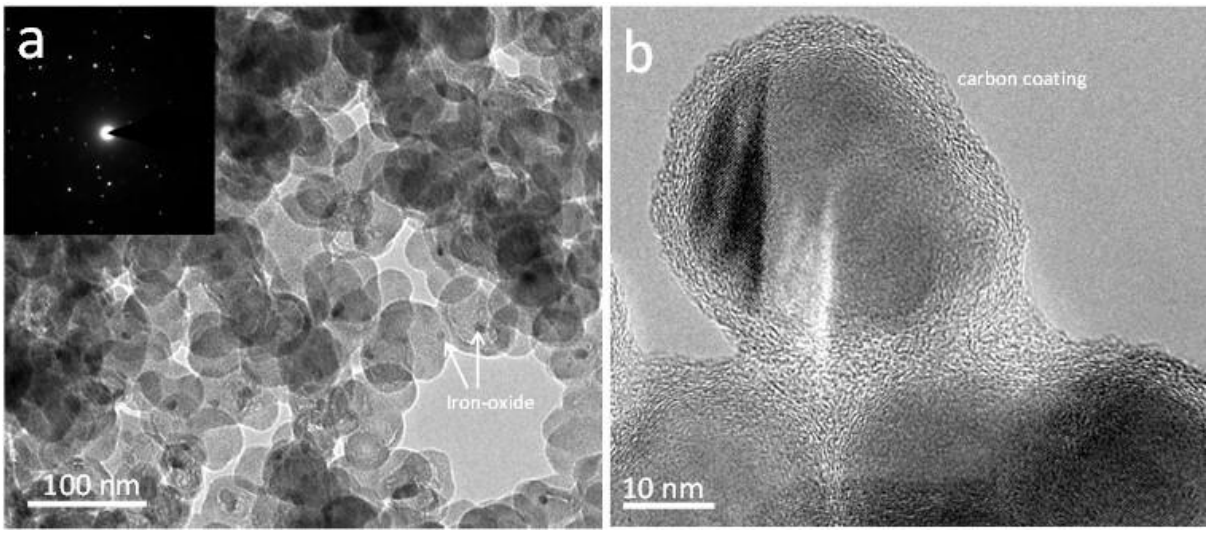


**Figure 3.6:** TEM (a) and HRTEM (b) images of Fe/C-$TiO_2$ nanoparticles (inset with electron diffraction pattern).

Figure 3.7 shows an additional HRTEM image, demonstrating that iron-oxide nanoparticles are encapsulated within carbon. Note that $d_{XRD}$ are comparable between C-$TiO_2$ and Fe/C-$TiO_2$ (Table 3.1), which is reasonable based on the sizes from TEM images. While the BET surface area of the Fe/C-$TiO_2$ nanoparticles was 55.3 $m^2/g$ ($d_{BET}$ = 27.0 nm), which is almost the double as compared with that of the C-$TiO_2$ nanoparticles having value of 27.6 $m^2/g$ ($d_{BET}$ = 54.1 nm). The difference in surface areas was due to the degree of aggregation (4.18 for C-$TiO_2$ and 0.42 for Fe/C-$TiO_2$). Such increase in BET surface area can be partially attributed to the formation of small iron-oxide nanoparticles (diameter ~5 nm) encapsulated within carbon. Note that iron-oxide nanoparticles are typically acting as seeds for the growth of carbon, where similar growth mechanism is used for carbon nanotubes [156]. Raman spectroscopy further confirmed the growth of carbon, as D and G peaks are clearly visible within the spectrum in Fig. 3.3.

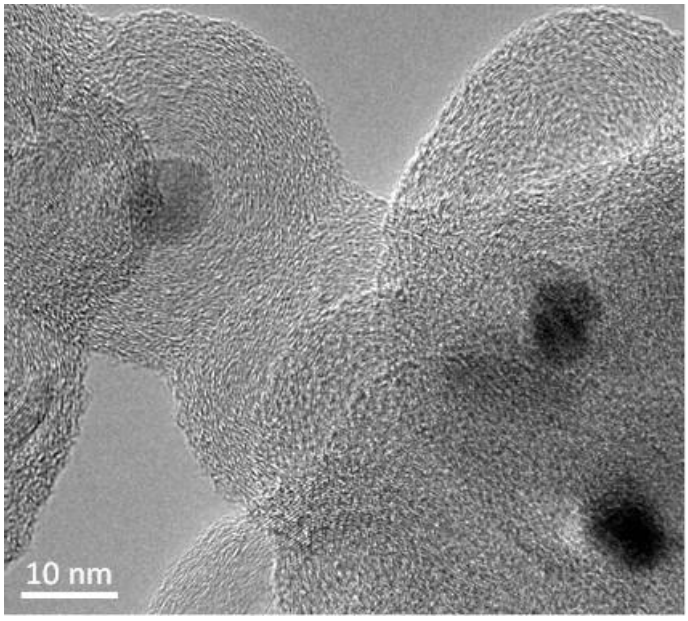


**Figure 3.7:** HRTEM image of iron-oxide nanoparticles encapsulated within carbon.

High resolution XPS spectrum of the Fe 2p core level is shown in Fig. 3.8. The Fe 2p core level in red color is fitted (thick black line) using four components located at 710.9 eV (Fe $2p_{3/2}$) and 719.5 eV (corresponding satellite peak), together with 724.4 eV (Fe $2p_{1/2}$), and 733.0 eV (corresponding satellite peak). The area ratio of Fe $2p_{3/2}$ / Fe $2p_{1/2}$ is equal to 2:1 and the doublet separation is equal to 13.5 eV. The same values are used for their corresponding satellites. The binding energies of the components of the Fe 2p doublet and their corresponding satellites are a characteristic of the $Fe^{3+}$ oxidation state of iron [157-159]. The other core levels are similar to the C-$TiO_2$ sample (Fig. 3.5), where $Ti^{3+}$ species represent 1-2% of the total Ti ions present on the surface of the Fe/C-$TiO_2$ powder.

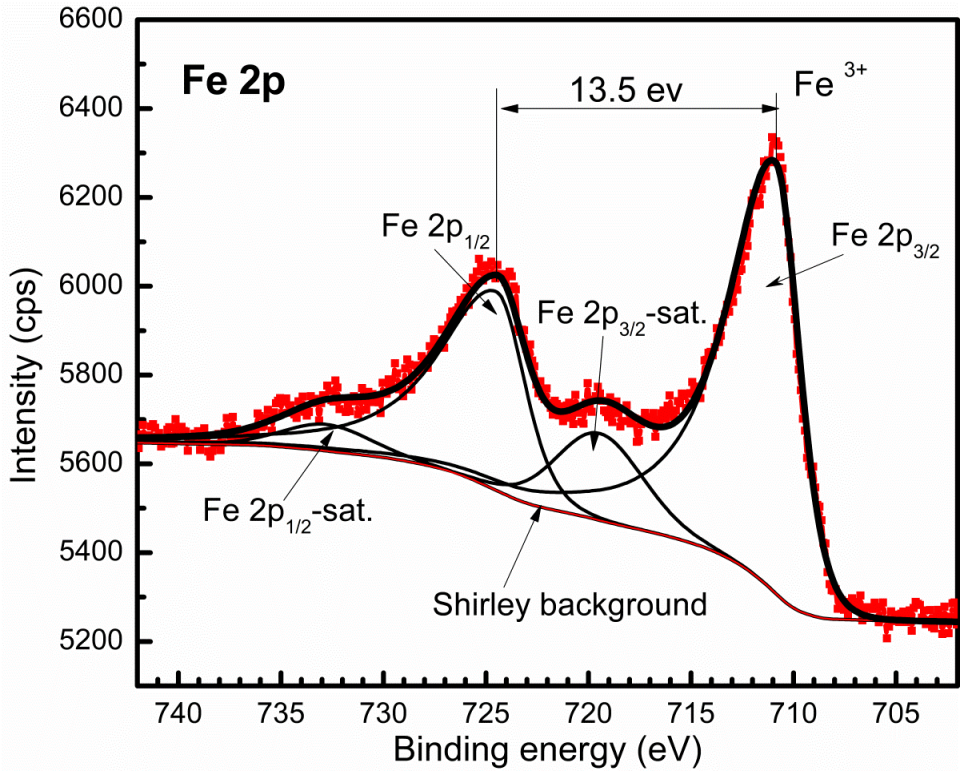


**Figure 3.8:** High resolution XPS spectra of Fe 2p core level.

## 3.5 Carbon Oxidation Kinetics

$TiO_2$ is an effective catalyst for carbon oxidation due to its mobility, reactivity, and thermal stability [160-162]. Several metal oxides consisting of Pt, Ce, Fe, V, and other metals have been investigated for the simultaneous reduction of soot and $NO_x$ [163, 164]. In this regard, non-isothermal oxidation experiments with different heating rates were performed with the carbon-coated samples in air environment using TGA. Figure 3.9 shows the weight loss of these samples as a function of temperature, at a heating rate of $\beta$ = 2 K/min. The C-$TiO_2$ sample contains 6.13% carbon while the Fe/C $TiO_2$ sample contains 17.37% carbon, which contains substantial amounts of amorphous carbon, as observed from HRTEM (Fig. 3.7). Even with the addition carbon, Fe/C-$TiO_2$ catalytically enhances the oxidation of carbon. The start and end oxidation temperatures for Fe/C-$TiO_2$ are 300$^o$C and 470$^o$C, respectively, which are much lower when compared to C-$TiO_2$, 440$^o$C (start temperature) and 610$^o$C (end temperature). For

both samples, the carbon is believed to be totally removed after the oxidation process, which can be visualized in Fig. 3.10, where the initial black samples becomes white for the C-$TiO_2$ samples and turns yellow for the Fe/C-$TiO_2$ sample. The yellow color is due to Fe doping.

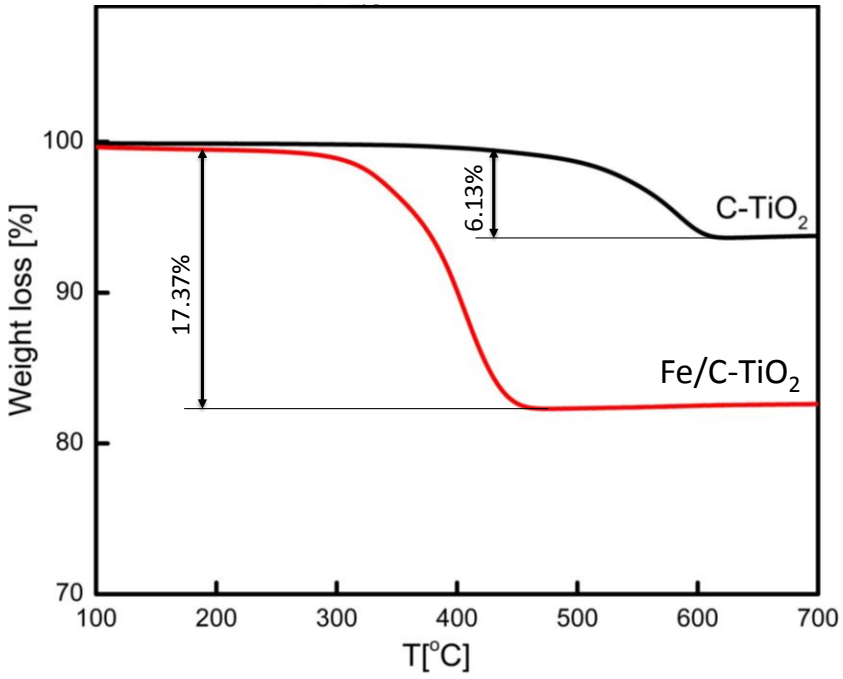


**Figure 3.9:** TGA results indicating the weight loss vs. temperature for C-$TiO_2$ and Fe/C-$TiO_2$ nanoparticles at constant heating rate of 2 K/min.

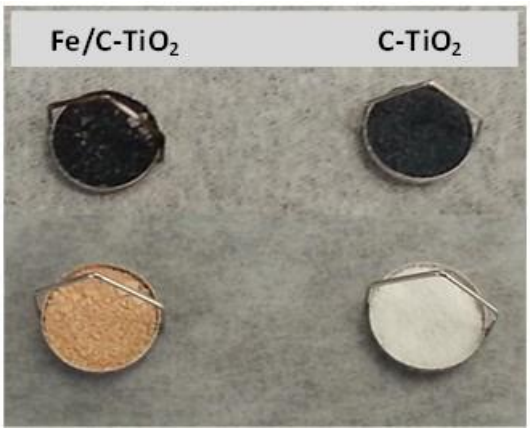


**Figure 3.10:** Images of carbon-coated samples (upper) before oxidation and (lower) after oxidation.

The kinetics of carbon oxidation can be considered using heterogeneous condensed phase reactions [165] and can be described by an Arrhenius reaction:

$$d\alpha/dt = A\mathrm{e}^{-E/RT} f(\alpha) \qquad (3.4)$$

where $\alpha$ is the degree of conversion (the extent at which carbon is burned), $t$ is the time, $A$ is the pre-exponential factor, $E$ is the activation energy, $R$ is the gas constant, $T$ is the temperature, and $f(\alpha)$ is the differential conversion function. For non-isothermal reaction with constant heating rate of $\beta = \Delta T/\Delta t$ = const., Eq. (4.4) becomes

$$d\alpha/dt = (A/\beta)\,\mathrm{e}^{-\mathrm{E}/RT(t)} f(\alpha) \qquad (3.5)$$

Here, a simplified algebraic expression proposed by Pérez-Maqueda et al. [166] is adopted with $f(\alpha) = c \times \alpha^m (1-\alpha)^n$, where $c$, $m$, and $n$ are fitting constants, which has the advantage of fitting all kinetic ideal models proposed for solid-state reactions and also fits for any deviation from these ideal kinetic models. By substituting $f(\alpha)$ into Eq. (4.5), the logarithmic form becomes

$$\ln(d\alpha/dt) - \ln[\alpha^m(1-\alpha)^n] = \ln cA - E/RT \qquad (3.6)$$

A linear regression analysis has been performed using the TGA data to determine the kinetic parameters, which are summarized in Table 3.2. The difference in $m$ between the two samples indicates a different oxidation mechanism due to the catalytic effect of iron. Fe/C-$TiO_2$ sample also shows smaller activation energy (123.1 kJ/mol as compared with 132.1 kJ/mol for C-$TiO_2$). The pre-exponential factor for Fe/C-$TiO_2$ of 1.17E+08 1/min is much larger than that for C-$TiO_2$ of 5.89E+6 l/min. The combination of lower activation energy and higher pre-exponential factor results in a large increase in the oxidation of carbon for the Fe/C-$TiO_2$ samples. Based on the results obtained, the iron-based $TiO_2$ samples can be regarded as a promising material for soot oxidation reactions. The Fe/$TiO_2$ sample (Fe/C-$TiO_2$ after oxidation) has the same oxidation state of iron ($Fe^{3+}$) as the original sample (before oxidation)

which is a good indication of using this sample multiple times for oxidation without losing its catalytic properties.

**Table 3.2.** Kinetic parameters (calculated from Eq. 3.6) for carbon oxidation in carbon-coated $TiO_2$ samples.

| | C-$TiO_2$ | Fe/C-$TiO_2$ |
|---|---|---|
| *m* | −0.74 | −1.0 |
| *n* | 0.13 | 0.13 |
| *E* [kJ/mol] | 132.1 | 123.1 |
| *A* [1/min] | 5.89E+06 | 1.17E+08 |

To emphasize the catalytic effect of the generated samples, the iron-containing sample (Fe/C–$TiO_2$) is used as a catalyst for soot oxidation and compared with C–$TiO_2$ and pure soot. A model soot (Printex-U) was mixed with the samples at a ratio of 1:4. The mixture was dissolved in ethanol and sonicated for 60 min to have tight contact between the soot particles and the Fe/C–$TiO_2$ and C–$TiO_2$ particles. After sonication, the samples were left to dry for 12 h then the mixtures were tested using TGA and compared to the raw soot material. In TGA, all samples are heated first to 100 $^{o}$C with nitrogen gas for 1 h to remove any moisture content and then cooled down to 60 $^{o}$C. Afterward the gas is changed to air before raising the temperature by 8 $^{o}$C /min up to 800 $^{o}$C. The temperature history of the samples in the TGA device is shown in Fig. 3.11.

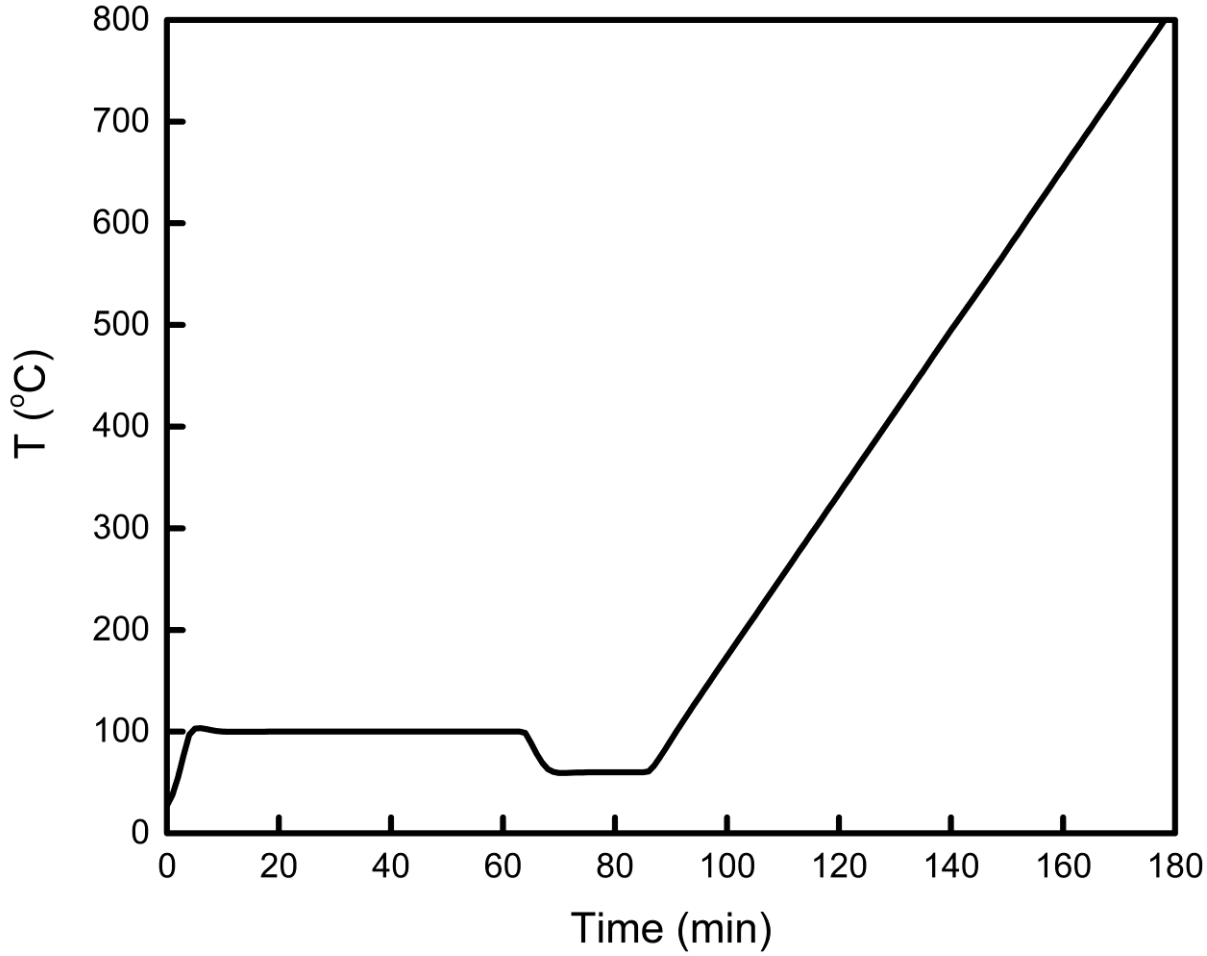


**Figure 3.11:** Temperature history of soot samples with catalytic nanoparticles in the TGA.

The weight loss of the soot samples with temperature changes are shown in Fig. 3.12. The soot sample starts oxidation (5 % oxidation) at a temperature of 505 $^{o}$C and ends oxidation (99 % oxidation) at 659 $^{o}$C. Mixing the soot sample with C–$TiO_2$ enables the oxidation temperature to start at 470 $^{o}$C with complete oxidation at 647 $^{o}$C. Finally mixing the soot sample with the Fe/C–$TiO_2$ enables the oxidation temperature to start at 348 $^{o}$C with complete oxidation at 604 $^{o}$C. The reduction in oxidation temperatures indicates that mixing the soot samples with iron-doped titania enhances the oxidation characteristics of the soot sample which is indicative of the catalytic effect of the Fe/C–$TiO_2$ sample.

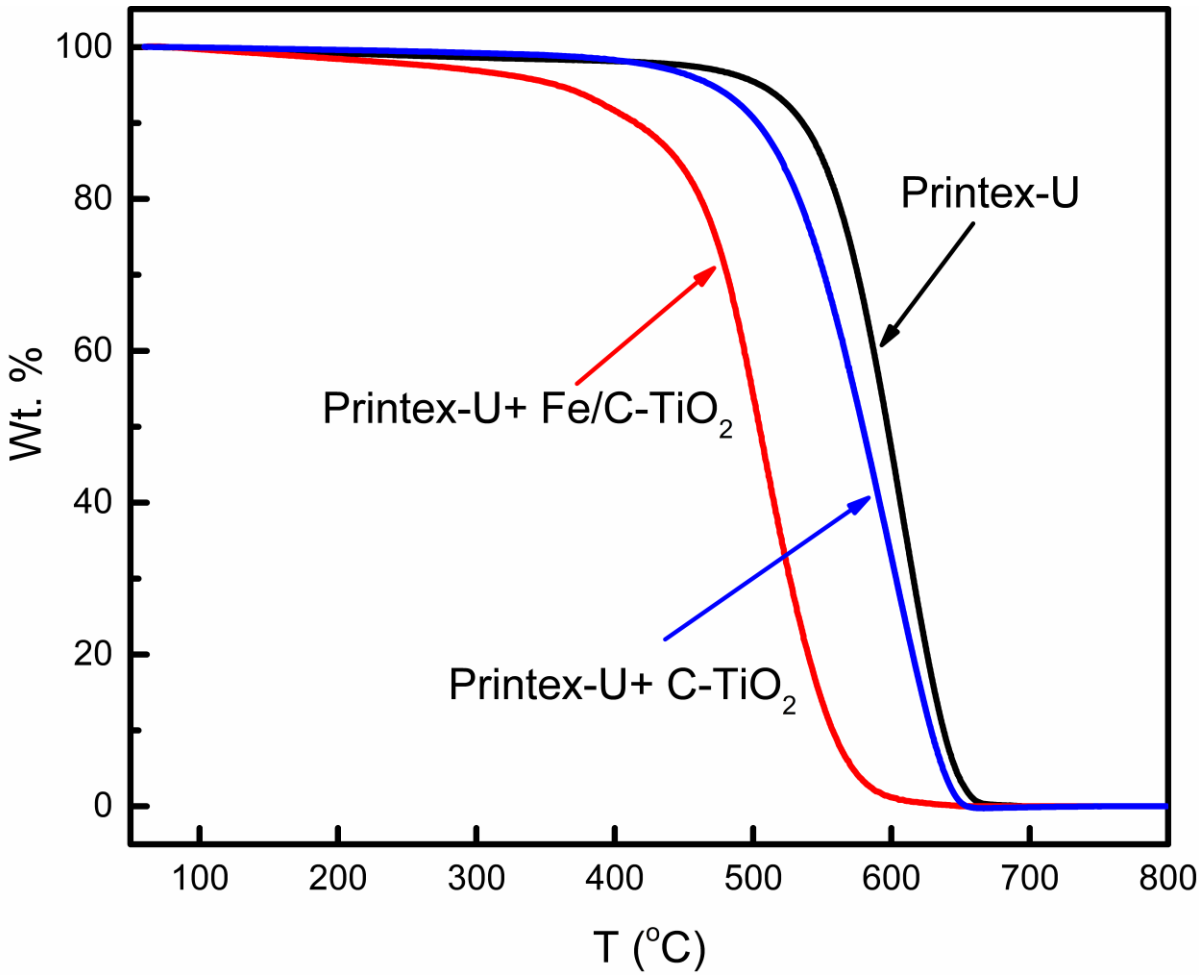


**Figure 3.12:** TGA results indicating the weight loss versus temperature for Printex-U, Printex-U mixed with C-$TiO_2$, and Printex-U mixed with Fe/C–$TiO_2$ nanoparticles at a constant heating rate of 8 K/min

## 3.6 Silica-Coated $TiO_2$ nanoparticles

The formation of $TiO_2$ containing silica is investigated by adding HMDSO to the TTIP precursor. $H_2$ was used as the precursor carrier gas to avoid any additional growth of carbon. The XRD data in Fig 3.2 confirmed that the $TiO_2$ nanoparticles were primarily in the anatase phase (~80 wt%), while a slight increase in rutile fraction was observed, as compared with carbon coated nanoparticles. Raman spectroscopy further substantiated the formation of anatase $TiO_2$ nanoparticles (Fig. 3.3). The surface area measured using BET was 23.14 $m^2/g$, which is similar to the C-$TiO_2$ nanoparticles. Figure 3.13 shows the TEM and HRTEM images, indicating that $TiO_2$ nanoparticles are covered by a layer of $SiO_2$, with thickness

ranging from 3 to 8 nm. Such coating could occur due to differences in chemical reaction rates of the precursors [167]. In this case, the oxidation of TTIP along with the formation of $TiO_2$ is faster as compared with the oxidation of HMDSO for the formation of $SiO_2$. Hence, $SiO_2$ ends up coating the $TiO_2$ nanoparticles.

Figure 3.14 shows the elemental mapping using electron energy loss spectroscopy (EELS). The result confirms that $SiO_2$ is formed around the $TiO_2$ sample and is not doped inside the particle. This is consistent with a previous result, however when the concentration of $SiO_2$ is increased significantly (> 40 wt%), the growth of segregated regions of $TiO_2$ and $SiO_2$ occurs [167].

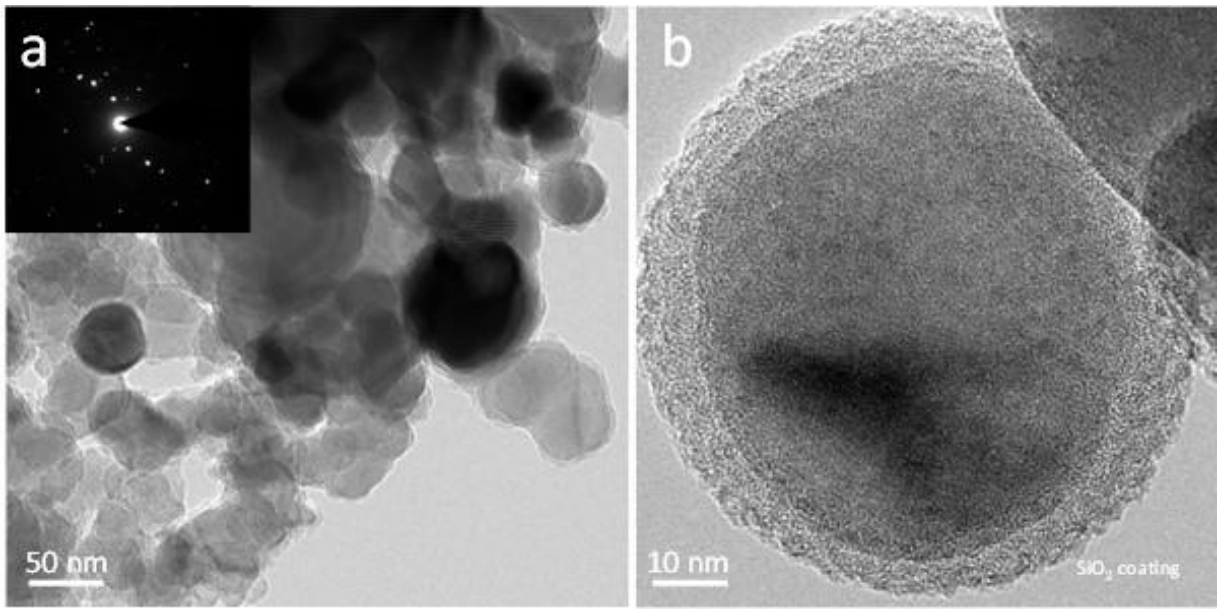


**Figure 3.13:** TEM (a) and HRTEM (b) images of Si-$TiO_2$ nanoparticles.

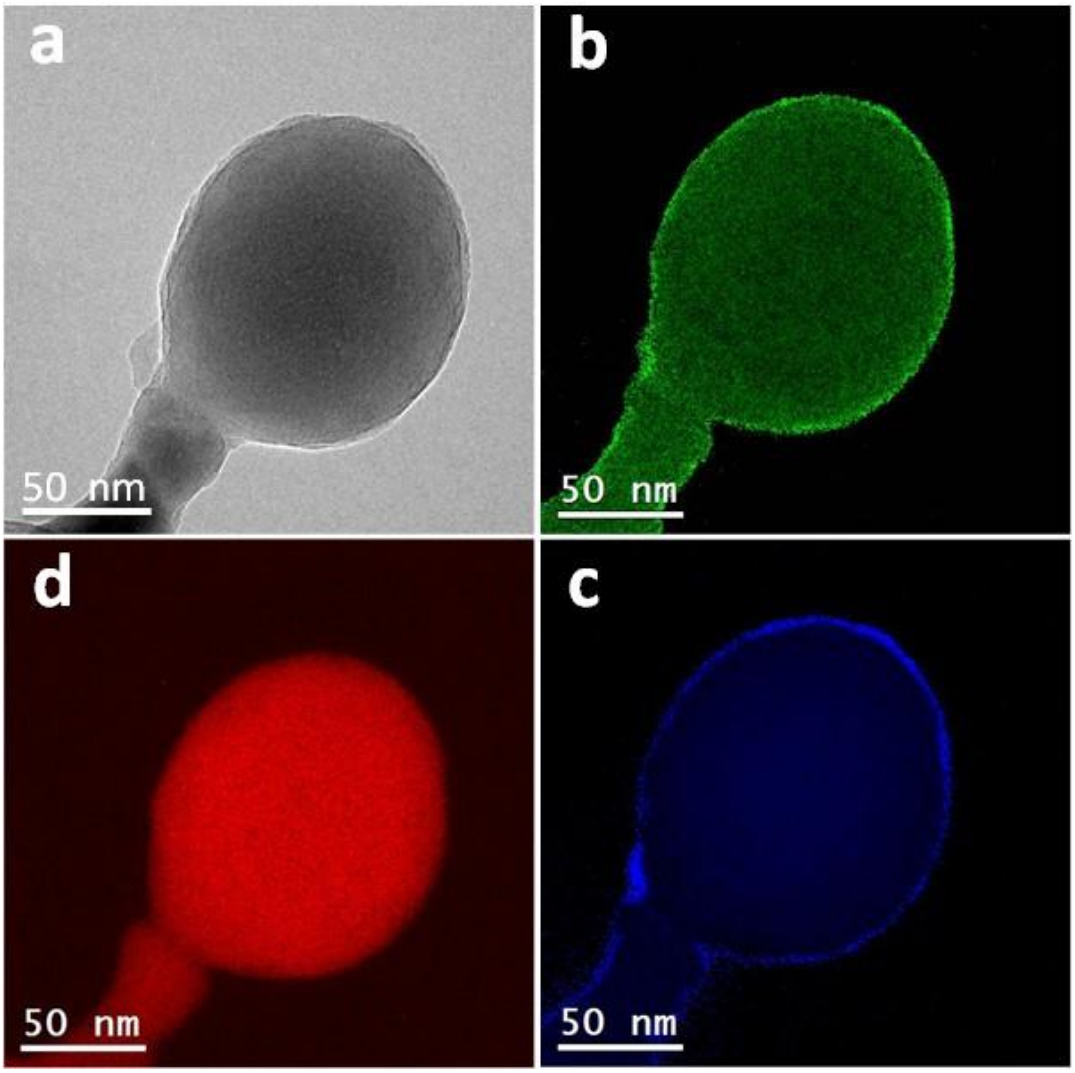


**Figure 3.14:** Elemental mapping of Si-$TiO_2$ nanoparticles, indicating (a) raw HRTEM image and elemental maps for (b) oxygen, (c) titanium, and (d) silicon.

A high resolution XPS spectrum of the Si 2p core level is shown in Fig. 3.15. The Si 2p core level (red line) is fitted with single peak centered at 103.5 eV (thick black line), corresponding to 4+ oxidation sate ($Si^{4+}$) [168, 169]. This confirms the existence of $SiO_2$ on the surface of the $TiO_2$ NPs. The other core levels are similar to the C-$TiO_2$ sample where $Ti^{3+}$ species represent 2% of the total Ti ions present on the surface of the Si-$TiO_2$ powder.

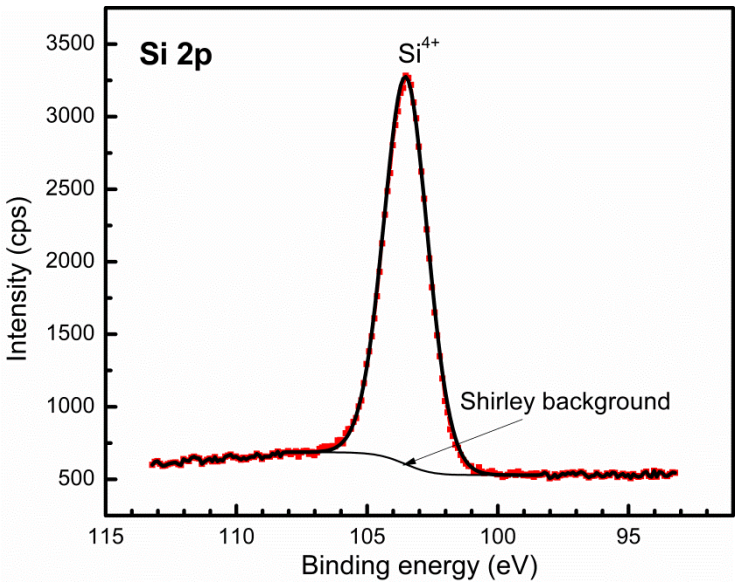


**Figure 3.15:** High resolution XPS spectra of Si 2p core level.

## 3.7 Vanadium-Doped $TiO_2$ Nanoparticles

For the addition of vanadium, V-oxytriisopropoxide, was added to the TTIP precursor. The nanoparticles were predominately in the rutile phase based on XRD, where the anatase percentage is 28.9 % (Table 3.1). The addition of dopants is known to cause a shift in the anatase to rutile percentage of $TiO_2$ nanoparticles [134]. Doping $TiO_2$ with some metal ions (including $V^{4+}$) increases the rutile content and changes the visible-light photo-reactivity of $TiO_2$ nanoparticles [170]. Raman spectroscopy (Fig 3.3) further confirmed the increase in the rutile ratio. Additionally, a broad peak from 700 to 900 $cm^{-1}$ as shown in Fig. 3.3 suggests the growth of polymeric vanadate [171, 172], while the formation of $V_2O_5$, which has a peak at ~990$cm^{-1}$ is not observed. This indicates that vanadium is most probably doped within the $TiO_2$ structure. The TEM images of V-$TiO_2$ are shown in Fig 3.16. The HRTEM image Fig. 3.16b shows spotted patterns, an indication of vanadium doping inside the $TiO_2$ nanoparticle.

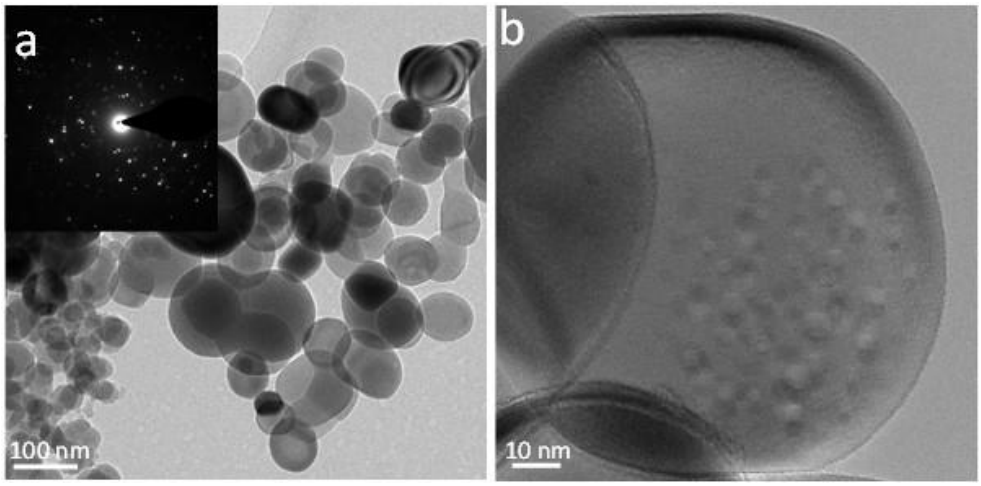


**Figure 3.16:** TEM (a) and HRTEM (b) images of V-$TiO_2$ nanoparticles.

High resolution XPS spectrum of O 1s/V 2p region is shown in Fig. 3.17. The V 2p core level is decomposed into 2 doublets V $2p_{3/2}$ – V $2p_{1/2}$ with a fixed area ratio equal to 2:1 and a doublet separation of 7.3 eV. The binding energies of V $2p_{3/2}$ for the two components are 515.8 eV, and 516.7 eV which is attributed to $V^{4+}$ and $V^{5+}$ oxidation states, respectively [173, 174]. A mixture of $V^{4+}$ and $V^{5+}$ is commonly observed when vanadium is doped within $TiO_2$ lattice [175].

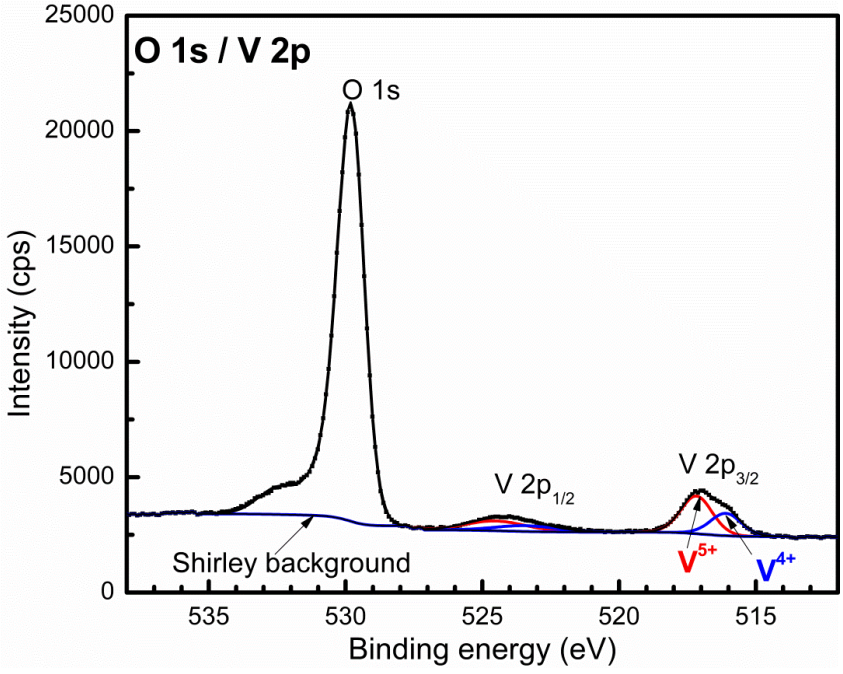


**Figure 3.17:** High resolution XPS spectra of the O 1s/V 2p core levels.

## 3.8 Concluding Remarks

Multiple diffusion flames were utilized to synthesize $TiO_2$ nanoparticles containing C, Fe, Si, and V in a single-step flame synthesis process. The growth of carbon-coated (C-$TiO_2$), carbon-coated with iron oxide (Fe/C-$TiO_2$), silica-coated (Si-$TiO_2$) and vanadium-doped (V-$TiO_2$) $TiO_2$ nanoparticles was demonstrated. XRD and Raman data confirmed that coating $TiO_2$ NP with carbon and the addition of iron does not have a significant effect on the anatase content (~90% anatase), whereas adding Si decreases the anatase content by ~10%. The addition of vanadium substantially changes the anatase phase to rutile (~29% anatase). A graphitic carbon layer with thickness of 3 to 5 nm was coated on $TiO_2$ nanoparticles for C-$TiO_2$. Adding iron to the sample (Fe/C-$TiO_2$) increases the carbon layer and small iron oxide nanoparticles were observed. TGA result showed that complete oxidation of carbon occurs at a temperature of 470$^o$C (iron based sample) compared to 610$^o$C (without iron) indicating the catalytic effect of iron based sample. XPS confirms the formation of $Fe^{3+}$ oxidation state of iron. With regards to Si-$TiO_2$ nanoparticles, a uniform coating of 3 to 8 nm of $SiO_2$ was observed around the $TiO_2$ particles. This coating can be attributed to the differences in the chemical reaction rates of the precursors. Finally, with regards to V-$TiO_2$, vanadium is doped within the $TiO_2$ nanoparticles, as observed from HRTEM, and XPS further confirms the formation of $V^{4+}$ and $V^{5+}$ oxidation states of vanadium.

# Chapter 4

# Synthesis of Iron-Doped $TiO_2$ Nanoparticles Using Flame Spray Pyrolysis (FSP)

Fe-doped $TiO_2$ nanoparticles, with varied iron to titanium atomic ratios from 0 to 10% were synthesized by flame spray pyrolysis (FSP), using a single-step process. Ferrocene, being nontoxic and readily soluble in liquid hydrocarbons, was used as the iron source, while titanium tetraisopropoxide was used as the precursor for $TiO_2$. Particle morphology, phase formation, and elemental structure were examined using XRD, Raman, ICP-OES, BET, TEM/HRTEM, EELS, EDS, and XPS. Finally, SQUID was used to observe the magnetic properties of the synthesized nanoparticles.

## 4.1 Introduction

Flame spray pyrolysis (FSP), has emerged as a cost effective method for large-scale synthesis of nanoparticles [5] and a number of large-scale pilot projects based on FSP have been recently demonstrated [176]. The Johnson-Matthey Company announced the use of FSP for the exploration of next-generation materials related to catalytic applications [47]. Wegner *et al.* [176], demonstrated that FSP can be used to produce nanoparticles at a rate of few kilograms per hour at a cost below 100 EUR/kg, where chemical precursors account for the majority of the cost. It is critical to explore research in different precursors for use in FSP, where future innovation may occur at the juncture of combustion, material, and aerosol engineering.

Titanium dioxide ($TiO_2$) is widely produced using flame-based methods [54, 141, 177] for various applications in catalysis, water-treatment, and solar cells. Doping $TiO_2$ nanoparticles with transition metals, such as Fe and Co, can result in better photocatalytic conversions due

to a reduction in the band-gap and the recombination rate of the electron hole pair [178-180]. Additionally, such transition metals can be used to produce $TiO_2$ nanoparticles with dilute magnetic semiconductor properties [110], that are important for spintronics applications.

Fe-doped $TiO_2$ nanoparticles have been synthesized using wet-chemistry based methods [181-183]. Typically, a number of steps are involved in using such methods (as well as post annealing), to obtain crystallized samples. Also higher doping concentrations (Fe 3 atom%), will result in phase segregation, due to annealing [183]. A key advantage of gas-phase methods is the ability to produce Fe-$TiO_2$ nanoparticles in a single-step process. Wang *et al*. [183], used an RF thermal plasma for the production of Fe-$TiO_2$ nanoparticles, with a Fe/Ti ratio ranging from 0 to 20%, where increased iron doping promoted the transformation from anatase to rutile nanoparticles. Teoh *et al.* [184], used FSP for synthesis of Fe-$TiO_2$ with titanium tetraisopropoxide (TTIP), and iron naphthenate as the precursor for Ti and Fe, respectively. The Fe/Ti ratio approached 5%, five times higher than conventional wet techniques that are followed by annealing. Increasing Fe concentration results in the transformation to rutile nanoparticles. The Fe-$TiO_2$ nanoparticles were also active under visible light and the rate of oxalic acid mineralization was 6.4 times greater compared to pure $TiO_2$ and Degussa P25. Magnetic properties were not reported for the FSP- made Fe-$TiO_2$ nanoparticles.

Ferrocene being nontoxic, air stable, and readily soluble in pure liquid hydrocarbons [185] was used as the source of iron in the synthesis of Fe-doped $TiO_2$ nanoparticles. Ferrocene has been widely studied in the combustion community as a fuel additive for soot reduction [185, 186]. It has also been used as a catalyst for the growth of carbon nanotubes [187, 188], and as an additive in diffusion flames for controlling the surface area of silica nanoparticles [189]. To the best of our knowledge, the use of ferrocene has yet to be reported using FSP. In the present study, ferrocene combined with TTIP was used as the precursor for the synthesis of Fe-doped

$TiO_2$ nanoparticles. Detailed characterization was carried out to verify the morphology and elemental composition of the particles. Finally, optical and magnetic properties were measured.

In this chapter the flame spray pyrolysis (FSP) burner will be discussed for the production of iron-doped $TiO_2$ nanoparticles and their optical, magnetic and photocatalytic properties.

## 4.2 Experiment

A flame spray pyrolysis process (FSP), was implemented to synthesize $TiO_2$ and Fe-$TiO_2$ nanoparticles. Figure 4.1 shows a schematic of the experimental setup, composed of a spray system with an annular pilot flame, a precursor delivery system and a particle collection system. The spray system was an air-assisted spray nozzle. The precursor flowed through the capillary tube while the dispersion gas passed through the annular gap. An annular slit (15.88 mm inner diameter and 1 mm thickness), surrounding the nozzle provided the supporting premixed pilot flame. Methane (purity 99.995%), with a flow rate of 1.25 l/min was mixed with 2.5 l/min of oxygen ($O_2$; purity 99.9995%), for the pilot flame; whereas 10.6 l/min of oxygen at pressure drop higher than 2.5 bar was used as the dispersion gas in the spray nozzle for precursor atomization.

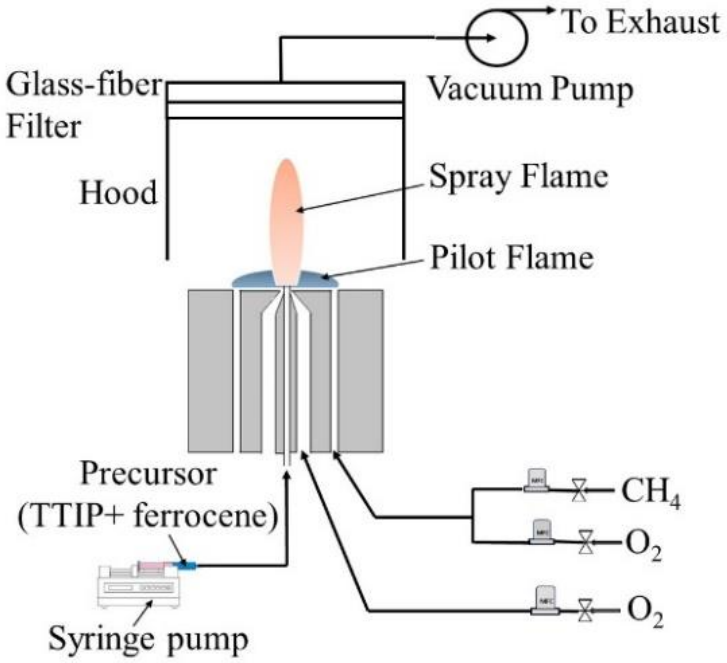


**Figure 4.1:** Schematic diagram for the Flame Spray Pyrolysis (FSP) apparatus

Titanium tetraisopropoxide (TTIP; Sigma-Aldrich, 97% purity) is used as the main precursor for $TiO_2$ NPs and ferrocene (Sigma-Aldrich, 98%) dissolved in m-xylene (Sigma-Aldrich, 99%) is mixed with TTIP to prepare iron-doped titania (Fe-$TiO_2$) NPs. The concentration of ferrocene was changed to have different doping level (from 1% to 10% Fe/Ti molar ratio). The doped samples were denoted as 1%, 3%, 5%, and 10% Fe-$TiO_2$ according to the iron concentration in the sample. The precursor is injected using a syringe pump directly into the spray nozzle with a flow rate of 450 ml/hr. The synthesized nanoparticles are collected on a glass-fiber filter with the aid of vacuum pump. The powder is scratched from the filter and stored in a glass veil for extra analysis.

Collected nanoparticles were characterized using X-ray diffraction (XRD) by an advance X-ray powder diffractometer (Bruker, D8) with CuK$\alpha$ ($\lambda$=1.5406 Å) radiation. Raman spectroscopy measurements were performed on a Raman spectrometer (Aramis, LabRAM HR Visible) using 473 nm excitation from a diode-pumped solid-state (DPSS) laser (7 mW with 1.1 $cm^{-1}$ spectral resolution). The specific surface area (SSA) was calculated based on multi-

point Brunauer–Emmett–Teller (BET) nitrogen adsorption (Micromeritics, ASAP 2420). Also, the nanoparticles were characterized using X-ray photoelectron spectroscopy (XPS) for surface chemistry, ultraviolet-visible spectroscopy (UV-vis, Varian Cary 500) for light absorbance, inductively coupled plasma (Varian ICP-OES 720 ES) for metal traces, and a superconducting quantum interference device (SQUID-VSM Quantum design, USA) determined the magnetic properties.

The primary particle size and morphology were examined by transmission electron microscopy (TEM). TEM specimens were prepared by mixing powder samples in Ethanol and followed by placing a small droplet (about 4 μL) onto holy carbon (C) copper (Cu) grids. These grids were then blotted from backside in order to remove Ethanol quickly so that relatively cleaner specimens get prepared for the TEM-analysis. Entire TEM investigations were carried out in a Titan 80-300 ST electron microscope from FEI Company which was equipped with an extra-brightness field-emission gun, X-ray energy-dispersive detector (EDS), electron energy filter and a charge-coupled devices (CCD) camera. The analysis was acquired by operating the microscope at the 300 keV of energy and it involved setting the microscope in various modes such as bright-field TEM (BF-TEM), high resolution TEM (HRTEM), selected area electron diffraction (SAED), valence electron energy-loss spectroscopy (VEELS), and energy-filtered TEM (EFTEM) modes to gather a specific information about the physical properties of samples. For instance, BF-TEM analysis in conjunction with EDS was utilized to determine the average size of the NPs as well as their overall elemental composition. The BF-TEM and SAED analyses were used to determine the crystal-structure of the Fe-doped $TiO_2$ NPs. In the same token, HRTEM analysis allowed determining the structure and morphology of NPs. The core-loss EELS method also provided the information on the elemental composition of the samples which was compared with composition numbers determined by TEM-EDS technique. The EFTEM analysis of the samples was carried out to determine the spatial distributions of

Ti, O, and Fe elements in the NPs. This was accomplished by operating the energy-filter in EFTEM-mode and the so called "3-window" method was employed to generate the elemental maps [190]. It should be noted that the entire TEM data were acquired and analyzed in Digital-Micrograph Software Package from Gatan, Inc.

## 4.3 Nanoparticle Characterization

Ferrocene (Fe precursor) was mixed with TTIP (Ti precursor) to prepare iron-doped titania nanoparticles. The concentration of ferrocene was changed to have different doping levels (from 1% to 10% Fe/Ti molar ratio). In chapter 3 when using multiple diffusion burner, the iron-doped samples were coated with carbon. But in this chapter (using FSP), there is no significant effect of carbon in the generated sample due to the high oxygen concentration and very high temperature gradient achieved by the FSP system.

XRD is commonly used to identify the crystalline structure of $TiO_2$ nanoparticles. Figure 4.2 shows the XRD patterns of the various synthesized Fe-doped $TiO_2$ nanoparticles. Anatase phase is dominant for the pure $TiO_2$ nanoparticles while iron doping changes the anatase phase monotonically with the iron concentration in the sample. At 10% of iron-doping, the rutile phase is dominant. The anatase percentage in the samples was calculated by integrating the respective XRD peak intensities (anatase (101) peak at $2\theta = 25.4^o$ and rutile (110) peak at $2\theta = 27.5^o$) using the following equation [142]

$$W_R = \frac{A_R}{0.884A_A + A_R} \qquad (4.1)$$

where $W_R$ is the weight fraction of rutile in the $TiO_2$ sample and $A_A$ and $A_R$ are the integrated areas under the anatase and rutile peaks, respectively. The values of anatase percentage in the mixtures are listed in Table 4.1.

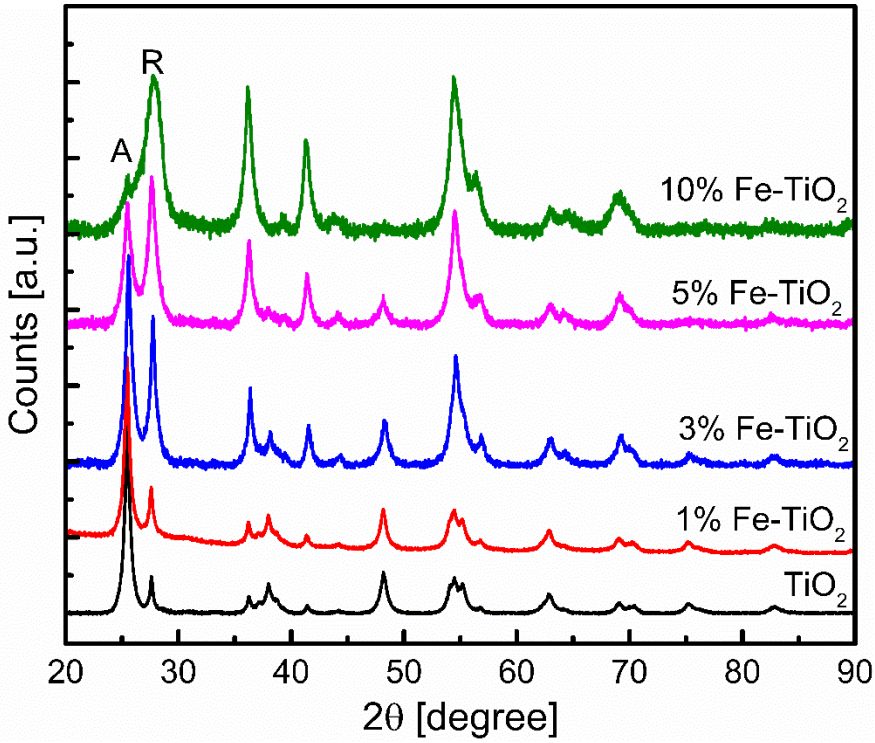


**Figure 4.2:** XRD pattern for iron-doped samples compared with the $TiO_2$ produced from the FSP.

The crystallite size $d_{XRD}$ of $TiO_2$ NPs can be obtained from the position of the (101) and (110) peaks using the Scherrer formula [143]

$$L = \frac{K.\lambda}{\beta.\cos\theta} = d_{XRD} \qquad (4.2)$$

where $L$ is the crystallite size, $K$ is 0.89, $\theta$ is the Bragg's angle, $\beta$ is the full width at half-maximum of the corresponding peaks, and $\lambda$ is the wavelength of X-ray radiation (Cu Kα 1.5418 Å). The crystallite size calculated from XRD experiments ranges from 12- 19 nm and is summarized in Table 4.1.

**Table 4.1:** Summary results for the properties of nanoparticles prepared by FSP.

| Sample | Anatase | $d_{XRD}$ | BET | $d_{BET}$ | Fe % from ICP |
|---|---|---|---|---|---|
| | % | [nm] | [$m^2$/g] | [nm] | |
| $TiO_2$ | 91.8 | 16.2 | 151 | 9.9 | - |
| 1% Fe-$TiO_2$ | 85.8 | 18.8 | 118 | 12.6 | 0.87 |
| 3% Fe-$TiO_2$ | 64.2 | 16.3 | 137 | 10.9 | 1.56 |
| 5% Fe-$TiO_2$ | 42.1 | 12.2 | 139 | 10.4 | 2.61 |
| 10% Fe-$TiO_2$ | 20.9 | 15.9 | 140 | 10.2 | 5.24 |

Raman spectroscopy was performed to further characterize the $TiO_2$ nanoparticles. It is known [144] that anatase $TiO_2$ has 15 optical modes and 6 of these are Raman active (irreducible representation of $A_{1g}$ (515 $cm^{-1}$), $2B_{1g}$ (399 and 519 $cm^{-1}$), and $3E_g$ (144, 197 and 639 $cm^{-1}$)), whereas rutile $TiO_2$ has 11 optical modes, among which 4 are Raman active (irreducible representation of $A_{1g}$ (612 $cm^{-1}$), $B_{1g}$ (143 $cm^{-1}$), $B_{2g}$ (826 $cm^{-1}$), and $E_g$ (447 $cm^{-1}$)). The Raman spectra in the visible region (Fig. 4.3) also show that the anatase phase is dominant for the $TiO_2$ samples, while the rutile phase is dominant for the Fe-$TiO_2$ samples, which are consistent with previous XRD data. Raman spectroscopy is a unique method in characterizing the order-disorder effect in carbonaceous materials, which typically have two major bands [145, 146], with the graphitic G-band around 1580 $cm^{-1}$ and the disordered or amorphous D-band around 1340 $cm^{-1}$. These two carbonaceous bands do not appear in the iron-doped samples, which indicate the absence of carbon in these two samples, unlike samples prepared by multiple flame burner in the previous chapter which contain carbon.

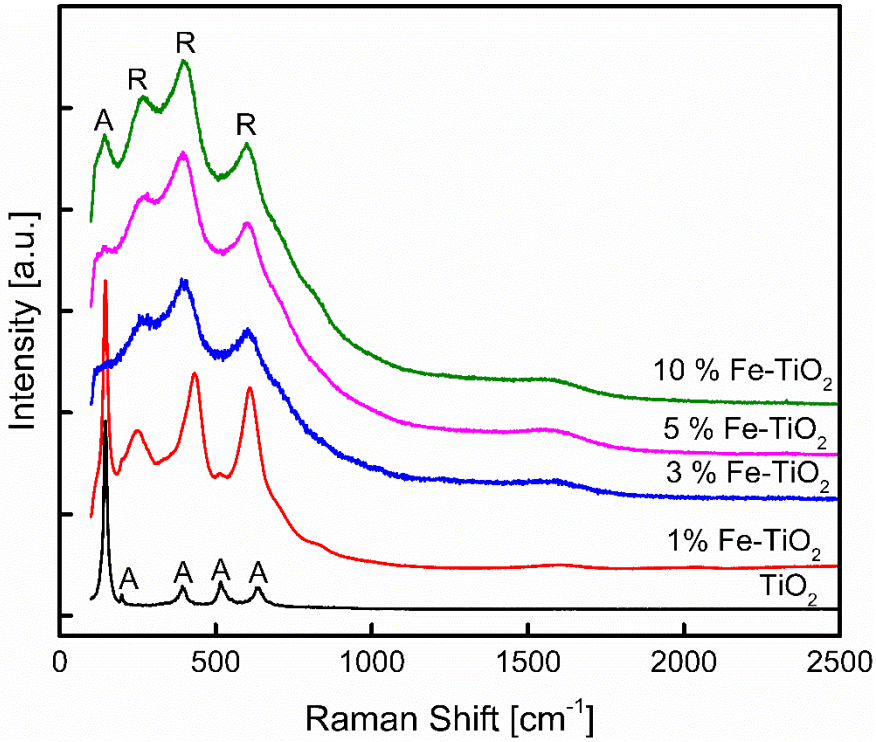


**Figure 4.3**: Raman spectra for $TiO_2$ and Fe-doped $TiO_2$ nanoparticles prepared by FSP; A (anatase), R (rutile).

The specific surface area (SSA) of the nanoparticles is measured using BET nitrogen adsorption technique and the results are shown in Table 4.1. The SSA for the iron-free $TiO_2$ sample was 151 $m^2/g$. the surface area reduced to 118 $m^2/g$ when doping with iron with 1%. This reduction of surface area may be due to the phase change from anatase to rutile which has larger crystal size. As increasing the iron content, the surface area increases again due to small clusters of iron oxides which are dispersed in the $TiO_2$ surface [109]. Based on the surface area obtained from BET analysis and assuming spherical particles, the average primary particle size $d_{BET}$ is calculated by [147]

$$d_{\mathrm{BET}} = \frac{6}{[V_A.\rho_A + V_R.\rho_R]\times SSA} \qquad (4.3)$$

where $V_A$ and $V_R$ are the volume fractions of anatase and rutile phase, respectively, $\rho_A$ is the density of anatase (3.99 $g/cm^3$) and $\rho_R$ is the density of rutile (4.26 $g/cm^3$) [147]. The average particle size, $d_{BET}$, was around 10 nm for all samples and is comparable to that calculated from

XRD analysis (Table 4.1). ICP-OES was employed to accurately measure the iron percentage in the doped samples and are shown in Table 4.1. The percentage of Fe in each sample is proportional to the amount of ferrocene added to the raw precursor but with lower values (almost half of the added percentages).

### 4.3.1 Nanoparticles' morphology

BF-TEM analysis in conjunction with EDS was performed first in order to check the quality of synthesized NPs and their overall elemental composition. Several electron micrographs at a relatively low magnification and EDS spectra were acquired from the various locations on the grid in order to have a good representation for the size and composition of NPs. Typical electron micrographs along with its corresponding EDS spectrum for pure $TiO_2$ sample are shown in Figure 4.4a and Figure 4.5, respectively. It contains several NPs whose average size was about 20 nm. The EDS analysis presented in Figure 4.5 thus confirms the presence of O and Ti elements, in the NPs shown in Figure 4.4. The presented EDS spectrum also contains a couple of extra peaks which are due to Cu-grids. The NPs that are shown in Figure 4.4a were then further analyzed at a higher magnification in order to have a closer look at their morphology (Fig. 4.4b). The corresponding SAED patterns were acquired as well to determine their crystal structure. The SAED micrograph (Fig. 4.4d) contains diffraction rings implying that the synthesized NPs are of crystalline phase. The distance of these spots from center represents the crystallographic inter-planar d-spacings and provides a direct evidence of crystalline phase of the NPs. Such analysis revealed that the distances of those spots correspond to the planes of anatase phase $TiO_2$, as confirmed by XRD and Raman results. A typical electron micrograph acquired with HRTEM conditions is shown in Figure 4.4c. The image reveals the high crystallinity and the ordered structure of the nanoparticle lattice planes

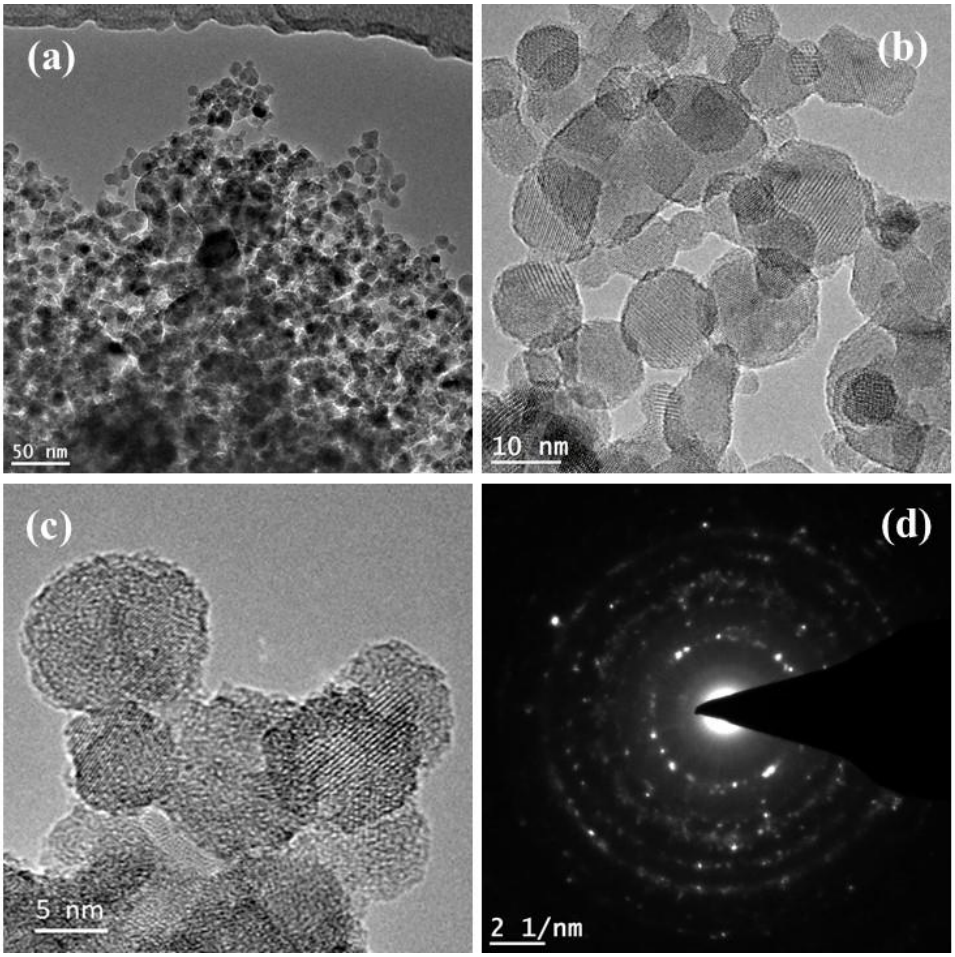


**Figure 4.4:** TEM (a) and high resolution TEM (b, c) images pure $TiO_2$ nanoparticles with (d) the corresponding SAED pattern containing the diffraction rings.

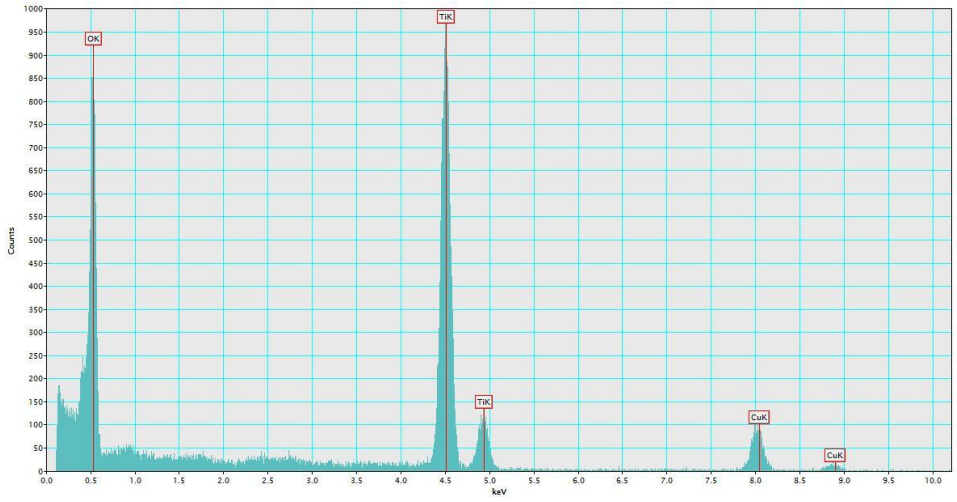


**Figure 4.5:** EDS spectrum acquired from the region of Figure 4.4a which confirms the presence of pure $TiO_2$ material.

TEM image of 3% Fe-$TiO_2$ nanoparticles is shown in Fig. 4.6a. The particle morphology is similar to that of pure $TiO_2$ sample. The HRTEM image of the doped-$TiO_2$ particles shown in Fig. 4.6b reveals the high crystallinity and the ordered structure of the nanoparticle lattice planes. Figures 4.6c and 4.6d show the corresponding SAED pattern containing the diffraction rings and the corresponding calculated FFT containing the spatial frequencies. In both diffraction patterns, the innermost ring-type patterns have a double layer pattern with diffraction spots very close to each other, an indication of the mixture of the anatase and rutile phases in agreement with XRD results.

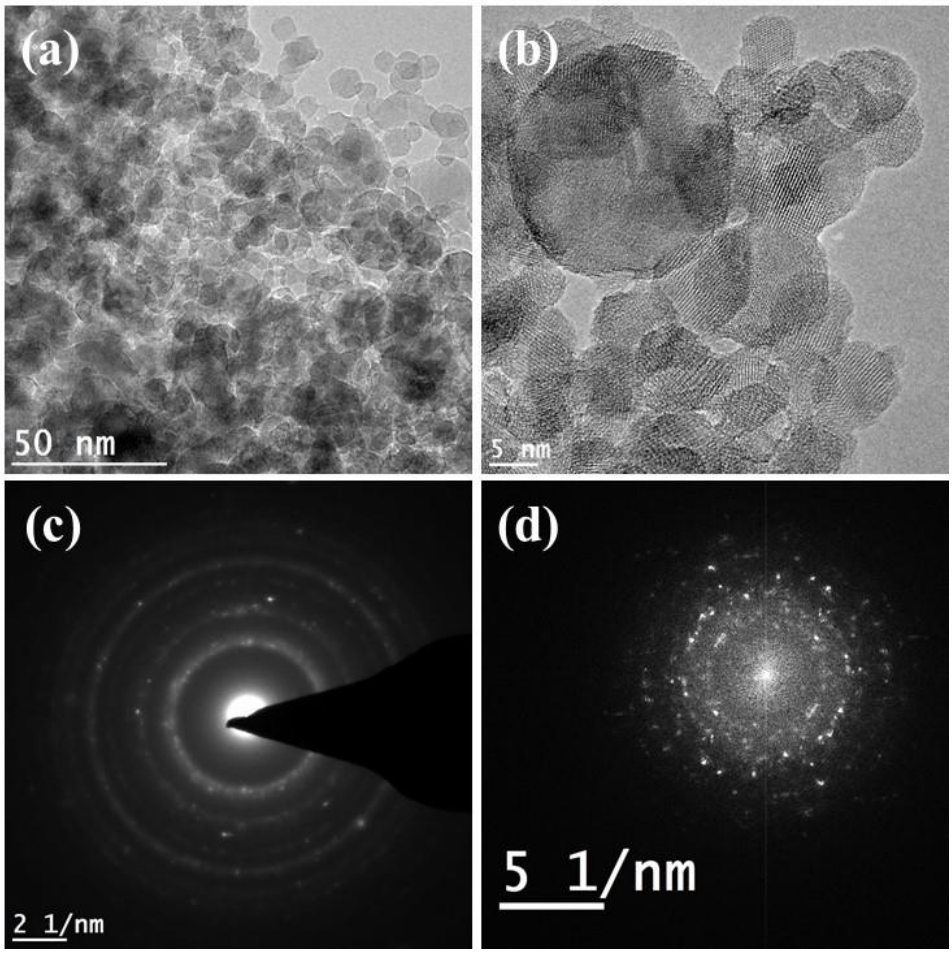


**Figure 4.6:** TEM (a) and high resolution TEM (b) images 3% Fe-$TiO_2$ nanoparticles with (c) the corresponding SAED pattern containing the diffraction rings and (d) the corresponding calculated FFT containing the spatial frequencies.

The EDS analysis presented in Figure 4.7 thus confirms the presence of all three elements, namely O, Ti, and Fe, in the NPs shown in Figure 4.6. The presented EDS spectrum also contains extra peaks which are due to Cu-grids with no evidence for carbon existence.

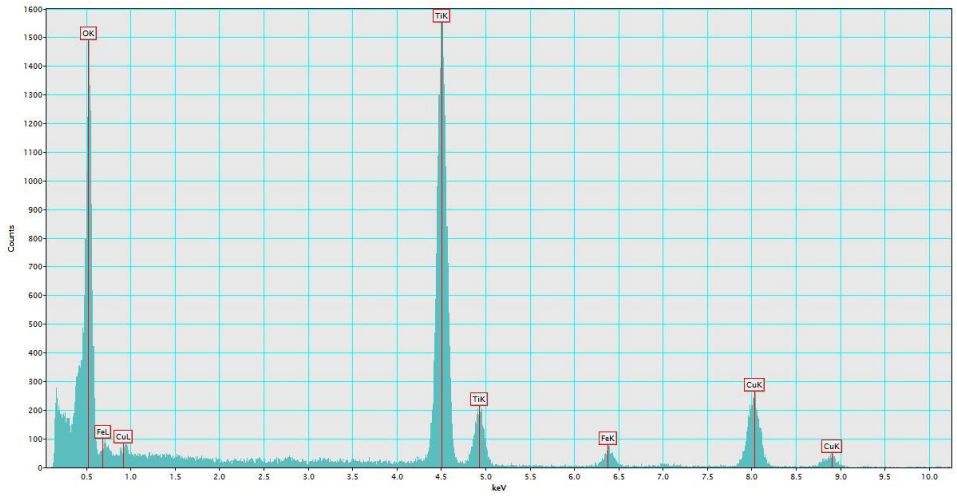


**Figure 4.7:** EDS spectrum acquired from the region of Figure 4.6a which confirms the presence of Fe in the 3% Fe-$TiO_2$ material.

Similar to 3% Fe-$TiO_2$ nanoparticles, Fig. 4.8 shows the TEM, HRTEM, SAED pattern and the corresponding FFT for 10% Fe-$TiO_2$ nanoparticles. The images reveal crystallined spherical particles with ring-type diffraction pattern indicating the presence of rutile and anatase phases. Figure 4.9 shows the EDS spectrum acquired from the TEM images for the same sample. The EDS analysis confirms the presence of all three elements, namely O, Ti, and Fe, in the iron-doped NPs shown in Figure 4.8. The presented EDS spectrum also contains extra peaks which are due to Cu-grids and one carbon peak from the grid background. Comparing the Fe peaks in both Fig. 4.7 and Fig. 4.9, we can realize that Fe peaks in the later one have larger values, which are in accordance with the iron content in the samples.

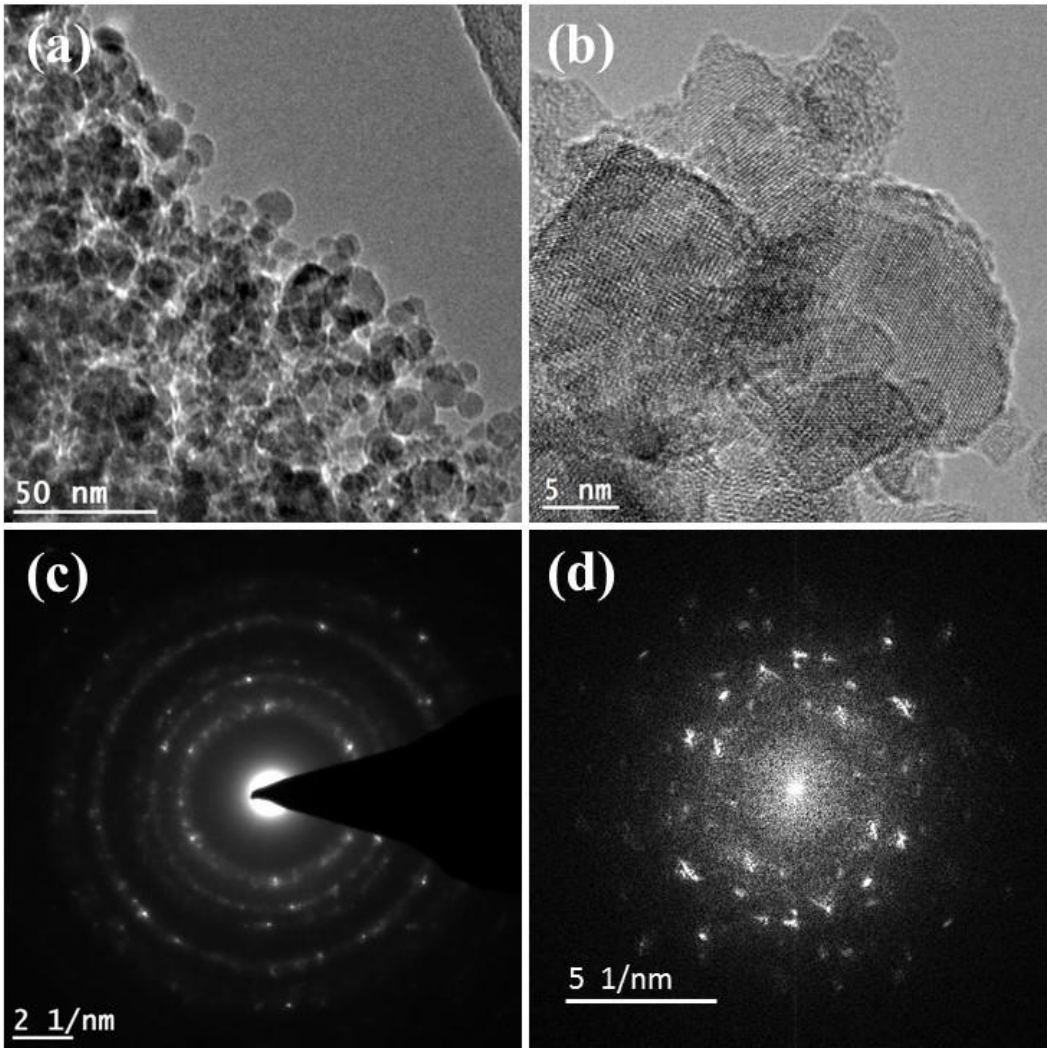


**Figure 4.8:** TEM (a) and high resolution TEM (b) images 10% Fe-$TiO_2$ nanoparticles with (c) the corresponding SAED pattern containing the diffraction rings and (d) the corresponding calculated FFT containing the spatial frequencies.

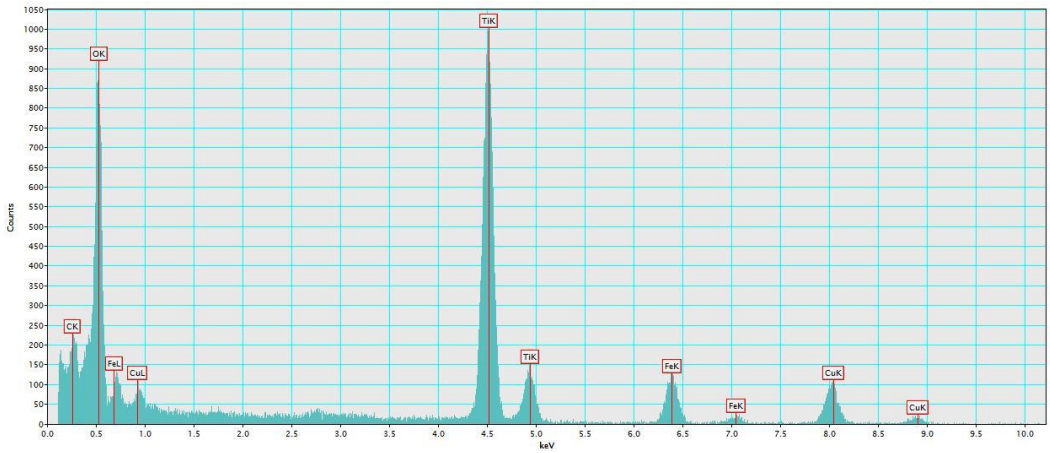


**Figure 4.9:** EDS spectrum acquired from the region of Figure 4.8a which confirms the presence of Fe in the 10% Fe-$TiO_2$ material.

The spatial distributions of all three elements comprising the Fe-doped $TiO_2$ NPs were important in judging their quality particularly in terms of finding any un-wanted phases. This task was completed by applying the EFTEM analysis to the NPs shown in Figure 4.8 and the corresponding results are shown in Figure 4.10. The presented elemental maps therein demonstrate that Ti, O, and Fe were present uniformly in the NPs and that Fe is totally doped in the $TiO_2$ nanoparticles.

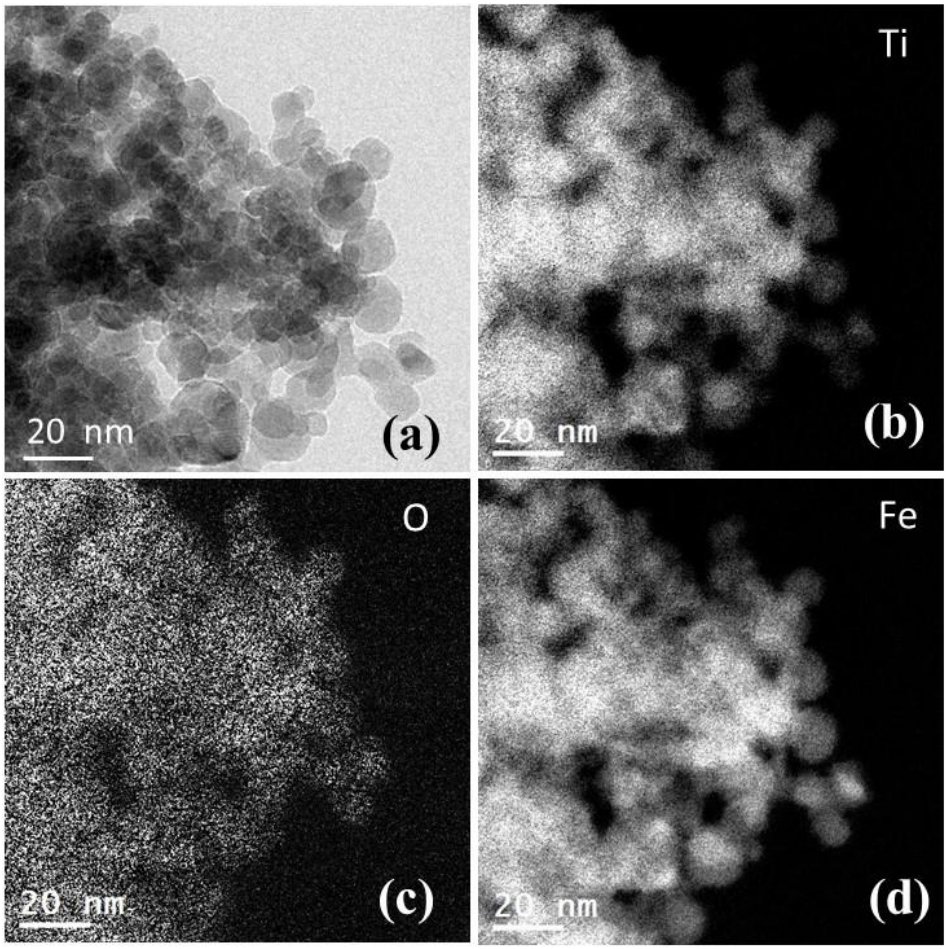


**Figure 4.10:** Elemental mapping of 10% Fe-$TiO_2$ nanoparticles indicating (a) raw TEM image, (b, c, d) are Ti, O, and Fe maps, respectively.

### 4.3.2 Magnetic properties

In order to know the intrinsic magnetic properties of the samples, the temperature variation of magnetization measurements (Moment (M) vs. Temperature (T)) were carried out. Initially the sample was cooled to 5 K under a nominal zero field then applied a field of H = 1kOe,

subsequently, M vs T data was measured under that constant magnetic field while warming the sample from 5-300 K and is depicted in Fig. 4.11. It shows that all the samples are typical paramagnetic and none showed any Curie transitions ($T_C$) within the temperature range of study, implying that Fe doping did not induce any long range ferromagnetic interactions in these samples.

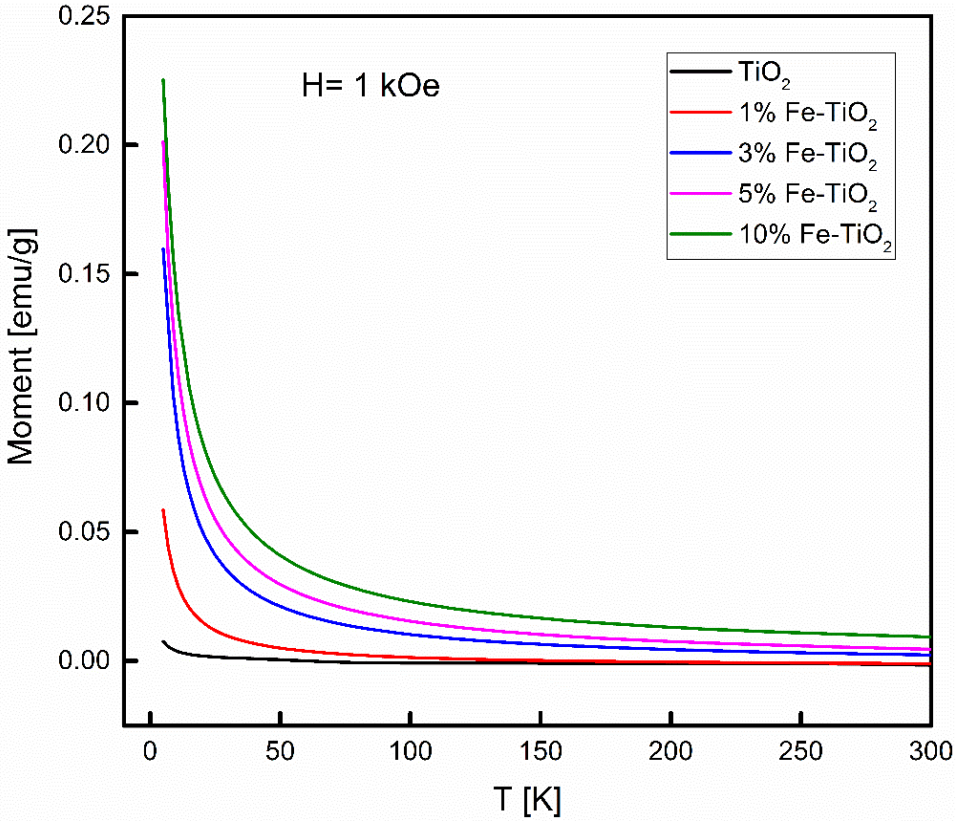


**Figure 4.11:** Temperature-dependent magnetizations measured under a constant magnetic field of 1 kOe.

Isothermal magnetization measurements (Magnetic moment (M) vs. magnetic field (H)) were carried out. Necessary diamagnetic correction corresponding to the bare sample holder was applied after the magnetization measurements on each sample. Figure 4.12 and 4.13 show the magnetic hysteresis (M-H) curves of the undoped and Fe-doped $TiO_2$ samples taken at 5 and 300 K, respectively. It is observed from the Figs 4.11- 4.13 that the magnetization increases monotonically with increasing Fe content. At room temperature, most of the doped samples have small moment values similar to undoped sample except for 10 % case which has higher

moment than all other samples. . The inset in Fig. 4.13 shows Narrow opening of the hysteresis loop for the Fe 10 atom% doped $TiO_2$ sample which has the paramagnetic behavior. Earlier reports have attributed absence of ferromagnetism or paramagnetism in Fe doped $TiO_2$ that depended on the sample preparation methods and/or dopant concentrations [191]. The reasons include, dopant Fe ions remaining as isolated ions, weakly interacting Fe clusters in the host $TiO_2$ or presence of secondary phases such as $\alpha$-$Fe_2O_3$ or $Fe_3O_4$ since the iron ions may coexist in different valance states. In addition, oxygen defects [192-194] could induce magnetic interactions. Since we observed only paramagnetic properties in the present study we attribute it to isolated Fe clusters within the $TiO_2$ matrix [195, 196].

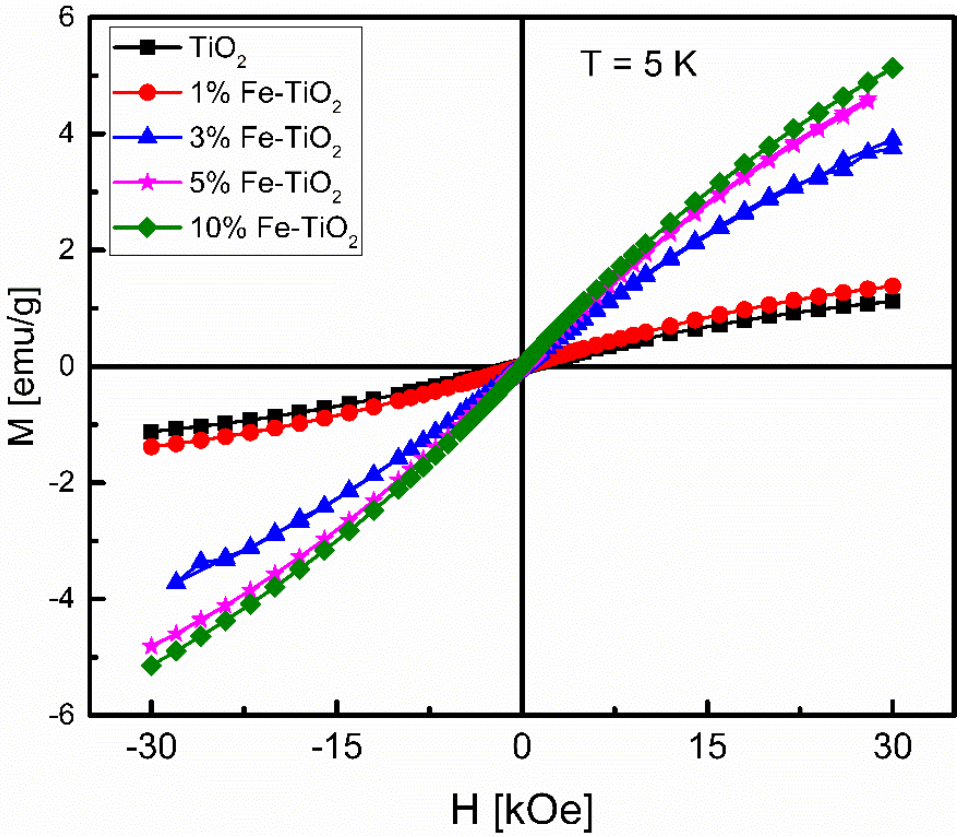


**Figure 4.12:** Magnetization (M-H) curves for the iron-doped titania nanoparticles compared to $TiO_2$ measured under external magnetic field (H) from -30 to 30 kOe at temperature of 5 K.

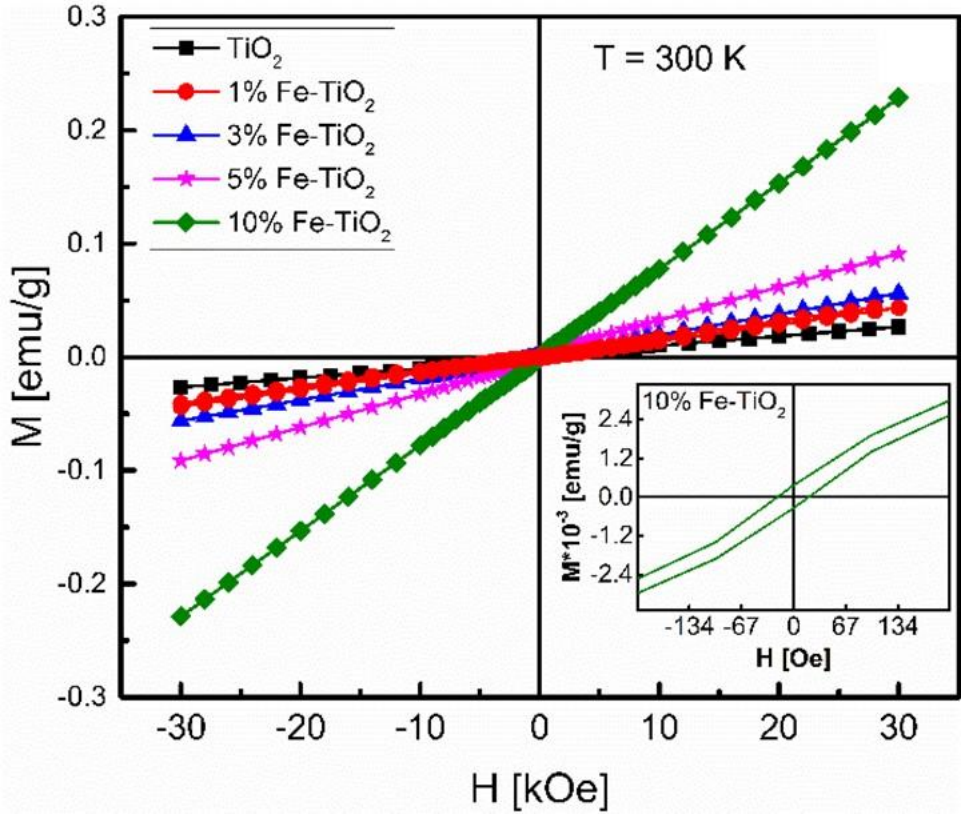


**Figure 4.13:** Magnetization (M-H) curves for the iron-doped titania nanoparticles compared to $TiO_2$ measured under external magnetic field (H) from -30 to 30 kOe at temperature of 300 K.

### 4.3.3 Surface chemistry

Chemical composition of the samples was analyzed using the X-ray photoelectron spectroscopy (XPS). Survey spectra from pure $TiO_2$ and from Fe-doped $TiO_2$ samples are obtained as shown in Fig. 4.14 and Fig. 4.15. Ti, O, C and Fe elements are detected (except Fe not detected from pure $TiO_2$).

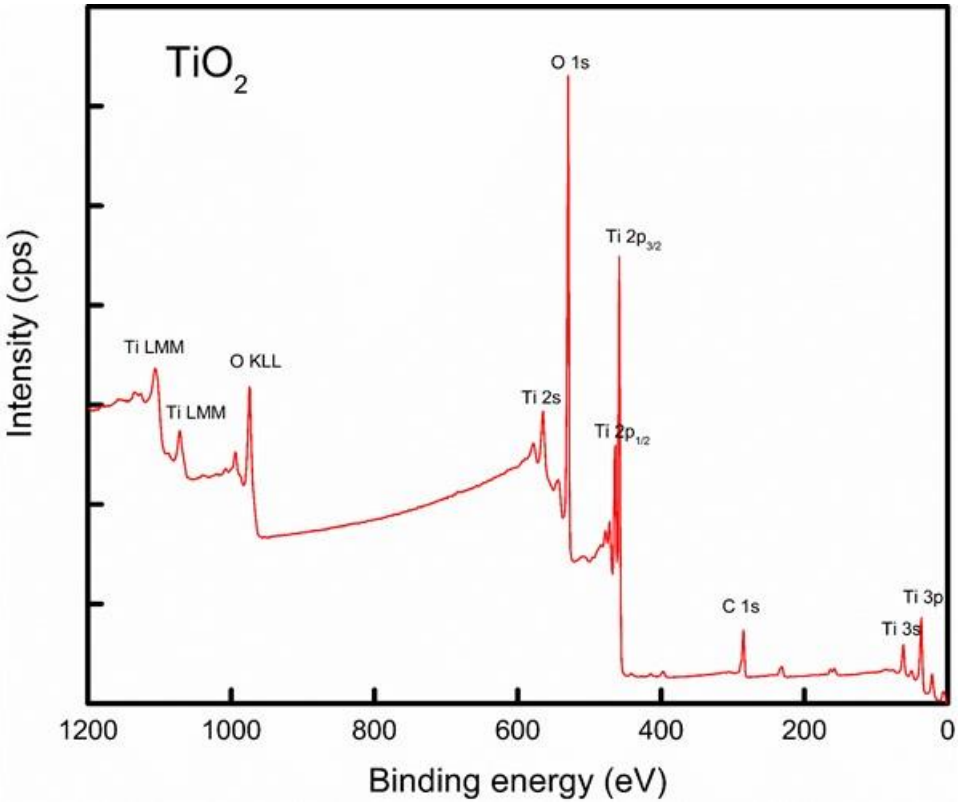


**Figure 4.14:** Survey scan spectra of pure $TiO_2$ nanoparticles.

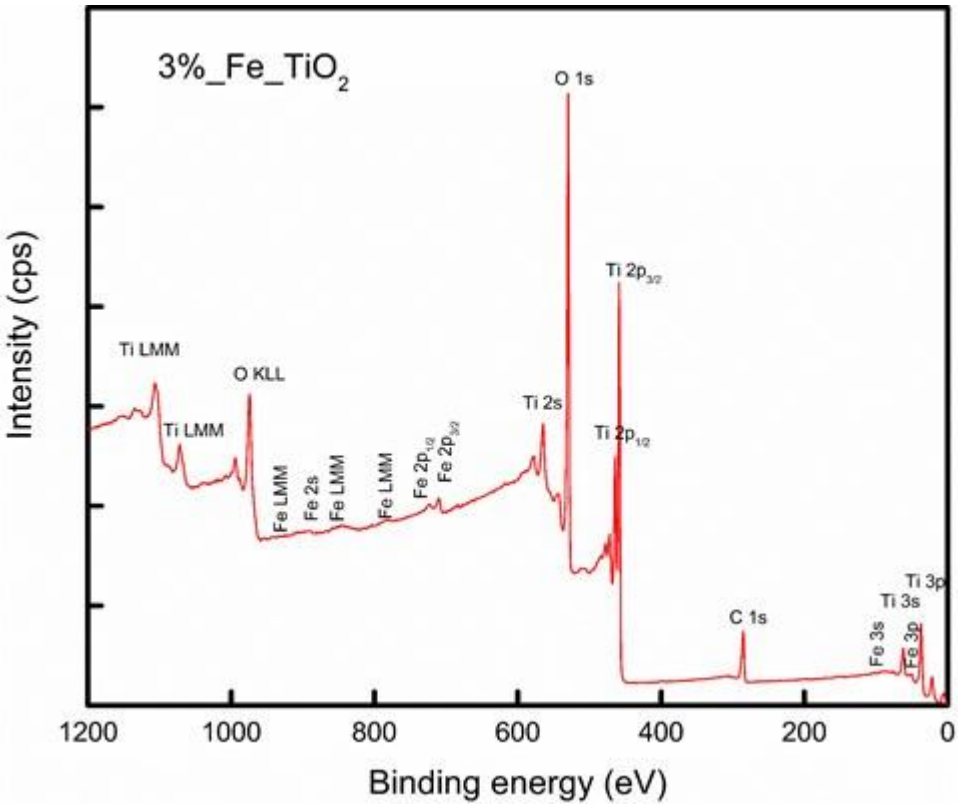


**Figure 4.15:** Survey scan spectra of 3% Fe-$TiO_2$ nanoparticles.

High resolution XPS spectra of Ti 2p and O 1s core levels from pure $TiO_2$ are shown in Fig. 4.16. The Ti $2p_{3/2}$ core level is fitted using two components. The dominant peak centered at 458.6 eV is associated to Ti ions with a formal valence 4+ ($Ti^{4+}$), while the peak at the lower binding energy ~ 456.6 eV is associated to Ti ions with a reduced charge state ($Ti^{3+}$) [151]. The O 1s core level is centered at 529.8 eV, which corresponds to the metal oxide ($TiO_2$) [151] and the C 1s core level (not shown) is centered at 284.4 eV. These C 1s, Ti 2p, O 1s peaks are also observed for all the Fe-doped $TiO_2$ samples.

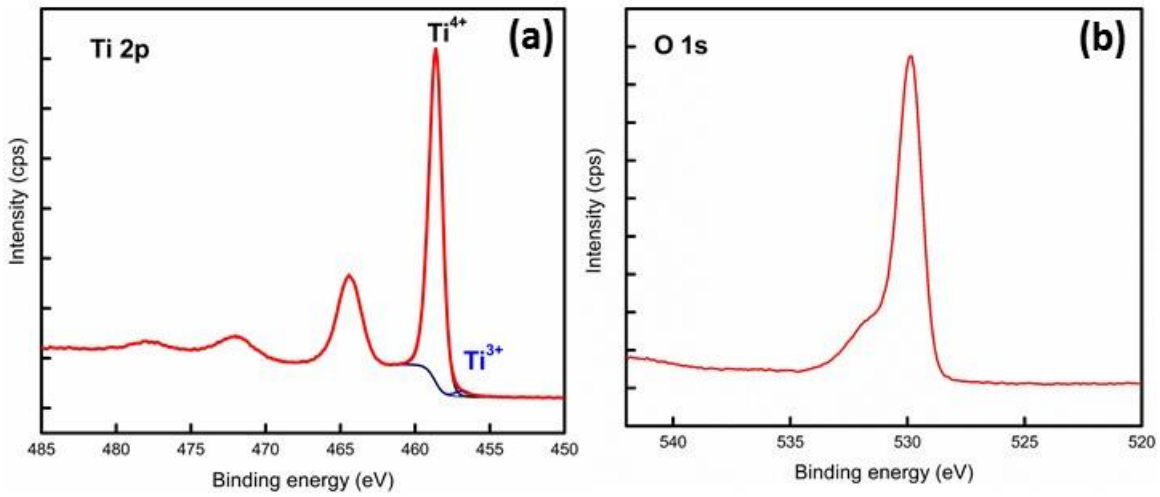


**Figure 4.16:** High resolution spectra of $TiO_2$ nanoparticles showing (a) Ti 2p peak and (b) O 1s peak.

High resolution XPS spectra of Fe 2p core level from Fe-doped $TiO_2$ at various iron percentages are obtained and shown in Fig. 4.17. The Fe 2p core level is fitted using eight components located at 710.8 eV, 709.1, 718.3, 719.4, 722.3, 724.2, 728.5 and 732.9 eV binding energy positions. The peaks at 710.8 eV (Fe $2p_{3/2}$ doublet) and 719.4 eV (corresponding satellite peak), together with 724.3 eV (Fe $2p_{1/2}$ doublet), and 732.9 eV (corresponding satellite peak) are characteristic of $Fe^{3+}$ oxidation state of iron [159, 197]. Also, the satellite peaks situated at 8.6 eV from the main peaks are the signature of $Fe^{3+}$ ions.

The peaks at 709.1 eV (Fe $2p_{3/2}$ doublet) and 715.3 eV (corresponding satellite peak), together with 722.3 eV (Fe $2p_{1/2}$ doublet), and 728.5 eV (corresponding satellite peak) are characteristic

of $Fe^{2+}$ oxidation state of iron [157, 159]. Also, the satellite peaks situated at 6.2 eV from the main peaks are the signature of $Fe^{2+}$ ions. The area ratio of Fe $2p_{3/2}$ – Fe $2p_{1/2}$ components is equal to 2:1 and the doublet separation is equal to 13.5 eV for $Fe^{3+}$ and to 13.2 for $Fe^{2+}$. The same values are used for their corresponding satellites. Increasing the percentage of the Fe dopant leads to the increase of the $Fe^{3+}/Fe^{2+}$ ratio from 0.5 at 3% Fe-$TiO_2$ to 1.8 at 10% Fe-$TiO_2$ sample.

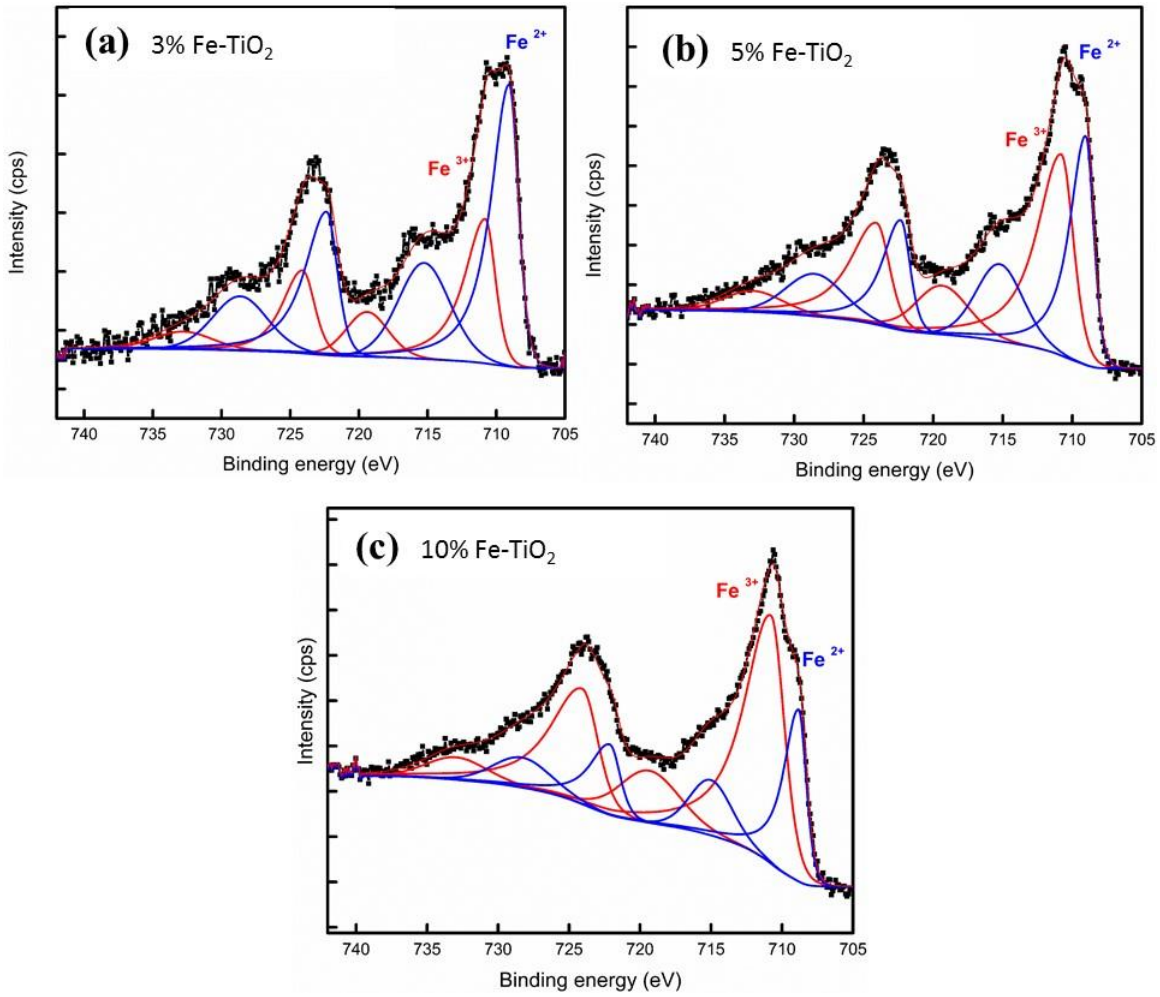


**Figure 4.17:** High resolution spectra of Fe 2p peaks for (a) 3% Fe-$TiO_2$, 5% Fe-$TiO_2$, and 10% Fe-$TiO_2$.

Valence band spectra from pure $TiO_2$ and Fe-doped $TiO_2$ nanoparticles at various percentages of iron are shown in Fig. 4.18. The spectrum of undoped $TiO_2$ contains three major features ( marked as A, B, and C) at binding energy positions around ~7.5, 5, and 1 eV respectively,

consistent with previous reported spectra for $TiO_2$ [198]. Features A and B are related to the O-2p derived states and are referred to as bonding and non-bonding orbital emissions respectively, while feature C corresponds to $Ti^{3+}$ 3d defect state. Features A and B are related to the O-2p derived states and are referred to as bonding and non-bonding orbital emissions respectively, while feature C corresponds to $Ti^{3+}$ 3d defect state. This feature is assigned to a mixed state of Fe 3d and Ti 3d derived states [198]. It was noticed also that the valence band edge from Fe-doped $TiO_2$ is shifted by ~1 eV to lower binding energy compared to undoped $TiO_2$, which enhance visible light absorption [199].

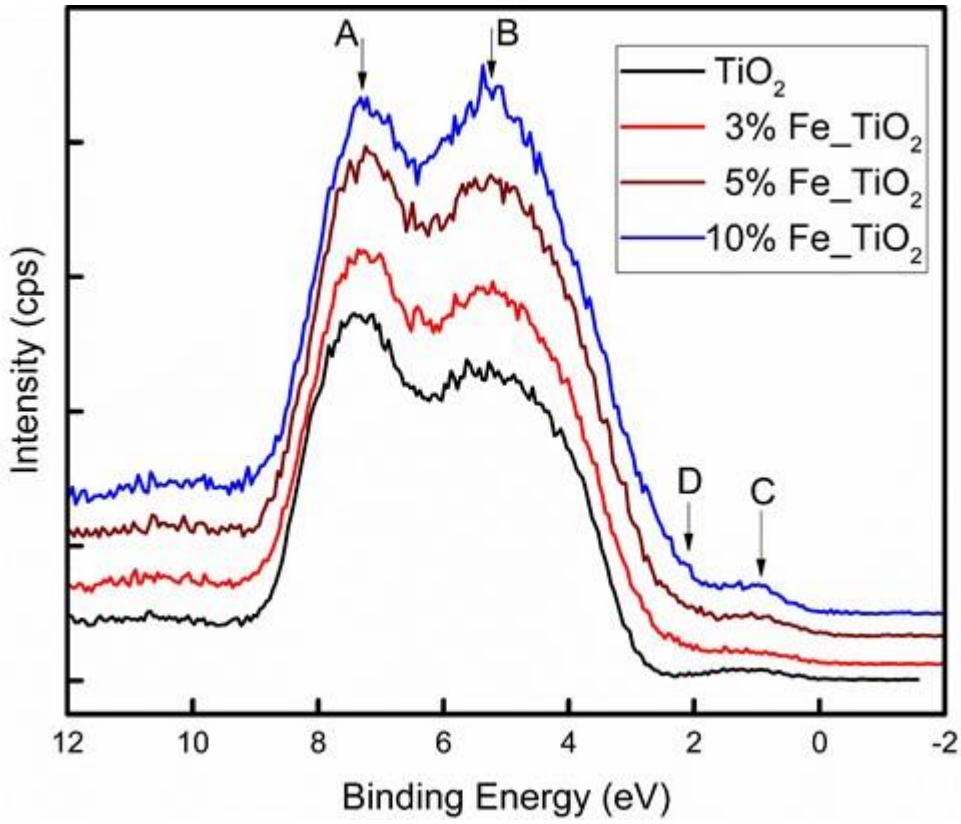


**Figure 4.18:** Valance band for the $TiO_2$ and Fe-doped $TiO_2$ samples indicating the structures A, B, and C for $TiO_2$ and structure D for Fe.

### 4.3.4 Optical properties

The UV-vis absorption spectra shown in Fig. 4.19 was used to identify that the light absorption from undoped and doped $TiO_2$ samples. Pure $TiO_2$ exhibited an absorption edge rising steeply toward the UV region below 400 nm, which could be attributed to the band-gap excitation of

anatase (3.2 eV), without absorption in visible region (>400 nm) [200]. Doping $TiO_2$ nanoparticles with iron has a significant enhancement of light absorption at 400~550 nm. The visible light absorption increases monotonically with increasing the iron concentration in the doped samples, accompanying with the change of powder color from white to brown (Fig. 4.20). This result satisfies the aim of the study which was to increase the visible light absorption of $TiO_2$ nanoparticles by doping them with iron.

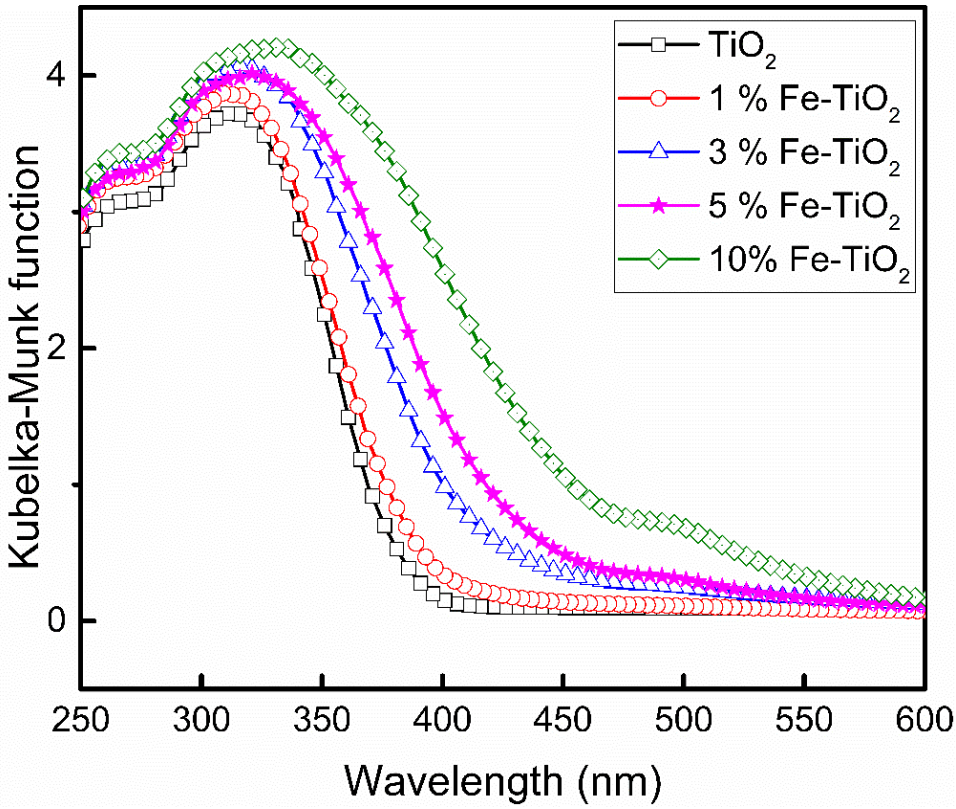


**Figure 4.19:** The ultraviolet-visible (UV-vis) spectra for the $TiO_2$ and Fe-doped $TiO_2$ samples.

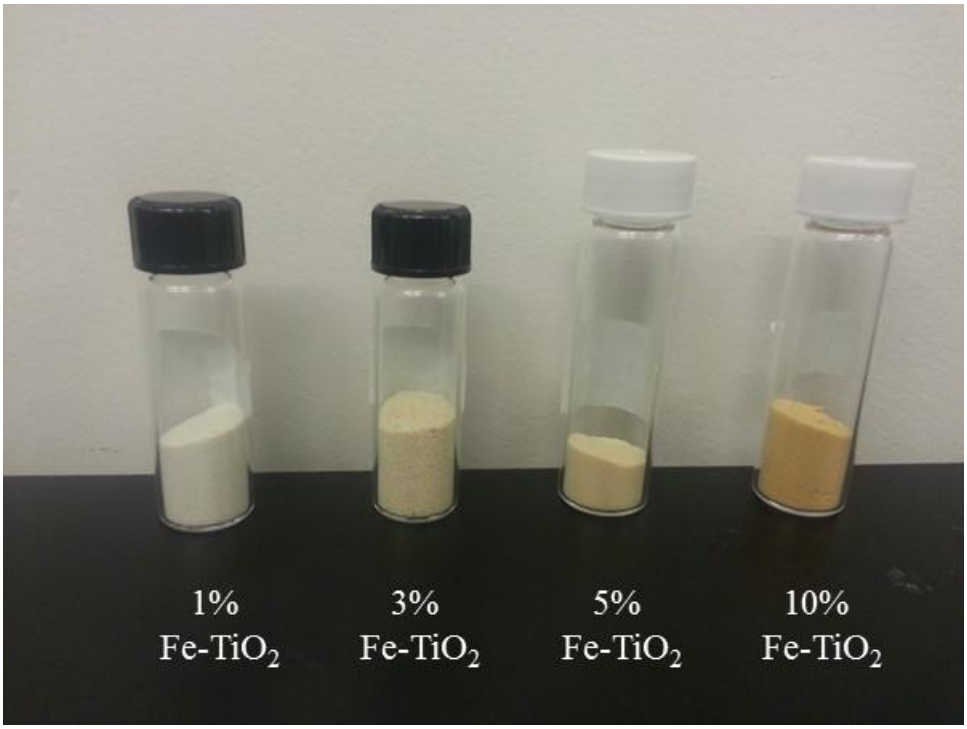


**Figure 4.20:** Fe-doped $TiO_2$ nanoparticles exhibiting color change.

## 4.4 Concluding Remarks

Flame spray pyrolysis (FSP) system was utilized to synthesize pure $TiO_2$ and Fe-doped $TiO_2$ nanoparticles with various iron concentrations in a single-step flame synthesis process. XRD, Raman, and BET data confirmed that anatase phase was dominant in pure $TiO_2$ nanoparticles (> 90% anatase) with an average particle diameter of 10 nm. The addition of iron substantially changes the anatase phase to rutile with anatase percentage changing from 86% to 21% when changing the iron concentration in the sample from 1% to 10%, respectively. XPS confirmed the formation of $Ti^{4+}$ and $Ti^{3+}$ oxidation states of Ti, which are signature of $TiO_2$ material. $Fe^{3+}$ and $Fe^{2+}$ were also confirmed. Increasing the percentage of the Fe dopant led to the increase of the $Fe^{3+}/Fe^{2+}$ ratio from 0.5 at 3% Fe-$TiO_2$ to 1.8 at 10% Fe-$TiO_2$ sample. Morphology of the generated nanoparticles using HRTEM revealed the crystallinity of spherical particles with information about phase change in agreement with XRD and Raman results. It was noticed also that the valence band edge from Fe-doped $TiO_2$ is shifted by ~1 eV

to lower binding energy compared to undoped $TiO_2$, which enhances visible light absorption of the doped samples as confirmed from UV-vis results. Regarding to the magnetic properties, iron doping enhances the magnetic properties of $TiO_2$ nanoparticles and changing them to paramagnetic materials.

In summary, FSP is an attractive method for the production of Fe-doped $TiO_2$, with ferrocene as the source of iron. The resulting material has desirable magnetic and optical properties, which may be used in various photocatalytic and electronic applications.

# Chapter 5

# Curved Wall-Jet (CWJ) Burner for Synthesizing Titania and Silica Nanoparticles

A novel curved wall-jet (CWJ) burner was designed for flame synthesis, by injecting precursors through a center tube and by supplying fuel/air mixtures as an annular-inward jet for rapid mixing of the precursors in the reaction zone. Titanium dioxide ($TiO_2$) and silicon dioxide ($SiO_2$) nanoparticles were produced in ethylene ($C_2H_4$)/air premixed flames using titanium tetraisopropoxide (TTIP) and hexamethyldisiloxane (HMDSO) as the precursors, respectively. Particle image velocimetry measurements confirmed that the precursors can be injected into the flames without appreciably affecting flow structure. The nanoparticles were characterized using X-ray diffraction, Raman spectroscopy, the Brunauer–Emmett–Teller (BET) method, and high-resolution transmission electron microscopy.

## 5.1 Introduction

Flame synthesis is widely used for the production of nanoparticles, as it readily offers the high temperature and oxidizing environment necessary for the growth of such particles. The global production of silicon dioxide ($SiO_2$) and titanium dioxide ($TiO_2$) nanoparticles relies mainly on flame-based processes [47], which offer simplicity, and can involve one-step and continuous processes. Complex phenomena are involved in flame synthesis, these being influenced by numerous parameters, as nanoparticles are formed within a few milliseconds of residence time [48]. For the continued advancement of flame synthesis technologies, it is important to develop novel reactors and to extend our understanding of growth processes.

Laminar flames are frequently used in laboratory scale experiments for flame synthesis of nanomaterials (both particles and one-dimensional materials [201-203]), these including coflow diffusion flames [53], multiple diffusion flames [54, 204], counter-flow diffusions flames [205], and premixed stagnation flames [52]. A detailed review of various burner geometries used for $TiO_2$ synthesis has been reported previously [54]. In industrial applications, turbulent flames are used for larger-scale production of nanomaterials [48], which add to the complexity of physical processes governing nanoparticle formation. These processes influence the crystallinity, size and morphology of the nanoparticles. As such, systematic lab-scale experimental data are limited. A turbulent premixed swirl flame [206, 207] was used for the synthesis of $TiO_2$ nanopowders and films and the particles were collected with the aid of a stagnation plate. Due to enhanced flame stabilization and lateral turbulent mixing, the growth of anatase $TiO_2$ particles with a size of 5-10 nm was demonstrated. Sung el al. [208] performed a computational study of a turbulent coflow diffusion flame, based on a large-eddy simulation with detailed gas-phase chemical kinetics including precursor oxidation. The model was used to simulate the growth of $TiO_2$, for which a mean particle size of 108 nm was predicted. Further analysis revealed that the particle diameter was larger near the centerline and decreased appreciably with radial distance.

In this chapter, we propose a novel turbulent burner for the flame synthesis of nanoparticles. The design is based on the curved wall-jet (CWJ) burner [6, 209], in which an annular-inward premixed jet was issued over a hemi-spherical surface of the burner center body, as shown schematically in Fig. 6.1a. The wall-jet initially adhered to the surface and then separated, forming a recirculation zone by the Coanda effect. Key advantages of the burner include the enhancement of turbulence due to the collision of the annular-inward jet in the interaction jet region, thus resulting in a small flame length. Additionally, blow-off can be delayed to larger jet velocities by the formation of a recirculation zone. Lastly, due to appreciable ambient air

entrainment by the streamline curvature, rapid mixing with ambient air was achieved, resulting in a blue flame with no visible soot, even when operating at highly fuel-rich conditions. Future designs will incorporate a spray atomizer within the curved-wall jet burner. Such a setup can be used to burn low cost chemical precursors due to the high temperature of the turbulent flame. Such setups can provide new pathways for scalable material synthesis.

The burner was modified for flame synthesis by introducing a central tube for precursor delivery. In the setup, vaporized precursor mixes with the supplied fuel/air mixture, where the combined effects of the collision of annular-inward jet and strong air entrainment enable rapid mixing of the precursor. The growth of nanoparticles within the turbulent CWJ burner was controlled by adjusting the equivalence ratio and precursor flow rate. The usefulness of the CWJ burner for material synthesis was demonstrated by synthesizing $TiO_2$ and $SiO_2$ nanoparticles.

## 5.2 Experiment

The apparatus consisted of a CWJ burner, precursor delivery system, nanoparticle collection system, and particle image velocimetry (PIV) setup. The CWJ burner (Fig. 5.1a) is composed of a center body of a cylinder (ϕ50 mm) with a hemi-spherical tip, and an outer cylinder (i.d. 61 mm) having an inner curved section (R30.5 mm). Premixed fuel/air was supplied through the slit as an annular-inward jet. The length of the annulus flow passage was 250 mm to allow the flow to be fully developed. The slit width at the exit between the center body and outer cylinder was 0.5 mm, which prevents flashback of the flame. The central hole in the center body for precursor delivery had i.d. 6 mm.

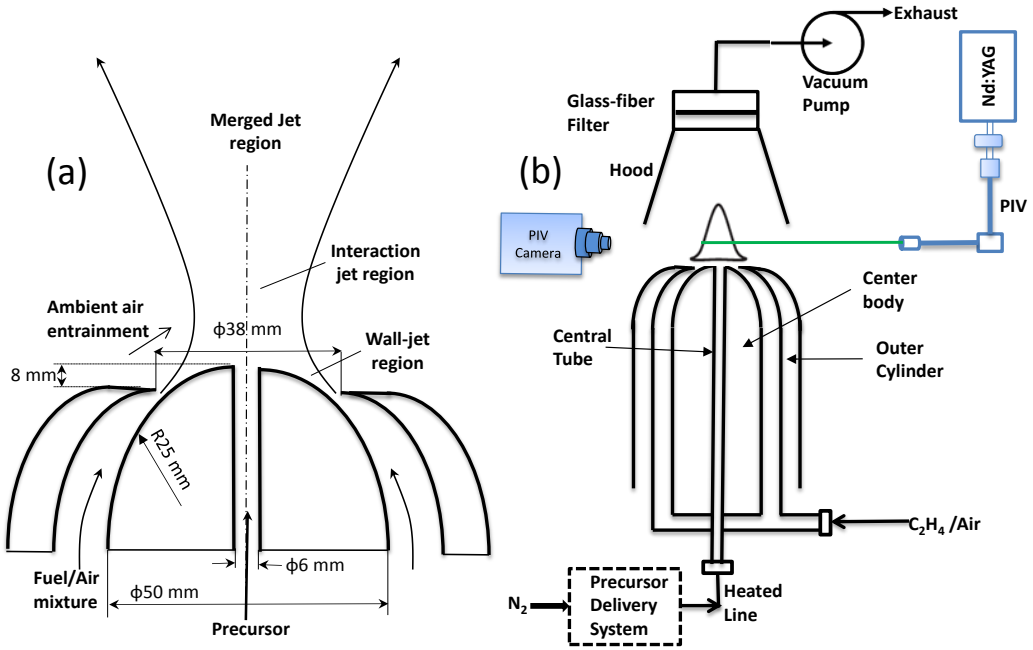


**Figure 5.1:** Schematics of (a) CWJ burner and (b) experimental setup.

Ethylene (99.95%) was used as the fuel and compressed air as the oxidizer, the flow rates being regulated using mass flow controllers (Fig. 5.1b). The equivalence ratio was in the range of 0.80-1.56. The precursors used were titanium tetraisopropoxide (TTIP) and hexamethyldisiloxane (HMDSO) for $TiO_2$ and $SiO_2$ synthesis, respectively. TTIP was heated in a bubbler to 100 $^oC$, the vapor being carried with nitrogen and supplied to the central tube, and the line heated to 180 $^oC$ to prevent condensation. The reason for not using a vaporizer for $TiO_2$ synthesis is that TTIP can react readily with moisture resulting in damage to the vaporizer. For $SiO_2$ growth, HMDSO was injected using a syringe pump into a vaporizer system (Bronkhorst) through a liquid MFC to control the flow rate. The vaporizer was maintained at 120$^oC$ and nitrogen carrier gas (2 SLPM) supplied the mixture to the central tube. The lines connecting the vaporizer and the central tube were heated to 180$^oC$ to prevent condensation. The nanoparticles generated were collected on glass-fiber filters using a vacuum pump. All experiments were conducted at atmospheric pressure.

The PIV setup (La Vision, LDY 300) consisted of a high-repetition (up to 10 kHz) twin-cavity pumped ND:YLF laser (Litron, LDY304-PIV; 527 nm, 28 mJ/pulse, 5 ns pulse duration, 20-

40 μs pulse separation) and a CCD camera (La Vision, Imager Pro HS 4M; 2016×2016 pixels). The output laser was formed into a sheet (1 mm thickness) for the measurement. The premixed fuel/air mixture was seeded with $TiO_2$ particles (0.18 μm nominal diameter). Visible flame height was measured using a cathetometer and the results were compared with the average values obtained from photographs. The temperature was monitored for the case without precursor using S-type thermocouples at 2.5 cm above the nozzle exit for reference. The measured temperatures are the averages of fluctuating temperatures within turbulent flames. These values are much lower than the flame temperatures; hence the uncorrected raw temperatures are presented.

The collected nanoparticles were characterized using X-ray diffraction (XRD) by an advance X-ray powder diffractometer (Bruker, D8) with CuKα (λ=1.5406 Å) radiation. Raman spectroscopy measurements were performed on a Raman spectrometer (Aramis, LabRAM HR Visible) using 473 nm excitation from a diode-pumped solid-state (DPSS) laser (7 mW with 1.1 $cm^{-1}$ spectral resolution). The primary particle size and morphology were examined by transmission electron microscopy (TEM) and high-resolution TEM (HRTEM) (FEI Titan, $G^2$ 80-300). The specific surface area (SSA) was calculated based on multi-point Brunauer–Emmett–Teller (BET) nitrogen adsorption (Micromeritics, ASAP 2050).

## 5.3 Flame Structure and Flow Field

The basic features of CWJ flames will be discussed prior to presenting the materials synthesis behavior of the burner. Photographs of flames stabilized in the burner at several equivalence ratios without supplying precursor are shown in Fig. 5.2. Details of the experimental conditions are listed in Table 5.1. The mixture Reynolds numbers (based on jet velocity, kinematic viscosity, and hydraulic diameter at jet exit of 8.73 mm) were around 10,000 for all cases.

**Table 5.1:** Operating conditions for the synthesis of $TiO_2$ nanoparticles using CWJ burner.

| $\phi$ | Flow Rates [SLPM] | | | Jet Velocity | Re |
|---|---|---|---|---|---|
| | Air | Fuel | Carrier gas | [m/s] | |
| 0.80 | 60 | 3.20 | 2 | 17.6 | 9971 |
| 1.05 | 60 | 4.28 | 2 | 17.9 | 10142 |
| 1.30 | 60 | 5.38 | 2 | 18.2 | 10520 |
| 1.56 | 60 | 6.03 | 1 | 18.4 | 10767 |

The lower part of the flame had a crown shape, similar to that observed previously [6, 209]. This can be attributed to flow separation along the curved wall by the formation of a recirculation zone near the top of the center body, where flames are stabilized. The flame heights H are in the range 73-180 mm (Table 5.2), an increase in flame height being exhibited with increase in equivalence ratio; this is reasonable since more air is required to burn the fuel. The reference temperatures T at the monitoring point (2.5 cm above the nozzle exit) are in the range of 1290 to 1562 K, and similarly increase with equivalence ratio (Table 5.2).

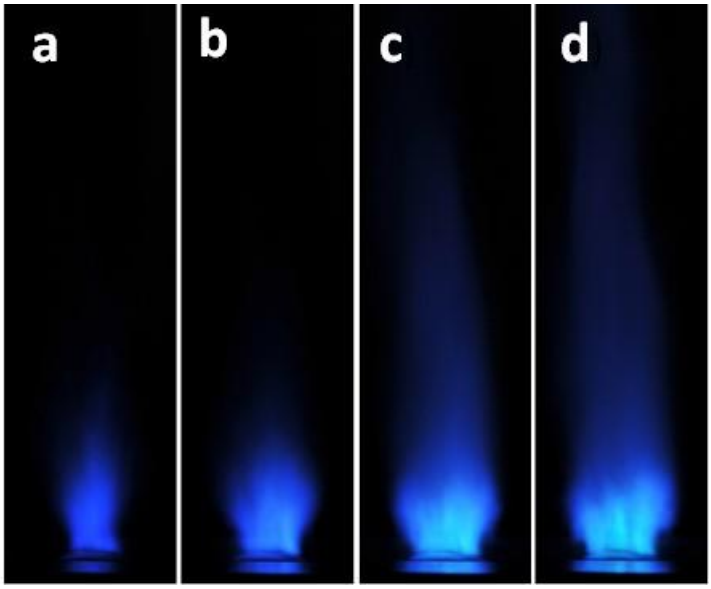


**Figure 5.2:** Photographs of the ethylene-air flame without precursor: (a) $\phi$ = 0.8, (b) 1.05, (c) 1.3, and (d) 1.56.

**Table 5.2:** Summary of results for $TiO_2$ nanoparticles.

| $\phi$ | H [mm] | T [K] | $d_{XRD}$ [nm] | Anatase % |
|---|---|---|---|---|
| 0.80 | 73 | 1290 | 26.2 | 49.0 |
| 1.05 | 140 | 1419 | 29.2 | 45.2 |
| 1.30 | 159 | 1534 | 38.4 | 82.5 |
| 1.56 | 180 | 1562 | 16.5 | 96.0 |

The velocity fields were measured with the PIV setup for the cases with and without supplying precursor. The precursor conditions are listed in Table 5.1 and the Reynolds number of the $N_2$ carrier gas at 2 SLPM (for precursor delivery) was 303, well within the laminar regime. Although not shown, the overall features of the flame were found not to vary much with the precursor. Figure 5.3 shows the spatial variation of the mean velocity field for the flame ($\phi$ = 1.3) without (a) and with (b) TTIP precursor. Although the axial velocity near the axis region increased slightly with the precursor, no appreciable differences were observed. Note that the velocity vectors are pointing inward near the nozzle axis region due to the annular-inward jet of the mixture. However near the nozzle region at large radius, the velocities are pointing outward because of the gas expansion due to the flame.

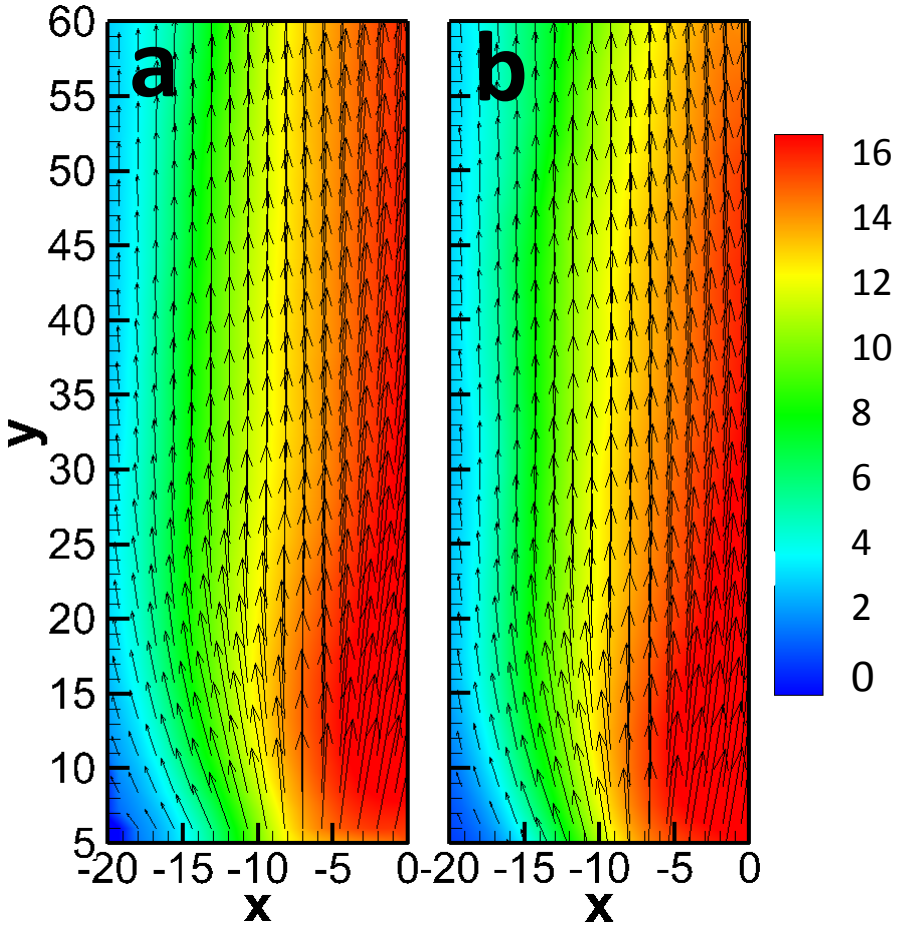


**Figure 5.3:** Time averaged velocity vector plot of the flow field for the ethylene-air mixture ($\phi$ = 1.3); (a) without and (b) with TTIP precursor.

For further understanding the velocity fields, Fig. 5.4 shows the variation of the axial velocity ($v$) along the axis ($y$). The axial velocity increases in the interaction jet region above the burner, reaching a peak near $y$ = 12 mm, and then decreases gradually in the merged jet region. The precursor increases the velocity due to added axial momentum and increased heat release [210]. The residence time of the precursor in the high temperature region ranges from 5.2-12.6 ms (based on the visible flame length).

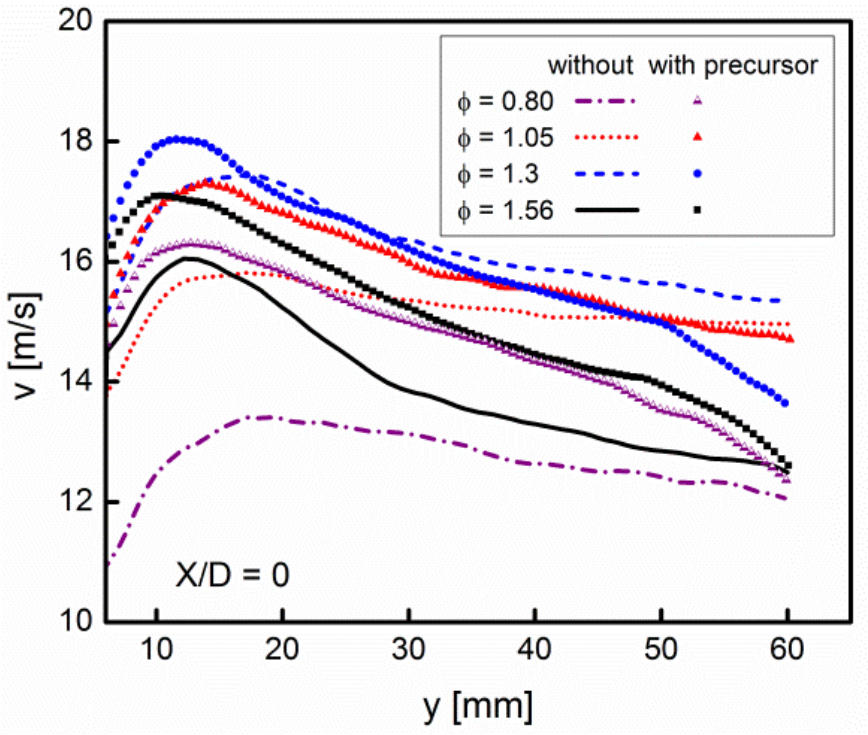


**Figure 5.4** Axial velocity distribution along the burner axis, with and without precursor.

## 5.4 Titanium Dioxide Synthesis

Titania nanoparticles are manufactured by adding TTIP with an estimated loading rate of 50 g/hr based on the vapor pressure [211] and a carrier gas flow rate of 2 SLPM. The flame temperature is expected to increase by 100-200$^{o}$C with the addition of the precursor [210]. The growth mechanism of the $TiO_2$ nanoparticles is vapor-solid mechanism, as vaporized precursors were introduced into the flame [71, 72]. $TiO_2$ particles were collected and analyzed with XRD at several equivalence ratios, as shown in Fig. 5.5, from which the crystal phase, average crystallite size, and rutile/anatase phase ratio could be determined. At $\phi$ = 0.80 and 1.05, both the peaks representing the anatase (A) and rutile (R) phases can be seen, an indication of the mixture of these two phases. As $\phi$ increases to 1.30, the rutile peaks decrease sharply. The anatase to rutile ratio in the samples was calculated by integrating the respective XRD peak intensities (anatase (101) peak at $2\theta = 25.4^{o}$ and rutile (110) peak at $2\theta = 27.5^{o}$) using the following equation [147]

$$\chi = \left(1 + \frac{I_A}{I_R}\right)^{-1} \qquad (5.1)$$

where $\chi$ is the weight fraction of rutile in the $TiO_2$ sample, and $I_A$ and $I_R$ are the integrated areas under the anatase and rutile peaks, respectively. The values of anatase percentage in the mixture are listed in Table 5.2. No significant change in the anatase content was observed when increasing the equivalence ratio from lean to near stoichiometric conditions. However, when the equivalence ratio was increased further to fuel rich conditions, the anatase content increased appreciably.

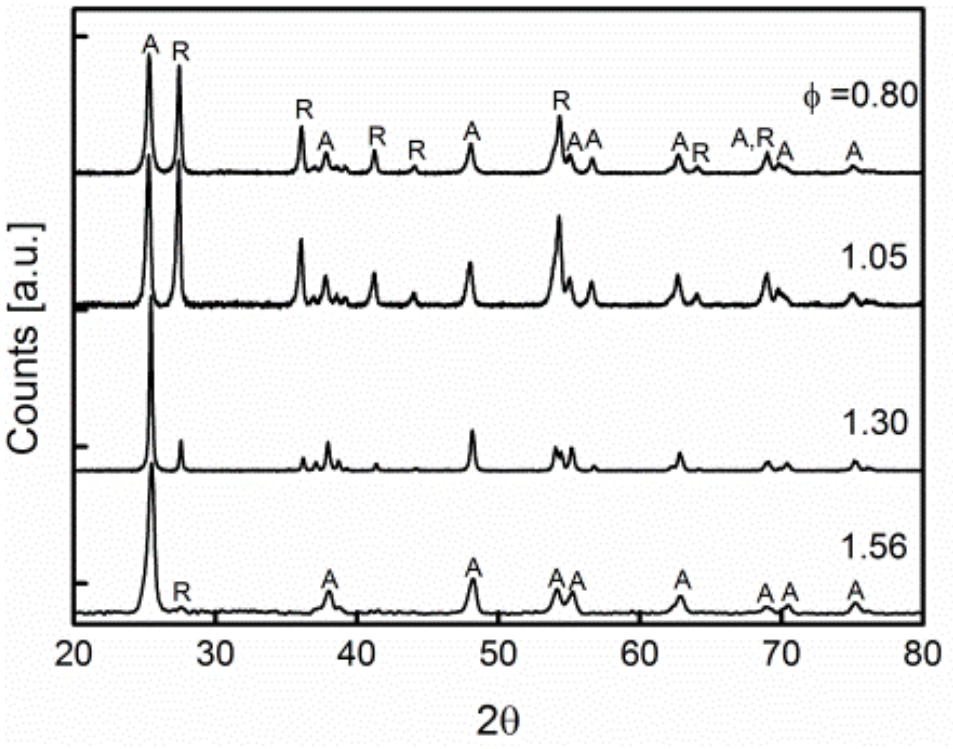


**Figure 5.5:** XRD patterns for $TiO_2$ nanoparticles at several equivalence ratios (A, anatase; R, rutile peaks).

An increase in the anatase content of $TiO_2$ particles can occur for several reasons. Typical parameters that control the growth of anatase include precursor loading rate, oxygen content, residence time, and heat flux [87, 212, 213]. Our results agree with those of Wegner and Pratsinis [213], who observed a higher anatase content when the residence time in high temperature region became longer and when the TTIP flow rate was smaller. In this work, a

higher equivalence ratio resulted in higher heat release, leading to increased flame temperature. The longer flame also provided an increased residence time. These conditions allow enhanced growth of anatase $TiO_2$ nanoparticles, which is also the thermodynamically more stable phase at elevated temperatures [212]. At $\phi = 1.56$ with a reduced carrier gas flow rate of 1 SLPM, the titania particles are in almost pure anatase phase (96 % anatase) with very low rutile content. This high content of anatase can be attributed to the increased residence time in the high temperature region and also to the lower TTIP loading rate.

To further examine the phases of $TiO_2$ nanoparticles, Raman spectroscopy measurements were performed. It is known from the literature [144] that rutile $TiO_2$ has 11 optical modes, amongst which only four are Raman active (irreducible representation of $A_{1g}$ (612 $cm^{-1}$), $B_{1g}$ (143 $cm^{-1}$), $B_{2g}$ (826 $cm^{-1}$), and $E_g$ (447 $cm^{-1}$)), whereas anatase $TiO_2$ has 15 optical modes and 6 of these are Raman active (irreducible representation of $A_{1g}$ (515 $cm^{-1}$), $2B_{1g}$ (399 and 519 $cm^{-1}$), and $3E_g$ (144, 197 and 639 $cm^{-1}$)). Figure 5.6 shows the visible region of the Raman spectra at two different equivalence ratios (1.05 and 1.56). The peaks for $\phi = 1.05$ correspond to the Raman modes of both anatase and rutile phases, whereas for the $\phi = 1.56$ case all peaks correspond to the anatase phase. This result is consistent with XRD measurements shown previously, where the predominant phase at higher equivalence ratios is the anatase phase.

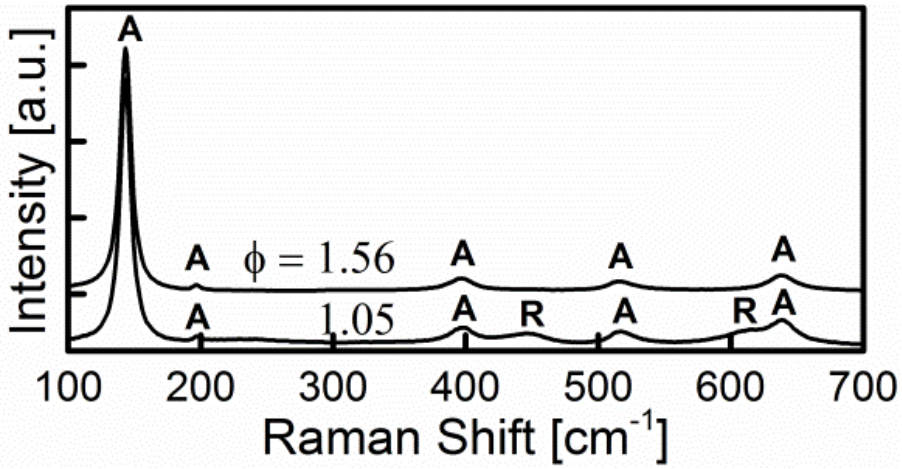


**Figure 5.6:** Raman spectra for $TiO_2$ nanoparticles (A, anatase; R, rutile peaks).

The crystallite size of the $TiO_2$ particles ($d_{XRD}$) was determined from XRD using Scherrer's formula (Eq. 3.2) [214]. The crystallite size increases with equivalence ratio as $d_{XRD}$ = 26.18, 29.21, and 38.2 nm for $\phi$ = 0.8, 1.05, 1.3, respectively (Table 5.1). At $\phi$ = 1.56, $d_{XRD}$ decreased appreciably to 16.5 nm with the carrier gas flow rate of 1 SLPM. Note that the flame with 2 SLMP carrier gas was unstable for $\phi$ = 1.56. This smaller size can partly be attributed to the reduction in collision frequency among $TiO_2$ particles [212].

The qualitative nature of the data is in agreement with the surface area equivalent diameter ($d_{BET}$) determined from the specific surface area (SSA) using the BET surface area analyzer, these being $d_{BET}$ = 32.5, 53.4, and 57.8 nm for $\phi$=0.80, 1.05 and 1.3, respectively. The increase in diameter with equivalence ratio can also be attributed to the higher flame temperature [215] and longer residence time [213]. The difference between $d_{BET}$ and $d_{XRD}$ can be attributed to particle aggregation [148].

The TEM images of $TiO_2$ nanoparticles at $\phi$ = 1.05 and 1.3 are shown in Fig. 5.7 and 5.8, respectively. The particles are mostly spherical with some polyhedral shapes. The images also suggest that the $TiO_2$ particles have bimodal size distribution, with an average size of about 10 nm in the lower range and 80 nm in the higher range. This bimodal nature can partially be attributed to non-uniform residence time in the high temperature zone along the radial plane above the burner [208].

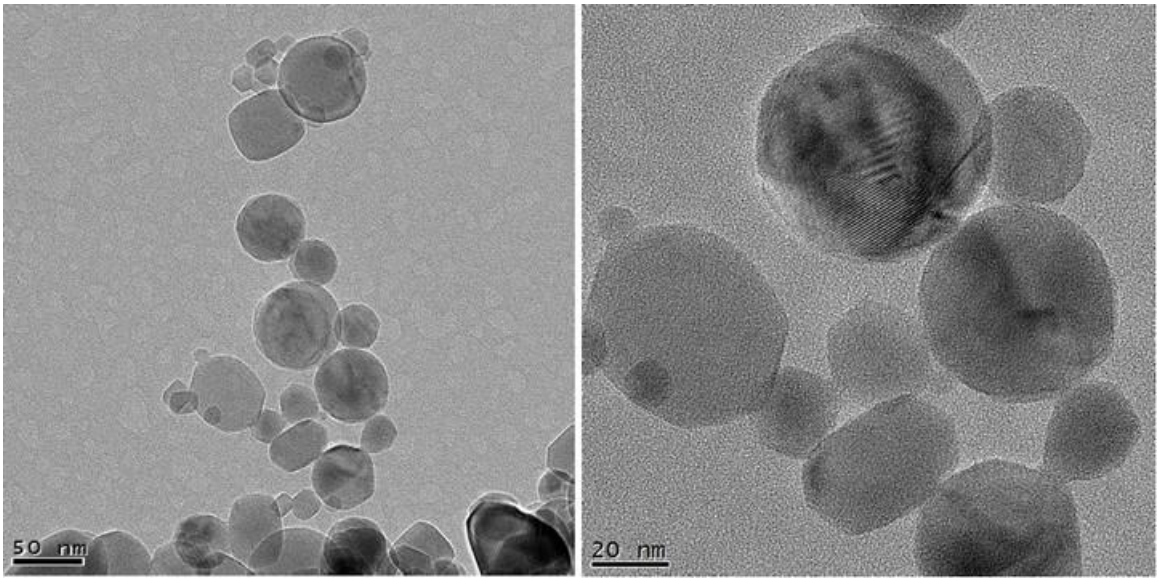


**Figure 5.7:** TEM images of $TiO_2$ nanoparticles $\phi$=1.05.

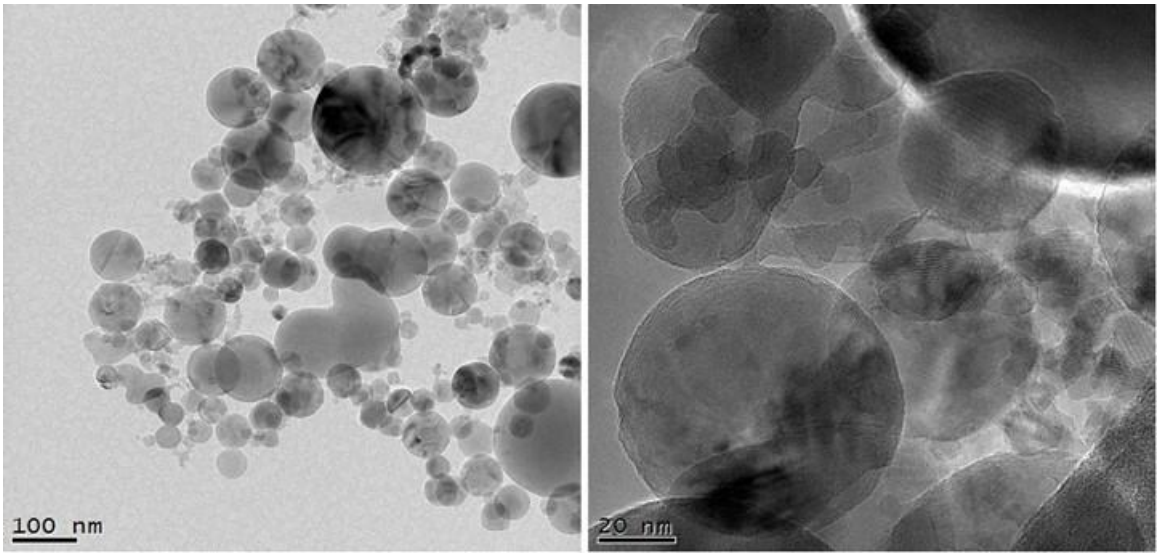


**Figure 5.8:** TEM images of $TiO_2$ nanoparticles: (a) $\phi$=1.3.

The diffraction patterns (Fig. 5.9) show a ring-type pattern. We picked around 5-10 particles for the TEM diffraction patterns. Since each nanoparticle has its own crystal orientation, the overall TEM pattern looks like a polycrystalline pattern. In Fig. 5.9a, the innermost ring-type pattern has a double layer pattern with diffraction spots very close to each other, an indication of the mixture of the anatase and rutile phases, whereas the diffraction pattern in Fig. 5.9b inset shows a single-ring type pattern corresponding to the anatase phase. These results are in

agreement with the XRD data. The HRTEM image of the $TiO_2$ particles ($\phi$=1.3) shown in Fig. 5.10 reveals the high crystallinity and the ordered structure of the nanoparticle lattice planes.

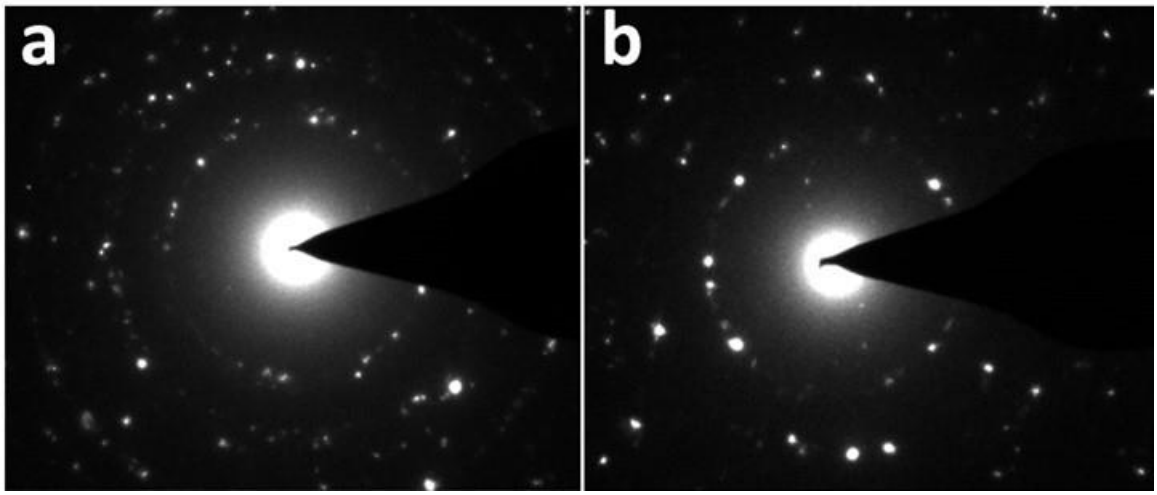


**Figure 5.9:** Electron diffraction pattern for $TiO_2$ nanoparticles: (a) $\phi$=1.05 and (b) $\phi$=1.3.

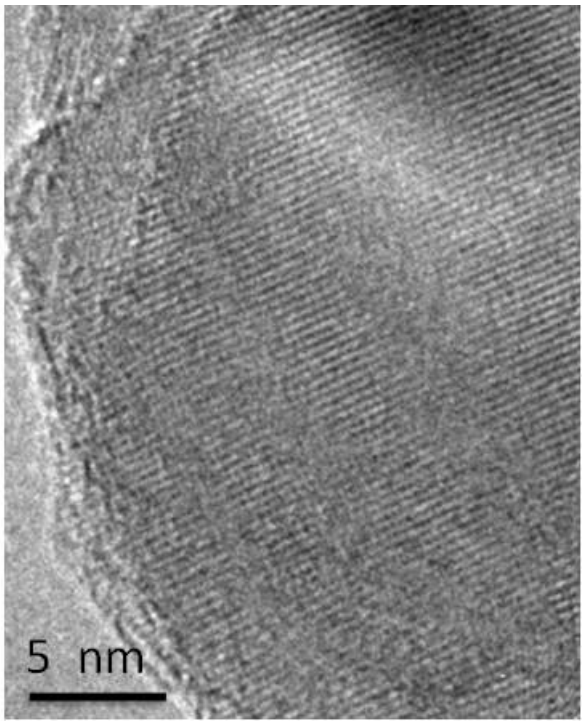


**Figure 5.10:** HRTEM image of a $TiO_2$ nanoparticle at $\phi$=1.3 showing the lattice planes.

Figure 5.11 shows TEM images of the $TiO_2$ nanoparticles at $\phi$=1.56. Note that the $TiO_2$ nanoparticles at this equivalence ratio are mostly in the anatase phase (96 wt%). The nanoparticles are of mixed morphology (spherical and polyhedral) and exhibit a bimodal

distribution with a generally smaller particle size compared with the cases shown in Fig. 5.7 and 5.8. The polyhedral morphology is not brookite but due to anatase and rutile phases only as confirmed by XRD and Raman experiments [216, 217]. The lower size range is 5-10 nm, whereas the higher size range is 40-60 nm. The HRTEM micrograph (inset) again exhibits high crystallinity. The degree of agglomeration of these nanoparticles is comparable to commercially available $TiO_2$ nanoparticles (e.g. Evonik P25 ~70% anatase) [218].

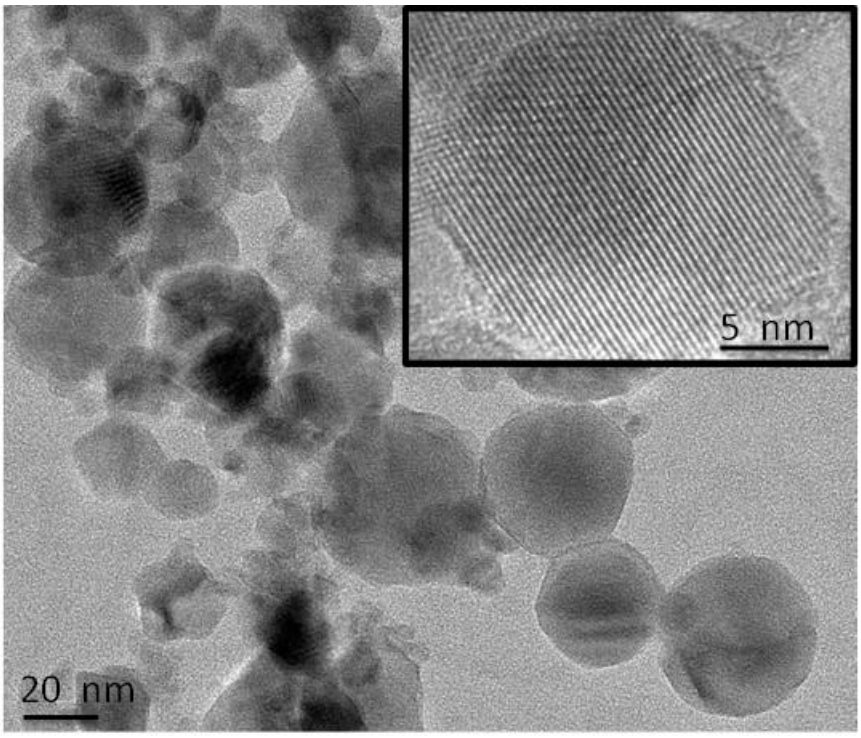


**Figure 5.11:** TEM images of $TiO_2$ nanoparticles at $\phi$=1.56 (inset showing an HRTEM image of a $TiO_2$ nanoparticle).

## 5.5 Silicon Dioxide Synthesis

The HMDSO precursor was used for $SiO_2$ nanoparticles, whereby the loading rate can be controlled using the vaporizer system with a liquid mass flow controller. The equivalence ratio was fixed at $\phi$=1.3 and the flow rates (for $C_2H_4$ and Air) as listed in Table 5.1 were used. The effect of precursor loading was investigated in the range of 5-40 ml/hr. The flame shape was found to remain nearly the same with the precursor. For high flow rates (over 30 ml/hr), a slight

yellowish color was seen within the blue premixed flame (Fig. 5.12) due to the luminousity of the generated particles. The silica samples collected were bright white in color.

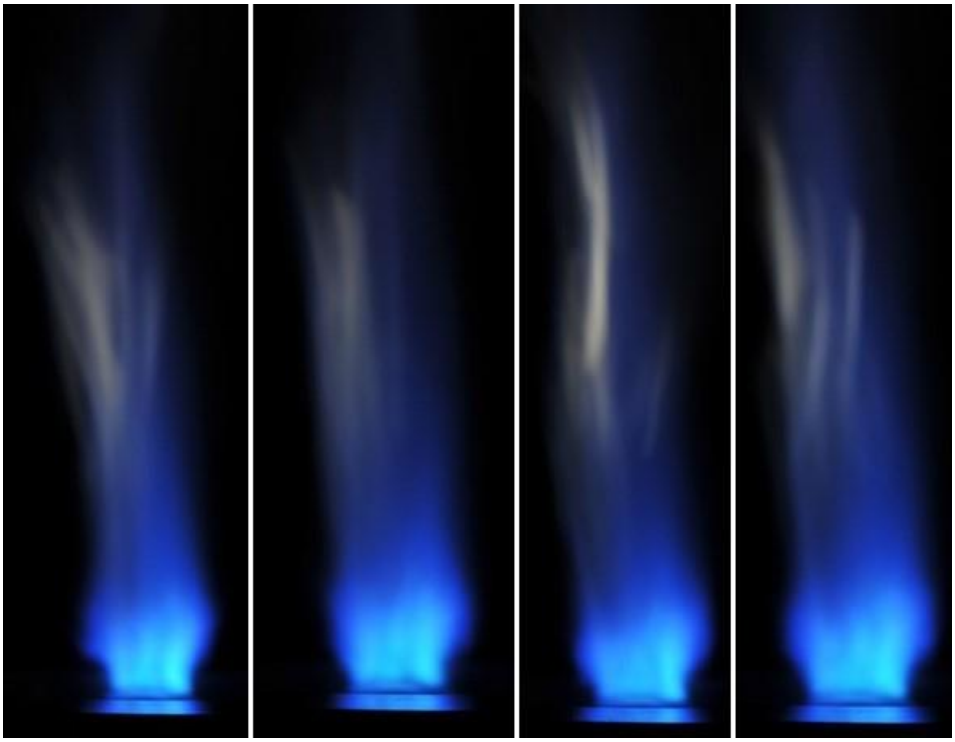

**Figure 5.12:** Different snap shots of CWJ flame using silica precursor at $\phi$=1.3 and precursor loading rate = 40 ml/hr.

The specific surface area (SSA) of the nanoparticles was measured using BET analysis and the results are shown in Fig. 5.13 as a function of precursor loading rate. At a loading rate of 40 ml/hr, SSA is 151 $m^2/g$. This value increases with a decreased loading rate of 10 ml/hr, and increases sharply when the loading rate is decreased to 5 ml/hr, reaching 240 $m^2/g$. The large surface area obtained at low precursor loading can be attributed to a small particle size with large pore volumes (based on single point adsorption, total pore volume is 0.622 $cm^3/g$ at 5 ml/hr precursor flow rate) [219, 220]. As particle size further increases, it can clog the structural pores and consequently reduce the surface area available for $N_2$ adsorption [221]. According to the surface area obtained from BET analysis and assuming spherical particles, the average primary particle size calculated is $d_{BET} = 6/(\rho \times SSA)$, where $\rho$ is the density of $SiO_2$ particles (2.196 $g/cm^3$ [222]). The average primary particle diameters, $d_{BET}$, at different precursor

loading are plotted in Fig. 5.13. The primary particle diameter increases with precursor loading rate with a minimum diameter of 11 nm and maximum diameter of 18 nm, at the precursor flow rates of 5 and 40 ml/hr, respectively. This result implies that $SiO_2$ particle size can be controlled with the CWJ burner by varying the precursor loading rate.

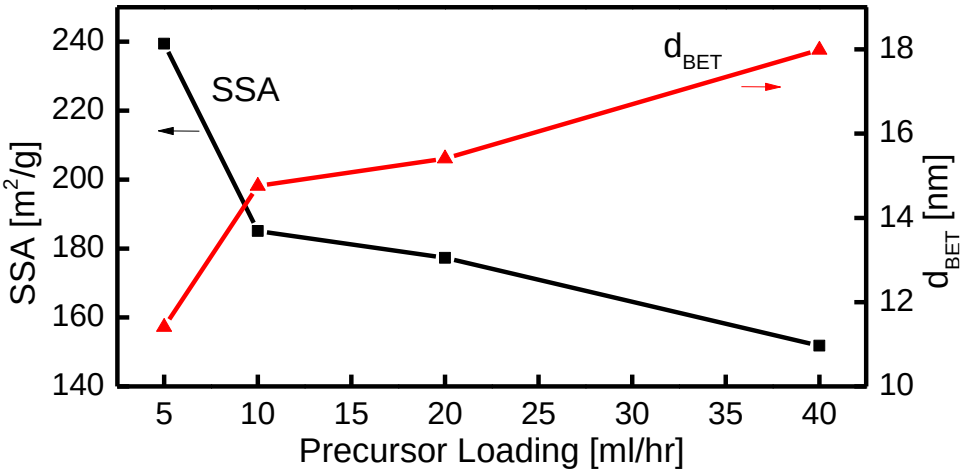


**Figure 5.13:** Effect of precursor loading on SSA and average particle diameter for $SiO_2$ nanoparticles.

Figures 5.14 and 5.15 show the TEM images of $SiO_2$ nanoparticles at two different precursor flow rates (30 and 5 ml/hr, respecti. Again, the particles are in bimodal size distribution with some aggregates. The primary particle size decreases with decreased precursor loading, in agreement with the BET measurements. The HRTEM images (insets) reveal the amorphous structure of the $SiO_2$ nanoparticles, which is common in silica nanoparticles obtained from flame synthesis [47, 51, 222].

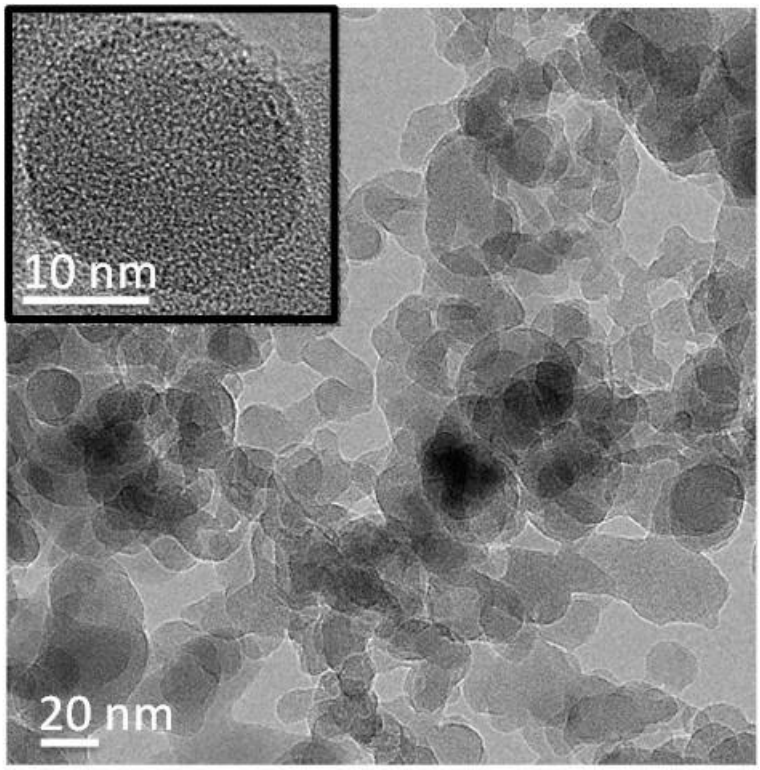


**Figure 5.14:** TEM image of $SiO_2$ nanoparticles at precursor loading rate of 30 ml/hr (inset is HRTEM image at the same loading rate illustrating amorphous structure).

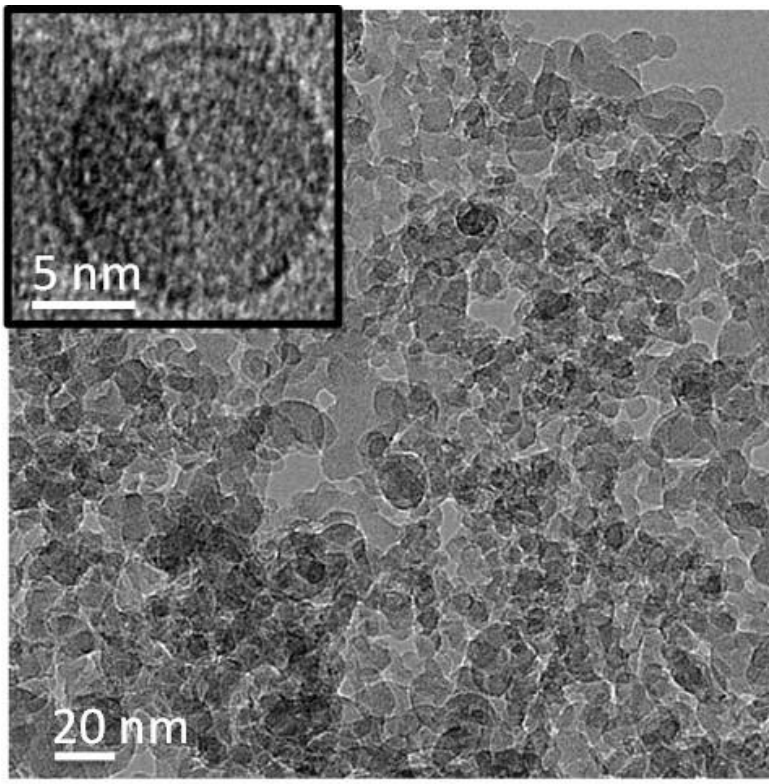


**Figure 5.15:** TEM image of $SiO_2$ nanoparticles at precursor loading rate of 5 ml/hr (inset is HRTEM image at the same loading rate illustrating amorphous structure).

## 5.6 Concluding Remarks

The usefulness of the CWJ burner for materials synthesis of nanoparticles has been demonstrated. The growth of both $TiO_2$ and $SiO_2$ nanoparticles has been reported, the key points being the following:

1) The CWJ burner can operate at a wide range of equivalence ratios and was found to exhibit small size turbulent flame characteristics. PIV data confirmed this behavior and the precursor flow had little impact on the flame behavior.
2) The crystal phase of the $TiO_2$ nanoparticles was strongly dependent on the equivalence ratio. At higher values, due to a longer residence time in high temperature region, the growth of anatase nanoparticle was dominant. At $\phi = 1.56$, the growth of almost pure anatase (96%) was demonstrated. The size of the particles depended on the equivalence ratio, due to an increase in the flame temperature. As the flame temperature increased, the growth of larger nanoparticles was observed.
3) Based on TEM imaging, both $TiO_2$ and $SiO_2$ nanoparticles exhibit a bimodal size distribution, which can be attributed to radial variation in the velocity field that results in an uneven residence time in the high temperature region.

By changing the precursor flow rate, the surface area and particle size of the $SiO_2$ nanoparticles could be controlled. The diameter of the $SiO_2$ nanoparticles based on BET varied from 11 nm (240 $m^2/g$) to 18 nm (151 $m^2/g$).

# Chapter 6

# Synthesis of Titania Nanoparticles Using Curved Wall-Jet Burner with Poppet Valve

A curved wall-jet (CWJ) burner was modified and designed for flame synthesis. A central port with poppet valve type of opening was used to deliver the precursor tangentially to the cavity region of the recirculating flow in the recirculation zone. This modified CWJ burner demonstrated appreciable mixing characteristics between the precursor and combustion gases within these regions, with a slight decrease in the axial velocity due to the precursor injection.

## 6.1 Introduction

Titanium oxide ($TiO_2$) particles have drawn worldwide interest in oxide semiconductors for future applications related to photocatalytic water splitting [116, 117], die-synthesized solar cells [115], and other photocatalytic applications [134]. Rutile phase of $TiO_2$ is mainly used for pigments while the anatase phase plays an important role in the photocatalytic applications.

In laboratory scale studies, small laminar flames have been typically used to investigate the growth process of $TiO_2$ nanoparticles [53, 54, 141], whereas industrial processes of flame synthesis use large scale turbulent burners [48]. Such growth process is strongly influenced by flow and flame conditions and appreciably differs when comparing laminar with turbulent flames. Systematic lab-scale experiments involving turbulent flames are required to enhance our understanding of nanoparticle formation, which will help to control crystallinity, size, and morphology of nanoparticles produced in flames.

Many parameters are controlling the growth of nanoparticles such as burner geometry, fuel/oxidizer flow rates, precursor loading rate, residence time, and fuel type [54]. Common fuels investigated include carbon monoxide [83], hydrogen [84], methane [3], propane [85] and ethylene (chapter 5).

For the scale-up of flame synthesis in a laboratory, we have previously adopted a curved wall-jet (CWJ) burner for nanoparticle synthesis by injecting precursors through a center tube and by supplying fuel/air mixtures as an annular-inward jet for rapid mixing of the precursors in the reaction zone (chapter 5). Nanoparticles were produced in ethylene ($C_2H_4$)/air premixed flames using titanium tetraisopropoxide (TTIP) and hexamethyldisiloxane (HMDSO) as the precursors for $TiO_2$ and $SiO_2$ nanoparticles, respectively. Particle image velocimetry measurements confirmed that the precursors can be injected into the flames without appreciably affecting flow structure. Temperature, residence time and equivalence ratio were found to be the major control parameters for the growth of the nanoparticles and their phase. Particles produced using the CWJ burner exhibited a bimodal size distribution due to non-uniform residence time in the high temperature zone along the radial plane above the burner [208]. This is because the flow through the central port obstructs the formation of recirculating flow inside the cavity.

In this chapter, we modified the burner to have a flow guide having a poppet valve type on top of the central port for the precursor delivery such that the precursor flow is aiding the recirculating flow in the cavity region. Thus, the main flow of premixture of fuel and air from the curved wall slit and the precursor flow from the central port are aiding each other in forming a recirculation zone to support the flame. Consequently, the precursor can be well-mixed with the recirculating burnt gases and is distributed reasonably uniformly in the main flame region. The influences of various operating parameters (equivalence ratio and Reynolds numbers) as well as the precursor's Reynold number were investigated using ethylene fuel.

## 6.2 Experiment

The apparatus consisted of a curved wall-jet burner, a precursor delivery system, a nanoparticle collection system, and high-speed PIV and OH PLIF setups. The burner, as schematically shown in Fig. 6.1, is composed of a center body of a cylinder (ϕ50 mm) with a hemi-spherical tip, and an outer cylinder with curved- converging section having an exit diameter of ϕ43 mm. The slit width between the center body and the outer cylinder is 0.8 mm and is long enough to prevent any flashback. This slit is used for the reactants (fuel/air) supply. A concave spherical cavity with R56 mm was created on top of the hemi-sphere (3.37 mm in depth and 24 mm in width at the tip) for better flame stabilization [6, 7] by promoting a recirculation zone. The height of the outer cylinder is adjustable. The converging section between the two cylinders guided fuel and air tangentially to the curved wall of the center body toward the axis to form an annular-inward jet. A central port of 10 mm in diameter was machined in the center body. A poppet valve type flow guide was placed on top of the central port having 2 mm gap for the precursor delivery to direct the precursor tangentially into the recirculation zone for better mixing. The burner surface was anodized to minimize light reflection.

Ethylene (99.995%) and air premixtures were supplied through the curved wall slit of the burner. Titanium tetraisopropoxide (TTIP) was used as the nanoparticle precursor, which was heated in a bubbler to 110 $^{o}$C and the vapor was carried with nitrogen at a fixed loading of 2 SLPM and supplied through the central port of the burner. The precursor delivery line after the bubbler was heated to 180 $^{o}$C to prevent condensation. Experiments were conducted by varying flow rates as well as equivalence ratio. Flames with various equivalence ratios are denoted as F1 to F4, whereas F5 to F7 refer to flames with various Reynolds numbers (see Table 6.1 for operating conditions). All the flames listed in Table 6.1 have the Re for the precursor $Re|_{Pre}$= 108 based on the carrier gas flow rate and the exit area between the poppet valve and the central

port. The generated nanoparticles were collected on glass-fiber filters using a vacuum pump. All experiments were conducted at atmospheric pressure.

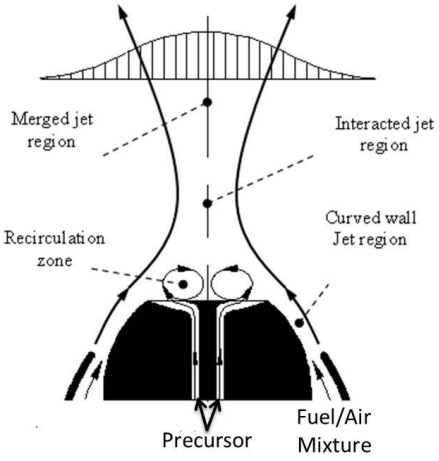


**Figure 6.1:** Schematic diagram of curved-wall jet burner with central port exhibiting the flow field.

Visible flame height was measured using a cathetometer and the results were compared with the average values obtained from photographs. The PIV system consisted of a high-repetition rate twin-cavity diode-pumped Nd:YLF laser (Litron, LDY304-PIV; 527 nm, 28 mJ/pulse, 5 ns pulse duration) and a CMOS camera (LaVision, Imager Pro HS 4M; 2016×2016 pixels) coupled with a controller. Double-pulses with a time separation of 20-40 μs were repeated at 1 kHz. The laser output formed a sheet approximately 1 mm in thickness and 100 mm in height by a series of lenses. Seed particles were titanium dioxide ($TiO_2$, nominal diameter 0.18 μm) and the seed levels were adjusted for spurious vectors in the image processing to be less than 5%. A perspective distortion from the camera system was calibrated by imaging a 3-D dot target (LaVision type 11). Velocity fields were determined through multi-pass vector computation software (Davis 8.1) with an interrogation size of 32×32 pixels and 50% overlap, yielding a 0.76×0.76 $mm^2$ spatial resolution.

The high-speed planar laser-induced fluorescence (PLIF) system consisted of a diode-pumped Nd:YAG laser (Edgewave, IS16II-E; 532 nm) and a dye laser (Sirah, Credo-Dye) whose output was frequency-doubled to 283.57 nm to excite $Q_1(8)$ line of A-X (1,0) OH transition with about

0.3 mJ/pulse at 10 kHz repetition rate. OH signals were detected at 295-345 nm with an intensified CMOS camera (Lavision, HSS8 and IRO; 1024×1024 pixels). Elastic scattering noise from the laser sheet and background noise were reduced by using a band-pass filter (>80% at 320 nm) and also by minimizing the intensifier gate time (200 ns). The spatial resolution was 0.11 mm/pixel.

**Table 6.1:** Operating conditions and summary of results for various flames.

| Flame | Re | $\phi$ | $H$ [mm] | $\tau$ [ms] | Anatase % |
|---|---|---|---|---|---|
| F1 | 13,142 | 1.2 | 138.1 | 8.85 | 69.9 |
| F2 | | 1.3 | 157.8 | 9.85 | 74.4 |
| F3 | | 1.6 | 214.8 | 12.40 | 86.2 |
| F4 | | 1.8 | 235.1 | 12.99 | 94.2 |
| F5 | 8,300 | 1.3 | 148.3 | 13.25 | 80.2 |
| F6 | 9,130 | | 154.6 | 11.2 | 81.5 |
| F7 | 18,676 | | 160.3 | 7.17 | 72.3 |

The collected nanoparticles were characterized using X-ray diffraction (XRD) by an advance X-ray powder diffractometer (Bruker, D8) with CuK$\alpha$ ($\lambda$=1.5406 Å) radiation. Raman spectroscopy measurements were performed on a Raman spectrometer (Aramis, LabRAM HR Visible) using 473 nm excitation from a diode-pumped solid-state (DPSS) laser (7 mW with 1.1 $cm^{-1}$ spectral resolution). The primary particle size and morphology were examined by transmission electron microscopy (TEM) and high-resolution TEM (HRTEM) (FEI Titan, G2 80-300). The particle size distribution was measured using Zeta Sizer (Malvern Instruments Ltd.) using ethanol as the dispersant for the nanoparticles.

## 6.3 Results and Discussion

### 6.3.1 Flame and flow characteristics

Basic flame features are discussed first to characterize the burner, including flame shape and reactive flow field characteristics.

Photographs of flames stabilized in the burner are shown in Fig. 6.2 at several operating conditions listed in Table 6.1 without (upper row) and with (lower row) precursor supply for the mixture Reynolds number (Re) based on jet velocity, mixture kinematic viscosity, and hydraulic diameter at jet exit of 60 mm was 13,142. The equivalence ratio $\phi$ was varied from 1.2 to 1.8 using ethylene fuel. The precursor Reynolds number was also changed from 108 to 178.

These flames have blue color with crown shape which stabilizes the flame by the formation of a recirculation zone. Previous studies [6, 7, 86] showed that the flame height measured from the tip of the concave cavity increases with equivalence ratio. The present flames are in accordance with this behavior. Although not shown, the effect of Reynolds number was also tested ranging from 8,300 to 18,676, which has a small effect on the flame height (H changed by < 6% with respect to Re).

When TTIP is added to these flames, they become more luminous, attributed to nanoparticles formation and surface radiation in these flames. The flame heights, H, (for flames without precursor addition) are in the range of about 138-236 mm (Table 6.1), an increase in flame height being exhibited with increase in equivalence ratio; this is reasonable since more air is required to burn the fuel. Also, a slight increase in the flame height is realized due to the increase of Re because of the increased heat flux entering the reaction region in the flame.

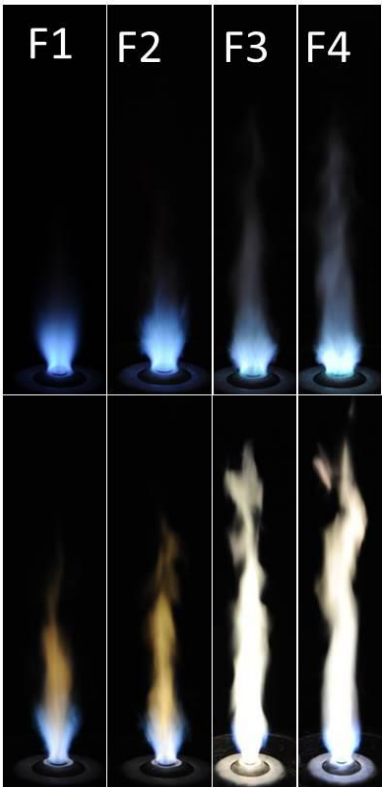


**Figure 6.2:** Direct flame images showing the effect of equivalence ratio at Re= 13,142 flames, top row without precursor and bottom row with precursor.

The PIV system was used to characterize the turbulent flow field. Figure 6.3 shows the time-averaged mean velocity vector fields for the rich ($\phi$=1.8) ethylene flame and Re = 19,871 with (a) and without (b) TTIP precursor, with the background color indicating velocity magnitude. Also shown are the typical streamlines in white color. The general features of the flow field exhibit typical flow characteristics of the CWJ burner [6, 7]. The flow field consists of a recirculation zone (RZ), an interaction jet (IJ) region with the collision of the annular-inward jets near $y$ = 6 mm, and a downstream merged jet (MJ) region. The velocity of the annular slit jet decreases toward the wall and ambient side, thus inner and outer shear layers (ISL and OSL) are surrounding the annular-inward jets (AJ) . The velocity gradients in these shear layers could generate turbulence, augmented by the collision of annular-inward jets. TTIP precursor has decreased the magnitude of the maximum velocity vector when it is supplied to the burner through the inner slit by small percentage (< 8%). This can be attributed to its entrainment in

the recirculation zone opposing the main flow and reducing its velocity. Because the precursor's Re is very low compared to the flow Re, this effect is small.

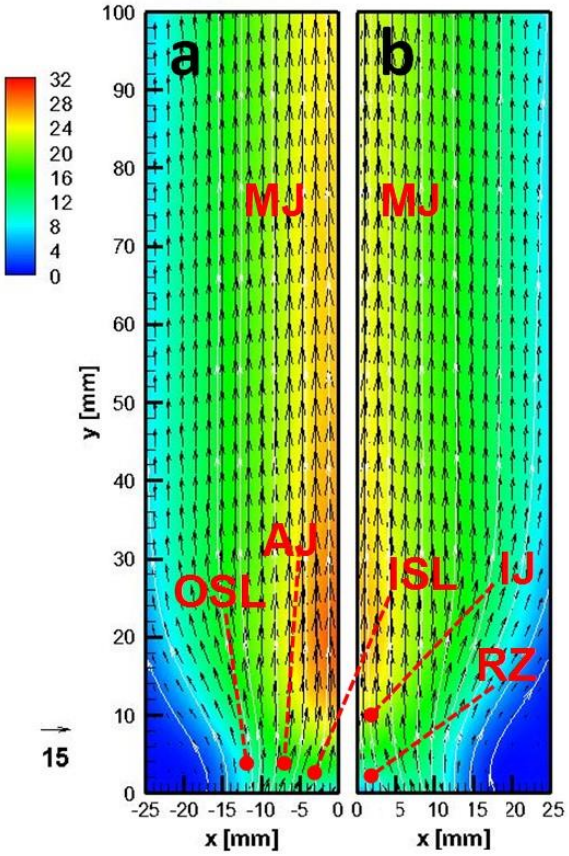


**Figure 6.3:** Time averaged velocity vector plot of flow field for a flame with ϕ=1.8 and Re= 19,871; (a) without and (b) with TTIP precursor (white lines indicate streamlines).

The axial profiles of the mean flow velocities, *v*, (at the burner's centerline) are plotted in Fig. 6.4. In the interaction jet region, *v* increases rapidly and then slightly decreases (F2 and F7) or maintains near uniform values (F5 and F6) up to *y* = 100 mm in the merged jet region. TTIP precursor has only small influence on the velocity values for F5 and F7 flames.

Such velocity quantification and visible flame height enabled in estimating the total residence time of the precursor within the hot gases. These are 8.85 and 13.25 ms corresponding to flames F1 and F5, respectively, as reported in Table 6.1. The increase in residence time with increasing $\phi$ using ethylene fuel is expected to increase the anatase content as concluded in our previous work [86].

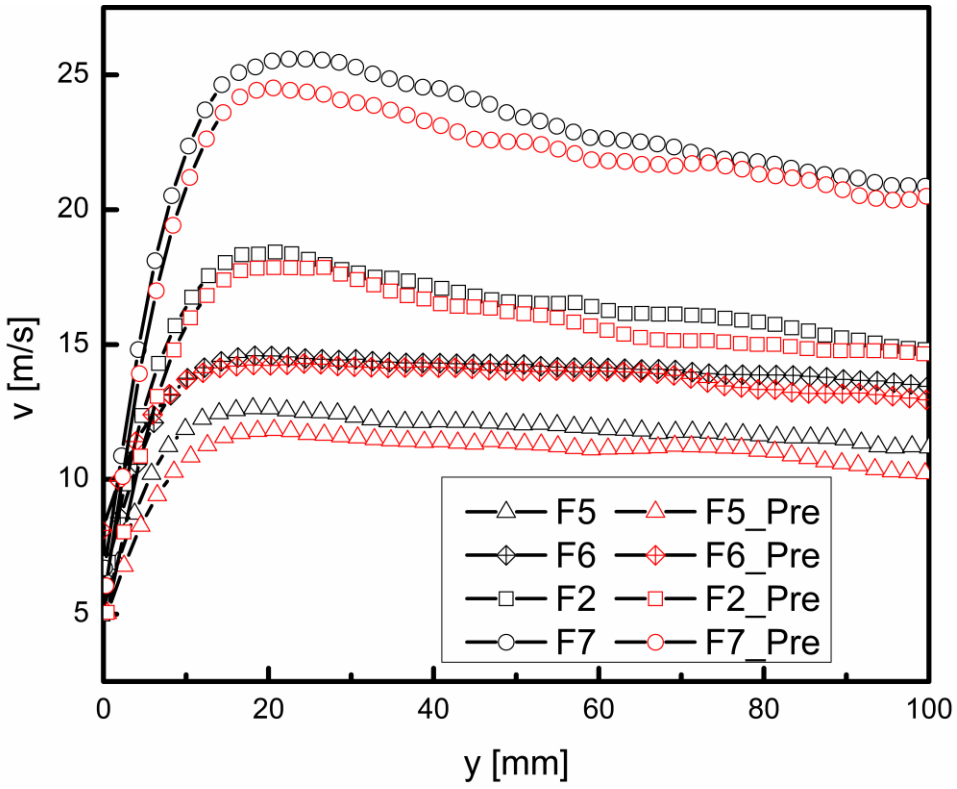


**Figure 6.4:** Axial profiles of flow velocity along the burner centerline (Pre denotes with TTIP precursor).

The time resolved, 10 kHz, OH-PLIF system was employed to provide insights on various dynamics of turbulent premixed flames and to investigate the flames structure. Figure 6.5 shows typical images of OH-PLIF (F5 and F7). The instantaneous images of OH reveal the existence of a recirculation zone upstream at the concave cavity followed by, for high Re flames (F7), thin necking zone at the interaction jet region and then the highest OH signal zone further downstream. TTIP precursor has a slight effect on the flame structure particularly F5 as there is a region without OH signal.

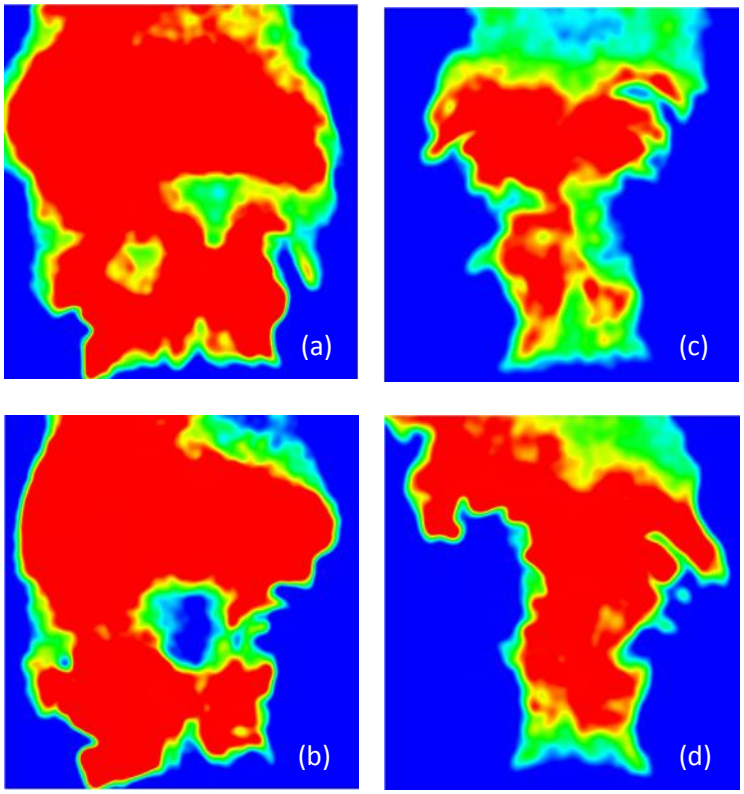


**Figure 6.5:** OH-PLIF images for flames F5 (a,b) and F7 (c,d) without (upper) and with (lower) TTIP precursor, showing their flame structure.

These images provide the following features: (1) the recirculation zone is somewhat clear and confined within the burner tip for flame F5; however, it moves slightly downstream in F7; (2) the production of OH radical in the recirculation zone is appreciably influenced in flames with precursor (Fig. 6.5b and d); (3) the wrinkled reaction sheets distribute predominantly along the shear layers in high Re flames (F7), however, in low Re flames (F5), less-wrinkled reactions zones appear further downstream associated with the abundance of OH species; (4) These images imply that flames are attached to the burner tip as they have high flame speed.

### 6.3.2 Nanoparticle characterization

TTIP (with loading rate of 50 g/hr based on vapor pressure [211]) and nitrogen carrier gas flow rate of 2 SLPM were used to synthesize titanium dioxide ($TiO_2$) nanoparticles. $TiO_2$ nanoparticles were collected and analyzed with the XRD at several operating conditions from

which the crystal phase, average crystallite size, and rutile/anatase phase ratio could be determined.

Fig. 6.6 shows the XRD pattern for different equivalence ratios at Re=13,142. For all cases, both the peaks representing the anatase (A) and rutile (R) phases can be seen, an indication of the mixture of these two phases. The anatase to rutile ratio in the samples was calculated by integrating the respective XRD peak intensities (anatase and rutile peaks at $2\theta = 25.4$ and $27.5^{o}$, respectively). It is clear from the relative anatase and rutile peak intensities that the percentage of anatase in the mixture increases with increasing $\phi$ in accordance with the increase in the residence time [86]. The values of anatase percentage in the mixture are listed in Table 6.1 and represented in Fig. 6.7, which shows near linear dependence on equivalence ratio.

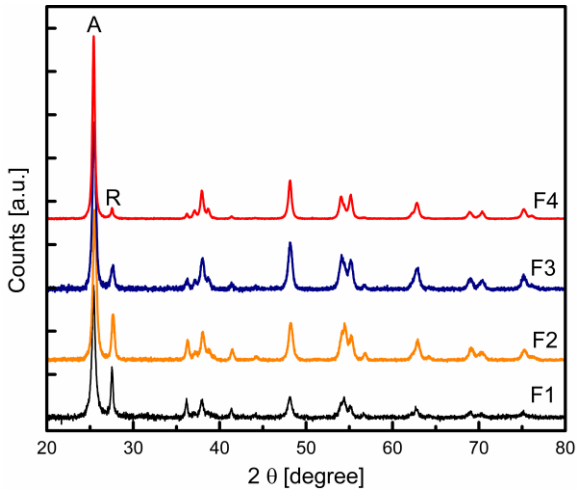


**Figure 6.6:** XRD pattern for $TiO_2$ NP synthesized using ethylene flames at different equivalence ratios (A and R stand for the first anatase and rutile peaks, respectively).

The Reynolds number has a small effect on the anatase content (Fig. 6.7). As Re increases from 8,300 to 18,676 the anatase content decreases by about 8% because of shorter residence time in the high temperature region. The effect of the precursor's Reynolds number $Re|_{Pre}$ was also investigated by changing the area between the poppet valve and the central port (area for precursor delivery). $Re|_{Pre}$ was changed from 108 to 187 at $\phi$=1.8 and Re=13,142. The influence

on anatase content was negligible, changing from 94.2 to 93.5 for $Re|_{Pre}$ of 108 1nd 187, respectively.

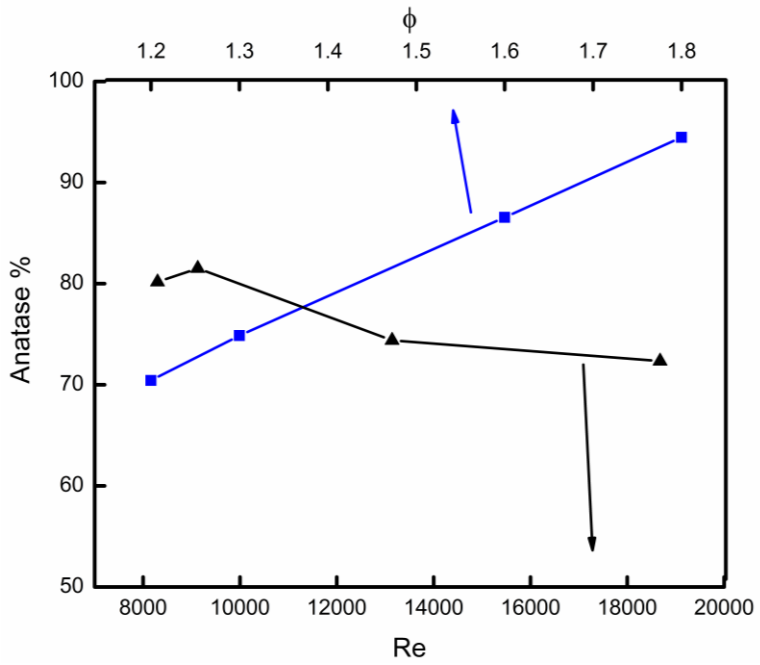


**Figure 6.7:** Effect of equivalence ratio and Re on the anatase content for different ethylene flames.

To further examine the phases of $TiO_2$ nanoparticles, the Raman spectroscopy measurements were performed. The visible region of the Raman spectra at different flames was determined. Although not shown here, the peaks for flames F1 and F2 correspond to the Raman modes of both anatase and rutile phases, whereas for F4 flame all peaks correspond to the anatase phase. This result is consistent with XRD data shown previously, where the predominant phase at higher equivalence ratio is the anatase phase.

The primary particle size was calculated from the XRD results using Scherrer's eq. [223] and found to be in the range of 18- 26 nm. The particle size was slightly affected by $\phi$ or Re in the tested range. The aggregate size was measured using Zeta Sizer and found to have a single peak of particle size distribution (NOT shown here) around 95 nm. This result indicates that the aggregation ratio of the produced $TiO_2$ nanoparticles is about 3.6 which is acceptable for those

generated by flames. This small range of size distribution with a single peak is a favorable advantage of the present configuration (poppet valve on top of the central port) as compared with the previous work [86].

The high resolution TEM images of $TiO_2$ nanoparticles for flames F1 and F3 are shown in Fig. 6.8. The particles are mostly spherical with some polyhedral shapes. The images reveal the high crystallinity and the ordered structure of the nanoparticle lattice planes in addition to some amorphous particles. By increasing the equivalence ratio to values higher than 1.6, a planar defect in some of the generated nanoparticles starts to appear in the HRTEM image (Fig. 6.8b). The average particle diameter calculated from TEM images has the value of 30 nm with some smaller particles which agrees with the results obtained from XRD experiments.

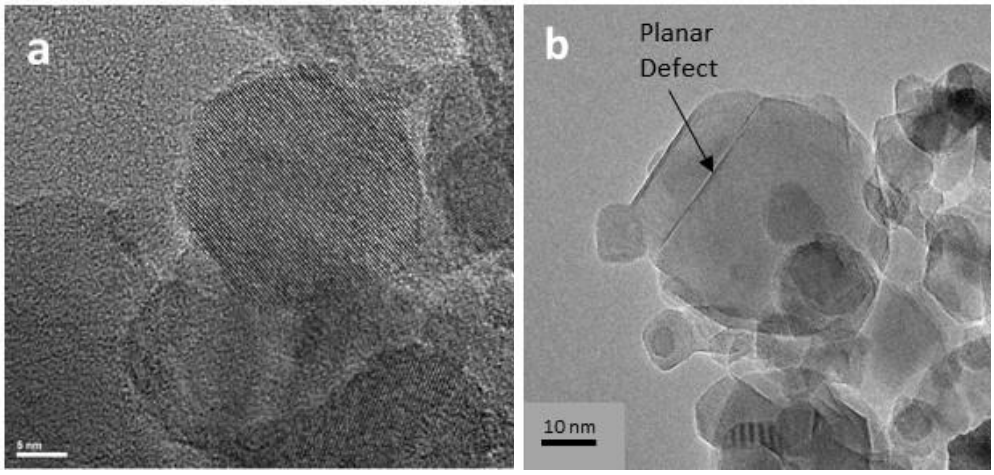


**Figure 6.8:** High resolution TEM for $TiO_2$ particles synthesized using flame (a) F1 and (b) F3 ethylene flames.

The planar defects located close to the boundary of the nanoparticle (not in the middle), which suggests that the planar defects were produced just before the complete growth of the nanoparticle [224]. The ratio of particles with a planar defect is very small compared to the total number of particles. The planar defects might be formed due to oriented attachment and growth including twin planes and other interfaces [225]. These microstructures are consequence of coarsening mechanism that involves the reduction of surface tension through

elimination of surfaces by attachment. The structurally different region (defect) may serve as a nucleation site for new phases.

## 6.4 Concluding Remarks

The usefulness of the curved wall-jet (CWJ) burner with a poppet valve shaped guide on top of the central port has been demonstrated for material synthesis of nanoparticles. The growth of $TiO_2$ nanoparticles has been reported with some key points affecting this growth. First, The CWJ burner can operate at a wide range of equivalence ratios and was found to exhibit small size turbulent flame characteristics. PIV data confirmed this behavior and the precursor flow had little impact on the flame behavior. Second, the crystal phase of the $TiO_2$ nanoparticles was strongly dependent on the equivalence ratio. At higher values, due to a longer residence time in high temperature region, the growth of anatase nanoparticles was dominant (flame F4). Finally, this configuration of the CWJ burner has a narrow range of particle size distribution (18-25 nm) with aggregation ratio f 3.6, which showed better results as compared with the original CWJ burner.

# Chapter 7

# Synthesis of Titania Nanoparticles Using Double-Slit Curved Wall-Jet (DS-CWJ) Burner

A novel double-slit curved wall-jet (DS-CWJ) burner was proposed and utilized for flame synthesis. This burner comprised of double curved wall-jet nozzles with coaxial slits; the inner slit was for the delivery of titanium tetraisopropoxide (TTIP) precursor while the outer one was to supply premixed fuel/air mixture of ethylene ($C_2H_4$), methane ($CH_4$), or propane ($C_3H_8$). This configuration enabled rapid mixing between the precursor and reactants along the curved surface and inside the recirculation zone of the burner. Particle growth of titanium dioxide ($TiO_2$) nanoparticles and their phases were investigated with varying equivalence ratio and Reynolds number. Flow field and flame structure were measured using particle image velocimetry (PIV) and OH planar laser-induced fluorescence (PLIF) techniques, respectively. The nanoparticles were characterized using high-resolution transmission electron microscopy (HRTEM), X-ray diffraction (XRD), and nitrogen adsorption BET for surface area analysis.

## 7.1 Introduction

Titanium dioxide ($TiO_2$) is an important semiconducting metal oxide and is expected to play an important role in future applications related to photonic crystals, energy storage, and photocatalysis [226]. The two most common crystal forms of $TiO_2$ are rutile and anatase, where the rutile phase is extensively used as white pigments. Anatase is a metastable crystal phase and has proven to be an effective photocatalyst.

Large-scale turbulent burners are utilized in flame synthesis [48]for an industrial production of $TiO_2$, whereas in lab settings, small laminar flames have been typically used to investigate

the growth process of $TiO_2$ nanoparticles [54, 141, 227]. Such growth process is strongly influenced by the flame conditions and appreciably differs when comparing laminar to turbulent flames. Systematic lab-scale experiments involving turbulent flames are required to enhance our understanding of nanoparticle formation, which will help to control crystallinity, size, and morphology of nanoparticles produced in flames.

A number of parameters such as burner geometry, fuel/oxidizer flow rates, precursor loading rate, and residence time can influence the growth of nanoparticles. Additionally, the use of different fuels has been of interest to the scientific community [54]. Common fuels investigated include methane [227], hydrogen [84], carbon monoxide [83], ethylene (chapter 5), and propane [85]. Of particular interest is the use of propane, as it can further reduce the cost of flame synthesized nanoparticles. Moreover, nanoparticles produced using a propane/air mixture resulted in nanoparticles with properties comparable to commercially made Degusa P25 $TiO_2$ [87].

For a scale-up of flame synthesis in laboratories, we have previously adopted a curved wall-jet (CWJ) burner for $TiO_2$ and $SiO_2$ syntheses by injecting precursors through a center tube and by supplying fuel/air mixtures as an annular-inward jet for rapid mixing of the precursors in the reaction zone (chapter 5). Nanoparticles were produced in ethylene ($C_2H_4$)/air premixed flames using titanium tetraisopropoxide (TTIP) and hexamethyldisiloxane (HMDSO) as the precursors for $TiO_2$ and $SiO_2$, respectively. Particle image velocimetry measurements confirmed that the precursors can be injected into the flames without appreciably affecting flow structure. Temperature, residence time and equivalence ratio were found to be the major control parameters for the growth of the nanoparticles and their phase. Particles produced using the CWJ burner exhibited a bimodal size distribution due to non-uniform residence time in the high temperature zone along the radial plane above the burner [208]. Turbulent spray flames

were stabilized using spray nozzle within the curved wall jet burner [228]. Such burners can be used to burn low cost chemical precursors and provide new pathways for scalable materials synthesis.

In this chapter, we used the modified CWJ burner [90] that has double-slit curved wall-jet (DS-CWJ) configuration to supply the TTIP precursor and reactants (fuel/air mixture) through inner and outer slits, respectively. This DS-CWJ burner can be used for premixed or diffusion flame configurations [90]. The precursor and reactants can be mixed along the curved wall before the premixed flame, resulted from these reactants, is stabilized in a recirculation zone. As a recirculation zone is formed upstream, the precursor is significantly mixed with the produced hot gases and distributes relatively uniformly above the burner. Particle image velocimetry (PIV) and OH planar laser-induced fluorescence (PLIF) techniques were applied [93] in order to understand the flame structure, flow field characteristics and precursor-turbulence-flame interaction. The impact of different gaseous fuels (ethylene, propane, and methane) on the size, phase and crystallinity of $TiO_2$ nanoparticles was investigated at various equivalence ratios ($\phi$) and Reynolds numbers (Re).

## 7.2 Experiment

The apparatus consisted of a double-slit curved-wall jet (DS-CWJ) burner, a precursor delivery system, nanoparticle collection system, and high-speed PIV and OH PLIF setups. The DC-CWJ burner (Fig. 7.1a) is composed of a center body of a cylinder ($\phi$50 mm) with a hemi-spherical tip, and two cylinders with curved-converging sections (see Fig. 7.1b for dimensions). A concave spherical cavity with R56 mm was created on top of the hemi-sphere (3.37 mm in depth and 24 mm in width at the tip) for better flame stabilization [6, 7]. The inner surfaces of the curved sections for the inner and outer cylinders have R28 and R51 mm, respectively, both

having an exit of 43 mm diameter, forming slits for the precursor and reactants (fuel/air) supplies. The heights of the two cylinders were adjustable. The converging sections of the two cylinders guided fuel and air tangentially to the curved wall of the center body toward the axis to form annular-inward jets. The burner surface was anodized to minimize light reflection.

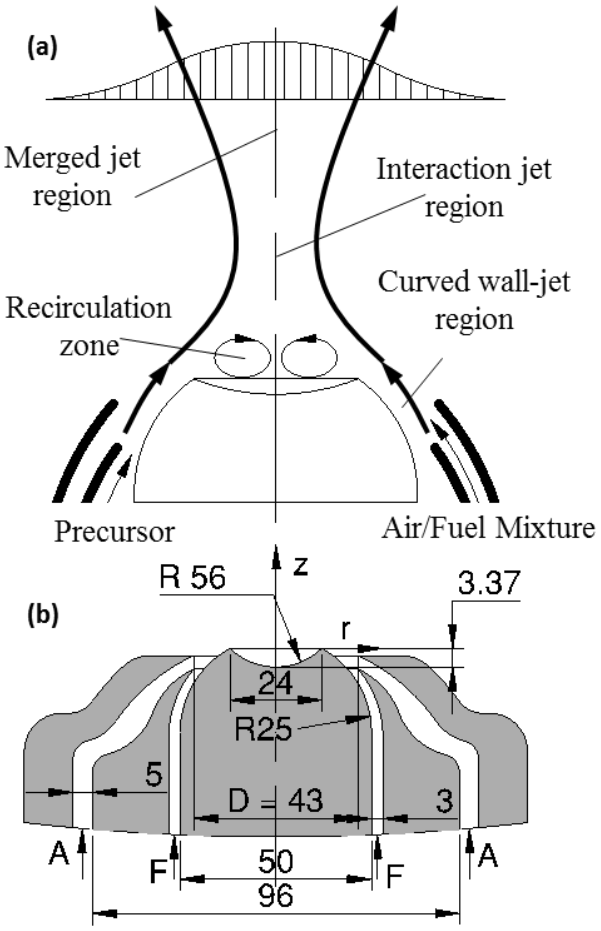


**Figure 7.1:** Schematic of double-slit curved-wall jet burner; (a) exhibiting overall flow field and (b) burner configuration [90].

Ethylene (99.995%), propane (99.5%), or methane (99.995%) and air were supplied as a premixture through the outer slit of the burner to provide the supporting flame. Titanium tetraisopropoxide (TTIP) (Sigma Aldrich, 97%) was used as the nanoparticles precursor, which was heated in a bubbler to 110 $^{o}$C. The precursor vapor was carried with nitrogen gas (2 SLPM) and supplied to the inner slit of the burner (Fig. 7.2). The precursor delivery line after the

bubbler and the burner body were heated to 180 $^{o}$C to prevent condensation. Experiments were conducted by varying fuel, flow rates as well as equivalence ratio. All flow rates were controlled using mass flow controllers (Brooks). Ethylene flames are denoted as E1 to E11, propane flames are denoted as P1 to P7, whereas M1 to M4 refer to methane flames (see Table 7.1 for operating conditions). The generated nanoparticles were collected on glass-fiber filters using a vacuum pump. All experiments were conducted at atmospheric pressure.

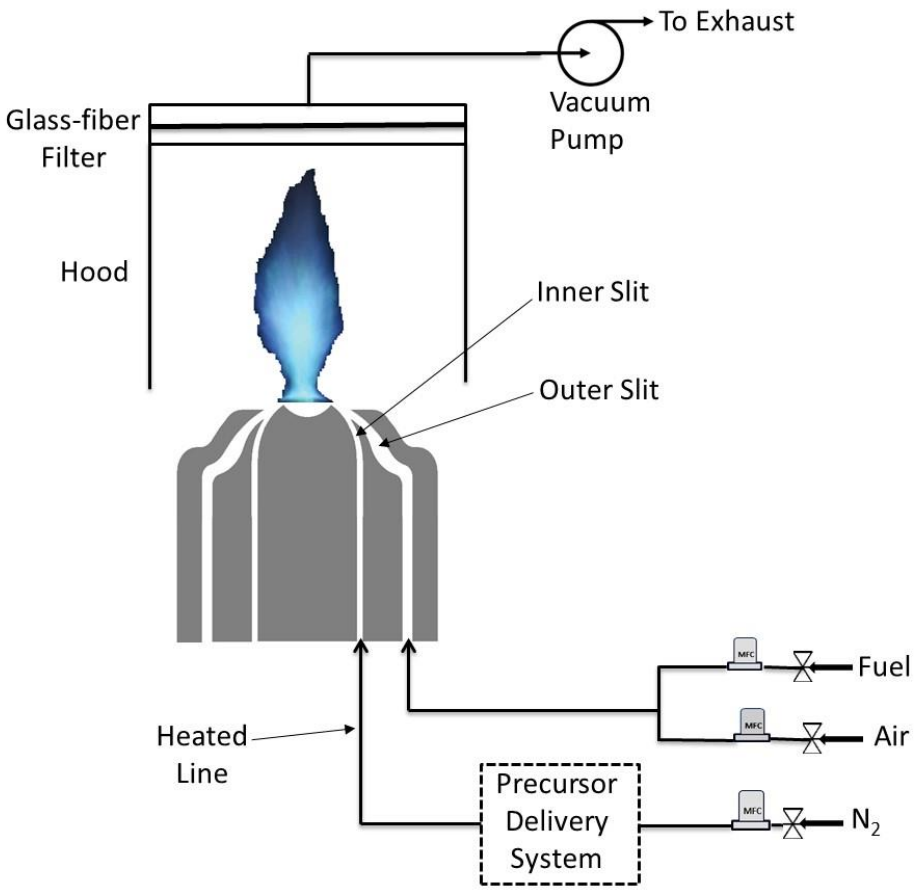


**Figure 7.2:** Experimental setup illustrating the double-slit curved-wall jet burner, fuel/air and precursor delivery systems, and particle collection system.

The PIV system consisted of a high-repetition rate twin-cavity diode-pumped Nd:YLF laser (Litron, LDY304-PIV; 527 nm, 28 mJ/pulse, 5 ns pulse duration) and a CMOS camera (La Vision, Imager Pro HS 4M; 2016×2016 pixels) coupled with a controller. Double-pulses with a time separation of 20-40 μs were repeated at 1 kHz. The laser output formed a sheet

approximately 1 mm in thickness and 70 mm in height by a series of lenses. Seed particles were titanium dioxide ($TiO_2$, nominal diameter 0.18 μm) and the seed levels were adjusted for spurious vectors in the image processing to be less than 5%. A perspective distortion from the camera system was calibrated by imaging a 3-D dot target (La Vision type 11). Velocity fields were determined through multi-pass vector computation software (Davis 8.1) with an interrogation size ranging from 128×128 to 32×32 pixels and 50% overlap, yielding a 0.76×0.76 $mm^2$ spatial resolution.

The high-speed PLIF system consisted of a diode-pumped Nd:YAG laser (Edgewave, IS16II-E; 532 nm) and a dye laser (Sirah, Credo-Dye) whose output was frequency-doubled to 283.57 nm to excite $Q_1(8)$ line of A-X (1,0) OH transition with about 0.3 mJ/pulse at 10 kHz repetition rate. OH signals were detected at 295-345 nm with an intensified CMOS camera (La Vision, HSS8 and IRO; 1024×1024 pixels). Elastic scattering noise from the laser sheet and background noise were reduced by using a band-pass filter (>80% at 320 nm) and also by minimizing the intensifier gate time (200 ns). The spatial resolution was 0.11 mm/pixel.

Visible flame height was measured using a cathetometer and the results were compared with the average values obtained from direct photographs. The temperature was monitored for the cases without precursor using S-type thermocouples at 2.5 cm above the nozzle exit for reference. The measured temperatures are the averages of fluctuating temperatures within turbulent flames corrected for radiation errors. The collected nanoparticles were characterized using X-ray diffraction (XRD) by an advance X-ray powder diffractometer (Bruker, D8) with CuKα (λ=1.5406 Å) radiation. The primary particle size and morphology were examined by transmission electron microscopy (TEM) and high-resolution TEM (HRTEM) (FEI Titan, G2 80-300).

**Table 7.1:** Operating conditions for the studied flames using DS-CWJ burner.

| Flame | Fuel | $V_0^*$ [m/s] | Re | $\phi$ |
|---|---|---|---|---|
| E1 | $C_2H_4$ | 19.66 | 13,142 | 1.0 |
| E2 | | 19.53 | 13,142 | 1.2 |
| E3 | | 19.53 | 13,142 | 1.3 |
| E4 | | 19.28 | 13,142 | 1.6 |
| E5 | | 19.15 | 13,142 | 1.8 |
| E6 | | 19.02 | 13,142 | 2.0 |
| E7 | | 19.02 | 13,232 | 2.2 |
| E8 | | 12.34 | 8,300 | 1.3 |
| E9 | | 27.76 | 18,676 | 1.3 |
| E10 | | 12.34 | 8,469 | 1.8 |
| E11 | | 27.76 | 19.054 | 1.8 |
| P1 | $C_3H_8$ | 19.55 | 13,600 | 1.2 |
| P2 | | 20.00 | 13,694 | 1.3 |
| P3 | | 19.55 | 13,983 | 1.8 |
| P4 | | 12.00 | 8,649 | 1.3 |
| P5 | | 12.35 | 8,831 | 1.8 |
| P6 | | 28.00 | 19,460 | 1.3 |
| P7 | | 27.78 | 19,871 | 1.8 |
| M1 | $CH_4$ | 12.35 | 7,790 | 1.3 |
| M2 | | 12.35 | 7,790 | 1.6 |
| M3 | | 12.35 | 7,790 | 1.8 |

*: Velocity of the premixed fuel/air mixture at burner exit.

The specific surface area (SSA) was calculated based on multi-point Brunauer–Emmett–Teller (BET) nitrogen adsorption (Micromeritics, ASAP 2050). UV–vis diffuse reflectance spectra (DRS) were obtained for the dry-powder samples using a scan UV–vis-NIR spectrophotometer (Varian Cary 500) equipped with an integrating sphere assembly, using $BaSO_4$ as reflectance sample.

## 7.3 Flame Characteristics

Basic flame features in DS-CWJ burner will be discussed prior to presenting a materials synthesis behavior. This includes flames shape and reactive flow field characteristics and structure.

### 7.3.1 Flame shape

Photographs of flames stabilized in the burner are shown in Fig. 7.3 at several operating conditions listed in Table 7.1 without (upper row) and with (lower row) precursor supply. The mixture Reynolds numbers (Re) based on the jet velocity, mixture kinematic viscosity, and hydraulic diameter at jet exit of 10 mm were changed from 8,300 to 19,870 to study the effect of Re on the characteristics of produced nanoparticles. To elaborate the effect of fuel type on nanoparticle features, ethylene, propane, and methane turbulent flames are investigated at several equivalence ratios.

These flames have blue color which is identical to premixed flames except some cases with reddish-blue (flames E9, P3 and P6) in the downstream region. Previous studies [6, 7, 177] showed that the flame height measured from the tip of the concave cavity increases with equivalence ratio as shown in Fig. 7.3 for a specified smaller jet velocity, $V_0$, and becomes insensitive to $V_0$ for sufficiently large values of $V_0$. The present flames are in accordance with this behavior since the flame height is sensitive to jet velocity for flames E2 to E5. It is of

interest for the flame shape near the tip region. As Re increases, the width of the flame base becomes similar to the diameter of the concave cavity, followed by necking by appreciably reduced their diameters. This corresponds to the interaction jet region. Toward the downstream, the flame width increases again in the merged-jet region as shown in Fig. 7.3. This can be partially attributed to the flow strain rate generated at the interaction jet region and the local flame speed. As $V_0$ approaches further to a critical value, over which the flame stabilizes only inside the concave tip region, the post flame extending downstream region (e.g., P7) entirely extinguishes (not shown). Ethylene and methane flames are not likely to be quenched as they propagate faster than propane flames and show better stabilization characteristics.

When TTIP is added to these flames, they become more luminous, attributed to the luminosity of the nanoparticles formed in these flames. The flame heights, *H*, are in the range of about 112-318 mm (Table 7.2), an increase in flame height being exhibited with increase in equivalence ratio; this is reasonable since more air is required to burn the fuel. Also, an increase in the flame height is realized due to the increase in Re because of the increased heat flux entering the reaction region in the flame. Difference in flame speeds among ethylene, propane, and methane is partially responsible for the difference in the flame height for these fuels [229].

To prevent any condensation from the precursor, the whole burner body was heated to 453 K and as a result, the incoming air was preheated to 336 K. The temperatures at the monitoring point (2.5 cm above the burner exit) are in the range of 900 to 1760 K, and increase with equivalence ratio (Table 7.2). The Reynolds number has small effect on the temperature and ethylene flames were found to have higher temperatures than propane and methane flames.

**Table 7.2:** Summary results for flames described in Table 7.1.

| Flame | H | T[a] | τ[b] | Anatase | $d_{XRD}$ | *BET* | $d_{BET}$ |
|---|---|---|---|---|---|---|---|
| | [mm] | [K] | [ms] | % | [nm] | [$m^2/g$] | [nm] |
| E1 | 111.6 | 1155 | - | 80.8 | 14.7 | 110.7 | 13.4 |
| E2 | 119.0 | 1343 | 8.2 | 83.9 | 14.3 | 92.5 | 16.1 |
| E3 | 132.7 | 1474 | 8.9 | 86.4 | 14.6 | - | - |
| E4 | 191.4 | 1617 | 12.6 | 90.1 | 15.7 | 78.5 | 19.0 |
| E5 | 234.7 | 1710 | 15.9 | 93.5 | 18.2 | 67.7 | 22.1 |
| E6 | 267.2 | 1740 | - | 95.6 | 19.3 | - | - |
| E7 | 298.7 | 1818 | - | 96.3 | 19.3 | - | - |
| E8 | 117.3 | 1486 | 11.5 | 80.8 | 16.1 | 105.2 | 14.2 |
| E9 | 175.8 | 1464 | 8.3 | 86.8 | 14.7 | 93.7 | 15.9 |
| E10 | 195.2 | 1760 | 18.1 | 93.1 | 18.8 | - | - |
| E11 | 257.8 | 1680 | 11.6 | 85.2 | 15.7 | - | - |
| P1 | 171.4 | 899 | 14.5 | 88.6 | 15.4 | - | - |
| P2 | 205.5 | 1253 | 14.9 | 84.9 | 14.8 | - | - |
| P3 | 288.9 | 1538 | 22.1 | 79.5 | 17.1 | - | - |
| P4 | 190.6 | 1353 | 20.1 | 90.4 | 15.6 | 116.4 | 12.8 |
| P5 | 291.8 | 1644 | 32.3 | 86.3 | 18.4 | 82.9 | 18.0 |
| P6 | 216.5 | 1300 | 12.3 | 89.0 | 12.8 | - | - |
| P7 | 317.5 | 1578 | 19.0 | 82.9 | 16.3 | - | - |
| M1 | 159.4 | 1043 | - | 77.3 | 17.3 | 81.2 | 18.2 |
| M2 | 175.5 | 1421 | - | 82.9 | 18.0 | 90.5 | 16.4 |
| M3 | 195.2 | 1607 | - | 86.2 | 18.5 | 70.5 | 21.1 |

[a]: Temperature at 2.5 cm height above the burner exit.

[b]: particle Residence time in the flame

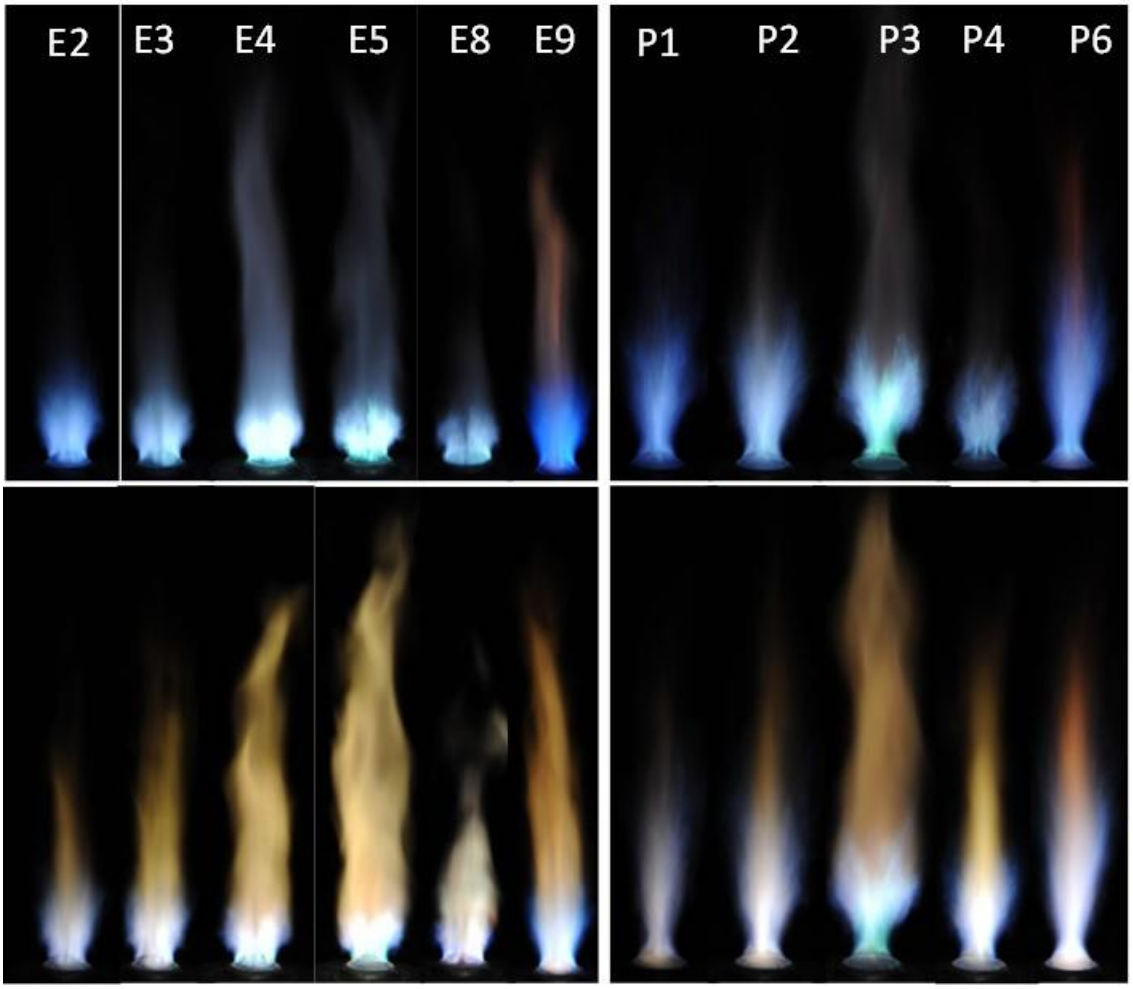


**Figure 7.3.** Direct photographs of flames; top row represents the fuel/air flames and bottom row represents flames with TTIP precursor.

### 7.3.2 Flow field characteristics

The PIV system was used to characterize the turbulent flow field. Figure 7.4 shows the time-averaged mean velocity vector fields for an ethylene (E9) and propane (P6) flames with the background color indicating velocity magnitude. The right images (a, c) indicate the flow field without TTIP precursor and the left ones (b, d) indicate the flow field with TTIP precursor. Both presented cases have an equivalence ratio of 1.3 and Re > 18,000. The white lines in Fig. 7.4 indicate streamlines of the flowing mixture. The general features of the flow field exhibit typical flow characteristics of the CWJ burner [6, 7]. The flow field consists of a recirculation zone (RZ), an interaction jet (IJ) region with the collision of the annular-inward jets near $z = 6$

mm, and a downstream merged jet (MJ) region. Inner and outer shear layers (ISL and OSL) surrounding the annular-inward jets (AJ) can also be identified. The velocity gradients in these shear layers generate turbulence, augmented by the collision of annular-inward jets. TTIP precursor has a negligible influence on the velocity vector field when it is supplied to the burner through the inner slit. This is due to its low volume flow rate (2 SLPM). The recirculation zone is very clear when using propane whereas it is weak for ethylene flames due to the lower flame speeds of propane and its tendency to stabilize in lifted flame mode. It is also clear from Fig. 7.4 that ethylene flames have higher average velocity than propane flames due to their higher flame speeds and weaker recirculation zones.

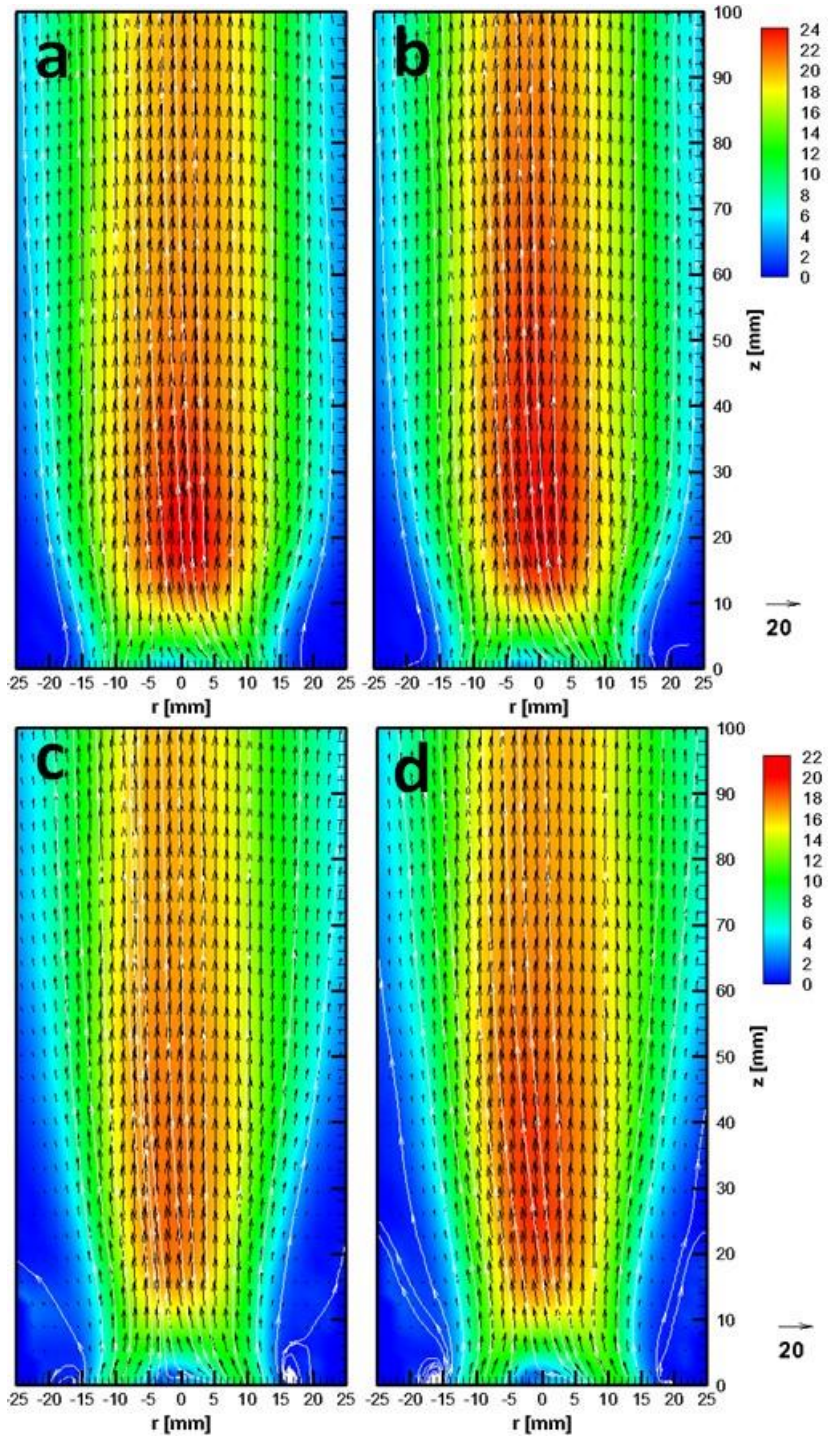


**Figure 7.4:** Time averaged velocity vector plot of flow field for; (a, b) E9 ethylene flame and (c, d) P6 propane flame. The right images (a, c) indicate the flow field without TTIP precursor and the left ones (b, d) indicate the flow field with TTIP precursor (white lines indicate streamlines).

The axial (at $r = 0$) profiles of the mean velocities are plotted in Fig. 7.5. The recirculation zone is clearly exhibited by $\boldsymbol{V_z}$, especially for propane, having negative values for $0 < z < 5$ mm, which approaches up to 3.8 m/s (case P6). In the interaction jet region, $\boldsymbol{V_z}$ increases rapidly and then slightly decreases (E3 and E9) or maintains near uniform values (E5 and E8) up to $z = 100$ mm in the merged jet region. As increasing the Re number for both fuels, an increase in the axial velocity is realized due to the higher momentum of flow gases (Fig. 7.5a and c). On the other hand, the equivalence ratio has no effect on the axial velocity as shown in Fig. 7.5b and d. TTIP precursor has only small influence on the velocity values for both propane and ethylene flames.

Such velocity quantification and visible flame height enabled in estimating the total residence time of the precursor within the hot gases. All calculated residence times are reported in Table 7.2 and they are in the range of 8.2- 18.1 for ethylene flames and 12.3- 32.3 for propane flames. It is important to note that hot gases in ethylene flames flow faster than the corresponding ones in propane flames as well as they have shorter flames. This decreases the residence time of the TTIP precursor particles in ethylene flames, altering its characteristics (Section 7.4). We expect that part of TTIP precursor is recirculated within RZ increasing its local residence time.

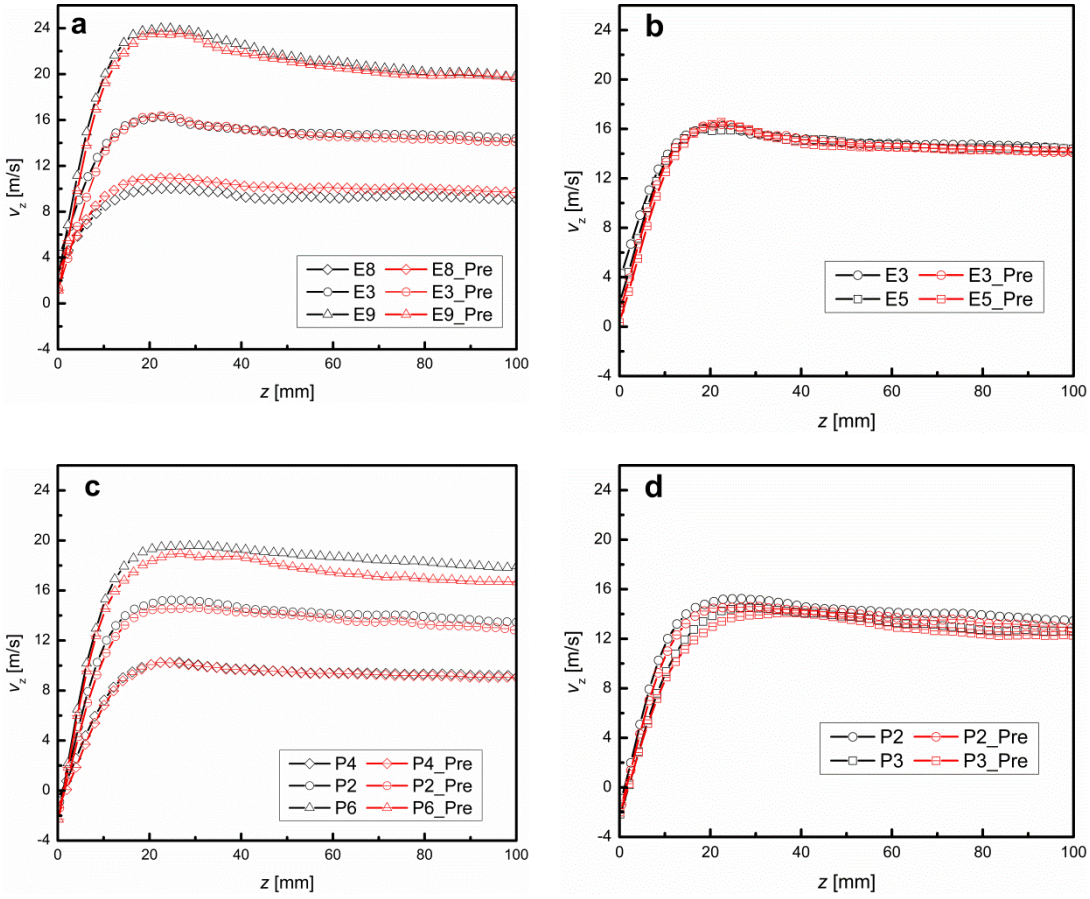


**Figure 7.5:** Axial profiles of flow velocity along the burner centerline; (a, b) ethylene flames, (c, d) propane flames (Pre denotes with TTIP precursor).

The axial profiles of rms turbulent velocities along the burner centerline, $u' = \sqrt{(V_r'^2 + V_z'^2)}$, are shown in Fig. 7.6 for several ethylene and propane flames listed in Table 7.1, with and without TTIP precursor. Values of $u'$ have large in RZ, peaking in the interaction jet region, and maintain reasonably uniform low values in the merged jet region for the investigated ethylene and propane flames. The higher the Re, the higher the level of turbulence particularly within the RZ and IJ region, resulting from the formed shear layers due to a significant velocity gradient. Also, these results indicate that the collision of annular-inward jet near the boundaries of RZ influences the generated turbulence. These rms velocities are expected to be appreciably influenced by the heat release when reacting and non-reacting flows are compared [230].

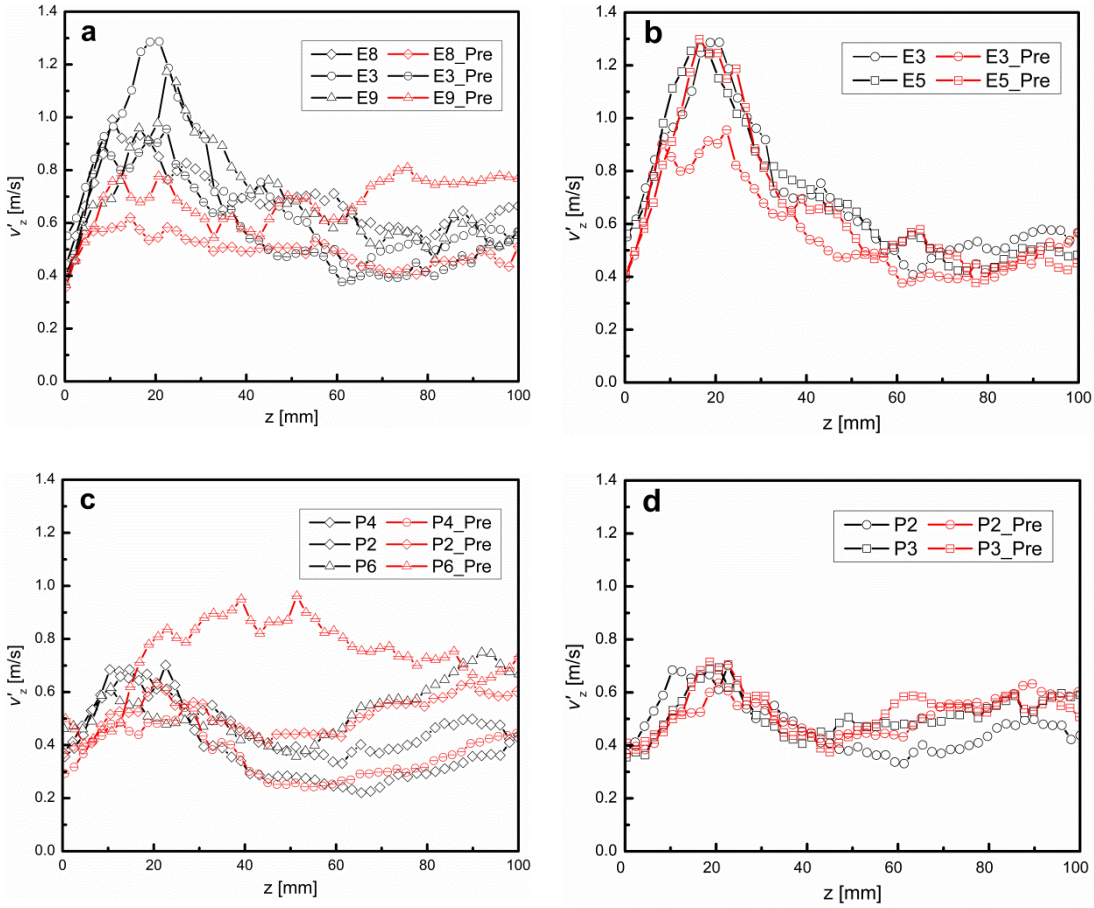


**Figure 7.6:** Axial profiles of rms velocity along the burner centerline; (a, b) ethylene flames, (c, d) propane flames (Pre denotes with TTIP precursor).

### 7.3.4 Flame structure

It can be concluded from previous results [90] that the proposed double-slit configuration enhances the mixing of precursor and combustion gases appreciably before reaching the recirculation zone for flame stabilization and the downstream interaction jet region, implying that the precursor can be burnt under partially premixed conditions despite they are supplied separately to the burner. The mixing characteristics could be influenced with flame through thermal expansion and buoyancy induced flow entrainment. The rapid mixing behavior of the fuel/air and precursors in the present double-slit CWJ burner supports the production of nanoparticles without having any carbonaceous contamination (soot).

The time resolved (10 kHz) OH-PLIF system was employed to provide insights on various dynamics of turbulent premixed flames and to investigate the flames structure. Figures 7.7 and 7.8 show typical samples of instantaneous OH-PLIF images for ethylene and propane flames, respectively. The images of OH reveal the existence of a recirculation zone upstream near the concave cavity followed by, for high Re flames particularly propane flames (P6), thin necking at the interaction jet region and then the strongest OH signal zone further downstream. TTIP precursor has a slight effect on the flame structure (enthalpy ratio of precursor compared to fuel is less than 6.8%).

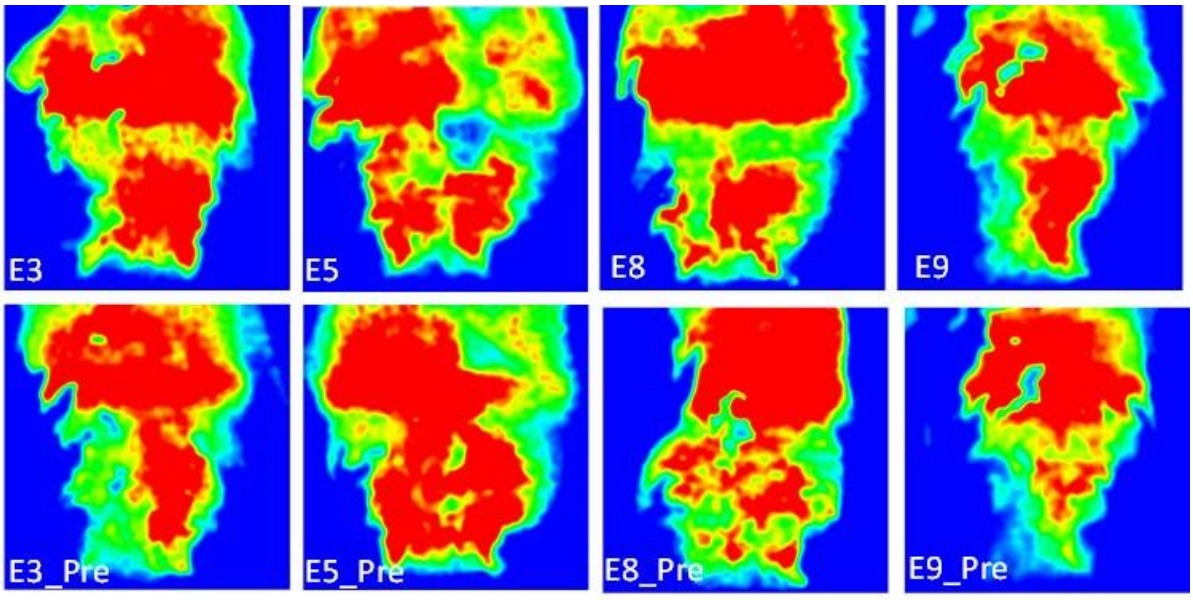


**Figure 7.7:** OH-PLIF images for selected ethylene flames showing their flame structure. _Pre denotes flames with adding TTIP precursor.

By inspecting these images, one can derive the following features: (1) the recirculation zone is somewhat clear and confined within the burner tip region for ethylene flames; (2) the production of OH radical in the interaction jet region is appreciably influenced in propane flame (P6) where OH intensity is low while a broadening zone of relatively higher OH intensity is observed in ethylene flames; (3) the reaction sheets distribute predominantly downstream in the merged jet region in propane flames within many isolated pockets associated with low OH

signals, however, in ethylene flames, the reactions take place over larger areas particularly upstream; (4) these images imply that the downstream part of the propane flame front is maintained by small flame elements detached from RZ, and its wrinkleness depends on the nature of flame seeds, emerging from RZ; this is not the case for ethylene flames.

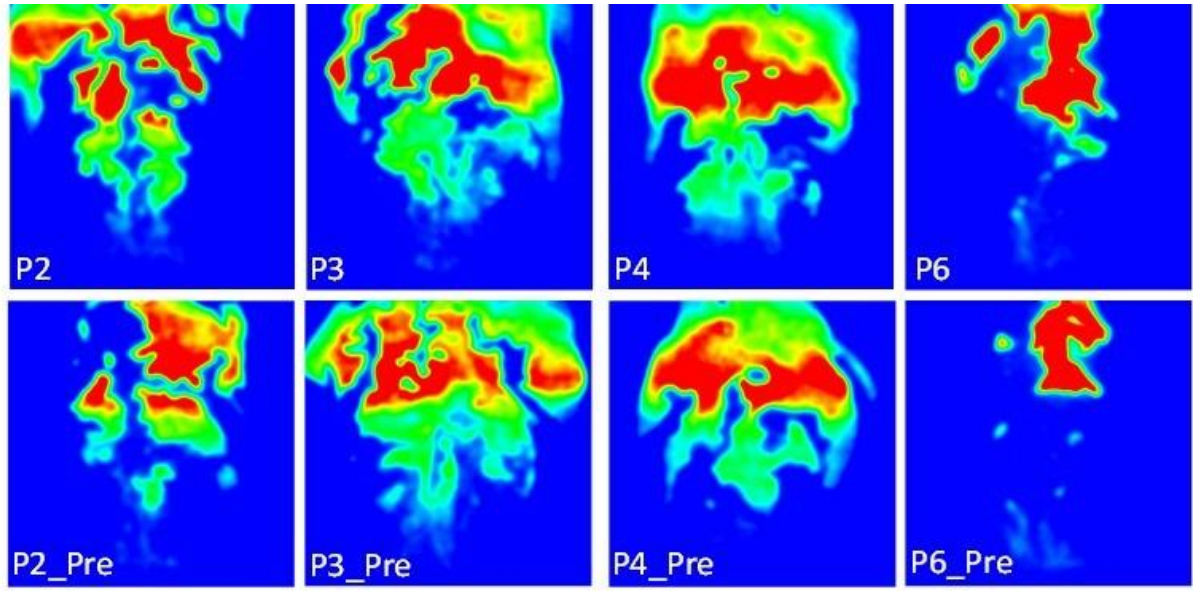


**Figure 7.8:** OH-PLIF images for selected propane flames showing their flame structure. _Pre denotes flames with adding TTIP precursor.

Frequent events of local flame extinction are observed at the interaction jet region for propane flames (P6). Some flame kernels that initiated in the recirculation zone are detached at the interaction jet region and convected downstream toward the merged-jet region. As they encounter a favourable combustion environment, these kernels induce a re-ignition process further downstream as shown in Fig. 7.8 for flame P6, increasing its flame length. This would interpret higher temperature values measured in ethylene flames compared with the corresponding ones of the propane flames. Flame quenching/re-ignition behaviour is likely in propane flames compared to ethylene flames. This is attributed to the high local burning velocity of the ethylene flames that is able to stabilize such flames in high speed environment.

Flame fronts in propane flames exhibit higher wrinkling degree and corrugation due to the energetic eddies and low local burning rate. Such wrinkles may engulf TTIP precursor and affect the production of nanoparticles.

## 7.4 Nanoparticle Characterization

TTIP (with loading rate of 50 g/hr based on vapor pressure [231]) and nitrogen carrier gas flow rate of 2 SLPM were used to synthesize titanium dioxide ($TiO_2$) nanoparticles. The flame temperature is expected to increase by 100-200 $^oC$ with the addition of the precursor [210]. $TiO_2$ nanoparticles were collected and analyzed with XRD at several operating conditions, as shown in Fig. 7.9, from which the crystal phase, average crystallite size, and rutile/anatase phase ratio could be determined.

For all cases, both the peaks representing the anatase (A) and rutile (R) phases can be seen, an indication of the mixture of these two phases. The anatase to rutile ratio in the samples was calculated by integrating the respective XRD peak intensities (anatase and rutile peaks at $2\theta$ = 25.4 and 27.5$^o$, respectively) using the following equation [147]

$$\chi = \left(1 + \frac{I_A}{I_R}\right)^{-1} \qquad (7.1)$$

where $\chi$ is the weight fraction of rutile in the $TiO_2$ sample, and $I_A$ and $I_R$ are the integrated areas under the anatase and rutile peaks, respectively. The values of anatase percentage in the mixture are listed in Table 7.2. For ethylene and methane flames, the anatase content in the nanoparticles was proportional to the equivalence ratio (Chapter 5). This proportionality was inverted in the case of propane fuel, the anatase content decreases as increasing the equivalence ratio. Re has slight effect on the anatase content for all fuels used (see Table 7.2 for comparison).

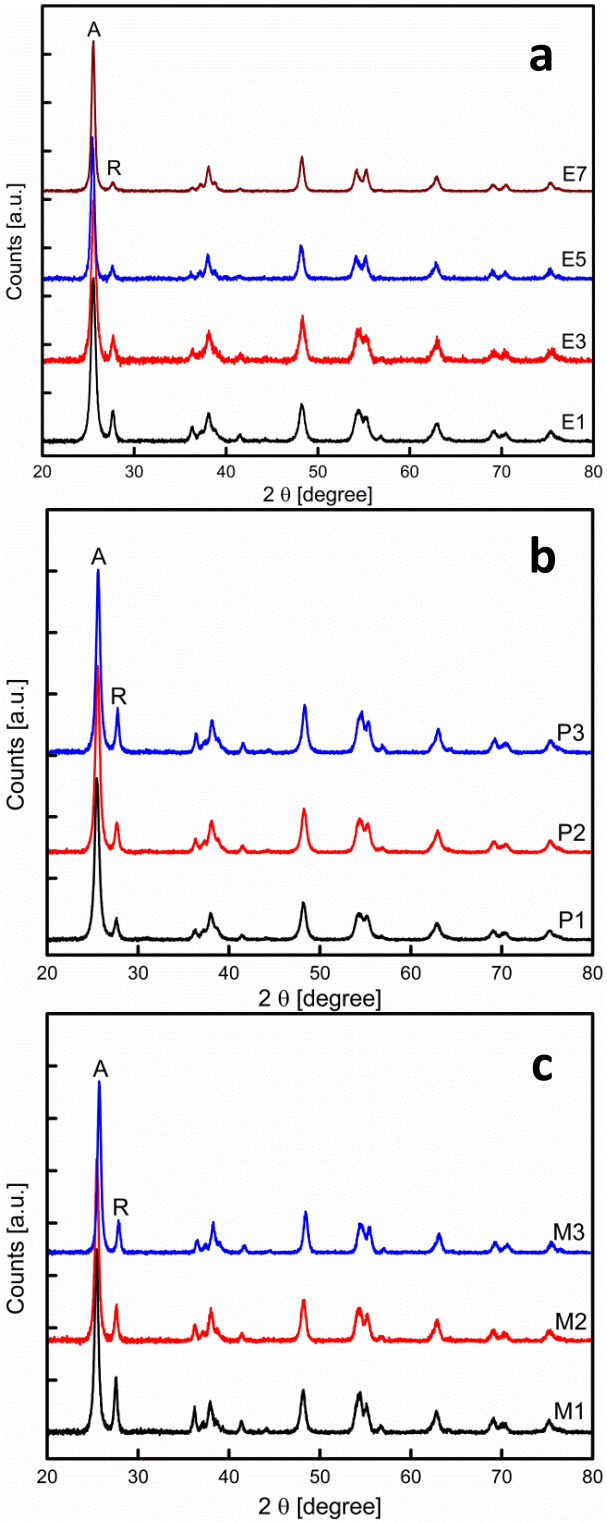


**Figure 7.9:** XRD pattern for $TiO_2$ particles indicating the effect of equivalence ratio using different fuels; (a) ethylene flames, (b) propane flames, and (c) methane flames. A and R stand for the first anatase and rutile peaks, respectively.

The change in the anatase content of $TiO_2$ particles can occur for several reasons. Typical parameters that control the growth of anatase include precursor loading rate, oxygen content, residence time, and heat flux [87, 212, 213]. The results for ethylene and methane flames (Fig. 7.10a) agree with those of Wegner and Pratsinis [213], who observed a higher anatase content when the residence time in high temperature region became longer and when the TTIP flow rate was smaller. In this work, a higher equivalence ratio resulted in higher heat release, leading to increased flame temperature. The longer flame also provided an increased residence time (8-18 ms). These conditions allow enhanced growth of anatase $TiO_2$ nanoparticles, which is also the thermodynamically more stable phase at elevated temperatures [212].

For propane flames (Fig. 7.9b and Fig. 7.10a), the anatase content decrease as increasing the equivalence ratio. This is due to the very long residence time of propane flames compared to ethylene ones (see Table 7.2 for the absolute values). As discussed previously from the PIV and OH-PLIF results, TTIP precursor enters the recirculation zone and travels with longer flames which increases the residence time. This long residence time (up to 32 ms) in hot regions may have the same effect as thermal annealing in which anatase starts to convert to rutile [232].

The crystallite size of the $TiO_2$ particles ($d_{XRD}$) was determined from XRD using Scherrer's formula [214]. The primary particle size calculated from XRD was in the range of 14-19 nm for all cases. The crystallite size increases by small amount with equivalence ratio for ethylene flames ($d_{XRD}$ = 14.7-19.3 nm) and for smaller amount for propane flames ($d_{XRD}$ = 15.4-17.1 nm). Methane flames have larger particle sizes but also depends slightly on equivalence ratio as shown in Fig. 7.10b. Figures 7.10c and d show the effect of Reynolds number on the anatase content and particle size calculated from the XRD results, respectively, for ethylene and propane flames. The change in anatase content is about 5% which can be considered within the experimental error limits. The particle size decreases with small amount as increasing Reynolds

number (< 4 nm change) due to lower residence time of the precursor in the hot flame region. One can see also from Table 7.2 that the fuel type has a slight effect on the particle size.

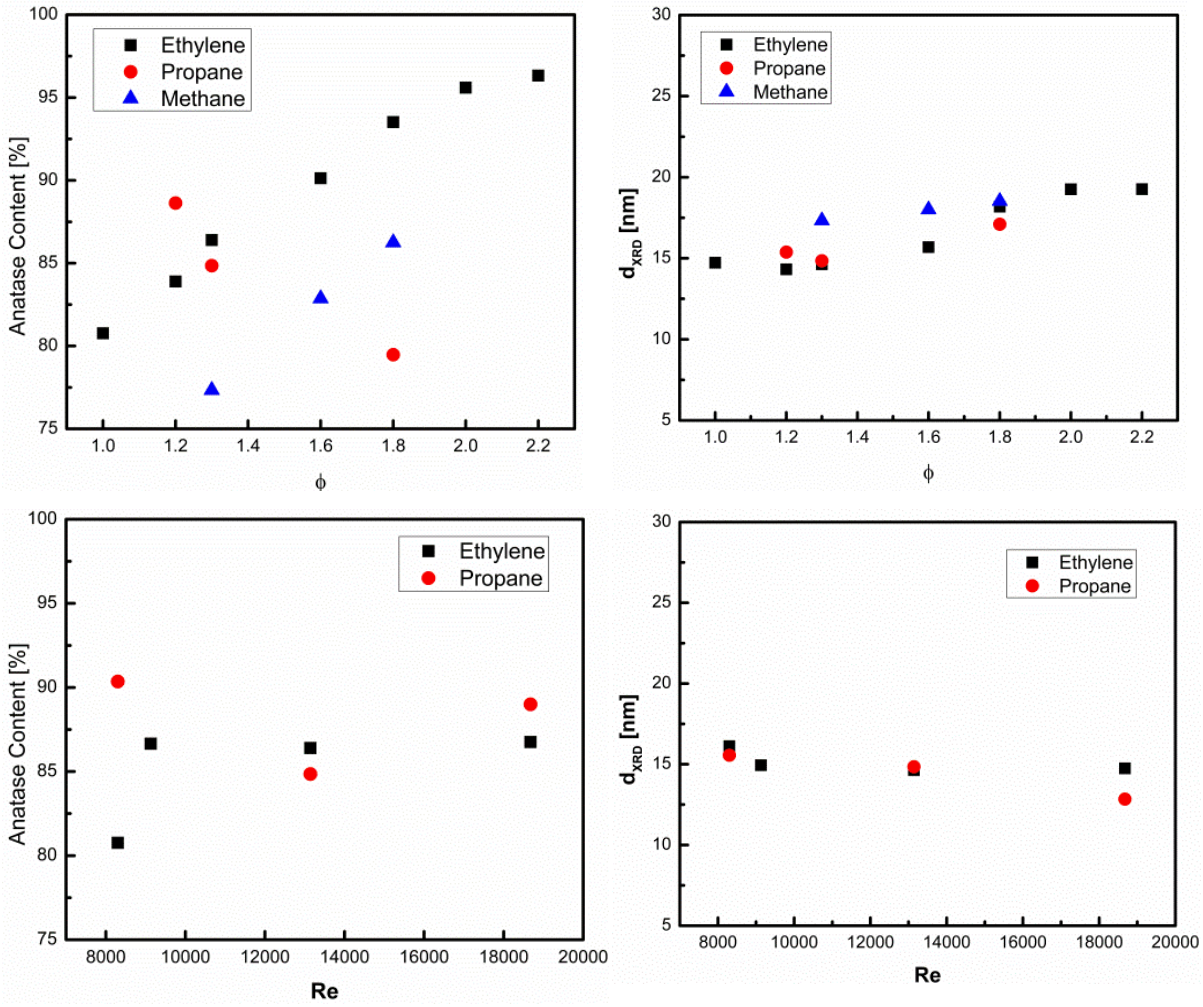


**Figure 7.10:** Anatase content and equivalent diameter calculated from XRD results for different fuels.

The specific surface area (SSA) was measured by the BET nitrogen adsorption technique for some cases and the resulting isotherms (type IV for mesoporous materials) are shown in Fig. 7.11. SSA is found to decrease as increasing the equivalence ratio or decreasing the Reynolds number as expected for larger particle size. There is a tendancy for the SSA to go beyond 100 $m^2/g$ for higher Reynolds numbers (Re>18,600) or lower equivalence ratios ($\phi$=1.0) for ethylene flames. The high SSA can be obtained with higher equivalence ratio for propane flames (SSA= 116.4 for case P4). As a result, the particle size can be calculated from the BET

surface area assuming spherical particles ($d_{BET}$). Note that the quantitative index of average particle size is most reliable when using the BET method [18]. The values of $d_{BET}$ are ranging from 12.8 to 22.1 nm (Table 7.2), which are in agreement with the data obtained from XRD ($d_{XRD}$). The difference between $d_{BET}$ and $d_{XRD}$ can be attributed to particle aggregation [148]. The total pore volume of $TiO_2$ nanoparticles generated from flame P4 is 0.613 $cm^3/g$, whereas it has the value of 0.336 $cm^3/g$ for flame P5. These large pore volumes and SSA indicate the mesoporous structure of $TiO_2$ nanoparticles [233] and are promising in catalytic applications.

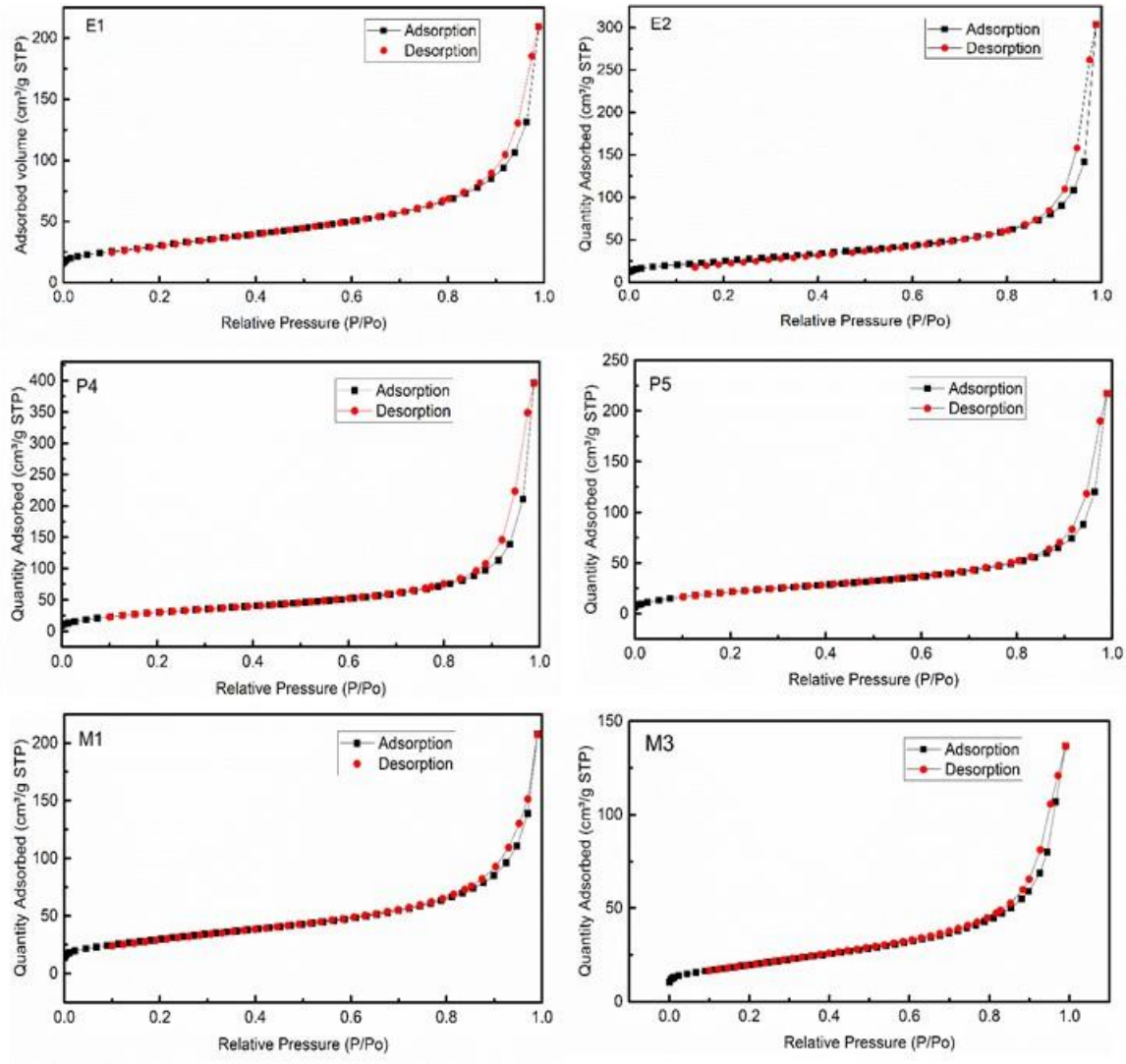


**Figure 7.11:** Isotherms measured by BET analysis for some studied cases.

The TEM images of $TiO_2$ nanoparticles generated from the ethylene flame at $\phi$ = 1.6 and Re =13,142 are shown in Fig. 7.12. The particles are mostly spherical with some polyhedral shapes. The images also suggest that the $TiO_2$ particles have a size distribution ranging from 5 to 30 nm. This nature can partially be attributed to non-uniform residence time in the high temperature zone along the radial plane above the burner [208]. The diffraction pattern (inset in Fig. 7.12a) shows a ring-type pattern. We picked around 5-10 particles for the TEM diffraction patterns. Since each nanoparticle has its own crystal orientation, the overall TEM pattern looks like a polycrystalline pattern. In Fig. 7.12a inset, the innermost ring-type pattern has a double layer pattern with diffraction spots very close to each other, an indication of the mixture of the anatase and rutile phases. These results are in agreement with the XRD data. The HRTEM image of the $TiO_2$ particles shown in Fig. 7.12b reveals the high crystallinity and the ordered structure of the nanoparticle lattice planes as well as some polyhedral particles.

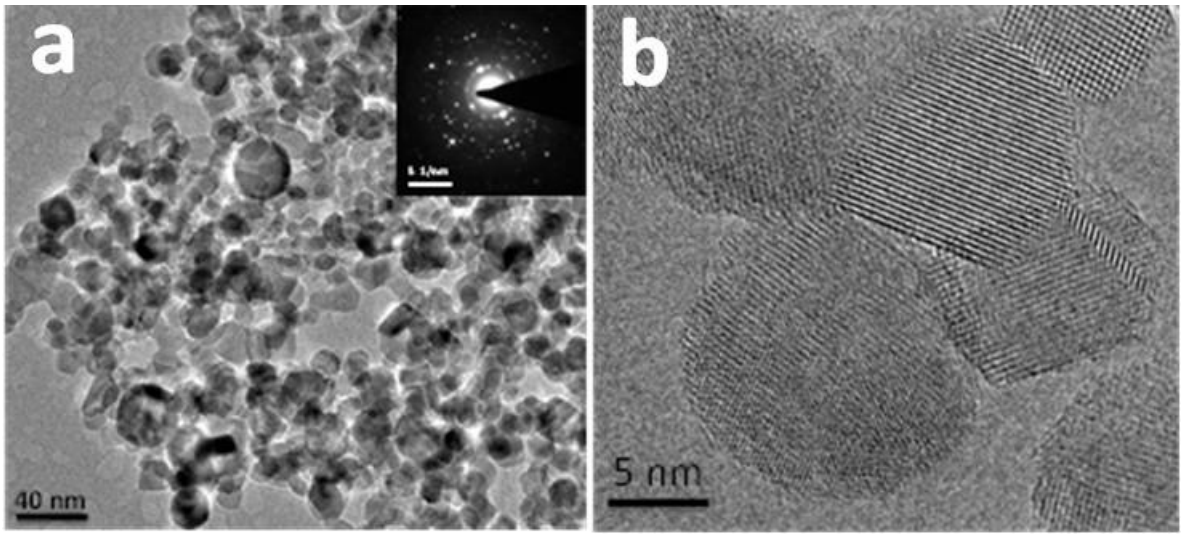


**Figure 7.12:** TEM and high resolution TEM for titanium dioxide nanoparticles synthesized using ethylene flame E4 ($\phi$ = 1.6 and Re = 13,142); (a) TEM with diffraction pattern in the top right inset and (b) HRTEM of the same particles.

Figure 7.13a shows TEM images of the $TiO_2$ nanoparticles generated from a propane flame at $\phi$ = 1.3 and Re = 13,694. The nanoparticles are of mixed morphology (spherical and polyhedral) and exhibit a size distribution similar to the ethylene flame shown in Fig. 7.12. The polyhedral morphology is not brookite but due to anatase and rutile phases only as confirmed in Chapters 5 and 6. The HRTEM micrograph (Fig. 7.13b) again exhibits high crystallinity and shows a square particle. The diffraction pattern (inset in Fig. 7.13a) shows a ring-type pattern related to anatase and rutile phases. Figure 7.14 shows TEM and HRTEM images of the $TiO_2$ nanoparticles generated from a propane flame at $\phi$ = 1.8 and Re = 7,790. The particles are very similar to that prepared using ethylene flame. The degree of agglomeration of these nanoparticles is comparable to commercially available $TiO_2$ nanoparticles (e.g. Evonik P25 ~70% anatase) [218].

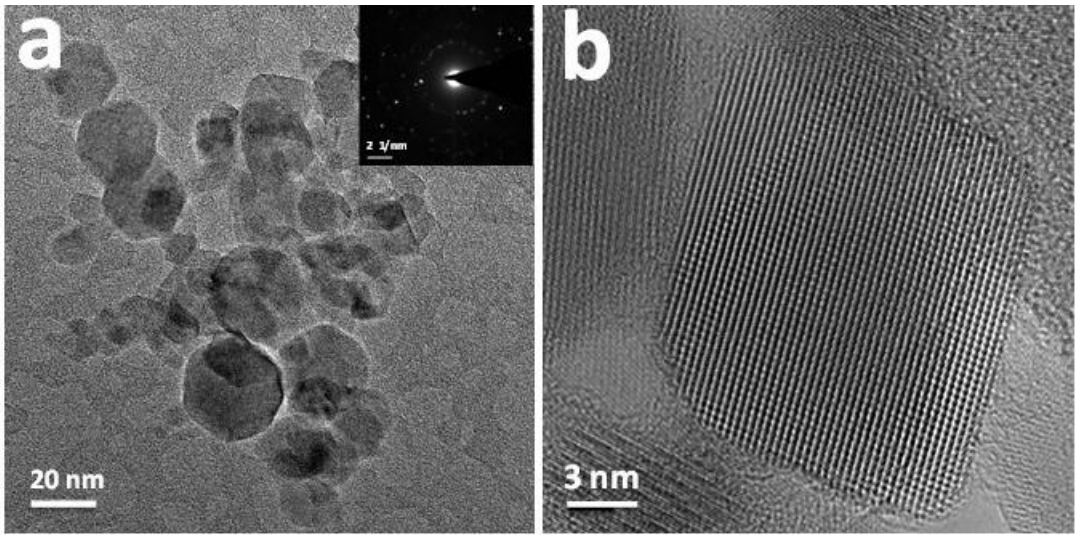


**Figure 7.13.** TEM and high resolution TEM for titanium dioxide nanoparticles synthesized using propane flame P2 ($\phi$ = 1.3 and Re = 13,694); (a) TEM with diffraction pattern in the top right inset and (b) HRTEM of one rectangular nanoparticle.

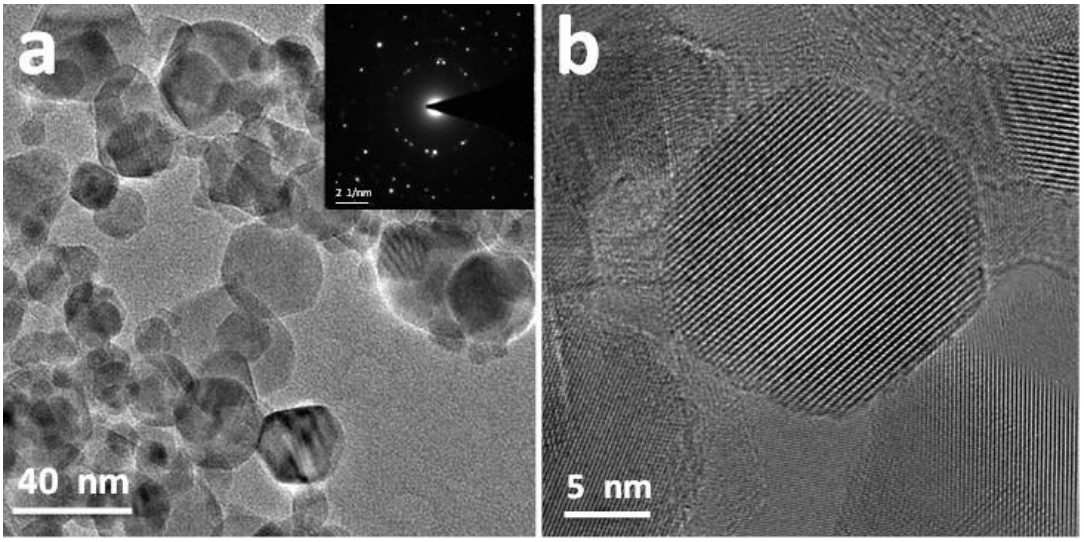


**Figure 7.14.** TEM and high resolution TEM for titanium dioxide nanoparticles synthesized using methane flame M3 ($\phi$ = 1.8 and Re = 7,790); (a) TEM with diffraction pattern in the top right inset and (b) HRTEM of one rectangular nanoparticle.

One of the most important properties of nanomaterial is its optical properties which can be measured using the UV-vis technique. Optical properties indicate the ability of the material to absorb visible light (highest ratio in solar radiation) for photocatalytic applications. Figure 7.15 displays the UV-vis absorption spectrum of some selected cases (operating conditions in Table 7.1) compared to the commercial P25 nanoparticles. P25 nanoparticles exhibited an absorption edge rising toward the UV region below 400 nm, which could be attributed to the anatase band-gap excitation (3.2 eV), without absorption in visible region (>400 nm). Compared to the P25 nanoparticles, all particles prepared by the DS-CWJ burner exhibited enhancement of light absorbance.

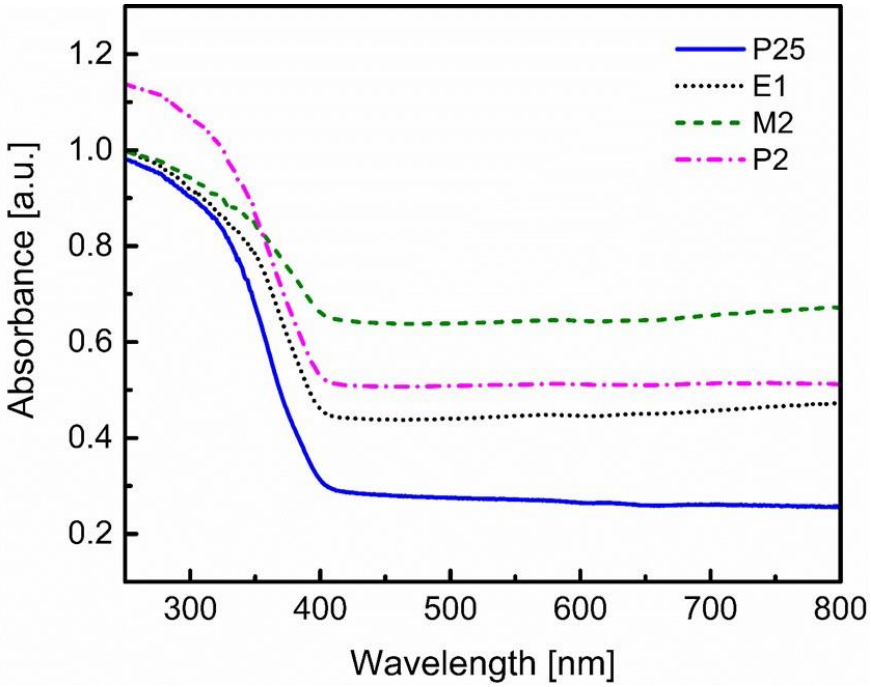


**Figure 7.15:** Comparison between UV-vis results of $TiO_2$ nanoparticles prepared using different fuels.

## 7.5 Concluding Remarks

The usefulness of the double-slit curved-wall jet (DS-CWJ) burner for materials synthesis of nanoparticles has been demonstrated. The growth of $TiO_2$ nanoparticles has been reported and the key points being the following:

1) The DS-CWJ burner stabilized premixed flames which are characterized with a flow field. This flow field consisted of a wall-jet region leading to a recirculation zone through flow separation, an interaction jet region, resulting from the collision of annular-inward jets, followed by a merged-jet region. This burner can be operated at a wide range of equivalence ratios and flow rates, exhibiting favorable combustion characteristics for material synthesis. PIV and OH-PLIF data confirmed these features and the precursor flow had little impact on the flame behavior.
2) The crystal phase of the $TiO_2$ nanoparticles was strongly dependent on the equivalence ratio and fuel type. The anatase content was proportional to the equivalence ratio for

ethylene and methane flames and was inversely proportional to it in the case of propane flames. The size of the particles depends on the equivalence ratio, due to an increase in the flame temperature. As the flame temperature increased, the growth of larger nanoparticles was observed.

3) Based on TEM imaging, $TiO_2$ nanoparticles exhibit a size range of 5-30 nm, which can be attributed to radial variation in the velocity field that results in an uneven residence time in the high temperature region.

# Chapter 8

# Conclusion and Future Work

Titanium dioxide ($TiO_2$) is an important semiconducting metal oxide and is expected to play an important role in future applications related to environment and energy sectors, especially for photocatalysis and hydrogen generation applications. Various flame configurations have been used in this study covering non-premixed, premixed, laminar, and turbulent flame configurations. The aim of the study is to use existing types of burners (multiple diffusion flames and FSP) to prepare functional nanomaterials for catalysis and photocatalysis applications, as well as introducing a new burner (curved wall-jet burner) that can be used for large scale production to the flame synthesis community. In this chapter, we will start with the summary and conclusions from all the flame types used in the study. Then we will finalize the chapter with some ideas for the future work related to our study.

## 8.1 Summary and Conclusions

### 8.1.1 Multiple diffusion flames

Multiple diffusion flames were utilized to synthesize $TiO_2$ nanoparticles containing C, Fe, Si, and V in a single-step flame synthesis process. The growth of carbon-coated (C-$TiO_2$), carbon-coated with iron oxide (Fe/C-$TiO_2$), silica-coated (Si-$TiO_2$) and vanadium-doped (V-$TiO_2$) $TiO_2$ nanoparticles was demonstrated. XRD and Raman data confirmed that coating $TiO_2$ NP with carbon and the addition of iron does not have a significant effect on the anatase content (~90% anatase), whereas adding Si decreases the anatase content by ~10%. The addition of vanadium substantially changes the anatase phase to rutile (~29% anatase). A graphitic carbon layer with thickness of 3 to 5 nm was coated on $TiO_2$ nanoparticles for C-$TiO_2$. Adding iron to

the sample (Fe/C-$TiO_2$) increases the carbon layer and small iron oxide nanoparticles were observed. TGA result showed that complete oxidation of carbon occurs at a temperature of 470$^o$C (iron based sample) compared to 610$^o$C (without iron) indicating the catalytic effect of iron based sample. XPS confirms the formation of $Fe^{3+}$ oxidation state of iron. With regards to Si-$TiO_2$ nanoparticles, a uniform coating of 3 to 8 nm of $SiO_2$ was observed around the $TiO_2$ particles. This coating can be attributed to the differences in the chemical reaction rates of the precursors. Finally, with regards to V-$TiO_2$, vanadium is doped within the $TiO_2$ nanoparticles, as observed from HRTEM, and XPS further confirms the formation of $V^{4+}$ and $V^{5+}$ oxidation states of vanadium.

### 8.1.2 Flame Spray pyrolysis (FSP)

Flame spray pyrolysis (FSP) system was utilized to synthesize pure $TiO_2$ and Fe-doped $TiO_2$ nanoparticles with various iron concentrations in a single-step flame synthesis process. XRD, Raman, and BET data confirmed that anatase phase was dominant in pure $TiO_2$ nanoparticles (> 90% anatase) with an average particle diameter of 10 nm. The addition of iron substantially changes the anatase phase to rutile with anatase percentage changing from 86% to 21% when changing the iron concentration in the sample from 1% to 10%, respectively. XPS confirmed the formation of $Ti^{4+}$ and $Ti^{3+}$ oxidation states of Ti, which are signature of $TiO_2$ material. $Fe^{3+}$ and $Fe^{2+}$ were also confirmed. Increasing the percentage of the Fe dopant led to the increase of the $Fe^{3+}/Fe^{2+}$ ratio from 0.5 at 3% Fe-$TiO_2$ to 1.8 at 10% Fe-$TiO_2$ sample. Morphology of the generated nanoparticles using HRTEM revealed the crystallinity of spherical particles with information about phase change in agreement with XRD and Raman results. It was noticed also that the valence band edge from Fe-doped $TiO_2$ is shifted by ~1 eV to lower binding energy compared to undoped $TiO_2$, which enhances visible light absorption of the doped samples as confirmed from UV-vis results. Regarding to the magnetic properties, iron doping enhances

the magnetic properties of $TiO_2$ nanoparticles and changing them to paramagnetic materials. In summary, doping $TiO_2$ nanoparticles with iron enhances the magnetic and optical properties of the materials making it a very good candidate for photocatalysis applications.

### 8.1.3 Curved wall-jet (CWJ) burner

The usefulness of the CWJ burner for materials synthesis of nanoparticles has been demonstrated. The growth of both $TiO_2$ and $SiO_2$ nanoparticles has been reported, the key points being the following:

1) The CWJ burner can operate at a wide range of equivalence ratios and was found to exhibit small size turbulent flame characteristics. PIV data confirmed this behavior and the precursor flow had little impact on the flame behavior.
2) The crystal phase of the $TiO_2$ nanoparticles was strongly dependent on the equivalence ratio. At higher values, due to a longer residence time in high temperature region, the growth of anatase nanoparticle was dominant. At $\phi = 1.56$, the growth of almost pure anatase (96%) was demonstrated. The size of the particles depended on the equivalence ratio, due to an increase in the flame temperature. As the flame temperature increased, the growth of larger nanoparticles was observed.
3) Based on TEM imaging, both $TiO_2$ and $SiO_2$ nanoparticles exhibit a bimodal size distribution, which can be attributed to radial variation in the velocity field that results in an uneven residence time in the high temperature region.

By changing the precursor flow rate, the surface area and particle size of the $SiO_2$ nanoparticles could be controlled. The diameter of the $SiO_2$ nanoparticles based on BET varied from 11 nm (240 $m^2/g$) to 18 nm (151 $m^2/g$).

### 8.1.4 Curved wall-jet burner with poppet valve

The usefulness of the curved-wall jet (CWJ) burner with a poppet valve shaped guide on top of the central port has been demonstrated for material synthesis of nanoparticles. The growth of $TiO_2$ nanoparticles has been reported with some key points affecting this growth.

1) The CWJ burner can operate at a wide range of equivalence ratios and was found to exhibit small size turbulent flame characteristics. PIV data confirmed this behavior and the precursor flow had little impact on the flame behavior.
2) The crystal phase of the $TiO_2$ nanoparticles was strongly dependent on the equivalence ratio. At higher values, due to a longer residence time in high temperature region, the growth of anatase nanoparticles was dominant.
3) This configuration of the CWJ burner has a narrow range of particle size distribution (18-25 nm) with aggregation ratio of 3.6, which showed better results as compared with the original CWJ burner.

### 8.1.5 Double-slit curved wall-jet burner

The usefulness of the double-slit curved wall-jet (DS-CWJ) burner for materials synthesis of nanoparticles has been demonstrated. The growth of $TiO_2$ nanoparticles has been reported and the key points being the following:

1) The DS-CWJ burner stabilized premixed flames which are characterized with a flow field. This flow field consisted of a wall-jet region leading to a recirculation zone through flow separation, an interaction jet region, resulting from the collision of annular-inward jets, followed by a merged-jet region. This burner can be operated at a wide range of equivalence ratios and flow rates, exhibiting favorable combustion characteristics for

material synthesis. PIV and OH-PLIF data confirmed these features and the precursor flow had little impact on the flame behavior.

2) The crystal phase of the $TiO_2$ nanoparticles was strongly dependent on the equivalence ratio and fuel type. The anatase content was proportional to the equivalence ratio for ethylene and methane flames and was inversely proportional to it in the case of propane flames. The size of the particles depends on the equivalence ratio, due to an increase in the flame temperature. As the flame temperature increased, the growth of larger nanoparticles was observed.
3) Based on TEM imaging, $TiO_2$ nanoparticles exhibit a size range of 5-30 nm, which can be attributed to radial variation in the velocity field that results in an uneven residence time in the high temperature region.

## 8.2 Recommendations for Future Work

Nanomaterial synthesis is a very hot topic in the current research due to the huge number of applications related to the generated nanomaterials. Fame spray pyrolysis can be used to prepare advanced materials and composites. First, FSP can be used to prepare bismuth-molybdate ($Bi_2MoO_6$) for catalytic oxidation. Second, cerium oxides ($CeO_2$) doped with different metals (Fe, V, and Mo) can be prepared and used for soot oxidation. Last but not least, many special elements such as yttrium (Y), antimony (Sb), zirconium (Zr), and tantalum (Ta) can be used for doping $TiO_2$ nanoparticles can be synthesized using FSP technique. These prepared nanoparticles can be used for large scale production of dye-synthesized solar cells.

In this study, we have used the curved wall-jet (CWJ) burner with three configurations. A fourth configuration can be proposed using spray-CWJ burner. This new configuration will combine the advantages of two systems. It will have rapid mixing and short flames (from the CWJ configuration), as well as large scale production and using of more dense and cheaper

precursors (from FSP system). The spray system to be used with CWJ burner can use pressurized or air-assisted atomizers. This system will be easy for the generation of pure, composites, and functional nanomaterials with large scale production. A detailed numerical simulation for the CWJ burner is needed to understand the fundamentals of combustion and material synthesis processes using this system.

# REFERENCES


[1] G. Cao, Nanostructures and Nanomaterials: Synthesis, Properties and Applications, Imperial College Press, London, 2004.

[2] M. Ni, M.K. Leung, D.Y. Leung, K. Sumathy, A review and recent developments in photocatalytic water-splitting using $TiO_2$ for hydrogen production, Renewable and Sustainable Energy Reviews, 11 (2007) 401-425.

[3] S. Ahmed, A. Du Pasquier, T. Asefa, D.P. Birnie, Improving Microstructured $TiO_2$ Photoanodes for Dye Sensitized Solar Cells by Simple Surface Treatment, Advanced Energy Materials, 1 (2011) 879-887.

[4] T. Ochiai, T. Hoshi, H. Slimen, K. Nakata, T. Murakami, H. Tatejima, Y. Koide, A. Houas, T. Horie, Y. Morito, Fabrication of a $TiO_2$ nanoparticles impregnated titanium mesh filter and its application for environmental purification, Catalysis Science & Technology, 1 (2011) 1324-1327.

[5] B. Schimmoeller, S.E. Pratsinis, A. Baiker, Flame aerosol synthesis of metal oxide catalysts with unprecedented structural and catalytic properties, ChemCatChem, 3 (2011) 1234-1256.

[6] Y. Gil, H. Jung, S. Chung, Premixed flame stabilization in an axisymmetric curved-wall jet, Combust. Flame, 113 (1998) 348-357.

[7] D. Kim, Y. Gil, T. Chung, S. Chung, Characteristics of Premixed Flames Stabilized in an Axisymmetric Curved-Wall Jet Burner with Tip Modification, Combust. Sci. Technol., 181 (2009) 1397-1412.

[8] S. Pratsinis, History of manufacture of fine particles in high-temperature aerosol reactors, Aerosol science and technology: History and reviews, RTI international, USA, (2011) 475-507.

[9] R. Strobel, S.E. Pratsinis, Flame aerosol synthesis of smart nanostructured materials, J. Mater. Chem., 17 (2007) 4743-4756.

[10] N.K. Memon, B.H. Kear, S.D. Tse, Transition between graphene-film and carbon-nanotube growth on Nickel alloys in open-atmosphere flame synthesis, Chem. Phys. Lett., 570 (2013) 90-94.

[11] N.K. Memon, S.D. Tse, M. Chhowalla, B.H. Kear, Role of substrate, temperature, and hydrogen on the flame synthesis of graphene films, Proceedings of the Combustion Institute, 34 (2013) 2163-2170.

[12] L. Sang, Y. Zhao, C. Burda, $TiO_2$ Nanoparticles as Functional Building Blocks, Chem. Rev., 114 (2014) 9283-9318.

[13] A. Fujishima, K. Honda, Electrochemical Photolysis of Water at a Semiconductor Electrode, Nature, 238 (1972) 37-38.

[14] H. Tributsch, Reaction of excited chlorophyll molecules at electrodes and in photosynthesis, Photochem. Photobiol., 16 (1972) 261-269.

[15] D. Dambournet, I. Belharouak, K. Amine, Tailored Preparation Methods of $TiO_2$ Anatase, Rutile, Brookite: Mechanism of Formation and Electrochemical Properties, Chem. Mater., 22 (2010) 1173-1179.

[16] D. Reyes-Coronado, G. Rodriguez-Gattorno, M. Espinosa-Pesqueira, C. Cab, R. De Coss, G. Oskam, Phase-pure $TiO_2$ nanoparticles: anatase, brookite and rutile, Nanotechnology, 19 (2008) 145605.

[17] E. Dickinson, Scale-Dominant Mechanisms in Nanomaterials, Nanomaterials: Mechanics and Mechanisms, (2009) 215.

[18] G. Ulrich, B. Milnes, N. Subramanian, Particle growth in flames. II: Experimental results for silica particles, (1976).

[19] M.T. Swihart, Vapor-phase synthesis of nanoparticles, Current Opinion in Colloid & Interface Science, 8 (2003) 127-133.

[20] K. Wegner, B. Walker, S. Tsantilis, S.E. Pratsinis, Design of metal nanoparticle synthesis by vapor flow condensation, Chem. Eng. Sci., 57 (2002) 1753-1762.

[21] K. Nakaso, M. Shimada, K. Okuyama, K. Deppert, Evaluation of the change in the morphology of gold nanoparticles during sintering, J. Aerosol Sci, 33 (2002) 1061-1074.

[22] K. Nanda, F. Kruis, H. Fissan, M. Acet, Band-gap tuning of PbS nanoparticles by in-flight sintering of size classified aerosols, J. Appl. Phys., 91 (2002) 2315-2321.

[23] A. Maisels, F.E. Kruis, H. Fissan, B. Rellinghaus, H. Zähres, Synthesis of tailored composite nanoparticles in the gas phase, Appl. Phys. Lett., 77 (2000) 4431-4433.

[24] T. Ohno, Morphology of composite nanoparticles of immiscible binary systems prepared by gas-evaporation technique and subsequent vapor condensation, J. Nanopart. Res., 4 (2002) 255-260.

[25] Y. Nakata, J. Muramoto, T. Okada, M. Maeda, Particle dynamics during nanoparticle synthesis by laser ablation in a background gas, J. Appl. Phys., 91 (2002) 1640-1643.

[26] W. Marine, L. Patrone, B. Luk'Yanchuk, M. Sentis, Strategy of nanocluster and nanostructure synthesis by conventional pulsed laser ablation, Appl. Surf. Sci., 154 (2000) 345-352.

[27] A. Harano, K. Shimada, T. Okubo, M. Sadakata, Crystal phases of $TiO_2$ ultrafine particles prepared by laser ablation of solid rods, J. Nanopart. Res., 4 (2002) 215-219.

[28] T. Makimura, T. Mizuta, K. Murakami, Laser ablation synthesis of hydrogenated silicon nanoparticles with green photoluminescence in the gas phase, Japanese journal of applied physics, 41 (2002) L144.

[29] S. Shinde, S. Kulkarni, A. Banpurkar, R. Nawathey-Dixit, S. Date, S. Ogale, Magnetic properties of nanosized powders of magnetic oxides synthesized by pulsed laser ablation, J. Appl. Phys., 88 (2000) 1566-1575.

[30] A.P. Weber, M. Seipenbusch, G. Kasper, Application of aerosol techniques to study the catalytic formation of methane on gasborne nickel nanoparticles, The Journal of Physical Chemistry A, 105 (2001) 8958-8963.

[31] E.F. Rexer, D.B. Wilbur, J.L. Mills, R.L. DeLeon, J.F. Garvey, Production of metal oxide thin films by pulsed arc molecular beam deposition, Rev. Sci. Instrum., 71 (2000) 2125-2130.

[32] F. Urban Iii, A. Hosseini-Tehrani, P. Griffiths, A. Khabari, Y.-W. Kim, I. Petrov, Nanophase films deposited from a high-rate, nanoparticle beam, Journal of Vacuum Science & Technology B, 20 (2002) 995-999.

[33] M.H. Magnusson, K. Deppert, J.-O. Malm, Single-crystalline tungsten nanoparticles produced by thermal decomposition of tungsten hexacarbonyl, J. Mater. Res., 15 (2000) 1564-1569.

[34] A.G. Nasibulin, O. Richard, E.I. Kauppinen, D.P. Brown, J.K. Jokiniemi, I.S. Altman, Nanoparticle synthesis by copper (II) acetylacetonate vapor decomposition in the presence of oxygen, Aerosol Science & Technology, 36 (2002) 899-911.

[35] M.L. Ostraat, J.W. De Blauwe, M.L. Green, L.D. Bell, H.A. Atwater, R.C. Flagan, Ultraclean two-stage aerosol reactor for production of oxide-passivated silicon nanoparticles for novel memory devices, J. Electrochem. Soc., 148 (2001) G265-G270.

[36] R. Schmechel, M. Kennedy, H. Von Seggern, H. Winkler, M. Kolbe, R. Fischer, L. Xaomao, A. Benker, M. Winterer, H. Hahn, Luminescence properties of nanocrystalline $Y_2O_3$: $Eu^{3+}$ in different host materials, J. Appl. Phys., 89 (2001) 1679-1686.

[37] R.A. Senter, Y. Chen, J.L. Coffer, L.R. Tessler, Synthesis of silicon nanocrystals with erbium-rich surface layers, Nano Lett., 1 (2001) 383-386.

[38] V.V. Srdić, M. Winterer, A. Möller, G. Miehe, H. Hahn, Nanocrystalline Zirconia Surface-Doped with Alumina: Chemical Vapor Synthesis, Characterization, and Properties, J. Am. Ceram. Soc., 84 (2001) 2771-2776.

[39] S.H. Ehrman, M.I. Aquino-Class, M.R. Zachariah, Effect of temperature and vapor-phase encapsulation on particle growth and morphology, J. Mater. Res., 14 (1999) 1664-1671.

[40] E. Borsella, S. Botti, M. Cesile, S. Martelli, A. Nesterenko, P. Zappelli, $MoS_2$ nanoparticles produced by laser induced synthesis from gaseous precursors, J. Mater. Sci. Lett., 20 (2001) 187-191.

[41] Y. Kamlag, A. Goossens, I. Colbeck, J. Schoonman, Laser CVD of cubic SiC nanocrystals, Appl. Surf. Sci., 184 (2001) 118-122.

[42] G. Ledoux, D. Amans, J. Gong, F. Huisken, F. Cichos, J. Martin, Nanostructured films composed of silicon nanocrystals, Materials Science and Engineering: C, 19 (2002) 215-218.

[43] J. Heberlein, O. Postel, S. Girshick, P. McMurry, W. Gerberich, D. Iordanoglou, F. Di Fonzo, D. Neumann, A. Gidwani, M. Fan, Thermal plasma deposition of nanophase hard coatings, Surf. Coat. Technol., 142 (2001) 265-271.

[44] P.P. Ahonen, J. Joutsensaari, O. Richard, U. Tapper, D.P. Brown, J.K. Jokiniemi, E.I. Kauppinen, Mobility size development and the crystallization path during aerosol decomposition synthesis of $TiO_2$ particles, J. Aerosol Sci, 32 (2001) 615-630.

[45] J.H. Kim, T.A. Germer, G.W. Mulholland, S.H. Ehrman, Size-monodisperse metal nanoparticles via hydrogen-free spray pyrolysis, Adv. Mater., 14 (2002) 518.

[46] D. Sarigiannis, J.D. Peck, G. Kioseoglou, A. Petrou, T. Mountziaris, Characterization of vapor-phase-grown ZnSe nanoparticles, Appl. Phys. Lett., 80 (2002) 4024-4026.

[47] W.Y. Teoh, R. Amal, L. Mädler, Flame spray pyrolysis: An enabling technology for nanoparticles design and fabrication, Nanoscale, 2 (2010) 1324-1347.

[48] H.K. Kammler, L. Madler, S.E. Pratsinis, Flame synthesis of nanoparticles, Chem Eng Technol, 24 (2001) 583-596.

[49] G. Ulrich, Flame synthesis of fine particles, Chem. Eng. News, 62 (1984) 22-29.

[50] S. Vemury, S.E. Pratsinis, Self-preserving size distributions of agglomerates, J. Aerosol Sci, 26 (1995) 175-185.

[51] M.S. Wooldridge, Gas-phase combustion synthesis of particles, Prog. Energy Combust. Sci., 24 (1998) 63-87.

[52] B. Zhao, K. Uchikawa, J.R. McCormick, C.Y. Ni, J.G. Chen, H. Wang, Ultrafine anatase $TiO_2$ nanoparticles produced in premixed ethylene stagnation flame at 1 atm, Proceedings of the Combustion Institute, 30 (2005) 2569-2576.

[53] S.E. Pratsinis, W.H. Zhu, S. Vemury, The role of gas mixing in flame synthesis of titania powders, Powder Technol, 86 (1996) 87-93.

[54] N.K. Memon, D.H. Anjum, S.H. Chung, Multiple-diffusion flame synthesis of pure anatase and carbon-coated titanium dioxide nanoparticles, Combustion and Flame, 160 (2013) 1848-1856.

[55] S.E. Pratsinis, Flame aerosol synthesis of ceramic powders, Prog. Energy Combust. Sci., 24 (1998) 197-219.

[56] L. Mädler, W. Stark, S. Pratsinis, Flame-made ceria nanoparticles, J. Mater. Res, 17 (2002) 1356-1362.

[57] S. Girshick, C.-P. Chiu, Homogeneous nucleation of particles from the vapor phase in thermal plasma synthesis, Plasma Chem. Plasma Process., 9 (1989) 355-369.

[58] K.A. Snail, C.J. Craigie, Synthesis of high quality diamond films in a turbulent flame, Appl. Phys. Lett., 58 (1991) 1875-1877.

[59] K. Snail, R. Vardiman, J. Estrera, J. Glesener, C. Merzbacher, C. Craigie, C. Marks, R. Glosser, J. Freitas Jr, Diamond growth in turbulent oxygen-acetylene flames, J. Appl. Phys., 74 (1993) 7561-7571.

[60] Y. Xiong, S.E. Pratsinis, Gas phase production of particles in reactive turbulent flows, J. Aerosol Sci, 22 (1991) 637-655.

[61] W.J. Stark, S.E. Pratsinis, Aerosol flame reactors for manufacture of nanoparticles, Powder Technol., 126 (2002) 103-108.

[62] L. Mädler, H. Kammler, R. Mueller, S. Pratsinis, Controlled synthesis of nanostructured particles by flame spray pyrolysis, J. Aerosol Sci, 33 (2002) 369-389.

[63] R. Strobel, S.E. Pratsinis, Direct synthesis of maghemite, magnetite and wustite nanoparticles by flame spray pyrolysis, Adv. Powder Technol., 20 (2009) 190-194.

[64] F. Iskandar, Nanoparticle processing for optical applications – A review, Adv. Powder Technol., 20 (2009) 283-292.

[65] M. Sokolowski, A. Sokolowska, A. Michalski, B. Gokieli, The "in-flame-reaction" method for $Al_2O_3$ aerosol formation, J. Aerosol Sci, 8 (1977) 219-230.

[66] H. Liang, Z. Wang, Facile synthesis and photocatalytic activity of cocoon-like hollow hematite nanostructures, Mater. Lett., 96 (2013) 12-15.

[67] M.J. Height, L. Mädler, S.E. Pratsinis, F. Krumeich, Nanorods of ZnO made by flame spray pyrolysis, Chem. Mater., 18 (2006) 572-578.

[68] T. Hinklin, B. Toury, C. Gervais, F. Babonneau, J. Gislason, R. Morton, R. Laine, Liquid-feed flame spray pyrolysis of metalloorganic and inorganic alumina sources in the production of nanoalumina powders, Chem. Mater., 16 (2004) 21-30.

[69] J. Marchal, T. John, R. Baranwal, T. Hinklin, R.M. Laine, Yttrium aluminum garnet nanopowders produced by liquid-feed flame spray pyrolysis (LF-FSP) of metalloorganic precursors, Chem. Mater., 16 (2004) 822-831.

[70] J.A. Azurdia, J. Marchal, P. Shea, H. Sun, X.Q. Pan, R.M. Laine, Liquid-Feed Flame Spray Pyrolysis as a Method of Producing Mixed-Metal Oxide Nanopowders of Potential Interest as Catalytic Materials. Nanopowders along the $NiO-Al_2O_3$ Tie Line Including $(NiO)_{0.22}(Al_2O_3)_{0.78}$, a New Inverse Spinel Composition, Chem. Mater., 18 (2006) 731-739.

[71] R. Strobel, A. Baiker, S.E. Pratsinis, Aerosol flame synthesis of catalysts, Adv. Powder Technol., 17 (2006) 457-480.

[72] A. Gurav, T. Kodas, T. Pluym, Y. Xiong, Aerosol Processing of Materials, Aerosol Sci. Technol., 19 (1993) 411-452.

[73] A.B.D. Nandiyanto, K. Okuyama, Progress in developing spray-drying methods for the production of controlled morphology particles: From the nanometer to submicrometer size ranges, Adv. Powder Technol., 22 (2011) 1-19.

[74] G.L. Messing, S.C. Zhang, G.V. Jayanthi, Ceramic powder synthesis by spray pyrolysis, J. Am. Ceram. Soc., 76 (1993) 2707-2726.

[75] L. Mädler, Liquid-fed aerosol reactors for one-step synthesis of nano-structured particles, Kona, 22 (2004) 107-120.

[76] K. Bray, Turbulent flows with premixed reactants, in: Turbulent reacting flows, Springer, 1980, pp. 115-183.

[77] B. Choi, S. Chung, An experimental study on turbulent lifted flames of methane in coflow jets at elevated temperatures, Fuel, 103 (2013) 956-962.

[78] J. Kim, S. Won, M. Shin, S. Chung, Numerical simulation of oscillating lifted flames in coflow jets with highly diluted propane, Proceedings of the Combustion Institute, 29 (2002) 1589-1595.

[79] R. Cheng, Velocity and scalar characteristics of premixed turbulent flames stabilized by weak swirl, Combust. Flame, 101 (1995) 1-14.

[80] G. Pilla, D. Galley, D.A. Lacoste, F. Lacas, D. Veynante, C.O. Laux, Stabilization of a turbulent premixed flame using a nanosecond repetitively pulsed plasma, Plasma Science, IEEE Transactions on, 34 (2006) 2471-2477.

[81] R. Balachandran, B.O. Ayoola, C.F. Kaminski, A.P. Dowling, E. Mastorakos, Experimental investigation of the nonlinear response of turbulent premixed flames to imposed inlet velocity oscillations, Combust. Flame, 143 (2005) 37-55.

[82] R. Cheng, I. Shepherd, The influence of burner geometry on premixed turbulent flame propagation, Combust. Flame, 85 (1991) 7-26.

[83] A. George, R. Murley, E. Place, Formation of $TiO_2$ aerosol from the combustion supported reaction of $TiCl_4$ and $O_2$, in: Faraday Symposia of the Chemical Society, Royal Society of Chemistry, 1973, pp. 63-71.

[84] M. Formenti, F. Juillet, P. Meriaudeau, S.J. Teichner, P. Vergnon, Preparation in a hydrogen-oxygen flame of ultrafine metal oxide particles. Oxidative properties toward hydrocarbons in the presence of ultraviolet radiation, J. Colloid Interface Sci., 39 (1972) 79-89.

[85] W. Zhang, S. Xue, X. Hongyong, Preparation of nano-titanium dioxide in propane/air diffusion flame, The Chinese Journal of Process Engineering, 4 (2004) 509-514.

[86] M.A. Ismail, N.K. Memon, M.S. Mansour, D.H. Anjum, S.H. Chung, Curved wall-jet burner for synthesizing titania and silica nanoparticles, Proceedings of the Combustion Institute, 35 (2015) 2267-2274.

[87] H. Xie, G. Gao, Z. Tian, N. Bing, L. Wang, Synthesis of $TiO_2$ nanoparticles by propane/air turbulent flame CVD process, Particuology, 7 (2009) 204-210.

[88] D. Florescu, I. Florescu, F. NEDELCUȚ, I. Nedelcu, Fuselage Airstream Simulation for a Coandă UAV, Review, (2010) 83.

[89] H.M. Coandă, Procédé de propulsion dans un fluide, in: B.d.i. France (Ed.), 1932.

[90] M.S. Mansour, S.H. Chung, Turbulent nonpremixed flames stabilized on double-slit curved wall-jet (CWJ) burner with simultaneous OH-PLIF and PIV measurements, Combust. Sci. Technol., 187 (2015) 1408-1424.

[91] R.J. Adrian, Twenty years of particle image velocimetry, Exp. Fluids, 39 (2005) 159-169.

[92] J. Westerweel, Fundamentals of digital particle image velocimetry, Meas. Sci. Technol., 8 (1997) 1379.

[93] A.C. Eckbreth, Laser diagnostics for combustion temperature and species, CRC Press, 1996.

[94] R.K. Hanson, Planar laser-induced fluorescence imaging, J. Quant. Spectrosc. Radiat. Transfer, 40 (1988) 343-362.

[95] R.K. Hanson, J.M. Seitzman, P.H. Paul, Planar laser-fluorescence imaging of combustion gases, Appl. Phys. B, 50 (1990) 441-454.

[96] W.H. Miller, A Treatise on Crystallography, For J. & J. J. Deighton, 1839.

[97] M. Eckert, Max von Laue and the discovery of X-ray diffraction in 1912, Annalen der Physik, 524 (2012) A83-A85.

[98] W. Bragg, W. Bragg, The reflection of X-rays by crystals, Proceedings of the Royal Society of London. Series A, Containing Papers of a Mathematical and Physical Character, (1913) 428-438.

[99] C. Hammond, The basics of crystallography and diffraction, 3rd ed., Oxford University Press Oxford, 2009.

[100] I.R. Lewis, H. Edwards, Handbook of Raman spectroscopy: from the research laboratory to the process line, CRC Press, 2001.

[101] G. Gouadec, P. Colomban, Raman Spectroscopy of nanomaterials: How spectra relate to disorder, particle size and mechanical properties, Prog. Cryst. Growth Charact. Mater., 53 (2007) 1-56.

[102] D.B. Williams, C.B. Carter, The transmission electron microscope, Springer, 1996.

[103] R. Egerton, Physical principles of electron microscopy: an introduction to TEM, SEM, and AEM, Springer Science & Business Media, 2006.

[104] R.F. Egerton, Electron energy-loss spectroscopy in the electron microscope, 3rd ed., Springer, New York, 2011.

[105] S. Brunauer, P.H. Emmett, E. Teller, Adsorption of Gases in Multimolecular Layers, J. Am. Chem. Soc., 60 (1938) 309-319.

[106] www.Micromertics.com.

[107] J.D.J. Ingle, S.R. Crouch, Spectrochemical analysis, 1988.

[108] J.M. Coey, Magnetism and magnetic materials, Cambridge University Press, 2010.

[109] S. Zhu, W. Liu, S. Wei, C. Fan, Y. Li, Local Structure around Iron Ions in Anatase $TiO_2$, X-Ray Absorption Fine Structure--XAFS 13, 882 (2007) 253-255.

[110] Z. Wang, W. Wang, J. Tang, L. Spinu, W. Zhou, Extraordinary Hall effect and ferromagnetism in Fe-doped reduced rutile, Appl. Phys. Lett., 83 (2003) 518-520.

[111] A. Stefánsson, I. Gunnarsson, N. Giroud, New methods for the direct determination of dissolved inorganic, organic and total carbon in natural waters by Reagent-Free™ Ion

Chromatography and inductively coupled plasma atomic emission spectrometry, Anal. Chim. Acta, 582 (2007) 69-74.

[112] J. Mermet, Is it still possible, necessary and beneficial to perform research in ICP-atomic emission spectrometry?, J. Anal. At. Spectrom., 20 (2005) 11-16.

[113] H. Chen, C.E. Nanayakkara, V.H. Grassian, Titanium dioxide photocatalysis in atmospheric chemistry, Chem. Rev., 112 (2012) 5919-5948.

[114] E. Grabowska, J. Reszczyńska, A. Zaleska, Mechanism of phenol photodegradation in the presence of pure and modified-$TiO_2$: A review, Water Research, 46 (2012) 5453-5471.

[115] M. Grätzel, Photoelectrochemical cells, nature, 414 (2001) 338-344.

[116] A.L. Linsebigler, G. Lu, J.T. Yates Jr, Photocatalysis on $TiO_2$ surfaces: principles, mechanisms, and selected results, Chem. Rev., 95 (1995) 735-758.

[117] P.J.D. Lindan, N.M. Harrison, J.M. Holender, M.J. Gillan, First-principles molecular dynamics simulation of water dissociation on $TiO_2$ (110), Chem. Phys. Lett., 261 (1996) 246-252.

[118] P. Xu, Zeng, G.M., Huang, D.L., Feng, C.L., Hu, S., Zhao, M.H. Lai, C., Wei, Z., Huang, C., Xie, G.X., Use of iron oxide nanomaterials in wastewater treatment: a review, Science of the Total Environment, 424 (2012) 1-10.

[119] J. Song, J. Wang, A.L. Boehman, The role of fuel-borne catalyst in diesel particulate oxidation behavior, Combust. Flame, 146 (2006) 73-84.

[120] P. Legutko, P. Stelmachowski, M. Trębala, Z. Sojka, A. Kotarba, Role of Electronic Factor in Soot Oxidation Process Over Tunnelled and Layered Potassium Iron Oxide Catalysts, Top. Catal., 56 (2013) 489-492.

[121] H. Wang, J. Liu, Z. Zhao, Y. Wei, C. Xu, Comparative study of nanometric Co-, Mn- and Fe-based perovskite-type complex oxide catalysts for the simultaneous elimination of soot and $NO_x$ from diesel engine exhaust, Catal. Today, 184 (2012) 288-300.

[122] J. Xu, J. Liu, Z. Zhao, J. Zheng, G. Zhang, A. Duan, G. Jiang, Three-dimensionally ordered macroporous $LaCo_xFe_{1-x}O_3$ perovskite-type complex oxide catalysts for diesel soot combustion, Catal. Today, 153 (2010) 136-142.

[123] C. Rodriguez-Torres, A. Cabrera, L. Errico, C. Adan, F. Requejo, M. Weissmann, S. Stewart, Local structure and magnetic behaviour of Fe-doped $TiO_2$ anatase nanoparticles: experiments and calculations, J. Phys.: Condens. Matter, 20 (2008) 135210.

[124] Y. Matsumoto, M. Murakami, T. Shono, T. Hasegawa, T. Fukumura, M. Kawasaki, P. Ahmet, T. Chikyow, S.-y. Koshihara, H. Koinuma, Room-Temperature Ferromagnetism in Transparent Transition Metal-Doped Titanium Dioxide, Science, 291 (2001) 854-856.

[125] T.L. Thompson, J.T. Yates, Surface Science Studies of the Photoactivation of TiO2New Photochemical Processes, Chemical Reviews, 106 (2006) 4428-4453.

[126] C. Belver, R. Bellod, S.J. Stewart, F.G. Requejo, M. Fernández-García, Nitrogen-containing $TiO_2$ photocatalysts: Part 2. Photocatalytic behavior under sunlight excitation, Applied Catalysis B: Environmental, 65 (2006) 309-314.

[127] B. Tryba, A.W. Morawski, M. Inagaki, M. Toyoda, The kinetics of phenol decomposition under UV irradiation with and without $H_2O_2$ on $TiO_2$, Fe-$TiO_2$ and Fe-C-$TiO_2$ photocatalysts, Applied catalysis. B, Environmental, 63 (2006) 215-221.

[128] L. Deng, S. Wang, D. Liu, B. Zhu, W. Huang, S. Wu, S. Zhang, Synthesis, characterization of Fe-doped $TiO_2$ nanotubes with high photocatalytic activity, Catal. Lett., 129 (2009) 513-518.

[129] K. Tiefenthaler, W. Lukosz, Sensitivity of grating couplers as integrated-optical chemical sensors, JOSA B, 6 (1989) 209-220.

[130] A. Fujishima, Electrochemical photolysis of water at a semiconductor electrode, Nature, 238 (1972) 37-38.

[131] A. Mills, S. Le Hunte, An overview of semiconductor photocatalysis, Journal of photochemistry and photobiology A: Chemistry, 108 (1997) 1-35.

[132] M. Grätzel, Artificial photosynthesis: Water cleavage into hydrogen and oxygen by visible light, Acc. Chem. Res., 14 (1981) 376-384.

[133] M. Yoshida, P.N. Prasad, Sol-gel-processed $SiO_2$/$TiO_2$/poly (vinylpyrrolidone) composite materials for optical waveguides, Chem. Mater., 8 (1996) 235-241.

[134] X. Nie, S. Zhuo, G. Maeng, K. Sohlberg, Doping of $TiO_2$ Polymorphs for Altered Optical and Photocatalytic Properties, International Journal of Photoenergy, 2009 (2009).

[135] A. Teleki, Suter, M.,Kidambi, P.R., Ergeneman, O., Krumeich, F., Nelson, B.J., Pratsinis, S.E., Hermetically coated superparamagnetic $Fe_2O_3$ particles with $SiO_2$ nanofilms, Chem. Mater., 21 (2009) 2094-2100.

[136] A. Teleki, S. Pratsinis, K. Wegner, R. Jossen, F. Krumeich, Flame-coating of titania particles with silica, J. Mater. Res., 20 (2005) 1336-1347.

[137] B. Tian, C. Li, F. Gu, H. Jiang, Y. Hu, J. Zhang, Flame sprayed V-doped $TiO_2$ nanoparticles with enhanced photocatalytic activity under visible light irradiation, Chem. Eng. J., 151 (2009) 220-227.

[138] W.J. Stark, K. Wegner, S.E. Pratsinis, A. Baiker, Flame aerosol synthesis of vanadia–titania nanoparticles: Structural and catalytic properties in the selective catalytic reduction of NO by NH 3, J. Catal., 197 (2001) 182-191.

[139] Y. Ren, Y. Zhang, S. Li, C.K. Law, Doping mechanism of Vanadia/Titania nanoparticles in flame synthesis by a novel optical spectroscopy technique, Proceedings of the Combustion Institute, (2014).

[140] H.K. Kammler, S.E. Pratsinis, Carbon-coated titania nanostructured particles: Continuous, one-step flame-synthesis, J. Mater. Res., 18 (2003) 2670-2676.

[141] D.H. Anjum, N.K. Memon, S.H. Chung, Investigating the growth mechanism and optical properties of carbon-coated titanium dioxide nanoparticles, Mater. Lett., 108 (2013) 134-138.

[142] W. Li, C. Ni, H. Lin, C. Huang, S.I. Shah, Size dependence of thermal stability of $TiO_2$ nanoparticles, J. Appl. Phys., 96 (2004) 6663-6668.

[143] H.X. Chen, R.A. Dobbins, Crystallogenesis of particles formed in hydrocarbon combustion, Combustion Science and Technology, 159 (2000) 109-128.

[144] Y.-H. Zhang, C.K. Chan, J.F. Porter, W. Guo, Micro-Raman spectroscopic characterization of nanosized $TiO_2$ powders prepared by vapor hydrolysis, J. Mater. Res., 13 (1998) 2602-2609.

[145] A. Williams, R.L. McCormick, R.R. Hayes, J. Ireland, H.L. Fang, Effect of biodiesel blends on diesel particulate filter performance, in, SAE Technical Paper, 2006.

[146] N.K. Memon, S.D. Tse, J.F. Al-Sharab, H. Yamaguchi, A.M.B. Goncalves, B.H. Kear, Y. Jaluria, E.Y. Andrei, M. Chhowalla, Flame synthesis of graphene films in open environments, Carbon, 49 (2011) 5064-5070.

[147] K.K. Akurati, A. Vital, U.E. Klotz, B. Bommer, T. Graule, M. Winterer, Synthesis of non-aggregated titania nanoparticles in atmospheric pressure diffusion flames, Powder Technol., 165 (2006) 73-82.

[148] K.M. Reddy, D. Guin, S.V. Manorama, A.R. Reddy, Selective synthesis of nanosized $TiO_2$ by hydrothermal route: Characterization, structure property relation, and photochemical application, J. Mater. Res., 19 (2004) 2567-2575.

[149] H.S. Jung, J.-K. Lee, M. Nastasi, S.-W. Lee, J.-Y. Kim, J.-S. Park, K.S. Hong, H. Shin, Preparation of nanoporous MgO-coated $TiO_2$ nanoparticles and their application to the electrode of dye-sensitized solar cells, Langmuir, 21 (2005) 10332-10335.

[150] S.D. Burnside, V. Shklover, C. Barbé, P. Comte, F. Arendse, K. Brooks, M. Grätzel, Self-organization of $TiO_2$ nanoparticles in thin films, Chem. Mater., 10 (1998) 2419-2425.

[151] M.C. Biesinger, L.W. Lau, A.R. Gerson, R.S.C. Smart, Resolving surface chemical states in XPS analysis of first row transition metals, oxides and hydroxides: Sc, Ti, V, Cu and Zn, Appl. Surf. Sci., 257 (2010) 887-898.

[152] J.M. Pan, B. Maschhoff, U. Diebold, T. Madey, Interaction of water, oxygen, and hydrogen with $TiO_2$ (110) surfaces having different defect densities, Journal of Vacuum Science & Technology A, 10 (1992) 2470-2476.

[153] S.N. Inamdar, S.K. Haram, Synthesis and Characterization of Uncapped $\alpha$-$Fe_2O_3$ Nanoparticles Prepared by Flame Pyrolysis of Ferrocene in Ethanol, Journal of nanoscience and nanotechnology, 6 (2006) 2155-2158.

[154] Z. Zhang, B. Wei, P. Ajayan, Self-assembled patterns of iron oxide nanoparticles by hydrothermal chemical-vapor deposition, Applied Physics Letters, 79 (2001) 4207-4209.

[155] R. Andrews, D. Jacques, A.M. Rao, F. Derbyshire, D. Qian, X. Fan, E.C. Dickey, J. Chen, Continuous production of aligned carbon nanotubes: a step closer to commercial realization, Chemical Physics Letters, 303 (1999) 467-474.

[156] M.C. Schnitzler, M.M. Oliveira, D. Ugarte, A.J.G. Zarbin, One-step route to iron oxide-filled carbon nanotubes and bucky-onions based on the pyrolysis of organometallic precursors, Chemical Physics Letters, 381 (2003) 541-548.

[157] M. Aronniemi, J. Sainio, J. Lahtinen, Chemical state quantification of iron and chromium oxides using XPS: the effect of the background subtraction method, Surf. Sci., 578 (2005) 108-123.

[158] T. Fujii, F. De Groot, G. Sawatzky, F. Voogt, T. Hibma, K. Okada, In situ XPS analysis of various iron oxide films grown by $NO_2$-assisted molecular-beam epitaxy, Physical Review B, 59 (1999) 3195.

[159] D. Barreca, G.A. Battiston, D. Berto, R. Gerbasi, E. Tondello, Chemical Vapor Deposited $Fe_2O_3$ Thin Films Analyzed by XPS, Surf. Sci. Spectra, 8 (2001) 240-245.

[160] J. Neeft, O.P. van Pruissen, M. Makkee, J.A. Moulijn, Catalysts for the oxidation of soot from diesel exhaust gases II. Contact between soot and catalyst under practical conditions, Applied Catalysis B: Environmental, 12 (1997) 21-31.

[161] M.C. Lee, W. Choi, Solid phase photocatalytic reaction on the soot/$TiO_2$ interface: the role of migrating OH radicals, The Journal of Physical Chemistry B, 106 (2002) 11818-11822.

[162] J. Oi-Uchisawa, S. Wang, T. Nanba, A. Ohi, A. Obuchi, Improvement of Pt catalyst for soot oxidation using mixed oxide as a support, Applied Catalysis B: Environmental, 44 (2003) 207-215.

[163] Y. Teraoka, K. Nakano, W. Shangguan, S. Kagawa, Simultaneous catalytic removal of nitrogen oxides and diesel soot particulate over perovskite-related oxides, Catal. Today, 27 (1996) 107-113.

[164] W. Shangguan, Y. Teraoka, S. Kagawa, Kinetics of Soot–$O_2$, Soot–NO and Soot-$O_2$-NO Reactions over Spinel-Type $CuFe_2O_4$ Catalyst, Applied Catalysis B: Environmental, 12 (1997) 237-247.

[165] S. Vyazovkin, Kinetic concepts of thermally stimulated reactions in solids: a view from a historical perspective, Int. Rev. Phys. Chem., 19 (2000) 45-60.

[166] L. Perez-Maqueda, J. Criado, P. Sanchez-Jimenez, Combined kinetic analysis of solid-state reactions: a powerful tool for the simultaneous determination of kinetic parameters

and the kinetic model without previous assumptions on the reaction mechanism, The Journal of Physical Chemistry A, 110 (2006) 12456-12462.

[167] A. Teleki, S.E. Pratsinis, K. Wegner, R. Jossen, F. Krumeich, Flame-coating of titania particles with silica, Journal of Materials Research, 20 (2005) 1336-1347.

[168] G. Ingo, S. Dire, F. Babonneau, XPS studies of $SiO_2$-$TiO_2$ powders prepared by sol-gel process, Appl. Surf. Sci., 70 (1993) 230-234.

[169] D.S. Jensen, S.S. Kanyal, N. Madaan, M.A. Vail, A.E. Dadson, M.H. Engelhard, M.R. Linford, Silicon (100)/$SiO_2$ by XPS, Surf. Sci. Spectra, 20 (2013) 36-42.

[170] J. Choi, H. Park, M.R. Hoffmann, Effects of single metal-ion doping on the visible-light photoreactivity of $TiO_2$, The Journal of Physical Chemistry C, 114 (2009) 783-792.

[171] W.J. Stark, K. Wegner, S.E. Pratsinis, A. Baiker, Flame Aerosol Synthesis of Vanadia–Titania Nanoparticles: Structural and Catalytic Properties in the Selective Catalytic Reduction of NO by NH3, Journal of Catalysis, 197 (2001) 182-191.

[172] G.N. Kryukova, G.A. Zenkovets, G. Mestl, R. Schlögl, Structural study of titanium doped vanadia and vanadium doped titania catalysts, Reaction Kinetics and Catalysis Letters, 80 (2003) 161-169.

[173] S. Lars, T. Andersson, An XPS study of dispersion and valence state of $TiO_2$ supported vanadium oxide catalysts, Catal. Lett., 7 (1990) 351-358.

[174] J. Mendialdua, R. Casanova, Y. Barbaux, XPS studies of $V_2O_5$, $V_6O_{13}$, $VO_2$ and $V_2O_3$, J. Electron. Spectrosc. Relat. Phenom., 71 (1995) 249-261.

[175] K. Bhattacharyya, S. Varma, A. Tripathi, S. Bharadwaj, A. Tyagi, Effect of vanadia doping and its oxidation state on the photocatalytic activity of $TiO_2$ for gas-phase oxidation of ethene, The Journal of Physical Chemistry C, 112 (2008) 19102-19112.

[176] K. Wegner, B. Schimmoeller, B. Thiebaut, C. Fernandez, T.N. Rao, Pilot plants for industrial nanoparticle production by flame spray pyrolysis, KONA Powder and Particle Journal, 29 (2011) 251-265.

[177] M.A. Ismail, N.K. Memon, M.S. Mansour, D.H. Anjum, S.H. Chung, Curved wall-jet burner for synthesizing titania and silica nanoparticles, Proceedings of the Combustion Institute, 35 (2015) 2267-2274.

[178] C.L. Luu, Q.T. Nguyen, S.T. Ho, Synthesis and characterization of Fe-doped $TiO_2$ photocatalyst by the sol–gel method, Advances in Natural Sciences: Nanoscience and Nanotechnology, 1 (2010) 015008.

[179] J. Yu, Q. Xiang, M. Zhou, Preparation, characterization and visible-light-driven photocatalytic activity of Fe-doped titania nanorods and first-principles study for electronic structures, Applied Catalysis B: Environmental, 90 (2009) 595-602.

[180] D. Chen, Z. Jiang, J. Geng, Q. Wang, D. Yang, Carbon and nitrogen co-doped $TiO_2$ with enhanced visible-light photocatalytic activity, Industrial & engineering chemistry research, 46 (2007) 2741-2746.

[181] M. Hirano, T. Joji, M. Inagaki, H. Iwata, Direct Formation of Iron (III)-Doped Titanium Oxide (Anatase) by Thermal Hydrolysis and Its Structural Property, Journal of the American Ceramic Society, 87 (2004) 35-41.

[182] Y. Zhang, S.G. Ebbinghaus, A. Weidenkaff, T. Kurz, H.-A. Krug von Nidda, P.J. Klar, M. Güngerich, A. Reller, Controlled iron-doping of macrotextured nanocrystalline titania, Chemistry of materials, 15 (2003) 4028-4033.

[183] X. Wang, J.-G. Li, H. Kamiyama, M. Katada, N. Ohashi, Y. Moriyoshi, T. Ishigaki, Pyrogenic iron (III)-doped $TiO_2$ nanopowders synthesized in RF thermal plasma: phase formation, defect structure, band gap, and magnetic properties, Journal of the American Chemical Society, 127 (2005) 10982-10990.

[184] W.Y. Teoh, R. Amal, L. Mädler, S.E. Pratsinis, Flame sprayed visible light-active Fe-TiO 2 for photomineralisation of oxalic acid, Catal. Today, 120 (2007) 203-213.

[185] T. Hirasawa, C.-J. Sung, Z. Yang, A. Joshi, H. Wang, Effect of ferrocene addition on sooting limits in laminar premixed ethylene–oxygen–argon flames, Combustion and Flame, 139 (2004) 288-299.

[186] J. Zhang, C.M. Megaridis, Soot suppression by ferrocene in laminar ethylene/air nonpremixed flames, Combustion and Flame, 105 (1996) 528-540.

[187] R.L. Vander Wal, L.J. Hall, Ferrocene as a precursor reagent for metal-catalyzed carbon nanotubes: competing effects, Combustion and flame, 130 (2002) 27-36.

[188] K. Kuwana, K. Saito, Modeling ferrocene reactions and iron nanoparticle formation: Application to CVD synthesis of carbon nanotubes, Proceedings of the combustion institute, 31 (2007) 1857-1864.

[189] G.P. Fotou, S.J. Scott, S.E. Pratsinis, The role of ferrocene in flame synthesis of silica, Combustion and flame, 101 (1995) 529-538.

[190] G. Kothleitner, F. Hofer, Optimization of the signal to noise ratio in EFTEM elemental maps with regard to different ionization edge types, Micron, 29 (1998) 349-357.

[191] L. Balcells, C. Frontera, F. Sandiumenge, A. Roig, B. Martínez, J. Kouam, C. Monty, Absence of ferromagnetism in Fe-doped $TiO_2$ nanoparticles, Applied Physics Letters, 89 (2006) 122501.

[192] R. Suryanarayanan, V.M. Naik, P. Kharel, P. Talagala, R. Naik, Room temperature ferromagnetism in spin-coated anatase-and rutile-$Ti_{0.95}Fe_{0.05}O_2$ films, J. Phys.: Condens. Matter, 17 (2005) 755.

[193] L. Balcells, C. Frontera, F. Sandiumenge, A. Roig, B. Martínez, J. Kouam, C. Monty, Absence of ferromagnetism in Fe-doped $TiO_2$ nanoparticles, Appl. Phys. Lett., 89 (2006) 2501.

[194] J. Coey, K. Wongsaprom, J. Alaria, M. Venkatesan, Charge-transfer ferromagnetism in oxide nanoparticles, J. Phys. D: Appl. Phys., 41 (2008) 134012.

[195] R. Janisch, P. Gopal, N.A. Spaldin, Transition metal-doped $TiO_2$ and ZnO—present status of the field, J. Phys.: Condens. Matter, 17 (2005) R657.

[196] J.M.D. Coey, P. Stamenov, R. Gunning, M. Venkatesan, K. Paul, Ferromagnetism in defect-ridden oxides and related materials, New Journal of Physics, 12 (2010) 053025.

[197] T. Fujii, F. De Groot, G. Sawatzky, F. Voogt, T. Hibma, K. Okada, In situ XPS analysis of various iron oxide films grown by $NO_2$-assisted molecular-beam epitaxy, Physical Review B, 59 (1999) 3195.

[198] K. Bapna, D. Phase, R. Choudhary, Study of valence band structure of Fe doped anatase $TiO_2$ thin films, J. Appl. Phys., 110 (2011) 043910.

[199] B. Chen, A.J. Haring, J.A. Beach, M. Li, G.S. Doucette, A.J. Morris, R.B. Moore, S. Priya, Visible light induced photocatalytic activity of $Fe^{3+}/Ti^{3+}$ co-doped $TiO_2$ nanostructures, RSC Advances, 4 (2014) 18033-18037.

[200] L. Sun, J.X. Lin, L. Wang, K.X. Song, Preparation and characterization of $Fe^{3+}$-doped $TiO_2$/diatomite composite, in: Applied Mechanics and Materials, Trans Tech Publ, 2013, pp. 15-18.

[201] F. Xu, S.D. Tse, J.F. Al-Sharab, B.H. Kear, Flame synthesis of aligned tungsten oxide nanowires, Appl. Phys. Lett., 88 (2006) -.

[202] W. Merchan-Merchan, A.V. Saveliev, L.A. Kennedy, Flame synthesis of molybdenum oxide whiskers, Chem. Phys. Lett., 422 (2006) 72-77.

[203] S. Li, M. Samy El-Shall, Synthesis and characterization of photochromic molybdenum and tungsten oxide nanoparticles, Nanostruct. Mater., 12 (1999) 215-219.

[204] D.H. Anjum, N.K. Memon, S.H. Chung, Investigating the growth mechanism and optical properties of carbon-coated titanium dioxide nanoparticles, Materials Letters, 108 (2013) 134-138.

[205] A.J. Rulison, P.F. Miquel, J.L. Katz, Titania and silica powders produced in a counterflow diffusion flame, Journal of Materials Research, 11 (1996) 3083-3089.

[206] J.J. Wang, S.Q. Li, W. Yan, S.D. Tse, Q. Yao, Synthesis of TiO2 nanoparticles by premixed stagnation swirl flames, P Combust Inst, 33 (2011) 1925-1932.

[207] Y. Zhang, L. Shuiqing, S. Deng, Q. Yao, S.D. Tse, Direct synthesis of nanostructured $TiO_2$ films with controlled morphologies by stagnation swirl flames, Journal of Aerosol Science, 44 (2012) 71-82.

[208] Y. Sung, V. Raman, R.O. Fox, Large-eddy-simulation-based multiscale modeling of $TiO_2$ nanoparticle synthesis in a turbulent flame reactor using detailed nucleation chemistry, Chemical Engineering Science, 66 (2011) 4370-4381.

[209] D. Kim, Y.S. Gil, T.W. Chung, S.H. Chung, Characteristics of Premixed Flames Stabilized in an Axisymmetric Curved-Wall Jet Burner with Tip Modification, Combust Sci Technol, 181 (2009) 1397-1412.

[210] O.I. Arabi–Katbi, S.E. Pratsinis, P.W. Morrison, C.M. Megaridis, Monitoring the flame synthesis of $TiO_2$ particles by in-situ FTIR spectroscopy and thermophoretic sampling, Combust. Flame, 124 (2001) 560-572.

[211] H. Zhao, X.F. Liu, S.D. Tse, Effects of pressure and precursor loading in the flame synthesis of titania nanoparticles, Journal of Aerosol Science, 40 (2009) 919-937.

[212] A.S. Barnard, H. Xu, An environmentally sensitive phase map of titania nanocrystals, ACS nano, 2 (2008) 2237-2242.

[213] K. Wegner, S.E. Pratsinis, Nozzle-quenching process for controlled flame synthesis of titania nanoparticles, AlChE J., 49 (2003) 1667-1675.

[214] J.R. Jensen, T. Johannessen, S. Wedel, H. Livbjerg, Preparation of $ZnO–Al_2O_3$ particles in a premixed flame, J. Nanopart. Res., 2 (2000) 363-373.

[215] H. Briesen, A. Fuhrmann, S.E. Pratsinis, The effect of precursor in flame synthesis of SiO2, Chemical Engineering Science, 53 (1998) 4105-4112.

[216] W. Li, C. Liu, Y. Zhou, Y. Bai, X. Feng, Z. Yang, L. Lu, X. Lu, K.-Y. Chan, Enhanced Photocatalytic Activity in Anatase/$TiO_2$ (B) Core− Shell Nanofiber, The Journal of Physical Chemistry C, 112 (2008) 20539-20545.

[217] I. Kholmanov, E. Barborini, S. Vinati, P. Piseri, A. Podesta, C. Ducati, C. Lenardi, P. Milani, The influence of the precursor clusters on the structural and morphological evolution of nanostructured $TiO_2$ under thermal annealing, Nanotechnology, 14 (2003) 1168.

[218] Z. Zhang, C.C. Wang, R. Zakaria, J.Y. Ying, Role of particle size in nanocrystalline $TiO_2$-based photocatalysts, The Journal of Physical Chemistry B, 102 (1998) 10871-10878.

[219] T. Peltola, M. Jokinen, H. Rahiala, E. Levänen, J. Rosenholm, I. Kangasniemi, A. Yli-Urpo, Calcium phosphate formation on porous sol-gel-derived $SiO_2$ and $CaO-P_2O_5-SiO_2$ substrates in vitro, Journal of biomedical materials research, 44 (1999) 12-21.

[220] T. Kokubu, M. Yamane, Thermal and chemical properties of $TiO_2-SiO_2$ porous glass-ceramics, Journal of Materials Science, 22 (1987) 2583-2588.

[221] M.B. Fernandes, J.O. Skjemstad, B.B. Johnson, J.D. Wells, P. Brooks, Characterization of carbonaceous combustion residues. I. Morphological, elemental and spectroscopic features, Chemosphere, 51 (2003) 785-795.

[222] M. Wooldridge, P. Torek, M. Donovan, D. Hall, T. Miller, T. Palmer, C. Schrock, An experimental investigation of gas-phase combustion synthesis of $SiO_2$ nanoparticles using a multi-element diffusion flame burner, Combust. Flame, 131 (2002) 98-109.

[223] A.L. Patterson, The Scherrer Formula for X-Ray Particle Size Determination, Physical Review, 56 (1939) 978-982.

[224] X.Y. Kong, Y. Ding, R. Yang, Z.L. Wang, Single-crystal nanorings formed by epitaxial self-coiling of polar nanobelts, Science, 303 (2004) 1348-1351.

[225] R.L. Penn, J.F. Banfield, Oriented attachment and growth, twinning, polytypism, and formation of metastable phases: Insights from nanocrystalline $TiO_2$, Am. Mineral, 83 (1998) 1077-1082.

[226] T. Tachikawa, M. Fujitsuka, T. Majima, Mechanistic Insight into the $TiO_2$ Photocatalytic Reactions: Design of New Photocatalysts, The Journal of Physical Chemistry C, 111 (2007) 5259-5275.

[227] S.E. Pratsinis, W. Zhu, S. Vemury, The role of gas mixing in flame synthesis of titania powders, Powder Technol., 86 (1996) 87-93.

[228] M.S. Mansour, I. Alkhesho, S.H. Chung, Stabilization and structure of n-heptane flame on CWJ-spray burner with kHZ SPIV and OH-PLIF, Exp. Therm Fluid Sci., (2015).

[229] T. Gautam, Lift-off Heights and Visible Lengths of Vertical Turbulent Jet Diffusion Flames in Still Air, Combust. Sci. Technol., 41 (1984) 17-29.

[230] G. Hartung, J. Hult, C. Kaminski, J. Rogerson, N. Swaminathan, Effect of heat release on turbulence and scalar-turbulence interaction in premixed combustion, Physics of Fluids (1994-present), 20 (2008) 035110.

[231] H. Zhao, X. Liu, D.T. Stephen, Effects of pressure and precursor loading in the flame synthesis of titania nanoparticles, J. Aerosol Sci, 40 (2009) 919-937.

[232] J.R. McCormick, B. Zhao, S.A. Rykov, H. Wang, J.G. Chen, Thermal stability of flame-synthesized anatase $TiO_2$ nanoparticles, The Journal of Physical Chemistry B, 108 (2004) 17398-17402.

[233] W. Zhou, W. Li, J.-Q. Wang, Y. Qu, Y. Yang, Y. Xie, K. Zhang, L. Wang, H. Fu, D. Zhao, Ordered mesoporous black $TiO_2$ as highly efficient hydrogen evolution photocatalyst, J. Am. Chem. Soc., 136 (2014) 9280-9283.

# Curriculum Vitae

Mohamed Anwar Ismail is a PhD Candidate in Mechanical Engineering (ME) program at King Abdullah University of Science and Technology (KAUST). He obtained his Bachelor and Master of Science (MSc) degrees in Mechanical Power Engineering from Faculty of Engineering, Zagazig University, Egypt. He worked as Teaching/Lecturer Assistant at Zagazig University for more than five years before joining KAUST on February 2011. He won the Best Oral Presentation Award at Nanotech Dubai 2015 in addition to the Academic Excellence Award at KAUST on December 2011. His research focuses on combustion synthesis and characterization of advanced/coated nanomaterials using various flame configurations as well as diesel soot oxidation.

## Publications

### Journal Publications

- **Mohamed A. Ismail**, Nasir K. Memon, Morkous S. Mansour, Dalaver H. Anjum, and Suk Ho Chung, Synthesis of titanium dioxide nanoparticles using a double-slit curved-wall jet burner. Combustion Science and Technology (2016) Vol. 188, Issues 4 and 5.
- **Mohamed A. Ismail**, Nasir K. Memon, Mohamed N. Hedhili, Dalaver H. Anjum, and Suk Ho Chung, Synthesis of $TiO_2$ nanoparticles containing Fe, Si, and V using multiple diffusion flames and catalytic oxidation capability of carbon-coated nanoparticles. Journal of Nanoparticle Research (2015) Vol. 18, Issue 1, Pages 1-14.
- **Mohamed A. Ismail**, Nasir K. Memon, Morkous S. Mansour, Dalaver H. Anjum, and Suk Ho Chung, Curved wall-jet burner for synthesizing titania and silica nanoparticles, Proceedings of the Combustion Institute (2015) Vol. 35, Issue 2, Pages 2267–2274.
- Abhijeet Raj, Russell Tayouo, Dongkyu Cha, Liang Li, **Mohamed A. Ismail**, and Suk Ho Chung, Thermal fragmentation and deactivation of combustion-generated soot particles, Combustion and Flame (2014) Vol. 161, Issue 9, Pages 2446-2457.
- M.R. Shaalan, H.A. El Salmawy, and **M. Anwar Ismail**, Prediction of Flow and Combustion Characteristics for a Gas Turbine Combustor Burning Low Heating Value Fuel, Proc. ASME. Vol.2 (2010), ASME paper GT2010-22156.

**Conferences and Presentations**

- **Mohamed A. Ismail**, Morkous Mansour, Nasir K. Memon, Dalaver H. Anjum, and Suk Ho Chung, Synthesis Of Titanium Dioxide Nanoparticles Using A Double-Slit Curved-Wall Jet Burner, 9th Mediterranean Combustion Symposium, Rhodes, Greece, June 7-11, 2015.
- Nasir K. Memon, **Mohamed A. Ismail**, Dalaver H. Anjum, and Suk Ho Chung, Catalytic Oxidation of Carbon using $TiO_2$ based Nanoparticles prepared using Flame Synthesis, TechConnect World Innovation Conference & Expo, Washington DC, June 14-17, 2015.
- **Mohamed A. Ismail**, Nasir K. Memon, Mohamed N. Hedheli, Dalaver H. Anjum, Suk Ho Chung, Flame Synthesis of doped/coated TiO2 nanoparticles using multiple diffusion flames, 5th Saudi Arabian Section of the Combustion Institute (SAS-CI) Annual Meeting, KACST, Ryiadh, Saudi Arabia, May 3-4, 2015.
- **Mohamed A. Ismail**, Morkous Mansour, Nasir K. Memon, and Suk Ho Chung, Synthesis of titanium dioxide nanoparticles using a curved-wall burner with central port, 7th European Combustion Meeting, Budapest, Hungary, March 30- April 2, 2015.
- **Mohamed A. Ismail**, Morkous Mansour, Nasir K. Memon, and Suk Ho Chung, Effects of different configurations of curved-wall jet (CWJ) burner on the flame synthesis of titanium dioxide nanoparticles, 2nd Edition Nanotech Dubai 2015 International Conference & Exhibition (Nanotech Dubai 2015), Dubai, United Arab Emirates, March 16- 18, 2015.
- **Mohamed A. Ismail**, Nasir K. Memon, Morkous S. Mansour, Dalaver H. Anjum, and Suk Ho Chung, Double-slit curved wall-jet burner for synthesizing titanium dioxide nanoparticles, 2014 MRS Fall Meeting & Exhibit, Boston, Massachusetts, USA, Nov. 30-Dec. 5, 2014.
- **Mohamed A. Ismail**, N.K. Memon, D.H. Anjum, and S.H. Chung, Synthesis of coated titanium dioxide nanoparticles using a multi-element diffusion flame burner, The 3rd biennial conference of the Combined Australian Materials Societies (CAMS 2014), University of Sydney, Sydney, Australia, Nov. 26- 28, 2014.
- **Mohamed A. Ismail**, Nasir K. Memon, Morkous S. Mansour, Dalaver H. Anjum, and Suk Ho Chung, Curved wall-jet burner for synthesizing titanium dioxide and silicon dioxide, 35th International Symposium on Combustion, San Francisco, USA, August 3- 8, 2014.

- **Mohamed A. Ismail**, Curved wall-jet burner for synthesizing nanoparticles, SAS-CI 4rd Annual Meeting, KAUST, Thuwal, Saudi Arabia, 29th April 2014.
- **Mohamed A. Ismail**, K. Al-Qurashi, L. Li, and S.H. Chung, Effect of MTBE-Blend on Diesel Soot Reactivity and Nanostructure, 9th Asia-Pacific Conference on Combustion, Gyeongju Hilton, Gyeongju, Korea, 19-22 May 2013.
- Nasir K. Memon, **Mohamed A. Ismail**, Dalaver H. Anjum, Suk Ho Chung, One-Step Combustion Synthesis of Carbon-Coated Nanoparticles using Multiple-Diffusion Flames, 8th U. S. National Combustion Meeting, the University of Utah, USA, May 19-22, 2013.
- **Mohamed A. Ismail** and Suk Ho Chung, Effect of MTBE-Blend on Diesel Soot Characteristics, SAS-CI 3rd Annual Meeting, Dhahran, Saudi Aramco, Saudi Arabia, 29th April 2013.